DUCTILE FRACTURE MECHANISMS IN A STRUCTURAL STEEL

by

YAO-WU SHI

A thesis submitted for the degree of

Doctor of Philosophy

Department of Metallurgy and Materials Engineering

The University of Aston in Birmingham

1982

PAGE NUMBERS CUT OFF IN ORIGINAL

ACKNOWLEDGEMENTS

The author is very grateful to his project supervisor, Professor J.T. Barnby, Head of the Metallurgy and Materials Engineering Department, for his guidance and encouragement. The author is grateful to the staff, technicians and his research colleagues for their help. The author wishes to thank Mrs. P. Durose for typing this thesis, and to thank Dr. J.D. Harrison and Dr. O.L. Tower, the Engineering Department at the Welding Institute, for meaningful advice and suggestions.

Finally, the author wishes to acknowledge the British Council and Chinese Government for their financial support of this work.

THE UNIVERSITY OF ASTON IN BIRMINGHAM

Title: DUCTILE FRACTURE MECHANISMS IN A STRUCTURAL STEEL

Name: YAO-WU SHI

Degree: Ph.D. 1982

ABSTRACT

Microstructural fracture processes in a BS4360 Grade 50D structural steel with lower sulphur content were studied in smooth tensile specimen tests and Charpy-size bend bar tests. Based on the experimental analysis, an experimental void growth relation with the plastic strain and stress triaxiality and multiplying factor on void growth were determined. Experimental results show that the void growth relation can be reasonably used to estimate the constraint in the specimens containing the notch or crack, also they can be used to evaluate the variations of the stress triaxiality in front of the notch and crack tip under general yielding condition. Side-grooves obviously increase the constraint of the CVN specimens. Strain hardening leads to increasing the stress triaxiality, and decelerating the net void growth. This is specially true for the values of stress triaxiality more than about one. Additionally, the effect of the stress triaxiality on the critical void growth corresponding to the onset of ductile tearing was preliminarily investigated.

In this work, a large number of smaller specimens were tested to investigate the ductile-brittle transition behaviour of the structural steel. A void growth rate explanation was suggested for evaluating the temperature transition behaviour. The elastic-plastic fracture toughness values based on small specimen tests, such as precracked side-grooved bending specimen and short bar tensile specimen, may give large overestimates of the plane strain fracture toughness.

KEY WORDS: Structural steel, ductile fracture, void nucleation, void growth, plastic strain, stress triaxiality, ductile-brittle transition behaviour

CONTENTS

SECTION PAGE

LIST OF TABLES

LIST OF FIGURES

LIST OF PLATES

Section 1

BASIC PRINCIPLES AND DEVELOPMENTS IN FRACTURE MECHANICS

1.1 INTRODUCTION

In spite of the best efforts of design engineers and material specialists, and in spite of well-thought-out procedures for quality assurance and control, engineering components still fail in service from time to time. In the majority of cases the failure does not lead to serious consequences. However, the occasional dramatic failure of steel structures such as bridges, ships, pressure vessels, pipelines and airplanes may lead to serious consequences which can cause serious financial loss, environmental contamination or loss of life [1, 2]. For example, on the 27th March 1980, a drilling platform "Alexander L Kielland" capsized completely for about half an hour. Of the 212 men on board when the accident took place, a total of 89 persons were saved. 123 men lost their lives in the accident. A fracture has been proven in the welding connection between the hydrophone fitting and horizontal brace. The facture was initiated by fatigue.[3]

Numerous factors such as material toughness, design rationality, manufacturing technology, residual stresses, constraint, service conditions, etc. can contribute to brittle fractures in large engineering structures. However, the approach of fracture mechanics has shown that there are three primary factors which control the

susceptibility of a structure to brittle fracture. They are material toughness (Kc), crack size (a) and stress level (σ). All other factors such as temperature, loading rate, stress concentrations, residual stresses, etc. only affect the above three primary factors.

If the relationship between material toughness, nominal stress, and crack size is researched, there are many combinations of stress and flaw size, which may cause fracture in a structure which is fabricated from a steel having a particular value of Kc at a particular service temperature, loading rate, and plate thickness. Therefore, it is possible to establish a fracture-resistance design criterion quantitatively using fracture mechanics approach. It is inconceivable today to make any significant assessments of structure safety without consideration of fracture mechanics. This is particularly true for the development of airplanes and spacecraft, pressure vessels (especially nuclear pressure vessels) ships and deep sea oil platforms. Fracture mechanics has now become an important branch of materials and engineering science.

Some limitation exists in engineering structures for the application of Linear Elastic Fracture Mechanics. They impose, for instance, a minimum size for specimens used for measuring plane strain fracture toughness. This limitation is, however, very often broken. This happens

for instance in structures made of thin plate, or in structures made of a touch material, or when there are space limitations (such as the surveillance programme specimens in a nuclear pressure vessel) or when for economic reasons the specimen size is smaller than the full size of so-called "valid specimens". In these cases, it is the task of Elastic Plastic Fracture Mechanics, which studies the relationship between geometry, the material parameters, ductile crack behaviour, and the mechanisms of the failure. The importance of this objective appears more and more obvious.

1.2 Linear Elastic Fracture Mechanics

Linear elastic fracture mechanics generally is described by two important approaches. The first is based on an energy balance approach, while the second is based on the singular nature of the stress distribution near a crack tip[4].

1.2.1 The Griffith Theory and its Modifications

Griffith [5] first developed the analysis of fracture behaviour of components which contain sharp discontinuities. Crack extension will require energy, which may be supplied from the work done by the applied external load and from the strain energy stored in the structure. Griffith calculated the change in stored energy due to the introduction of a through-thickness crack into a thin infinite plate. The change in elastic strain energy per unit thickness is given by

$$U_e = \frac{\sigma^2 \pi a^2}{E} \qquad \text{.....(1.1)}$$

where a is the half-length of a through-thickness crack, σ is the uniform stress, applied at infinity and E is Young's modulus. The supply of energy will increase with crack extension. Griffith compared the change in strain energy U_e, with the surface energy of the crack, given by

$$U_s = 4\ a\ \gamma \qquad \text{.....(1.2)}$$

where γ is the surface energy per unit area. This approach is that instability would occur where a small increment of crack extension, da, generated $dU_e > dU_s$. Thus the equilibrium condition for crack extension is

$$\frac{d}{da}\ (U_e - U_s) = \frac{d}{da}\ \left(\frac{\sigma^2 \pi a^2}{E} - 4a\gamma\right) = 0 \qquad \text{.....(1.3)}$$

or the strain energy release rate

$$\frac{\sigma^2 \pi a}{E} = 2\gamma$$

which leads to the well-known Griffith relationship

$$\sigma_c = \left[\frac{2E\gamma}{\pi a_c}\right]^{\frac{1}{2}} \qquad \text{.....(1.4)}$$

In the above equation the subscript c denotes the critical value of stress and crack size. And it is appropriate to thin plate and plane stress conditions. For fracture under plane strain conditions it would be appropriate to substitute $E/(1-\nu^2)$ for E in the above equations, where ν is Poisson's ratio. Irwin [6] suggested that the Griffith theory for ideally brittle materials could be modified and applied to metal materials. Fracture in these materials

is preceded by plastic flow. The plastic deformation caused at the crack tip region is transformed in plastic work per unit increase in area of the crack surface, and which is therefore equivalent to an increased surface energy. Thus, the material resistance to crack extension is equal to the sum of the elastic surface energy, γ_e, and plastic strain work, γ_p, accompanying crack extension. Consequently, Eq. (1.4) becomes

$$\sigma_c = \left[\frac{2E\ (\gamma_e + \gamma_p)}{\pi\ a_c} \right]^{\frac{1}{2}} \quad \ldots\ldots\ldots\ldots\ldots (1.5)$$

It should be noted that Eq.(1.5) is strictly relevant to a through-thickness crack in an infinite plate in which fracture is preceded by the formation of a near-tip plastic zone which is small in comparison to the crack size and plate thickness.

Irwin and Kies [7, 8] further showed that for a crack tip the strain energy release rate per unit thickness was given by

$$\frac{dUe}{da} = \frac{d}{da}\left[\frac{P^2C}{2}\right] = \frac{P^2}{2}\ \frac{dC}{da} \quad \ldots\ldots\ldots\ldots\ldots (1.6)$$

where P is the applied force, C is the elastic compliance per unit thickness. This relationship has made a very important contribution to fracture mechanics, since it can be applied to any geometry subjected to elastic loading. By measuring the linear elastic compliance of similar specimens containing different crack lengths it might be possible to compute values of dC/da as a function of crack length. Furthermore, the fracture load for a test

specimen and the appropriate value of dC/da could be substituted in Eq (1.6) to give a critical strain energy release rate for fracture initiation.

1.2.2 Irwin's Stress Intensity Approach

Irwin [9] has shown that the stress field at the crack tip is characterised by a singularity of stress which decreases in proportion to the inverse square root of the distance from the crack tip. Furthermore, the stress field in the region dominated by the singularity of stress can be regarded as one or combination of three invariant loading modes. The three loading modes are: Mode I, opening or tensile mode; Mode II, forward or in-plane shear mode, Mode III, paraller or anti-plane shear mode, as shown in Fig. 1.1.

The singular stress and displacement fields in the vicinity of crack tip for Mode I may be written as follows

$$\begin{matrix}\sigma_{xx}\\ \sigma_{yy}\\ \tau_{xy}\end{matrix} = \frac{K_I}{(2\pi r)^{\frac{1}{2}}} \begin{bmatrix} \cos\frac{\theta}{2}\left(1-\sin\frac{\theta}{2}\sin\frac{3\theta}{2}\right) \\ \cos\frac{\theta}{2}\left(1+\sin\frac{\theta}{2}\sin\frac{3\theta}{2}\right) \\ \sin\frac{\theta}{2}\cos\frac{\theta}{2}\cos\frac{3\theta}{2} \end{bmatrix} + \cdots$$

$$\sigma_{zz} = \nu\,(\sigma_{xx} + \sigma_{yy}) \text{ for plane strain.}$$
$$\sigma_{zz} = 0 \text{ for plane stress.} \qquad \ldots\ldots\ldots\ldots\ldots\ldots (1.7)$$

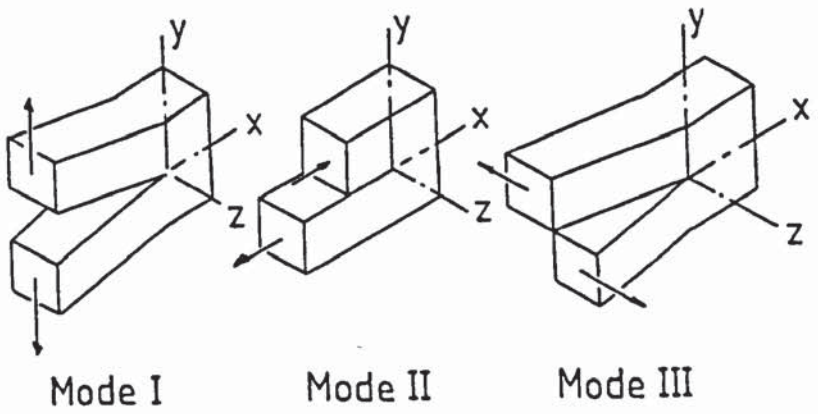

FIGURE 1.1 Basic modes of crack surface displacements (After M. G. Dawes)

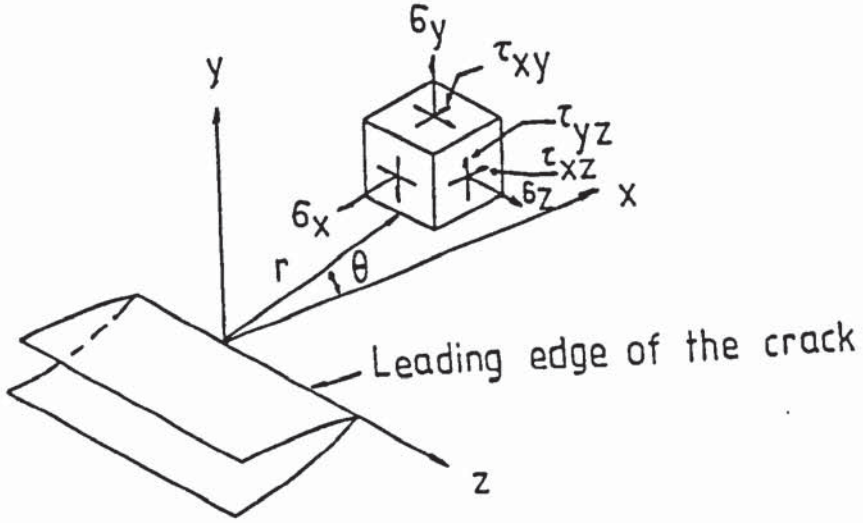

FIGURE 1.2 Co-ordinate system and stress components ahead of a crack tip (After S. T. Rolfe and J. M. Barsom)

$$\begin{matrix} u \\ v \end{matrix} = \frac{K_I}{G}\left(\frac{r}{2\pi}\right)^{\frac{1}{2}} \begin{bmatrix} \cos\frac{\theta}{2}\left(1-2\nu+\sin^2\frac{\theta}{2}\right) \\ \sin\frac{\theta}{2}\left(2-2\nu-\cos^2\frac{\theta}{2}\right) \end{bmatrix} + \cdots$$

$w = 0$ for plane strain

$w = -\frac{\nu}{E}\int (\sigma_{xx} + \sigma_{yy})\, dz$ for plane stress,

where the stress components and the co-ordinates r and θ are shown in Fig. 1.2; u, v, and w are the displacements in the X, Y and Z directions, respectively; ν is Poisson's ratio ; and G is the shear modulus of elasticity. Mode I loading is the most important form. Similar expressions could be derived for Mode II and III, but they are omitted here.

This analysis indicates that the stress and displacement fields in the vicinity of the crack tip can be characterised by a single parameter,K, called the stress intensity factor. The stress intensity factor is independent of r and θ and the distribution of the stresses for each mode. However, it expresses the magnitude of the loading forces and also depends on the crack size. Thus the stress intensity governs the magnitude of the forces acting in the crack tip region. The Mode I stress intensity may be expressed in the general form

$$K_I = C_I\, \sigma\, (\pi a)^{\frac{1}{2}} \qquad \text{.....(1.8)}$$

where σ is the applied stress in y direction, remote from the crack; C_I is the relevant constant. Since K_I provides

a one parameter measure of the severity of the crack tip environment, it is logical to characterise resistance to fracture by a critical value, K_{IC} called fracture toughness, which can be measured in laboratory tests. Irwin established a relationship between K_I and the strain energy release rate, G, as follows

$$G_I = \frac{K_I^2}{E'} \qquad \text{.....(1.9)}$$

where G could be regarded as a force tending to cause crack extension. $E' = E$ for plane stress, and $E' = E/(1-\nu^2)$ for plane strain.

1.2.3 Plastic Zone at Crack Tip

In metallic materials a plastic zone propagates at the crack tip, even though the macroscopic behaviour is approximately elastic. Since nowhere ahead of the crack tip the stress can exceed the relevant yield stress, we may estimate the size of the plastic zone in terms of its radius, r_y, assuming it to have a circular shape. At the onset of fracture this is

$$r_y = \frac{1}{A}\left(\frac{K_{IC}}{\sigma_{ys}}\right)^2 \qquad \text{.....(1.10)}$$

A is equal to 2π for plane stress condition and is 5.6π for plane strain condition. σ_{ys} is the uniaxial yield stress.

The crack may be thought as having an imaginary tip at a distance, r_y, ahead of the real tip, as shown in Fig. 1.3. When the plastic zone is very small, the imaginary and real crack tips virtually coincide. However, for larger plastic zones, the effective crack length is greater than the real crack length by a small addition of r_y. If it is acceptable to replace the real crack by the effective crack, the scope of LEFM can be extended to the elastic body with the small scale yielding.

1.2.4 Effect of Thickness or Constraint on Fracture Toughness

A variation in fracture toughness with increasing plate thickness or constraint is shown in Fig. 1.4. For thin sheets in tension, there is a condition of plane stress. Fracture occurs by local shearing. Crack faces are therefore at 45^{o} to the gross tensile stress direction. For thicker plate, the through-thickness stress is developed. The material very close to the crack tip undergoes a triaxial stress condition. Under the triaxial stress conditions the resolved shear components of the local stress are reduced and yielding cannot take place until the local stress reaches a value of nearly three times the uniaxial yield stress. The result of the higher local stress at yield is a smaller yield zone. This smaller plastic zone fractures through plate centre and consumes much less energy than the plastic zone under plane stress condition, as small plastic zone represents the small volume of metal affected by plastic flow.

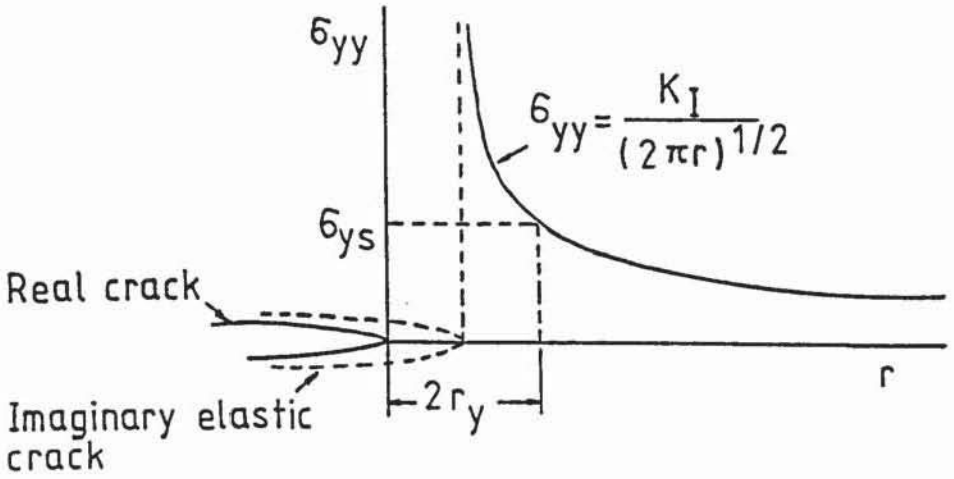

FIGURE 1.3 Imaginary elastic crack and assumed elastic stress field

FIGURE 1.4 Effect of thickness on fracture toughness (from W. J. Vol. 60, 1981, pp.38)

Of course, there is no constraint stress at the side free surfaces in the thickness direction, so that near these surfaces the conditions are similar to plane stress for thin sheets. Fig. 1.5 demonstrates the change of plastic zone shape in the crack tip vicinity for thicker plate. The plastic zone in cylinder is in the centre of plate thickness, and the bell-shaped ends of the cylinder are in the plate surfaces. Though the plane strain fracture always has shear fracture regions at its edges, termed shear lips, these are negligible once the fracture is of the plane strain type over 90% of the thickness. In this case, toughness reaches a critical value K_{IC} [10].

Recently, considerable effort has been devoted to investigate the effects of side grooves on the fracture toughness of ductile materials [11, 12, 13]. Side-grooves effectively thicken the specimen by restricting or eliminating regions of through-thickness deformation. Therefore, small specimens may be used to characterise the toughness of large structures. It should be noted that the notch acuity and crack depth have a considerable influence upon the fracture toughness. For example, a compact specimen with crack length to specimen width ratio of greater than 0.5 and full proportional thickness to width ratio, 0.5, have a geometric constraint which will give it a constraint nearly equivalent to that of a larger specimen [14].

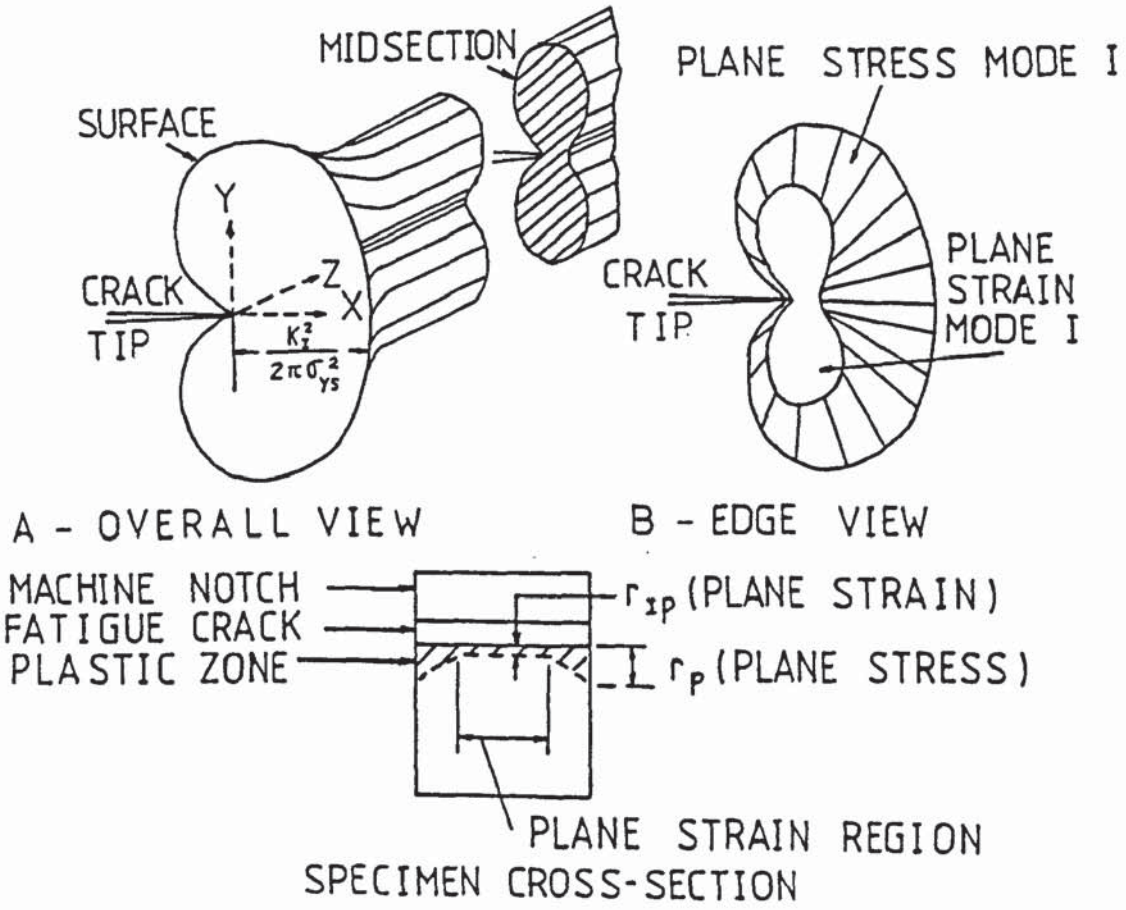

FIGURE 1.5 Schematic representation of plastic zone ahead of a crack tip (After S. T. Rolfe and J. M. Barsom).

1.2.5. Effect of Temperature on Fracture Toughness

For ferritic structural steels, some unstable fracture behaviours are shown schematically in Fig. 1.6. This figure also demonstrates the relevance of LEFM and yielding fracture mechanics (YFM) to the well-known brittle to ductile transition with rising temperatures[4]. It shows that LEFM and K_{IC} is applicable to the predominantly elastic fractures which occur in the lower shelf region of the fracture transition, whereas YFM based on CTOD and J-integral applies to the quasi-brittle fractures in the transition region. On the upper shelf, failure in structural steels is generally controlled by plastic collapse and it will be sufficient to ensure that the net stress does not exceed the flow stress.

Usually, there are two transitions in fracture behaviour with temperature. One is referred to as a fracture mode transition with temperature, the other is a transition from plane strain to plane stress (elastic-plastic) behaviour with increasing temperature. Fractographic analysis shows that the fracture toughness transition temperature is associated with the onset of change in the microscopic fracture mode ahead of the crack tip. The microscopic fracture behaviour can change with increasing temperature from complete cleavage or quasi-cleavage to a mixture of quasi-cleavage with tear dimples, and large flat tear area, even though the macroscopic state of stress is still

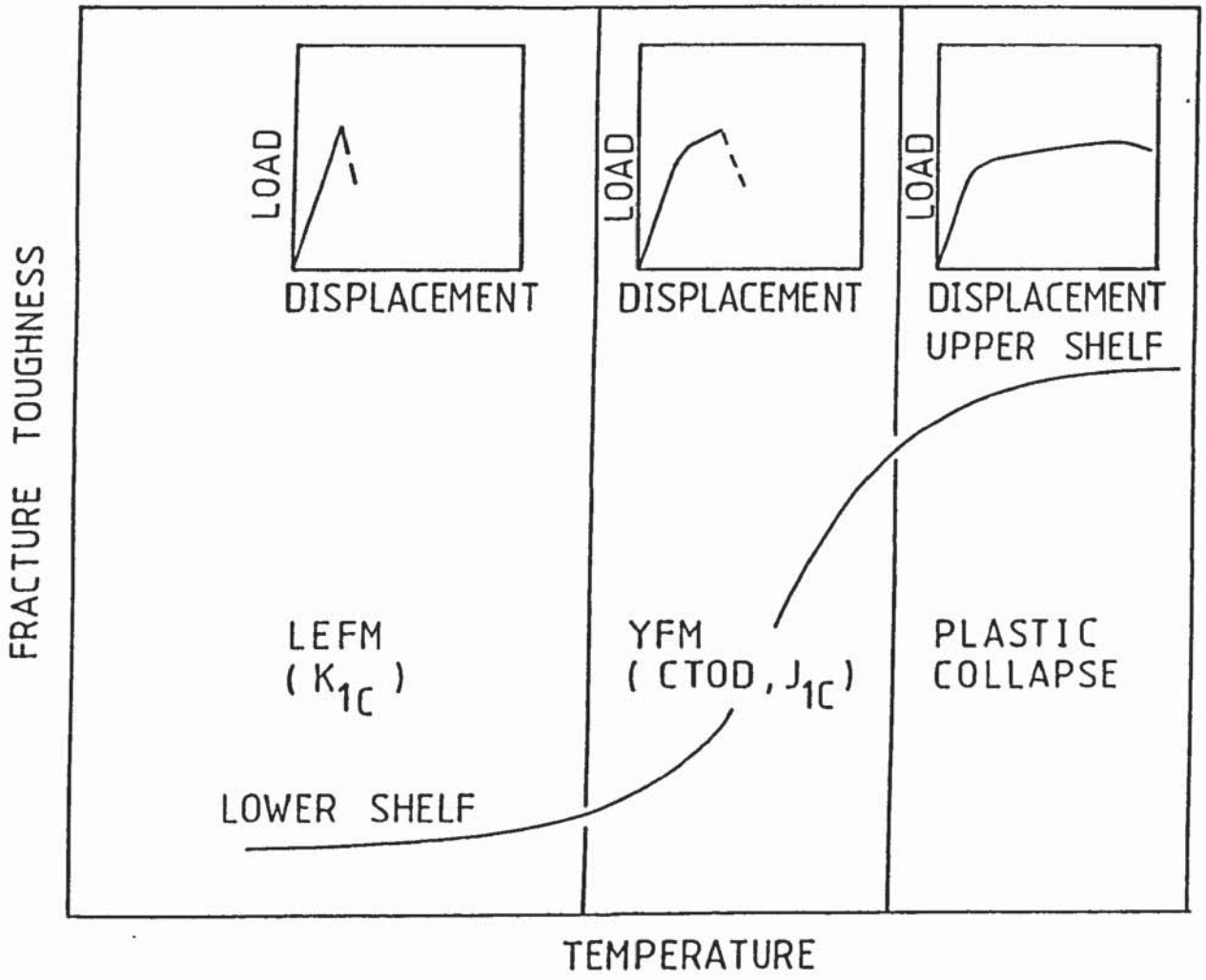

FIGURE 1.6 Fracture behaviour transition of ferritic steels (After M. G. Dawes)

the state of plane strain. This transition in microscopic fracture behaviour leads to the rapid change in the plane strain fracture toughness. As a test specimen is loaded, some local plastic flow will occur at the crack tip, and the crack tip will be blunted slightly. Specially, if the inherent toughness of the structural material is ductile at the particular test temperature and loading rate, the crack tip is blunted by plastic deformation. As a result, the limit of plane-strain constraint is exceeded. At temperatures above this test temperature the inherent toughness begins to increase rapidly with increasing test temperature because the effects of the crack blunting and relaxation of plane-strain constraint are combined. That is, the crack blunting leads to a relaxation in constraint which causes increased plastic flow, which leads to additional crack blunting. Thus elastic-plastic behaviour begins to occur rapidly at increasing test temperatures once this plane-strain constraint (thickness plus notch acuity) is exceeded.

Therefore, the structural materials first undergo a gradual increase in toughness with increasing temperature, referred to as the fracture mode transition. Then as the inherent toughness increases, and the constraint at the crack tip decreases, the materials undergo a very rapid increase in toughness as they begin to exhibit elastic-plastic behaviour. At this point, the LEFM analysis is no longer valid because of the excessive yielding at the crack tip. The loss of plane strain conditions results in a significant

increase in the strain to fracture. The small increase in load after net section yielding in laboratory specimens may be accompanied by a relatively large increase in displacement or strain to fracture. Such fractures may or may not be preceded by stable crack growth.

1.2.6 Experimental Determination of K_{IC}

The property K_{IC} characterises the resistance of a material to fracture in the presence of a sharp crack under severe constraint. K_{IC} value is believed to represent a lower limiting value of fracture toughness. Standard test method for plane strain fracture toughness of metallic materials was recommended in U.K. [15] and U.S. [16]. Basically, the specimens currently recommended are the single edge notch bend (SENB) specimen and the compact tension (CT) specimen. At the present time only the E399 Standard allows the use of C-shaped specimen, which is intended for tests on portions of hollow cylinder. The main differences in specimen dimensions between the two standards are that E399 allows test on specimens down to 6.4 mm thickness, whereas BS 5447 limits the minimum thickness to 13 mm. For tension specimen, BS 5447 allows a wide range of alternative B/W values (0.25 to 1.25) to those in E399 (0.25 to 0.5).

During the tests an autographic record of load versus displacement at the open end of the notch is monitored. The K_I values are assessed at the onset of significant measurable crack extension. This is defined by a maximum

of 2% crack growth, which is determined by a 5% deviation from linearity of the load versus displacement record. For a valid K_{IC} measurement, the specimen dimension requirements are

$$a \text{ and } B \geq 2.5 \left(\frac{K_{IC}}{\sigma_{ys}}\right)^2 \qquad \text{.....(1.11)}$$

here a is the crack length, and B is the thickness of the specimen. It may be noted that in the above specimen requirements a and B, and by implication, (W-a), have to be greater than approximately 50 times the estimated radius of the plane strain plastic zone ahead of the crack tip.

A conditional result, K_Q, can be derived using the stress analysis relationship for the specific type of the specimen. When the requirements of Eq. (1.11) and other validity checks are met, $K_Q = K_{IC}$.

1.3 Elastic-Plastic Fracture Mechanics

Almost all low and medium strength structural steels which are widely used for large complex structures such as bridges, ships, pressure vessels, offshore constructions, etc., are of insufficient thickness to maintain plane strain conditions under slow loading conditions at normal ambient temperatures. Thus for many structural applications, the linear-elastic analysis used to determine K_{IC} values is invalidated by the formation of large plastic zones and

elastic-plastic behaviour. Valid quantitative results can only be obtained at very low temperatures, or in thick heavy sections, or at high strain rates, or in material heavily embrittled during welding or fabrication. Recently, considerable effort is being devoted to the development of elastic-plastic fracture mechanics analysis as an extension of the linear-elastic analysis.

Fracture analysis in the elastic-plastic regime has a number of complications not present in the elastic regime. The first is the inherent nonlinearities in the material deformation and large geometry changes. The second complication is the fact that there is a significant amount of crack tip blunting prior to initiation and stable crack extension prior to final fracture. This is very different from the brittle mode of fracture, in which the crack initiation and rapid crack propagation are essentially coincident. Sometimes the ductile crack might be propagated with mixed fracture mode in both flat and slant modes.

Two powerful techniques for analysing elastic-plastic failure are based on the crack tip opening displacement (CTOD) and J-integral. The crack opening displacement concept is now increasingly used in the United Kingdom and Japan, whereas the J-integral concept is the favoured methodology in the United States.

1.3.1. Definition of the CTOD

Wells [17, 18] proposed the CTOD concept as an elastic-plastic failure parameter. The opening displacement at the crack tip is a relative movement of the two crack faces at the crack tip. The fracture process is controlled primarily by the intense deformation adjacent to the crack tip. The crack opening displacement (COD) is a measure of the strong deformation, and in general reflects the magnitude of the strain rather than the stress in the vicinity of the crack tip. Failure occurs when the CTOD attains a critical value, which characterises the strain and stress ahead of the crack tip necessary to initiate the failure mechanism.

Based on an energy balance for a small increment of crack growth, Wells [17] suggested that

$$G = \sigma_{ys}\, \delta \qquad \text{.....(1.12)}$$

where G is the strain energy release rate, δ is the crack tip opening displacement. Using the Eq. (1.9) in the small scale yielding regime, it is clear that

$$\delta = K_I^2 / \sigma_{ys}\, E' \qquad \text{.....(1.13)}$$

It must be consistent with the LEFM failure criterion, the critical CTOD value will be related to the fracture toughness as follows

$$\delta_c = K_{IC}^2/\sigma_{ys} E' \qquad \text{.....(1.14)}$$

Using a crack tip plasticity model proposed by Dugdale[19], it is possible to relate the COD to the applied stress and crack length. The model consists of a through-thickness crack of length 2a in an infinite plate which is subjected to a tensile stress normal to the plane of the crack. Under the action of the tensile stress, σ, the crack is considered to have a length equal to $(2a + 2r_y)$, as shown in Fig. 1.7. At each end of the crack there is a length, r_y, which is subjected to yield stress, which tends to close the crack. The relation is

$$\delta = \frac{8\ \sigma_{ys}\ a}{\pi\ E} \ln\left(\sec \frac{\pi}{2}\frac{\sigma}{\sigma_{ys}}\right) \qquad \text{.....(1.15)}$$

If the ln (sec) term is expanded

$$\delta = \frac{8\sigma_{ys}\ a}{\pi E}\left[\frac{1}{2}\left(\frac{\pi\sigma}{2\sigma_{ys}}\right)^2 + \frac{1}{12}\left(\frac{\pi\sigma}{2\sigma_{ys}}\right)^4 + \frac{1}{45}\left(\frac{\pi\sigma}{2\sigma_{ys}}\right)^6 + \ldots\right]$$

Taking the first term only, there is

$$\delta = \frac{\pi\sigma^2 a}{E\sigma_{ys}} \qquad \text{.....(1.16)}$$

For nominal stress values less than $\frac{3}{4}\ \sigma_{ys}$, this approximation is reasonable.

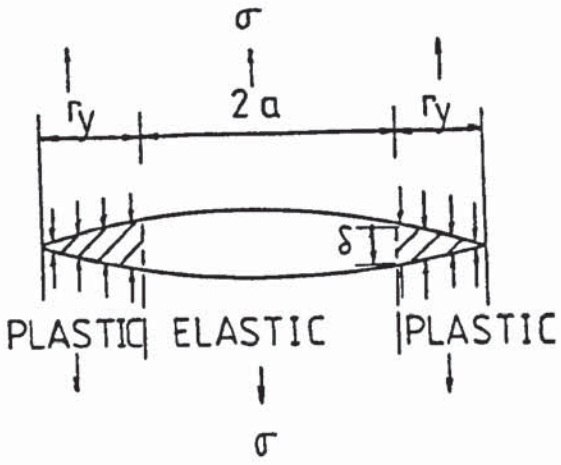

FIGURE 1.7 Crack-tip plasticity model
(After R. W. Nichols et al)

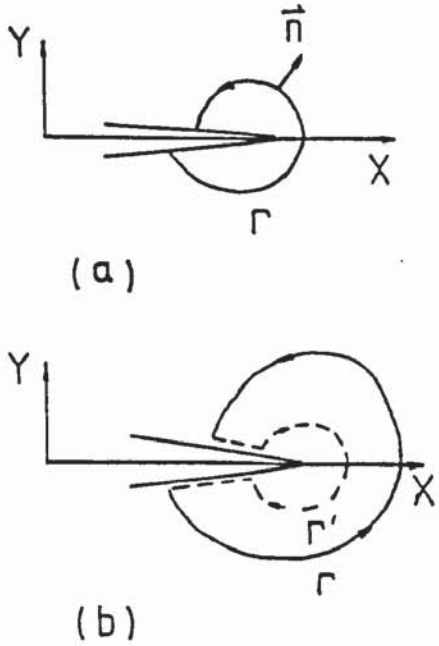

FIGURE 1.8 The J-integral and a closed path
(After P. C. Paris)

1.3.2. Experimental Determination of CTOD

The recommended technique for CTOD measurement is based on monitoring the mouth opening in a precracked three-point bend specimen [20]. CTOD can be calculated from clip gauge measurements at the mouth of the specimen notch. The principle of the analysis is the assumption of a rotation centre at r (W-a) below the tip. The value of r depends on the degree of deformation and is in the range of 0.3 to 0.4 for the rather deeper notch three-point bend specimens. The relationship between the critical crack tip opening displacement, δc, and clip gauge displacement, V, for specimens having $0.15 \leq a/W \leq 0.7$, is recommended as follows.

$$\delta_c = \frac{K^2(1-\nu^2)}{2\sigma_{ys}E} + \frac{0.4(W-a)Vp}{0.4W + 0.6a + z} \quad \text{.....(1.17)}$$

Where stress intensity factor, $K = \frac{YP}{BW^{\frac{1}{2}}}$, and P and Vp are the force and plastic component of clip gauge opening displacement respectively, which correspond to the certain relevant values. Y is the stress intensity coefficient, which is tabulated in the standard. B and W are the thickness and width of the specimen. a is the effective crack length. z is the distance of clip gauge location from specimen surface. σ_{ys} is the yield stress at temperature of interest. E and ν are Young's modulus and Poisson's ratio, separately. The fracture toughness then depends on the choice of a suitable measurement point.

The slow stable crack growth occurs in ductile materials

before reaching maximum load. It was reported that CTOD at initiation of ductile tearing was relatively independent of specimen dimension, but the amount of growth varied from one geometry to another [21]. In this case, the resistance curve technique can be applied to testing δ_i for the onset of crack extension. δ values are plotted versus crack growth, Δa, for a series of specimens. Extrapolation to zero crack growth provides the fracture toughness, δ_i. Single specimen method was also reported. The onset of crack extension was monitored by the electrical potential method [22,23]. It will be discussed later. In the absence of techniques to measure the onset of crack extension, the maximum load δ_m can be used as a means of material comparison.

Some studies were made using micro-indentations spaced across the notch face. During three-point bending test, photographs were periodically taken of the notch root area. CTOD values can be directly measured from these photographs or from extrapolating the values in the vicinity of the tip to the tip [24,25]. Additionally, the crack infiltration method was proposed [26]. The crack tip was infiltrated by a hardening silicone rubber and then the specimen was broken open to obtain a cast of the crack. CTOD may be measured from the cast crack profile.

Based on BS5762, the standard specimen shall be of thickness equal to that of the material under examination. And it has been found [27] that the high δ_i value occurs for the thinnest specimen, whereas for a thickness equal to or greater than 5 mm the fracture thoughness is

independent of specimen thickness.

1.3.3 Definition of the J-integral

Another powerful technique for analysing elastic-plastic failure is based on the J-integral. For the linear elastic behaviour, the J-integral is identical to the strain energy release rate, G. However, it should be noted that the derivation of J is strictly true only for linear and non-linear elastic materials, where unloading occurs along the same path as the initial loading, whereas with plasticity the unloading path would be roughly parallel to the original linear elastic path. Conceptually this drawback appears insuperable at present. In practice, the use of J for ductile materials can be supported in part by direct experimentation, which will be discussed later, and in part by rather indirect analysis [28].

For the non-linear elastic behaviour, the normal expression for J is given by [29]

$$J = \int_{\Gamma} \left(W dy - T_i \cdot \frac{\partial u_i}{\partial x} ds\right) \quad \ldots\ldots\ldots\ldots (1.18)$$

Where Γ is an integral path which goes from the bottom crack surface to the top in an anti-clockwise direction as shown in Fig. 1.8. The strain energy density W is

$$W = \int \sigma_{ij} d\varepsilon_{ij} \qquad \text{.....(1.19)}$$

where σ_{ij} and ε_{ij} are the stress and strain tensors, and summation of repeated indices is implied. The components of the traction vector, T_i, are $\sigma_{ij} n_j$, where n_j are the coefficients of a unit vector normal to Γ, u_i is the displacement vector in the direction of T_i, and ds is an increment of arc length. Rice showed for any closed path J = o (30). A closed path, $\Gamma + \Gamma' +$ along the crack surfaces, is shown in Fig. 1.8. Thus the J-integral value can be computed by evaluating this integral along any contour around the crack tip from very small to encompassing the outside boundaries of the specimen or body.

From a physical viewpoint, J may be interpreted as the potential energy difference between two identically loaded bodies having neighbouring crack sizes, or

$$J = -\frac{1}{B} \left(\frac{\partial U}{\partial a}\right)\Big|_q \qquad \text{.....(1.20)}$$

where U is the total absorbed energy, or area under the load versus load-point deflection curve at load-point deflection, q, as shown in Fig 1.9.

The failure criteria is suggested by

$$J = J_c = K_c^2/E' \qquad \text{.....(1.21)}$$

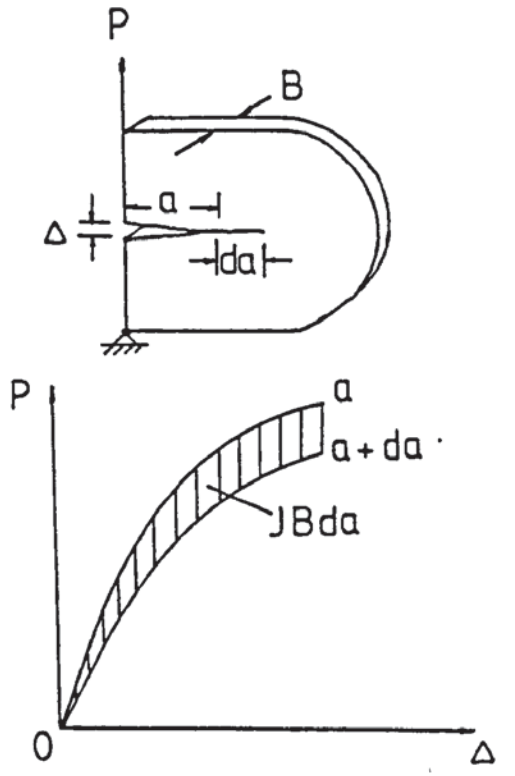

FIGURE 1.9 Physical interpretation of J-integral at constant displacement (After S. T. Rolfe and J. M. Barsom)

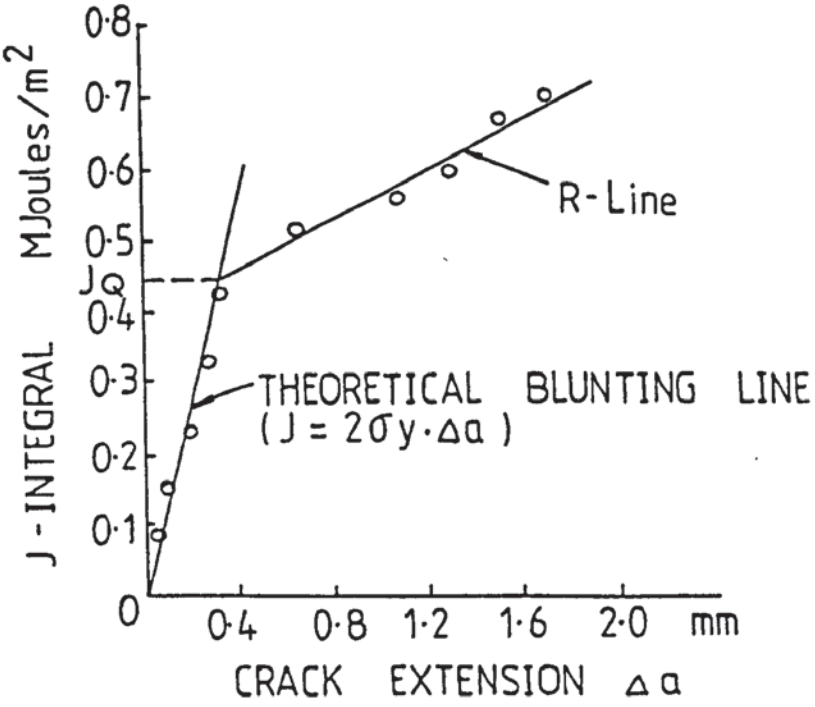

FIGURE 1.10 J versus Δa, R-curve showing best-fit R-line and theoretical blunting line (After G. A. Clarke et al)

provided J_c is a material constant independent of the degree of plastic deformation.

1.3.4 Experimental Determination of J_{Ic}

The various measuring techniques for J all derive from the relationship of Eq (1.20). At an early stage, J is obtained from the change in potential energy, U, associated with a change in crack length, a. The potential energy is equal to the area under load versus load-point deflection curve. At a given deflection the area may be found for bodies with different crack lengths. J may be determined from the slope of a plot of U versus a at a given deflection which is $(\partial U/\partial a)\big|_q$. The final plot is J versus the applied deflection and this curve depends on the crack length, a. If the applied deflection is found for the initiation of crack growth the critical J value, J_{Ic}, may be determined [2].

A procedure was recently proposed by Clarke et al [31] for determining J from the J resistance curve. This procedure obviates the need for tedious J compliance calibration. A number of specimens are first loaded to various deflections to provide different amounts of crack growth. The specimens are unloaded and the extent of crack growth is marked by heat tinting or other techniques. The specimens are broken open and the extent of crack growth is measured optically. The J value for each specimen may be calculated by

$$J = \frac{2A}{Bb} \qquad \text{.....(1.22)}$$

for three-point bend specimen, and

$$J = \frac{2A}{Bb}\left[\frac{1 + \alpha}{1 + \alpha^2}\right] \qquad \text{.....(1.23)}$$

$$\alpha = \left[\left(\frac{2a_o}{b}\right)^2 + 2\left(\frac{2a_o}{b}\right) + 2\right]^{\frac{1}{2}} - \left(\frac{2a_o}{b} + 1\right)$$

for compact tension specimens with $a/w \geq 0.6$, where A is the area under the load versus load-point displacement curve; B is the thickness of the specimen; b is the remaining ligament; a_o is the original crack length.

Finally, the applied J value for each specimen is plotted versus the amount of crack extension, Δa, as shown in Fig. 1.10. The conditional J_Q point is determined by extrapolating the J versus Δa curve to the onset of crack growth. The onset of crack extension is taken as the point where the J versus Δa curve meets a blunting line. The theoretical blunting line is given by

$$J = 2\sigma_{ys}\Delta a \qquad \text{.....(1.24)}$$

The blunting line becomes important for structural steels where extrapolation to a zero Δa can lead to fictitiously low J_{Ic} value. The J_Q value is considered as a valid J_{Ic} value when full plane strain constraints are developed. Otherwise, it is a J_c value. The quantitative limits on the specimen size have been generalized as follows [32],

$$a,\ W-a,\ B \geq \alpha\ J_{Ic}/\sigma_{ys} \qquad \text{.....(1.25)}$$

σ_{ys} may also be substituted by the flow stress, $\sigma_{flow} = (\sigma_{ys} + \sigma_u)/2$.

Experimental studies of size effects in J_{Ic} testing indicate that α should be of the order 25. The method of using several specimens to determine J_{Ic} value has some disadvantages. In addition to the higher cost there is sometimes not enough material to prepare four to six specimens. Thus, several single-specimen methods have been proposed to measure J_{Ic} value. Rice et al [33] proposed that J integral values may be estimated from the following expression

$$J = \frac{2}{B(W-a)} \int_0^{\delta_{crack}} P.d\delta_{crack} \qquad \text{.....(1.26)}$$

where δ_{crack} is the load-point displacement which results from the reduction in specimen stiffness due to the crack. The total load-point displacement, corresponding to the crack initiation is given by

$$\delta_{total} = \delta_{crack} + \delta_{non\text{-}crack} \qquad \text{..(1.27)}$$

Using the superposition principle, and to obtain δ_{crack} from the measured δ_{total}, the $\delta_{non\text{-}crack}$ is obtained from beam theory for the specimen containing non-crack as follows

$$\delta_{\text{non-crack}} = \frac{PL^3}{48EI} \qquad \text{.....(1.28)}$$

where L is the specimen span of 4W, and I is the second moment of area for the uncracked beam. J values are obtained by numerical integration of the P versus δ_{total} curve and then subtraction of the P versus $\delta_{non\text{-}crack}$ area. The point of crack initiation is detected by the electrical potential method.

Clarke et al [34] proposed another single-specimen method to determine the entire curve of J versus Δa and hence the J_{Ic} value. J values are determined for each point along a load versus load-point displacement curve, and the crack length is determined from partially unloading compliance of the specimen at any point of load and displacement during the test. Here it is assumed that the small amounts of unloading, 10% of maximum load, do not affect the overall load-displacement record of the test. One method of determining the crack length from the compliance is to use the empirically developed compliance versus crack length curves for the particular specimen being used. Another method for determining crack length might be the electrical potential method. However, it should be noted that the plasticity component in the potential drop must be subtracted from the total drop in order to determine the component only due to crack extension[35].

Finally, it should be noted that there is a quantitative relation between CTOD and J integral in the generalised

form

$$J = m\sigma_{ys}\delta \qquad \text{.....(1.29)}$$

where m is related with the work-hardening and yield stress of the materials. Usually for all studies $1 \leq m \leq 3$ [28]. The work of Robinson [36] shows that J_{Ic} and δ_i are compatible and in fact interchangeable toughness parameters. It would be advantageous to obtain both J_{Ic} and δ_i values from the same test [37].

1.3.5 HRR Crack Tip Field

Stress and strain distributions inside the plastic zone at the crack tip were studied independently by Hutchinson [38, 39] and by Rice and Rosengren [40]. The stresses and strains in the vicinity of the crack tip under yielding conditions varying from small scale to fully plastic have the form (frequently termed the HRR field)

$$\sigma_{ij} = \sigma_o \left[\frac{EJ}{\alpha\sigma_o^2 I_n r}\right]^{\frac{1}{n+1}} \tilde{\sigma}_{ij}(\theta,n)$$

$$\varepsilon_{ij} = \alpha\varepsilon_o \left[\frac{EJ}{\alpha\sigma_o^2 I_n r}\right]^{\frac{n}{n+1}} \tilde{\varepsilon}_{ij}(\theta,n) \qquad \text{.....(1.30)}$$

where

J = J - integral

E = elastic modulus.

θ,r = crack tip co-ordinates, as shown in Fig. 1.11.

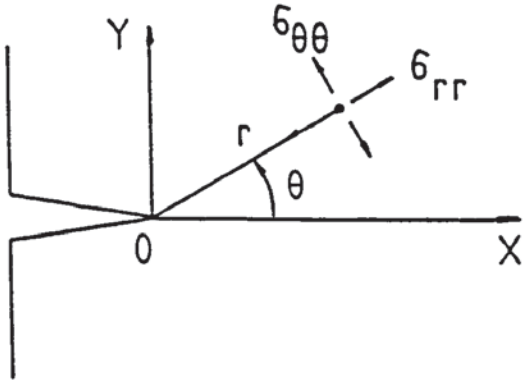

FIGURE 1.11 Polar co-ordinates at crack tip

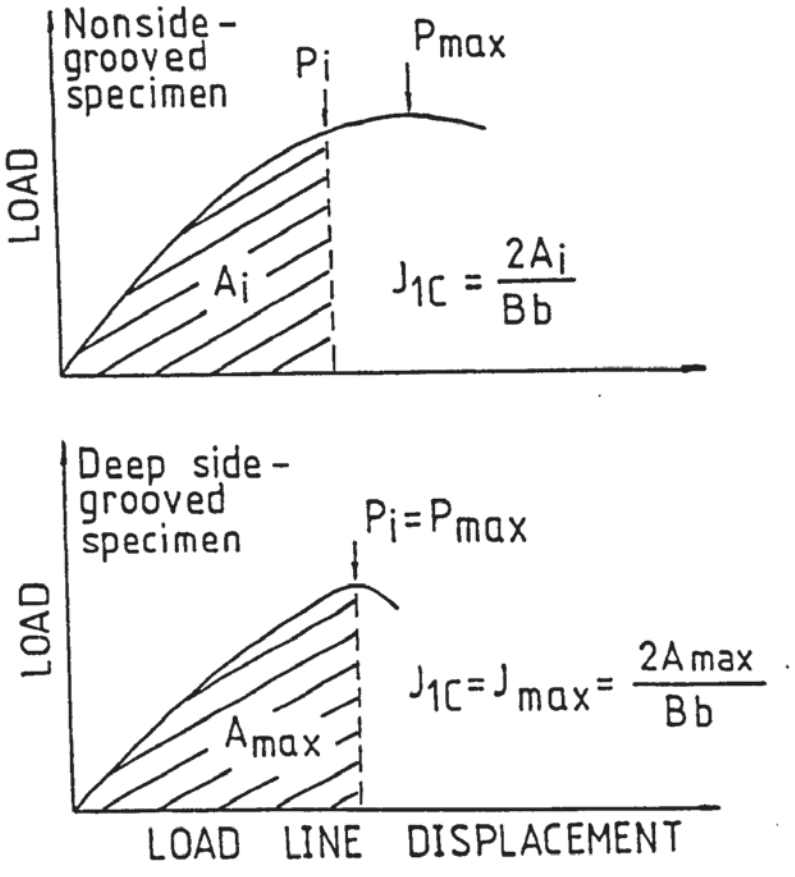

FIGURE 1.12 Schematic load vs load-line displacement curve for nonside-grooved and side-grooved three-point bend specimens showing procedure for estimating J_{IC} (After R. O. Ritchie et al)

$\tilde{\sigma}_{ij}$ $\tilde{\varepsilon}_{ij}$ = dimensionless functions of the circumferential position θ and the hardening exponent n,

I_n = integration constant which is a function of n only,

σ_o; ε_o; n = yield stress, yield strain, and strain hardening exponent, respectively, in the Ramberg - Osgood formulation of the plastic deformation curve, as given in

$$\frac{\varepsilon}{\varepsilon_o} = \alpha \left(\frac{\sigma}{\sigma_o}\right)^n \qquad \text{.....(1.31)}$$

where α is a material constant. In Eq (1.30) the J - integral is the amplitude of the crack tip singularity fields, that is similar to the use of the stress intensity factor, K, as the amplitude of the elastic singular field for small scale yielding. Thus the same J values means the same conditions imposed on the crack tip region. Furthermore, the conditions at the crack tip derive the power of the singularity in stress as $r^{-(1/(n+1))}$ and in strain as $r^{-n/(n+1)}$ so that the singularity of the specific energy density, $\sigma\varepsilon$, is r^{-1}.

If the crack tip opening displacement, δ_t, is defined as the distance between the intersections of two 45° lines (a total angle of 90°) drawn back from the tip with the deformed crack surface [29]. The relation between J and δ_t may be written in the form, $\delta_t = d_n (J/\sigma_o)$, where the

coefficient, d_n, is strongly dependent on n and mildly dependent on ε_o (41). Therefore, the crack tip field can also be expressed in terms of the crack tip opening displacement as follows

$$\sigma_{ij} = \sigma_o \left[\frac{E\delta_t}{\sigma_o d_n I_n r} \right]^{\frac{1}{n+1}} \tilde{\sigma}_{ij}(\theta,n) \qquad \ldots\ldots\ldots(1.32)$$

If a finite size specimen is deformed such that relatively large shape changes occur then the crack tip stress and strain fields are no longer described by the HRR field. Shih and German have investigated three major kinds of specimen shapes, namely a single edge cracked panel in tension (SECP), a cracked bend bar (CBB), and a centre cracked panel in tension (CCP). The investigations show that the size of the region at the crack tip dominated by the HRR singularity is much larger in the bend specimen than in the centre-cracked panel and similar configurations where the ligament is subjected primarily to tension for contained and large scale plasticity. The hardening properties also increase the size of this region.

1.4 Inexpensive Methods for Estimating K_{Ic}

The testing procedure for plane strain fracture toughness, K_{IC}, requires that the size of the specimen must increase with the square of the ratio of the K_{IC}/σ_{ys}. This results in prohibitively large sizes for high-toughness, low-strength materials. To overcome this disadvantage,

many specimens which are smaller and less costly than standard K_{IC} specimens have been used to measure the fracture toughness or to measure the notch toughness and then convert it to the fracture toughness by empirical equations.

1.4.1 Standard CVN Impact or Slow-Bend Test Specimens

Prior to the development of fracture mechanics, the Charpy V- notch impact test specimen [42] is the one most widely used to determine the toughness behaviour of structural materials. In fact, even today it is still widely used for quality control, which is based on empirical correlations between Charpy tests, and more appropriate tests or service experience, because it is very fast to conduct, inexpensive, and simple to use, although it has a blunt notch and small size.

Based on a lot of experimental data accumulated, it is possible to establish empirical correlations between K_{IC} and CVN test results. Furthermore, it is considered that there is a possible theoretical basis for such empirical correlations due to the recent development of the J-integral concept [2], although it has been considered [43] that the empirical Charpy-K_{IC} correlations could be extremely misleading.

The Barsom-Rolfe-Novak correlation [2] was established for the upper shelf region, as follows

$$\left(\frac{K_{IC}}{\sigma_{ys}}\right)^2 = 0.65\left(\frac{CVN}{\sigma_{ys}} - 0.009\right) \quad \text{.....(1.33)}$$

Where K_{IC} is the plane strain fracture toughness at low loading rate ($MN/m^{3/2}$); σ_{ys} is the yield strength at the upper shelf temperature (MN/m^2); CVN is standard Charpy V-notch impact test values at upper shelf temperature (Joules). At the upper shelf temperature, the effects of loading rate and notch acuity are not so critical as in the transition temperature region.

Sailors and Carten [44] established another correlation for the lower shelf and transition temperature, it is

$$K_{IC} = 14.62\ (CVN)^{\frac{1}{2}} \quad \text{.....(1.34)}$$

where K_{IC} and CVN are in $MN/m^{3/2}$ and Joules, separately.

1.4.2 Precracked CVN Impact or Slow-Bend Test Specimens

The precracked Charpy V-notch specimen is introduced to eliminate the machined notch in the standard Charpy V-notch specimen [45]. The specimens can be tested under the condition of slow or impact loading. By instrumenting an impact testing machine with strain gauges, the output from which is recorded with an oscilloscope, measurements of fracture load can be obtained then values of K_{Id} are estimated [46]. A correlation in the transition temperature region is given by [47]

$$\frac{K_{IC}^2}{E} = A\ (CVN) \quad \text{.....(1.35)}$$

Where E is Young's modulus, A is a constant, which equal to 5 for low strength structural steels. K_{IC} and CVN values are obtained at a particular test temperature, and at the same strain rate.

1.4.3 Charpy V-notch Specimen with Side Grooves

Side-grooved Charpy specimens have been proposed for estimating J_{IC} fracture toughness values of nuclear pressure vessel steel in reactor surveillance programmes. Then the equivalent stress intensity fracture toughness values K_{JC} can be calculated from J_{IC}:
The Charpy size specimens were pre-cracked to a crack length/width ratio of 0.5, and to introduce 0.25 mm root radius 45 deg V-notch side groove of varying depth along the edge of the test piece, with total side groove depth ranging from 0 to 6 mm [12].

Side grooves effectively increase lateral constraint in the specimen. Furthermore, at sufficient side groove depth, the point of initiation of slow crack growth approaches maximum load or fracture instability, as shown in Fig. 1.12. It is apparent from the experimentation that with a precracked Charpy specimen containing 30% side groove depths, values of K_{JC} can be determined within 10% (J_{IC} within 17%) simply from maximum load J_{max} measurements for SA533B-1 steel. Furthermore, it has been found that this procedure using side-grooves to

promote instability at crack initiation may not be so effective for all materials. For example, it is indicated that in the specimens with total side-groove depths of 40% and 60% of thickness on mild steel crack extension of the order of 1 mm occurs before maximum load is attained [48].

1.4.4 Short Rod and Short Bar

1.4.4.1 Specimen

Recently, short rod and short bar methods for measuring plane strain fracture toughness were proposed [49]. The specimen configurations are shown in Fig 1.13 [50]. The short rod or short bar method of measuring the fracture toughness is much more obviously based on the steady-state crack configuration. No fatigue precracking of the specimen is necessary and no crack position measurement is made. The fracture toughness test is very simple to perform. The method is applicable to elastic and elastic-plastic materials.

The difficulty of maintaining plane-strain conditions along the crack tip can be largely overcome by using specimens in which very thin slots along the sides of the specimen serve as crack guide [51]. When the plastic zone is smaller than the slot thickness, the non-plane strain regions will be comparable in size with the plastic zone, as shown in Fig. 1.14(a). However, when the plastic zone is larger than the slot thickness, the non-plane strain region may be

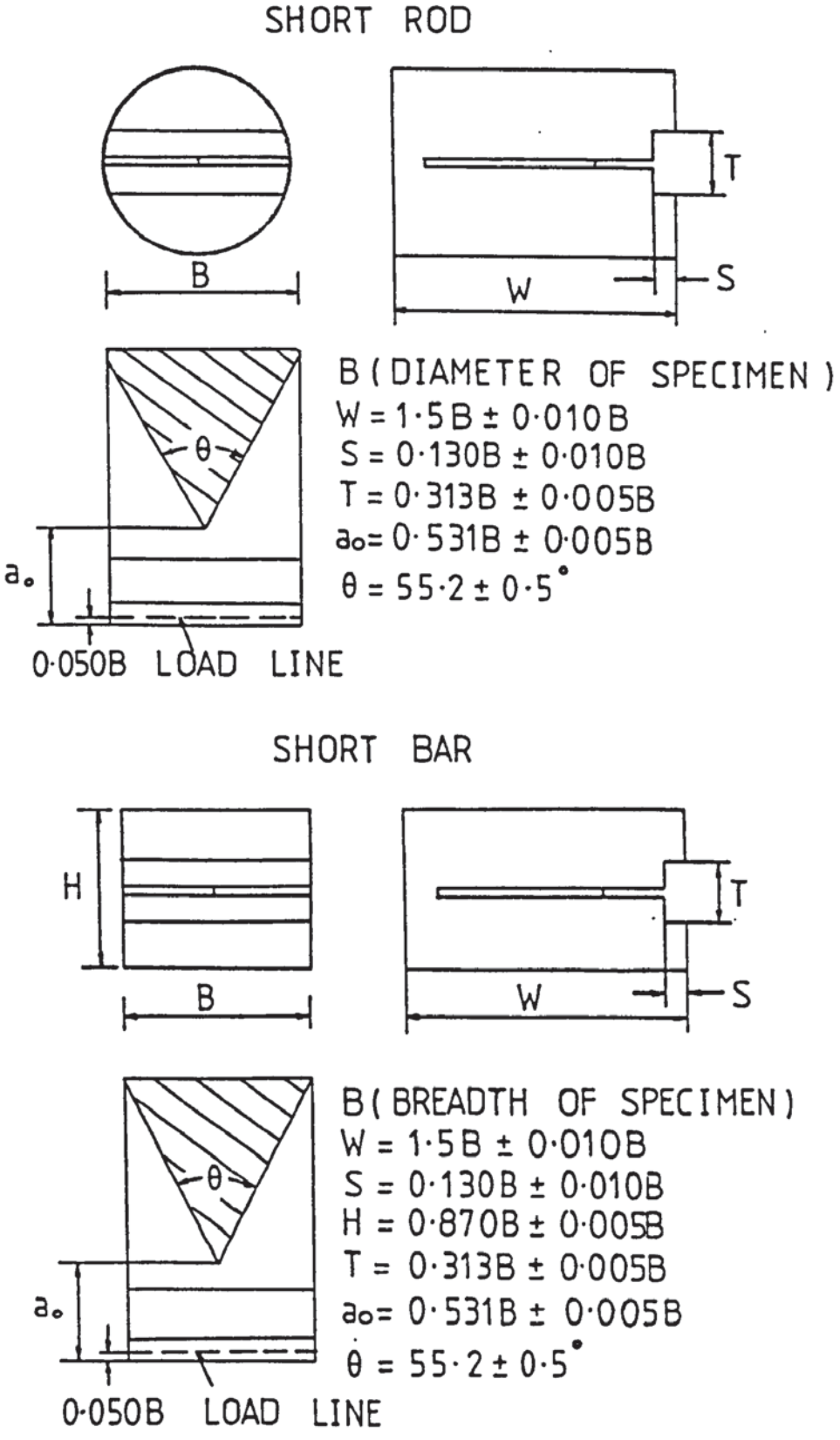

FIGURE 1.13 Short rod and short bar specimens with straight chevron slots (After L. M. Barker)

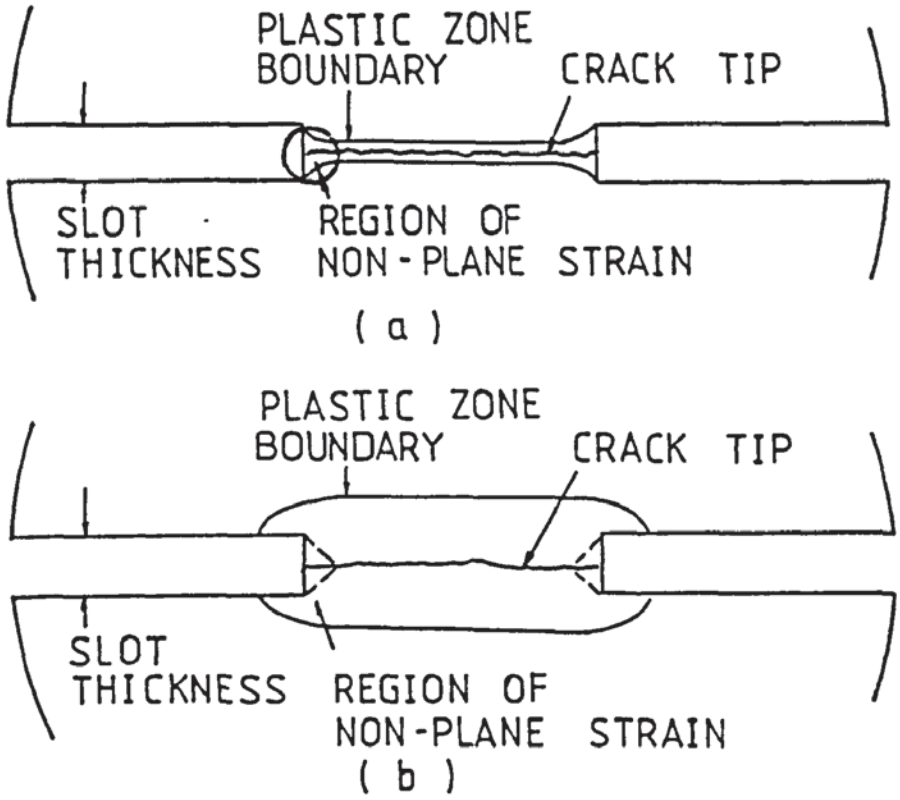

FIGURE 1.14 Schematic of the plastic zone boundary at the crack front (After L. M. Barker)

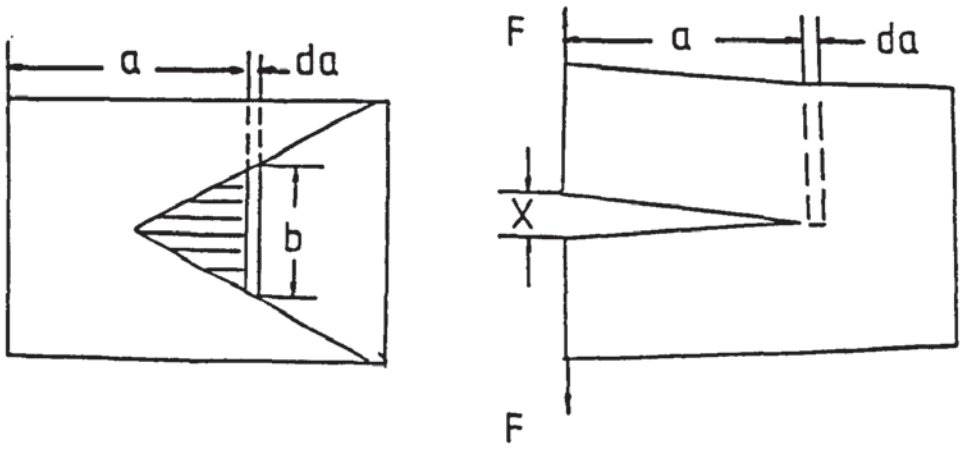

FIGURE 1.15 Plane view and side view of specimen with crack advance increment

limited primarily by the thinness of the slots, as shown in Fig. 1.14(b).

The results of a recent study on the effects of Chevron slot thickness and the sharpness of the slot bottoms indicates that slot both thinness and bottom sharpness help to promote good plane-strain conditions along the crack front [50].

1.4.4.2 Process and Theory

The short rod or short bar specimen is tested by a slow tensile load on the specimen. The crack initiates at the chevron tip with a low load level so that the associated energy release rate is too low to maintain continuing crack growth, therefore additional load is necessary for crack extension until it reaches a critical length. Thereafter, the load decreases with increasing crack length, but the crack growth can still be stable with controlled displacement loading. It has been found experimentally that the critical crack length is a constant for a given specimen geometry and loading manner. The peak load, occurring when the crack passes through the critical crack length, is used for calculating the fracture toughness.

In order to find the relationship between the maximum load F_C, the specimen geometry, and fracture toughness K_{IC} Barker used a short rod or short bar specimen of fixed

overall geometry, and obtained the relationship between F_C and K_{IC} by comparing with materials of known K_{IC} values determined by standard methods. Recently, calibration factor, A, of the short rod and short bar specimens was made by means of experimental compliance measurements [52, 53]. During the compliance calibration, the assumption was based on that the change in compliance with crack extension for the chevron notch specimen is the same as that for a straight-through crack. Additionally a three-dimensional finite element method was also employed to calibrate the stress intensity coefficient in the short rod specimen [54]. It is reported that the results are in very good agreement with the experimentally obtained values.

The LEFM derivation

Because the critical crack length, a_c, at the peak load, F_C, is a property of the specimen geometry and is independent of the specimen material for LEFM tests, the peak load F_C, is used in a simple equation to calculate K_{IC}.

Under plane strain conditions, the energy required to advance the steady-state crack a small distance, Δa (see Fig. 1.15) is

$$\Delta W = G_{IC} b \Delta a \qquad \text{.....(1.36)}$$

where b = average width of the crack front between a and $a+\Delta a$,

ΔW = energy, which comes from the irrecoverable work done on the specimen

G_{IC} = created energy per unit area of new crack surface

Because the force F causes the front of the specimen to open an amount, X, the irrecoverable work, ΔW, done in advancing the crack the additional distance, Δa, is given by the shaded area in the triangle OAB (see Fig. 1.16). This area is given by

$$\Delta W = \tfrac{1}{2}\bar{F}\Delta X \qquad \text{.....(1.37)}$$

where $\bar{F}$ is average load between A and B, ΔX is longitudinal separation of the release paths at the $\bar{F}$. The incremental change in elastic compliance in loading from A to B is

$$\Delta C = \frac{\Delta X}{\bar{F}} \qquad \text{.....(1.38)}$$

From Eqs. (1.36), (1.37), and (1.38), we obtain

$$G_{IC} = \frac{F^2}{2b}\left(\frac{dC}{da}\right) \qquad \text{.....(1.39)}$$

Essentially, this equation is the same as the Eq. (1.6). Using the plane strain equation relating G_{IC} and K_{IC}, after some manipulation, Eq. (1.39) becomes

$$K_{IC} = \frac{F}{B^{3/2}(1-\nu^2)^{\frac{1}{2}}} f(a/B) \qquad \text{.....(1.40)}$$

where B is the specimen diameter, and

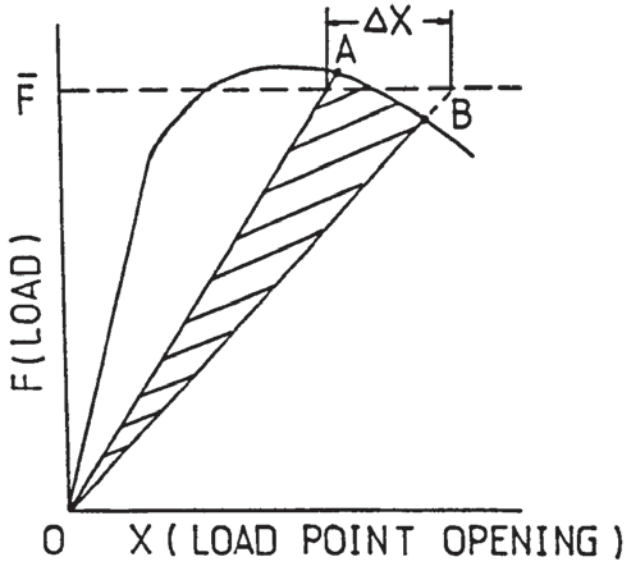

FIGURE 1.16 Schematic of elastic specimen behaviour (After L. M. Barker)

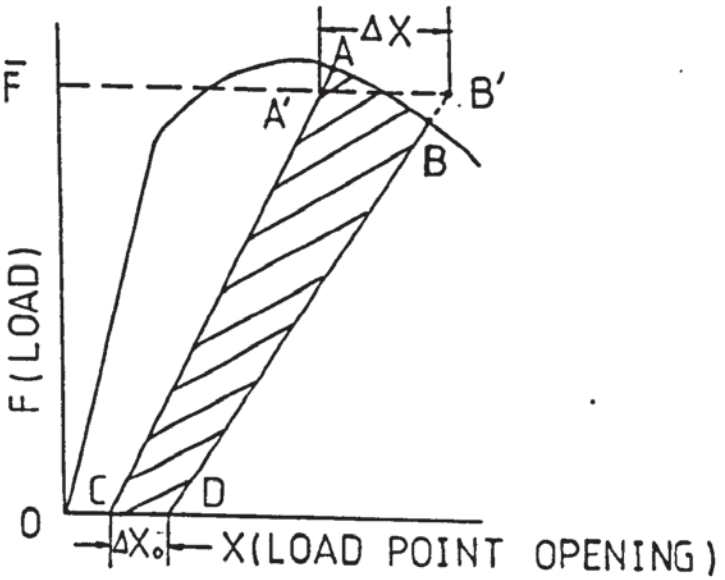

FIGURE 1.17 Schematic of elastic-plastic specimen behaviour (After L. M. Barker)

$$f(a/B) = \left[\frac{Bd(cEB)}{2bd(a/B)} \right]^{\frac{1}{2}} \qquad \text{.....(1.41)}$$

Since the critical crack position scaled, $^{a}c/B$, is a constant, the value of $f(^{a}/B)$ in Eq. (1.40) at the maximum load, F_c, is a constant, $A = f(^{a}c/B)$. Therefore, we have

$$K_{IC} = \frac{AFc}{B^{3/2}(1-\nu^2)^{\frac{1}{2}}} \qquad \text{.....(1.42)}$$

or simply

$$K_{IC} = \frac{AF_c}{B^{3/2}} \qquad \text{.....(1.43)}$$

Comparing to the ASTM standard specimen for K_{IC}, the short rod calibration constant, A, has been found to be 22 [55]. From compliance calibration of the short bar specimen with $\theta=55^{o}$, $^{ao}/B = 0.516$, the constant A = 22.28 [53].

The Elastic-Plastic derivation

The relaxation path no longer leads back to the origin in the elastic-plastic case, because of finite plastic deformation around the crack tip during the loading path [56]. The shaded area CABD (see Fig. 1.17) is the additional irrecoverable work done in loading from A to B to create the new crack area, $b\Delta a$. The area CABD is approximated by the trapezoidal area CA'B'D, which is given by

$$\Delta W = \tfrac{1}{2}\,(1 + p)\,\bar{F}\,\Delta X \qquad \ldots\ldots\ldots\ldots (1.44)$$

where $p = \frac{\Delta X_o}{\Delta X}$, which is the degree of plasticity exhibited by the specimen between two points on the loading curve. p can be measured experimentally by making a plot of load vs. load-point opening of the specimen, being sure to draw relaxation slopes from two points A and B.

A value p = 0 would mean that the specimen suffered no additional plastic bending during the loading from A to B. A value p = 1 would mean that no crack growth had occurred, and that ΔX is entirely attributable to plastic deformation of the specimen.

The change in compliance between the two relaxation paths is

$$\Delta C = (1-p)\frac{\Delta X}{\bar{F}} \qquad \ldots\ldots\ldots\ldots (1.45)$$

From Eqs. (1.37), (1.44), and (1.45), we obtain

$$G_{IC} = \left(\frac{1+p}{1-p}\right) \frac{F^2}{2b} \left(\frac{dc}{da}\right) \qquad \ldots\ldots\ldots\ldots (1.46)$$

Applying the LEFM translation to G_{IC}, then we obtain

$$K_{IC} = \left(\frac{1+p}{1-p}\right)^{\frac{1}{2}} \frac{AF_c}{B^{3/2}} \qquad \ldots\ldots\ldots\ldots (1.47)$$

It should be noted that F_c may not be the peak load in

elastic-plastic specimens, and p is not a constant with the crack length generally.

Recently, experimental procedure and data analysis method in details for short rod and short bar fracture toughness tests of metallic materials were suggested by Barker [57]. It is well known that the larger plasticity precludes meaningful short rod K_{IC} results. The minimum specimen diameter,B, for a valid K_{IC} test should satisfy $B \geq 1.0(K_{IC}/\sigma_{ys})^2$. Additionally, the magnitude of the plasticity parameter, p, should be less than 0.20 [57].

1.5 Microscopic Features of Fracture

A general approach is to divide microscopic mechanisms of fracture under monotomic loading into two groups [58]:

Transgranular fracture, by:

- Microvoid coalescence
- Cleavage
- Quasicleavage (combination of cleavage and microvoid coalescence)

Intergranular fracture, by:

- Grain-boundary separation, with or without microvoid coalescence.

1.5.1. Cleavage Fracture

Cleavage may occur in BCC and HCP metals and is usually associated with rapid loading and low temperature. Cleavage leads to a fracture surface composed of flat, shiny

facet because of its crystallographic nature. The crack is essentially flat and approximately normal to the operative tensile stress axis, but cleavage fracture propagation will probably have to change direction as it crosses a grain boundary, a twin boundary or a subgrain boundary, because of the different orientations of adjacent grain and because the crack follows specific planes (eg {100} in α-iron). If the boundary is a high angle, the crack may restart in the adjacent grain. However in the case of a low angle boundary, many small parallel cracks may form, with cleavage steps between them. These steps run together to form larger steps and lead to the characteristic river patterns,

Although cleavage is crystallographic in nature, in metals local plastic flow will begin when the local stress reaches the shear yield stress, and a cleavage crack can initiate after some critical displacement has occurred at the crack tip. A number of models have been proposed to explain the nucleation of cleavage cracks on the basis of dislocation movement. For example, Smith [59] proposed a following process:

1. plastic deformation leads to the pile-up of dislocations along the slip plane of a grain at an obstacle.
2. build up of shear stress at brittle grain boundary cementite particles nucleates a microcrack.

Because the propagation of crack nuclei is governed by tensile stress, thus carbide microcracks propagate into the ferrite matrix under the combined influence of the applied tensile stress and dislocation pile-up stresses, although the dislocation pile-up stress usually makes a rather small contribution to the total fracture stress.

1.5.2 Intergranular Fracture

Intergranular fracture occurs by grain boundary separation, with intergranular cleavage or microvoid coalescence. Most intergranular fractures have a distinguishable appearance. However, some intergranular fractures seem to be similar with other types of fractures. The reason is probably the presence of grain-boundary phases which are weak or brittle, or environmental factors such as stress corrosion.

Many intergranular fractures, such as those caused by hydrogen embrittlement, stress corrosion, brittle grain-boundary phases and quench cracking show little or no evidence of dimples and they have a rocky appearance, but in some instances, intergranular fractures exhibit dimples within a thin layer of metal at the grain interfaces, such as high strength alumium alloy [58], hydrogen embrittlement of 15MnVN steel in welding HAZ.

Intergranular fracture is usually formed because residual

elements such as P, Sb or Sn have segregated to prior-austenite grain boundaries. They reduced the intergranular cohesive energy. Recently, the local intergranular fracture stress has been measured as a function of the grain-boundary concentration of embrittling elements[60].

1.5.3 Microvoid Coalescence Fracture

There is now abundant evidence that the ductile failure of polycrystalline metals occurs by the nucleation, growth, and subsequent coalescence of internal voids. Inclusions and hard second-phase particles are generally believed to be principally responsible for the initiation of microvoids. Even when they are present in a relatively small quantity, such as oxide inclusions in electrolytic copper [58]. In low-strength steels, voids form by the separation often, at very low local strains, of the interface between the ferrite matrix and non-metallic inclusions, such as sulphide, and aluminium oxide particles. Fracture of rod-shaped chromium carbide particles, $(Fe,Cr)_{23}C_6$, in stainless steel can cause the nucleation of the voids [61]. The ductile fracture of steels containing a significant volume fraction of cementite follows a dual scale process of void nucleation and coalescence with large voids forming at non-metallic inclusions and finer more numerous voids at cementite particles [62,63]. The intermetallic dispersoids can also be provided sites for void nucleation in aluminium alloys [64].

As strain increases, microvoids grow, coalesce, and eventually form a continuous fracture surface consisting of the small dimples, which show evidence of the initiation points at the particles. Depending on the mode of fracture (tension, shear and tensile tearing) the dimples may have equiaxed or elongated shapes.

1.6 Prediction of Fracture Toughness from Critical Fracture Stress and Fracture Strain

Recently, considerable attention has been directed to determine the relationship between uniaxial flow properties and the plane strain fracture toughness. Developing this relationship brings several benefits. First, the present knowledge of the effects of metallurgical variables on the uniaxial flow properties could be used to predict changes in K_{IC}. Secondly, K_{IC} values could be predicted for such conditions as laboratory test specimens are too large to test practically. Furthermore the influence of operating pressure-temperature and irradiation to the possibility of failure of the ferritic reactor vessel materials could be determined.

The fracture process initiates in the plastic zone encompassing the crack tip. The material in this zone yields, flows and finally fractures. Consequently, fracture toughness must be determined partly by the mechanical properties of the material near the crack tip on a microstructural scale. Empirical and theoretical

models have been developed to predict the fracture toughness from the mechanical and metallurgical parameters.

1.6.1 Critical Fracture Stress Model

Early, Hahn et al [65] developed an empirical correlation for cleavage fracture between the mechanical, metallurgical parameters and fracture toughness, after examining a number of representative sets of data:

$$\frac{\sigma_f^*}{\sigma_y} = \alpha\left[\frac{K_{IC}}{\sigma_y}\right]^{\beta} \qquad \text{.....(1.48)}$$

where α and β are empirical constants having most suitable values of $\alpha = 2.35$, and $\beta = 0.33$; σ_f^* is cleavage fracture stress; σ_y is yield stress of the material at the crack tip.

Since σ_f^* appears to be independent of temperature, strain rate and irradiation, variations in K_{IC} should directly reflect variations in yield stress.

Tetelman et al [66] proposed a theoretical model. The cleavage fracture will initiate in cracked specimen of low alloy steel, when the maximum tensile stress level in the plastic zone ahead of crack, σ_{yy}^{max}, reaches a critical value σ_f^*. This value is a microscopic

cleavage stress and is a function of grain size and other metallurgical variables. The relationship between K_{IC} and microscopic strength for low alloy steels is that

$$K_{IC} = 2.9 \left[\exp\left(\frac{\sigma_f^*}{\sigma_y} - 1\right) - 1 \right]^{\frac{1}{2}} \rho_o^{\frac{1}{2}} \quad \ldots\ldots\ldots\ldots (1.49)$$

Here σ_f^* is microscopic cleavage stress, σ_y is uniaxial tensile yield strength; ρ_o is a critical value of the notch radius which is equal to 0.002 in. for a fatigue cracked specimen of A533B steel. Thus, K_{IC} can be predicted at low temperatures where unstable fracture occurs when a critical tensile stress, σ_f^*, is achieved in the plastic zone ahead of the crack.

Ritchie et al [67] have presented an analysis which related σ_f^* to K_{IC}. This analysis is based on accurate numerical elastic-plastic solutions for the stress distribution ahead of a sharp crack. This criterion for unstable slip-initiated cleavage ahead of sharp cracks requires the local tensile stress, σ_{yy}, to exceed a critical fracture stress, σ_f^*, over a microstructurally significant characteristic size-scale, ℓ_o^*. The fracture toughness of a ferritic steel is the stress intensity which must be applied to achieve the critical combination of stress and distance at ahead of the crack tip, an expression for the fracture toughness is obtained,

$$K_{IC} = \beta^{-((N+1)/2)} \ell_o^{*\frac{1}{2}} \left[\frac{\sigma_f^{((N+1)/2)}}{\sigma_y^{((N-1)/2)}} \right] \quad \text{.....(1.50)}$$

where $\beta = f(N) \left[\frac{(1-\nu^2)}{\varepsilon_o I} \right]^{1/(N+1)}$

and values of I, f(N), and β are function of hardening exponent, N; ε_o is yield strain. Therefore, failure at the lower shelf has been modelled using the critical fracture stress criterion. Quantitative prediction of the variation with temperature of the cleavage fracture toughness in mild steel using a characteristic distance of the order of two ferritic grain diameters is shown in Fig. 1.18.

Experimental determination of critical fracture stress, σ_f^*, values is achieved by fracturing V-notched four-point bend bars at low temperatures [68]. The nominal bending stress at the onset of instable failure is measured and using the finite element stress distribution for this particular specimen geometry, the critical values of the maximum principal stress at the crack tip ($\sigma_{yy}^{max} = \sigma_f^*$) can be computed. Values of yield stress used in computation is corrected for the particular crack tip strain rates.

1.6.2 Critical Fracture Strain Model

In metals, plastic flow is induced by shear stresses, which cause dislocation movement, and which may be measured by

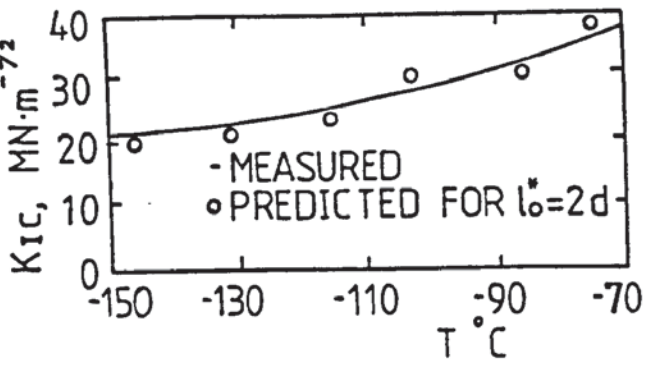

FIGURE 1.18 Comparison of the variation of fracture toughness with temperature between experimental values and predicted values for characteristic distance of two grain diameters (After R. O. Ritchie et al)

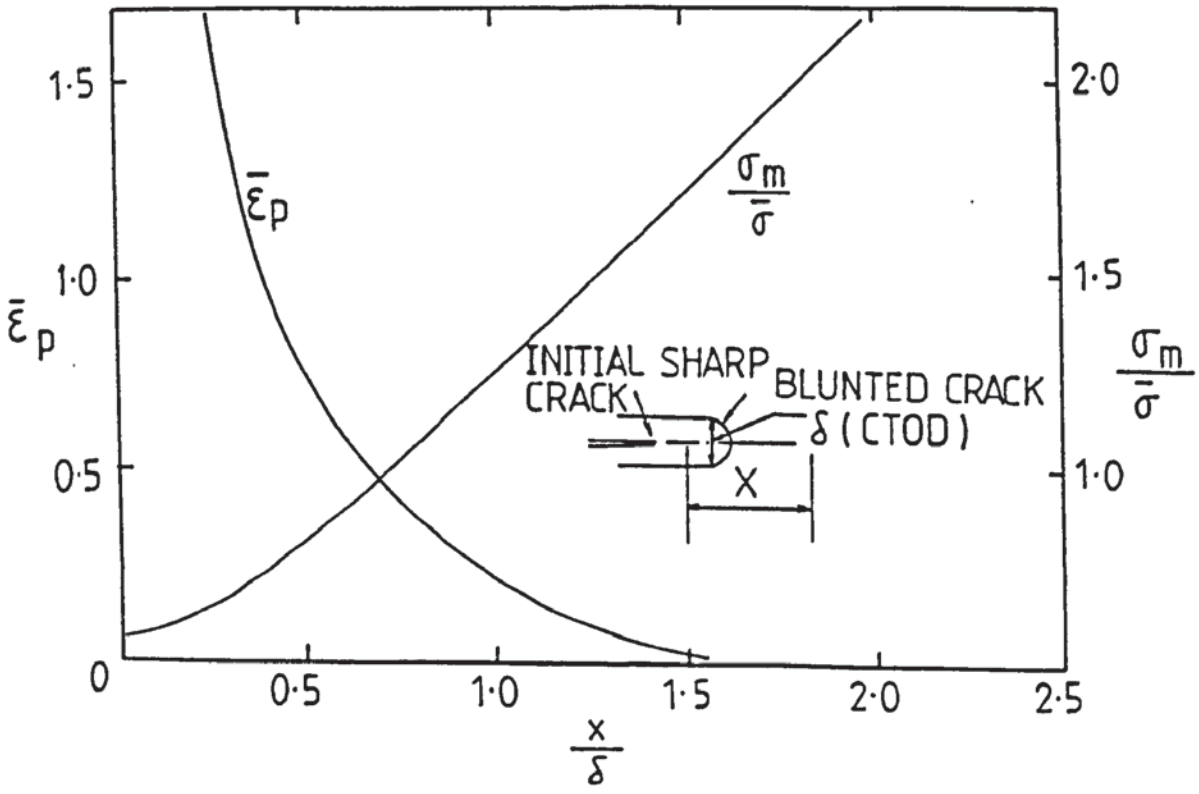

FIGURE 1.19 Distribution of plastic strain and stress state near crack tip for small scale contained yielding (After A. C. Mackenzie et al).

an effective stress, $\bar{\sigma}$, which is proportional to the root-mean-square of the principal stresses σ_{11}, σ_{22}, and σ_{33} that is

$$\bar{\sigma} = \left[\tfrac{1}{2}\{(\sigma_{11}-\sigma_{22})^2 + (\sigma_{22}-\sigma_{33})^2 + (\sigma_{33}-\sigma_{11})^2\}\right]^{\frac{1}{2}} \quad \ldots(1.51)$$

The mean or hydrostatic stress is

$$\sigma_m = \tfrac{1}{3}(\sigma_{11}+\sigma_{22}+\sigma_{33}) \quad \ldots\ldots\ldots(1.52)$$

which may be combined with $\bar{\sigma}$ into a single non-dimensional parameter, $\frac{\sigma_m}{\bar{\sigma}}$, which characterizes a stress state and is a measure of its tri-axiality.

The extent of plastic flow is usually expressed by an effective plastic strain, $\bar{\varepsilon}_p$. For the notched round tensile specimen the stress state and effective plastic strain at the centre of the neck at failure initiation, which is a point when the average axial stress dropped sharply prior to final failure, are respectively expressed by [69]

$$\frac{\sigma_m}{\bar{\sigma}} = \frac{1}{3} + \ell n\left(1+\frac{d_{min}}{2\rho}\right) \quad \ldots\ldots\ldots(1.53)$$

$$\bar{\varepsilon}_p = 2\ell n\left(\frac{d_o}{d_{min}}\right) \quad \ldots\ldots\ldots(1.54)$$

where d_o and d_{min} are the original and minimum radii of the notched cross-section respectively; ρ is the notch root radius.

Mackenzie et al [69] have proposed a stress modified strain criterion for ductile failure where a critical fracture strain, $\bar{\varepsilon}_f^*$, is locally exceeded over some microstructurally significant characteristic distance, ℓ_o^*, which may be expected to be the inclusion (or void) spacing, or some small multiple of the inclusion spacing. Fracture strain, $\bar{\varepsilon}_f$, values are determined from notched round tensile tests. Thus a plot of fracture strain vs. stress state can be obtained. The critical fracture strain, $\bar{\varepsilon}_f^*$, used to predict fracture toughness is taken as the value of $\bar{\varepsilon}_f$ corresponding to the particular stress state at the characteristic distance, ℓ_o^*, from the crack tip in Fig. 1.19.

The critical fracture strain model can be expressed in the form [70]

$$K_{IC} = C \left[\bar{\varepsilon}_f^* . \ell_o^* . \sigma_y . E \right]^{\frac{1}{2}} \quad \ldots\ldots\ldots (1.55)$$

where C is a constant which is related to the distribution of the effective plastic strain near the crack tip. Ritchie et al [68] have considered that this model provided a good prediction of fracture toughness in SA533B steel.

1.7 Computational Model for Ductile Fracture Derived from Experimental Void Kinetics Data

The ductile fracture generally occurs by the formation and subsequent growth and coalescence of voids or cavities, both in nominally uniform stress fields and ahead of an extending crack [71]. Void formation occurs either by particle fracture or by separation of the particle-matrix interface. The nucleation in A533B steel occurs at manganese sulfide and alumina inclusions [72]. Then the voids grow by plastic flow around the voids. The coalescence occurs by localized fracture on sheets between the voids, where the sheets consist of smaller voids, which nucleate at iron carbide inclusions.

1.7.1 Nucleation of Voids

A variety of criteria for void nucleation have been proposed in the literature. Goods and Brown [73] have recently reviewed a number of theoretical descriptions of this phenomenon. They are based on consideration of local energy balance, normal stresses or shear strains at the particle-matrix interface.

There is evidence in the literature that nucleation is mainly a function of the plastic shear strain, $\bar{\varepsilon}^p$, and there exists a critical or threshold strain to cause

void nucleation. Below this strain voids do not occur. It has been found[74] that some voids start to form from the larger inclusions at very small strains and continued to form during the subsequent deformation. It has also been shown that this nucleation strain is affected by a number of parameters including particle shape and orientation, particle strength and the strength of the particle-matrix interface, and stress state. Thus void nucleation often occurs at different strains for different types of particles or in different steels.

EPRI report [72] has indicated from experimental observations in A533B steel that after a threshold strain is reached, the number of voids rapidly increases with continued loading to a second threshold strain level. Thereafter, the number of voids increases much slowly with further strain. These observations are summarized into a bilinear nucleation process:

$$N_o = N_1 \ (\bar{\varepsilon}^p - \varepsilon_1), \ \varepsilon_1 < \bar{\varepsilon}^p < \varepsilon_2$$

$$N_o = N_1 \ (\varepsilon_2 - \varepsilon_1) + N_2(\bar{\varepsilon}^p - \varepsilon_2), \ \varepsilon_2 < \bar{\varepsilon}^p \quad \ldots\ldots (1.56)$$

where N_o is the total number of voids per unit volume; N_1 and N_2 are constants representing specific void densities, ε_1 and ε_2 are strain thresholds; $\bar{\varepsilon}^p$ is plastic shear strain. The results of the tensile tests for A533B

steel suggest that $N_1 = 5 \times 10^6$ cm^{-3}, $N_2 = 1 \times 10^5$ cm^{-3}, and $\varepsilon_1 = 0.11$, $\varepsilon_2 = 0.13$.

1.7.2 Growth of Voids

After nucleation, the voids grow gradually by plastic flow, elastic strain, and thermal expansion [72]. As compared with plastic flow, however, influence of elastic strain, and thermal expansion is usually small.

McClintock [75], Rice and Tracey [71] have shown that void growth depends strongly on both plastic strain and degree of stress-triaxiality. The void growth rate is significantly elevated by the super-position of hydrostatic tension on a remotely uniform plastic deformation field.

The theoretical Rice-Tracey law for void growth in a non-hardening material may be simplified and rewritten for

$$\frac{\Delta R}{R_1} = 0.558 \Delta \bar{\varepsilon}^p \sinh\left(\frac{-3\sigma_m}{2\bar{\sigma}}\right) \qquad \text{.....(1.57)}$$

where $\frac{\Delta R}{R_1}$ is the average radius change of the void; $\bar{\sigma}$ is the effective stress; $\Delta \bar{\varepsilon}^p$ is the change of plastic shear strains; σ_m is the average stress and tensile (negative) value leads to void expansion. It is apparent that the void growth depends on both plastic strain and degree of stress triaxiality. Rice and Tracey have also noted

that a tensile test ductility is independent of the absolute void size or spacing, but dependent only on the volume fraction. The void volume change may be calculated from

$$\frac{V_v}{V_o} = (1 + \frac{\Delta R}{R_1})^3 \simeq \exp(3(0.558)\Delta\bar{\varepsilon}^p \sinh(\frac{-3\sigma_m}{2\bar{\sigma}})) \quad .....(1.58)$$

where Vo and Vv are the initial and final void volume, separately.

The alternative linear growth law was obtained experimentally from measurements on a series of notched and unnotched tensile specimens [72].

$$V_v = V_o \exp \left[-T_1 \frac{\sigma_m}{\bar{\sigma}} (\bar{\varepsilon}^p - \bar{\varepsilon}^p_o) \right] \quad .....(1.59)$$

where V_v is the measured final relative void volume, which is the cumulative sum of the nucleation and growth histories for each material element; V_o is the specific volume of inclusion; $\bar{\varepsilon}^p$ and $\bar{\varepsilon}^p_o$ are the final and nucleation plastic shear strains, respectively; T_1 is a dimensionless growth coefficient, which is the slope of the linear fit to the experimental data in a plot of void volume versus strain. For SA533 Grade B Class I steel, T_1 is equal to 3.2.

It is found in the EPRI report that the theoretical Rice-Tracey growth law appears to agree fairly well with the experimental growth law, when the ratio, $\frac{\sigma_m}{\bar{\sigma}}$ is less than one.

1.7.3 Coalescence of Voids

Hancock and Mackenzie [74] have shown that the deformation before the marked drop in average stress, which is defined as failure initiation, is characterized by homogeneous void growth. Shockey et al [72] have shown from experimental observation on the A533B steel that material failure is defined to begin or void coalescence is assumed to be triggered, when a critical relative void volume of about 1% is attained. During the linking up of voids, the large voids often do not touch each other at failure initiation, but are linked by localization in sheets containing a second generation of much smaller void growth based on carbides or other precipitates between the large voids. In order to produce the necessary amount of small-scale void growth, high local strain and an enhanced stress-state is required. And these conditions may be produced by a plastic instability. The current void kinetics model does not describe void coalescence realistically and therefore cannot be used with confidence to predict stable crack growth and eventual structural instability.

Based on observed fracture phenomenology and experimental void kinetics data, a computational program for ductile damage in the form of voids with computed stress and strain histories was constructed [72]. The model may be used to calculate standard measures of fracture toughness such as J_{1c}, COD, and COA. Lautridou and Pineau [96]

have proposed that a mean value for the void growth, R / R_o can be calculated as a function of the loading parameter COD at every position in front of the crack. Then the critical COD corresponding to the critical void growth R_c/R_o determined in notched tensile specimens can be calculated from the curves which express the relation between R/R_o and COD.

Section 2

TEST MATERIAL

All the experimental work was carried out on a normalized carbon-manganese steel plate, which was supplied by the British Welding Institute. The plate of 50mm thickness is to the BS4360 Grade 50D specification, which is widely used in the North Sea offshore structures. The prime requirements for this steel are a combination of strength and brittle fracture resistance with good weldability.

2.1 Chemical Composition and Mechanical Properties

The chemical composition is given in Table 2.1. Tensile tests were carried out using a 5000 Kgf Instron testing machine at a crosshead speed of 0.05cm/min. The tensile specimens were designed to Hounsfield No. 12, as shown in Fig. 2.1. The orientation of the specimens is along the rolling direction. The test was conducted at room temperature, 20°C. The results obtained from the tensile specimen tests are listed in Table 2.2, combined BS4360. The uniaxial tensile load-extension curve is shown in Fig. 2.2. The load-plastic extension curve is shown in Fig. 2.3.

Hardness survey was carried out using a Vickers pyramid hardness testing machine, with a 5kg load, HV5 average/ range = 174/(170-180) at the midsection of the plate.

Table2.1: Chemical composition (element weight, %)

Item	Chemical analysis for test plate (2A52-1, No.3571)	BS4360 Grade 50D specification [76]
C	0.18	0.20(max)
Mn	1.42	1.50(max)
Si	0.23	0.10/0.50
S	0.008	0.040(max)
P	0.007	0.040(max)
Al	0.03	-
V	0.006	0.003/0.10*
Nb	0.006	0.003/0.10*
Cu	0.11	-
Ni	0.25	-
Cr	0.21	-
Mo	0.03	-
Co	0.01	-
Sn	0.008	-
Fe	balance	balance

*The total amount of (Nb+V) shall be less than 0.10%.

Table2.2 : Mechanical properties

Item	Test value	BS4360 Grade 50D specification
Tensile strength, MP_a	542	490/620
Yield strength, MP_a	349	340(min)
Elongation, %	40*	18(min)
Reduction in area, %	76%	-

*Values were measured by TENSOMETER

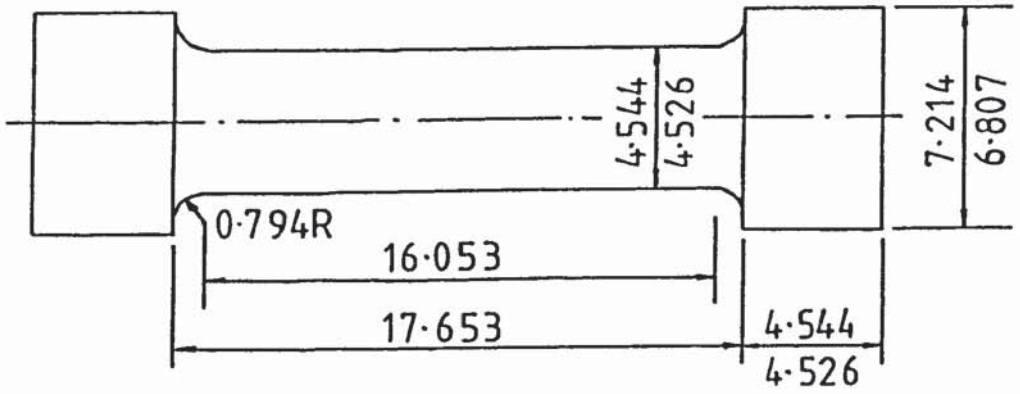

All the dimensions are in mm
Ratio = 4 : 1

FIGURE 2.1 Hounsfield No. 12 tensile specimen

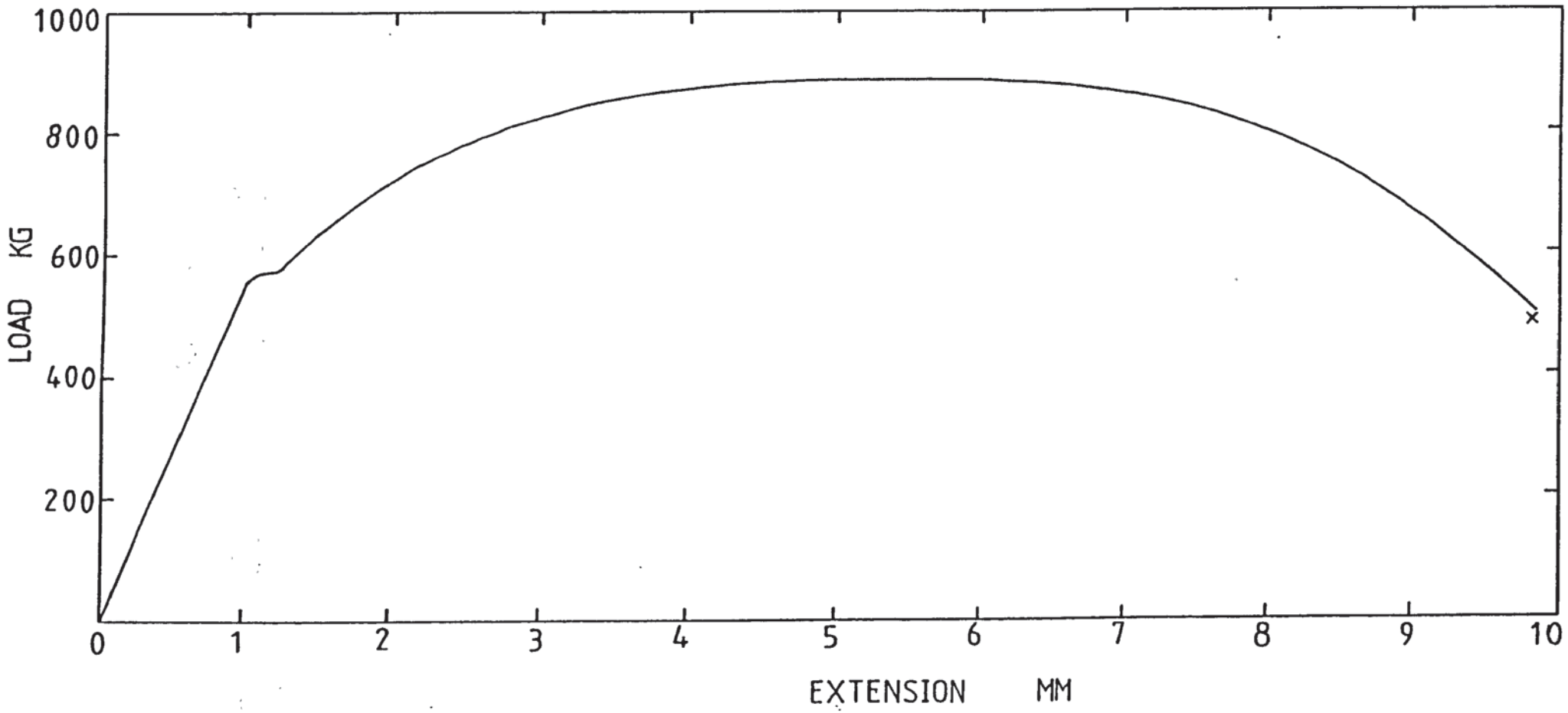

FIGURE 2.2 Load-extension curve of Hounsfield No. 12 tensile specimen (BS 4360 Grade 50D, tested at 20°C with loading rate of 0.05 cm/min)

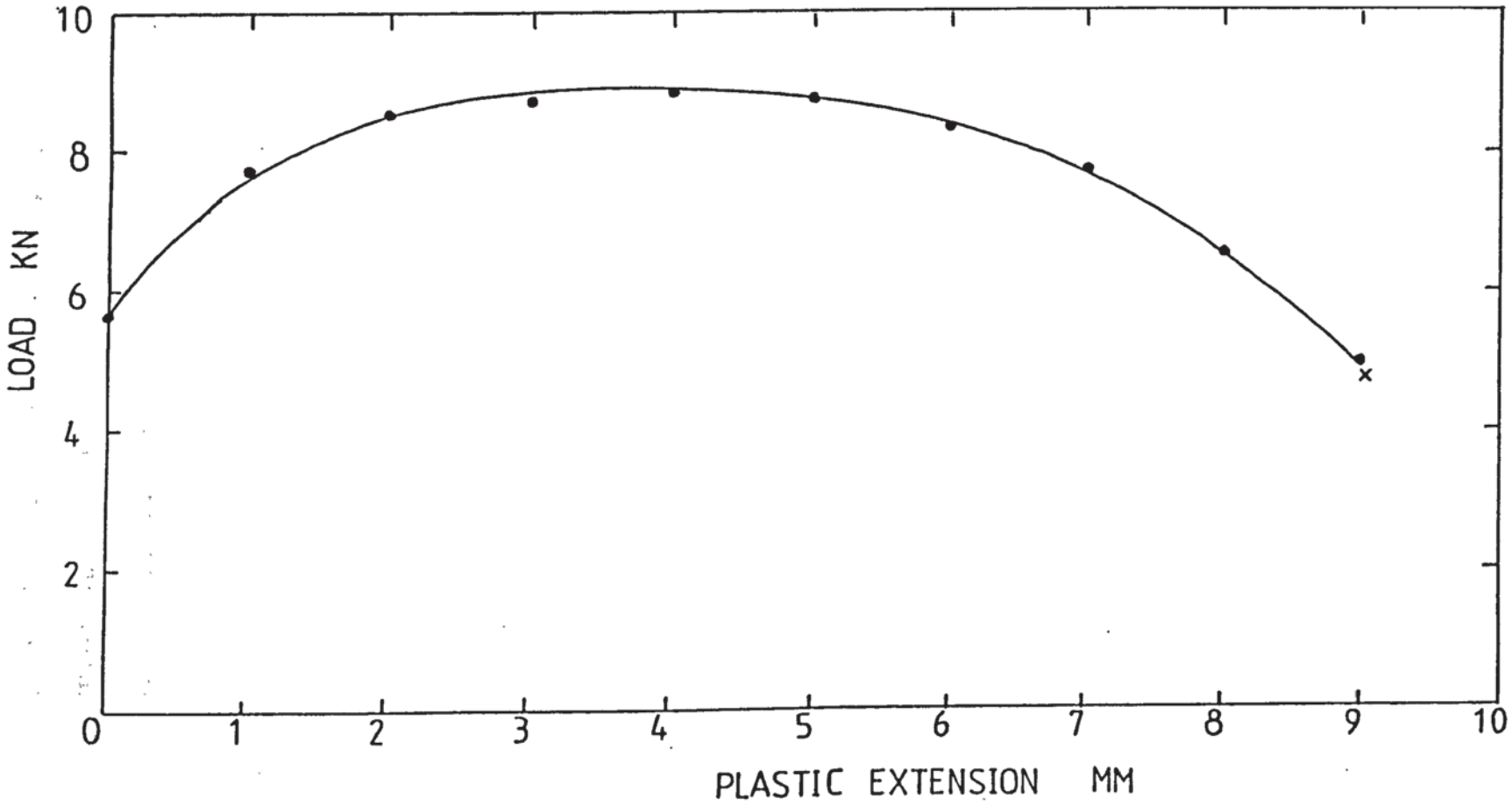

FIGURE 2.3 Load-plastic extension curve of Hounsfield No. 12 tensile specimen (BS 4360 Grade 50D steel, normalised, along rolling direction, tested at 20°C)

2.2 Metallography

In order to investigate the steel microstructures in the transverse section of the plate, standard metallographic grinding and polishing were performed. The etching reagent was 2% Nital.

2.2.1 Micro-constituents and Grain Size

Optical microscopes and a replica transmission electron microscope were used to examine the micro-constituents in the steel. Microstructural examination indicated that the basic micro-constituents are ferrite and pearlite. Upper bainite has not been found in this steel. Typical micrographs are shown in Plate 2.1. In Plate 2.1(b), the lamellae of ferrite and cementite are arranged in colonies within which the lamellae are roughly parallel and uniformly spaced. There are slight changes in lamellar orientation across a visible boundary.

A point counting method [77] was used to determine the proportion of the phase constituents. This analysis was carried out at 500 x magnification, measuring a total of 100 points in a 10cm x 10cm square on the optical microscope screen, taking average values from three arbitrary counting sampling locations. The results of the quantitative metallographic measurements showed that the proportions of ferrite and pearlite phases are 57% and 43% respectively.

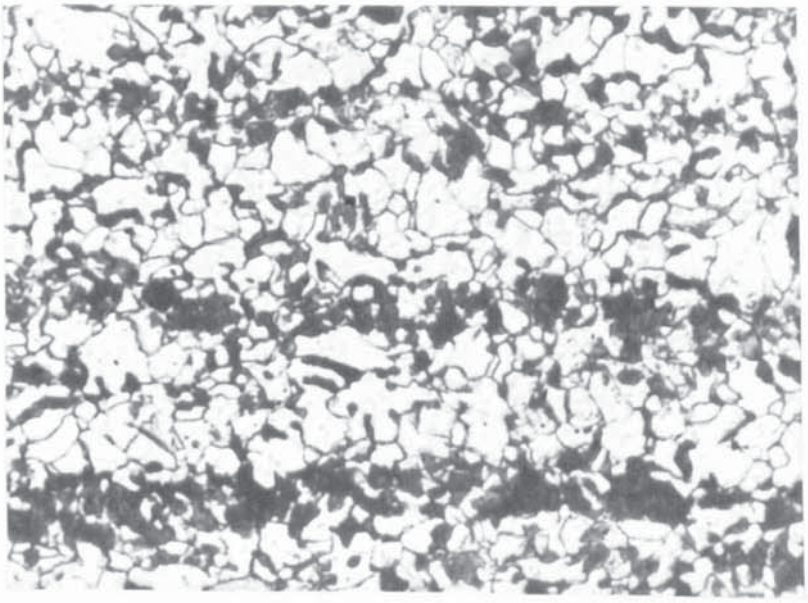

(a) : Optical micrograph, 2% Nital.

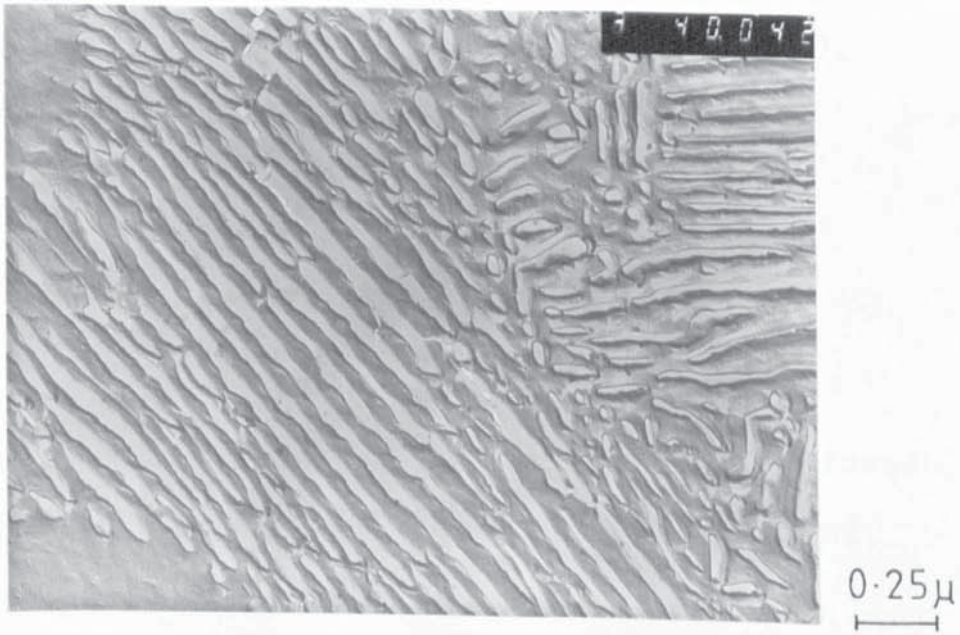

(b) : Electron micrograph of a platinum carbon-shadowed two-stage carbon replica, 2% Nital.

Plate 2.1 : Typical micrographs of pearlite and ferrite in BS.4360 Grade 50D Steel.

The mean grain diameters for each phase have been measured by the mean linear intercept method in seven arbitrary directions and locations at 500 x magnification with the measured length of 10cm on the microscope screen, calculated by the following relationship

$$\bar{d}_\alpha = \frac{LV_{f\alpha}}{N_\alpha} \qquad \text{.....(2.1)}$$

where $\bar{d}_\alpha$ is the mean linear intercept value for the α phase; $V_{f\alpha}$ is the volume fractions of the α phase, L is the total traverse length; and N_α is the number of grain of α phase in the total traverse length. The mean linear intercept values of ferrite and pearlite are 6.89 μ and 8.62μ, respectively. These values can be respectively converted to ASTM No. 11 and No. 10 grain size numbers [78]. This quantitative examination indicated a fine grained, normalized structure.

2.2.2 Banded Structure and Surface Decarburisation

A segregated structure of parallel or nearly parallel bands which run in the direction of rolling has been found in the rolled and normalized BS4360 Grade 50D steel and shown in Plate 2.2.

During the solification of the C-Mn steel ingot, the alloy element C, Mn, et al can be segregated in the interdendritic area. Because the manganese dissolves substitutionally in iron, it is very difficult to

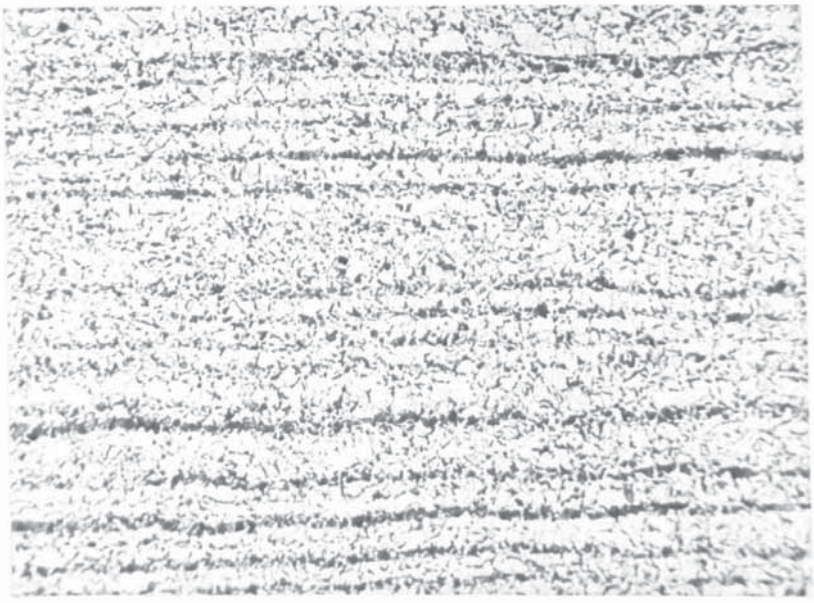

Plate 2.2 : Alternate bands of pearlite (dark) and ferrite, 2% Nital.

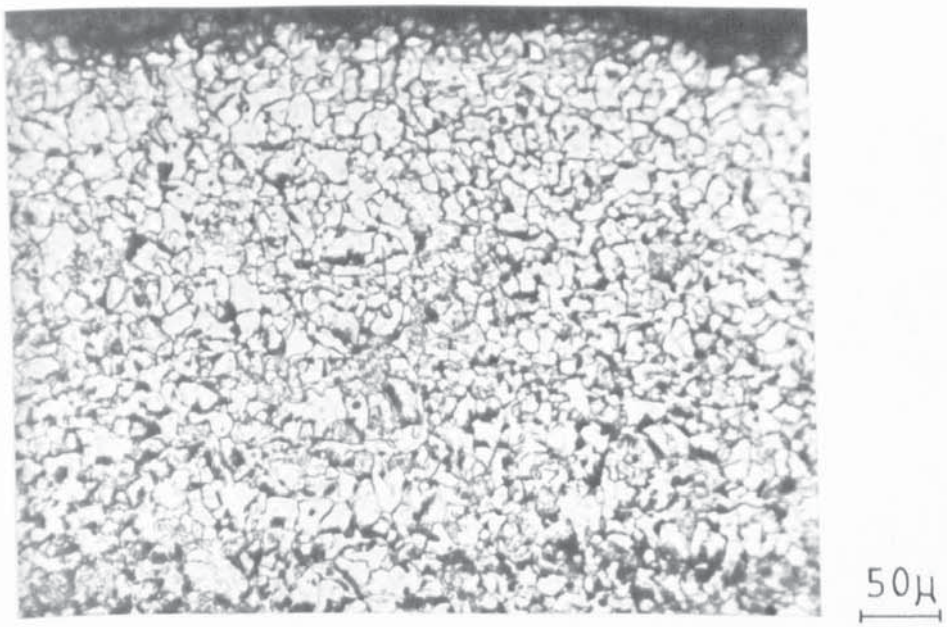

Plate 2.3 : Micrograph at the decarburisation layer, 2% Nital.

redistribute by diffusion during hot working. Thus, the dark band in the micrograph is a Mn-rich band.

This fact could be witnessed by using electron probe micro-analysis and scanning across a pearlite band. Before examining, two lines have been marked by microscopic hardness. The graphic recording is given in Fig. 2.4. The measured values were corrected by a computer programme.

Surface decarburisation occurred probably during the normalized process. The average thickness of the decarburisation layer is about 0.25 mm. Vickers hardness was measured with a 5kg load. HV5 average/range = 152/(145-164). The principal micro-constituent is ferrite, as shown in Plate 2.3.

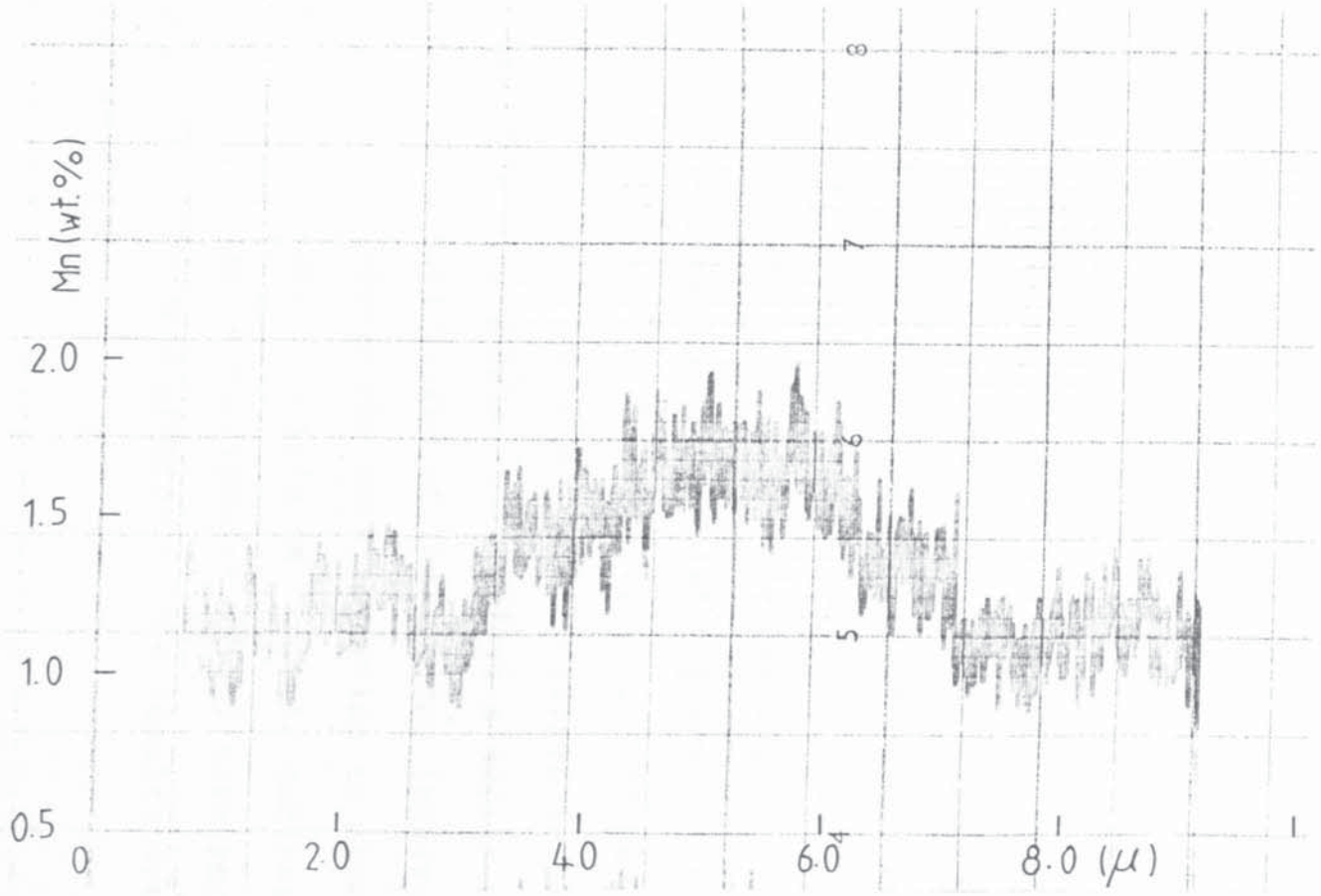

FIGURE 2.4 Concentration profiles of Mn across a pearlite band in BS 4360 Grade 50D steel, target voltage was 20 KV

Section 3

VOID NUCLEATION PROCESS

3.1 Smooth Tensile Bar Tests

Smooth tensile bar tests were used for investigating the characteristics of the void nucleation, and its growth. The tensile specimens were designed to Hounsfield No. 12. The orientation of the specimens is along the rolling direction. The tensile tests were carried out using a 5000 kgf Instron testing machine with a crosshead speed of 0.05 ^{cm}/min at room temperature, 20^{o}C. The load cell of 1000 kgf was chosen. Because the material in the necking region may experience complicated stress state and strain histories after neck formation. It may lead to error, if the final state of plastic strain is used to correlate the void growth. Therefore a series of tensile specimens were pulled at the various interrupted uniform elongation before the neck formation to observe the effect of the plastic strain on the void nucleation and its growth. The load-extension curves were recorded by Farnell Model W211 X-Y plotter. The results are listed in Table 3.1.

The true stresses were measured as the instantaneous load divided by the instantaneous cross-sectional area of specimen. The true strains, ε_T, were measured as the change in diameter across the mid-length in the tensile specimens, according to the equetion,

Table3.1: Results obtained from tensile specimen test

Specimen No.	Initial diameter d_o, mm	Interrupted diameter d, mm	Plastic extension ΔL_p, mm	True strain ε_T	Plastic shear strain $\bar{\varepsilon}^p$	Interrupted load P, KN	True stress σ_T, MP_a
8T*	4.53	4.08	3.10	0.209	0.105	8.65	662
9T	4.53	4.13	2.81	0.185	0.093	8.78	655
10T	4.53	4.19	2.35	0.156	0.078	8.73	633
11T	4.52	4.23	2.00	0.133	0.067	8.58	611
12T	4.53	4.28	1.73	0.114	0.057	8.56	595
13T	4.53	4.34	1.26	0.086	0.043	8.38	566
14T	4.53	4.38	1.04	0.067	0.034	8.19	543
15T	4.53	4.40	0.74	0.058	0.029	7.75	509
16T	4.54	4.46	0.40	0.036	0.018	7.09	454
17T	4.54	4.49	0.24	0.022	0.011	6.35	401

*This specimen was just pulled beyond the maximum load.

$$\varepsilon_T = 2\ell n(\frac{d_o}{d}) \qquad \text{.....(3.1)}$$

where d_o is the original diameter of the round tensile specimen; d is the current value of diameter holding the load. The measured true stress-strain curve at room temperature was constructed point by point, as shown in Fig. 3.1. This curve is only formed for strains lower than about 0.185 which corresponds to the point of the maximum load. Any point on the curve can be considered as the yield stress for the steel strained in tension by the amount shown on the curve.

The simple power curve relation for the true stress-strain curve can be expressed in the form,

$$\sigma_T = K\varepsilon_T^n \qquad \text{.....(3.2)}$$

where n is the strain-hardening exponent and K is the strength coefficient. Using the regressive computation, the following relationship is obtained

$$\sigma_T = 977\varepsilon_T^{0.229} \qquad \text{.....(3.3)}$$

where the true stress, σ_T, is in MPa. This expression is obtained in the true strain interval from 0.022 to 0.185.

Based on the Eq. (1.54), the plastic strain ε_p, in the smooth tensile bars can be expressed as follows

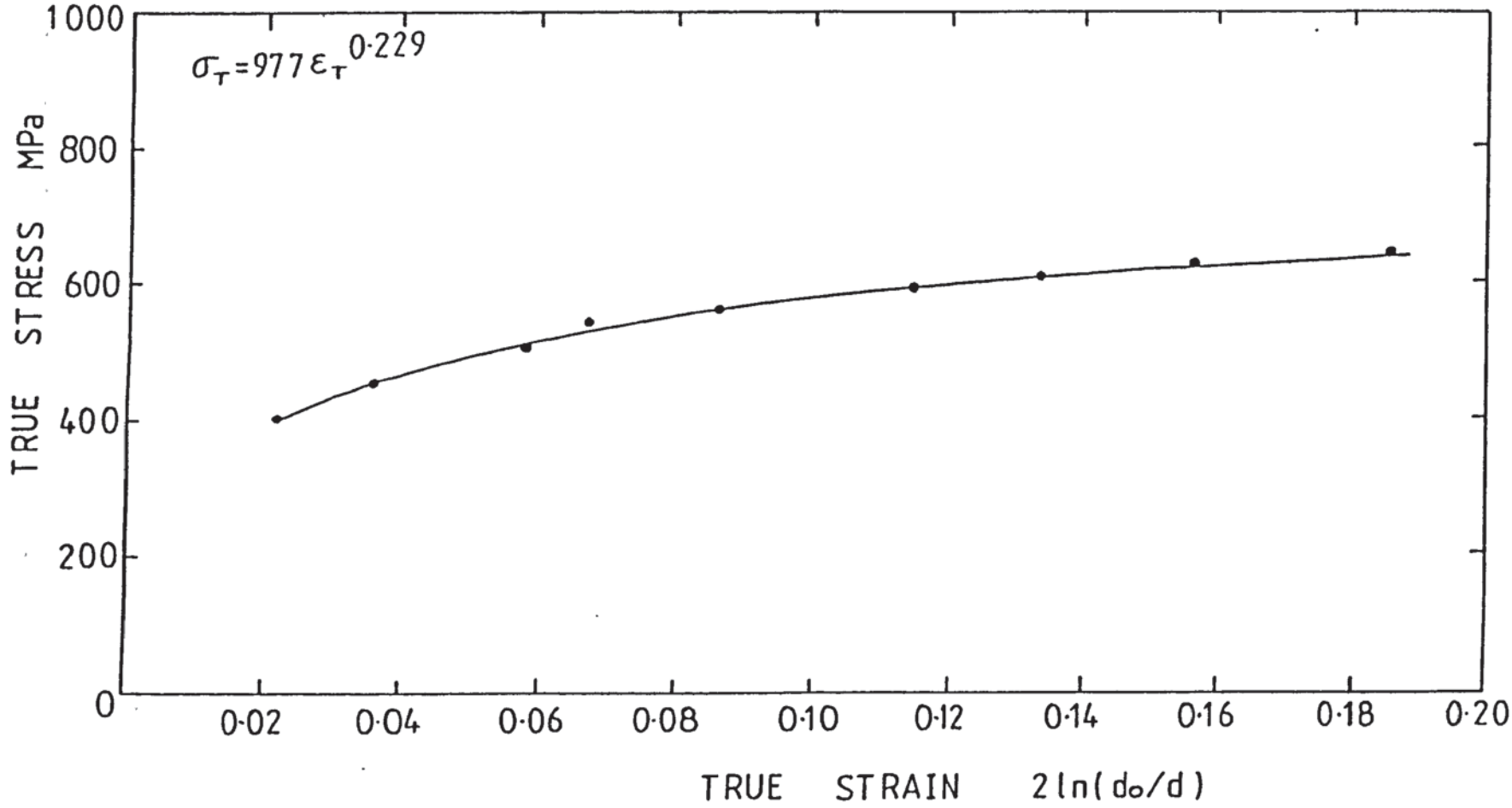

FIGURE 3.1 True stress-strain curve of Hounsfield No. 12 tensile specimens (BS 4360 Grade 50D steel, normalised, along rolling direction, tested at 20°C)

$$\varepsilon_p = 2\,\ell n\left(\frac{d_o}{d_{res}}\right) \quad \ldots\ldots\ldots\ldots (3.4)$$

where d_o is the original diameter of the round tensile specimen; d_{res} is the residual value of diameter after unloading. It was found from the practical measurement that the quantitative differences between the true strain and the true plastic strain are negligible.

As viewed from the volume constancy during plastic flow and Mohr's circle of strain, it is known that using small strain theory:

$$\varepsilon_{11}+\varepsilon_{22}+\varepsilon_{33}=0 \quad \ldots\ldots\ldots\ldots (3.5)$$

and

$$\frac{\bar{\varepsilon}^p}{2} = \frac{\varepsilon_{11}-\varepsilon_{33}}{2} \quad \ldots\ldots\ldots\ldots (3.6)$$

where ε_{11}, ε_{22}, and ε_{33} are the principle plastic strains, $\bar{\varepsilon}^p$ is the diameter of Mohr's circle or plastic shear strain. In the round tensile specimen test, in which $\varepsilon_{22}=\varepsilon_{33}$, it is assumed that ε_{11} is positive strain, and ε_{22} and ε_{33} are negative strains. Thus we obtain

$$\bar{\varepsilon}^p = \frac{\varepsilon_{11}}{2} \quad \ldots\ldots\ldots\ldots (3.7)$$

by the expression of the plastic strain, Eq. (3.4), the plastic shear strain, $\bar{\varepsilon}^p$, can be written as

$$\bar{\varepsilon}_p = \tfrac{1}{2}\varepsilon_p = \ln\left(\frac{d_o}{d_{res}}\right) \qquad \text{.....(3.8)}$$

3.2 Methods Revealing the Voids

Metallographic examination of the deformed specimens was performed on longitudinal section through the tensile axis. The longitudinal plane was often prepared by means of mechanical cutting [79]. And then the sectioned plane was mechanically polished, with diamond paste down to a grain size of 1μm, and treated by ultrasonic cleaning for 1 to 2 min. to prevent masking of the true void population by extraneous matter. Plate 3.1 is the appearance of the voids which were treated by the above procedure. Unfortunately, this procedure often changes the shape and size of the voids by removing the edges of the voids, and a sharp contour of voids cannot be obtained on the mechanically polished plane. Thus, this method can be used for counting the number of voids per unit area of the sample, but it may not be a good method for measuring the void volume fraction. Furthermore, new voids would probably form, as some inclusions were taken away during the mechanical polish.

Test on the void growth model requires accurate techniques to observe the void shapes and to measure the relative void volume during the various strain-stages of the tensile test. One possible technique for removing a thin layer metal from the sample surface is the ion beam etching.

(a) : Optical micrograph (336x)

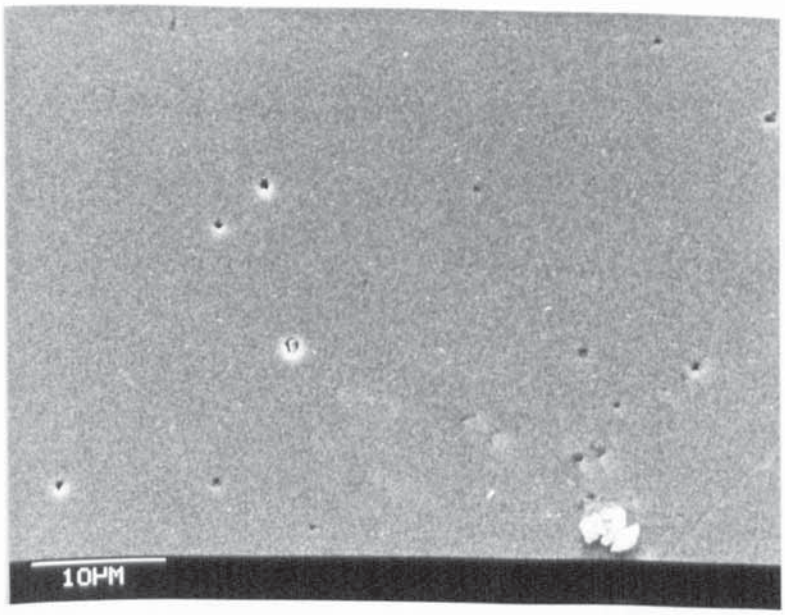

(b) : SEM micrograph

Plate 3.1 : Mechanically polished surface, unetched, tensile specimen No. 1V with $\bar{\varepsilon}^p = 0.079$.

The method makes use of standard ion beam thinning equipment, which is originally used to prepare thin foils for transmission electron microscopy. The sample mechanically ground with grinding paper No. 1200 is fixed to a rotating holder in the equipment, as shown in Fig. 3.2. Ionized argon beams are directed at the sample at an angle of 25-30^{o} to its surfaces. Plate 3.2(a) to (c) shows the void appearance on the specimen surface, which had been bombarded for 9 hrs at an accelerating voltage of 5KV. Thus, this method might be used for the quantitative study of the void growth, because it reveals the true nature of the void shapes well. An obvious disadvantage of this method is that the preparation of sample is complex, and time-consuming. Furthermore, the area for each sample-piece is smaller than that prepared by other methods.

Brittle fracture of the strained specimen in liquid nitrogen was finally chosen to prepare the longitudinal section. Fig.3.3 shows a set for fracturing the sample. It consists of three parts: wedge, container and base plate. In order to keep big differences in temperature between the ambient and liquid nitrogen inside the container, the container and base plate are made by asbestonite, and the size of the container has a bigger height/diameter ratio. The container and base plate can be separated with ease. In order to prevent the fracture

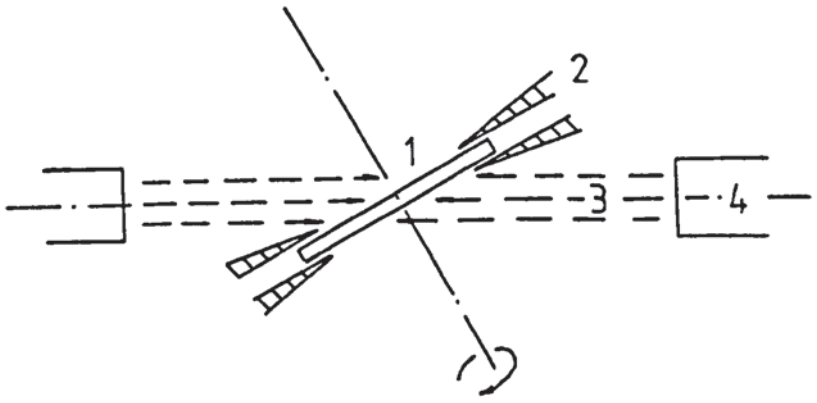

FIGURE 3.2 Schematic diagram of the ion beam thinning equipment
(1) Sample; (2) Sample holder;
(3) Ion beam; (4) Ion gun

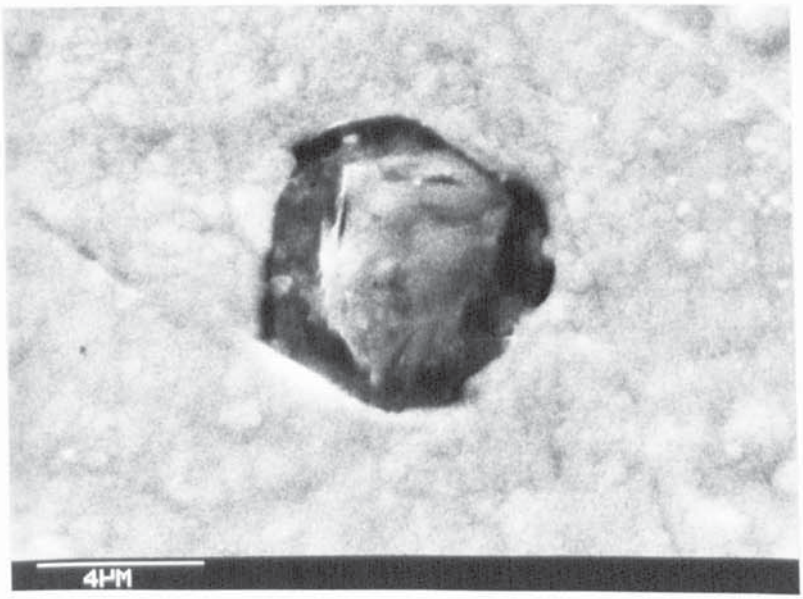

(a) : Ion beam etched surface, tensile specimen No. 3V, $\bar{\varepsilon}^p$ = 0.023. Nucleation occurs at Al-Ca inclusions.

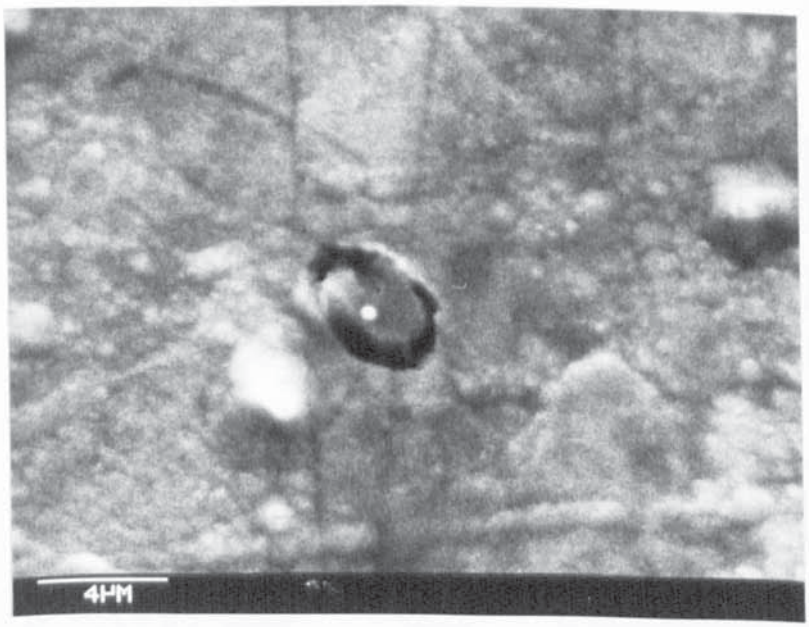

(b) : Ion beam etched surface, tensile specimen No. 3V, $\bar{\varepsilon}^p$ = 0.023. Nucleation occurs at Al-S-Ca-Mn-Fe inclusions.

Plate 3.2 Typical inclusions sited in voids, and their compositions.

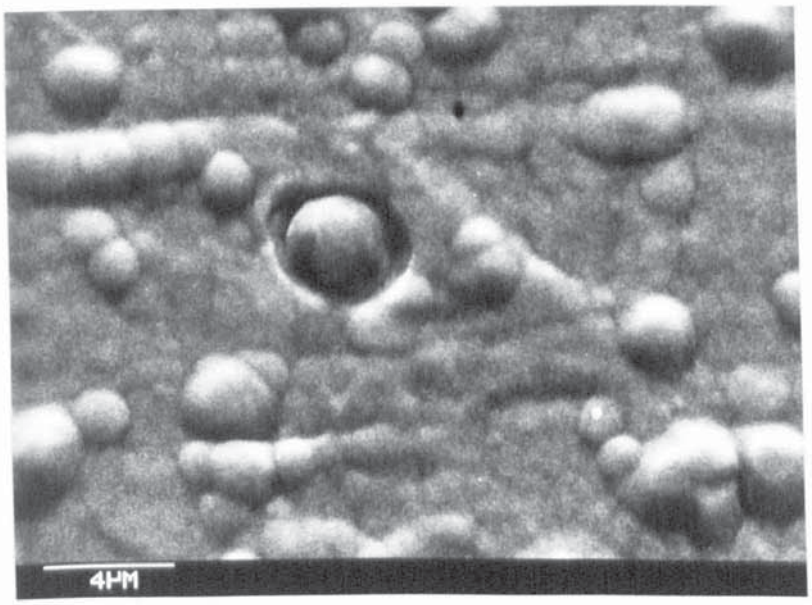

(c) : Ion beam etched surface, tensile specimen No. 3V, $\bar{\varepsilon}^p$ = 0.023. Nucleation occurs at S-Ca-Mn-Fe inclusions.

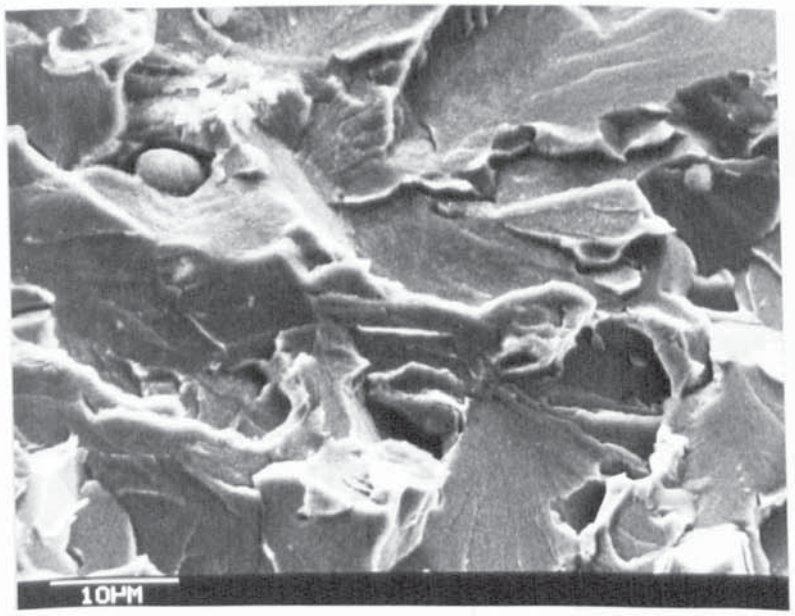

(d) : Fracture surface by liquid nitrogen, tensile specimen No. 14T, $\bar{\varepsilon}^p$ = 0.034. Nucleation occurs at Mn-Fe inclusions.

Plate 3.2 : Typical inclusions sited in voids and their compositions.

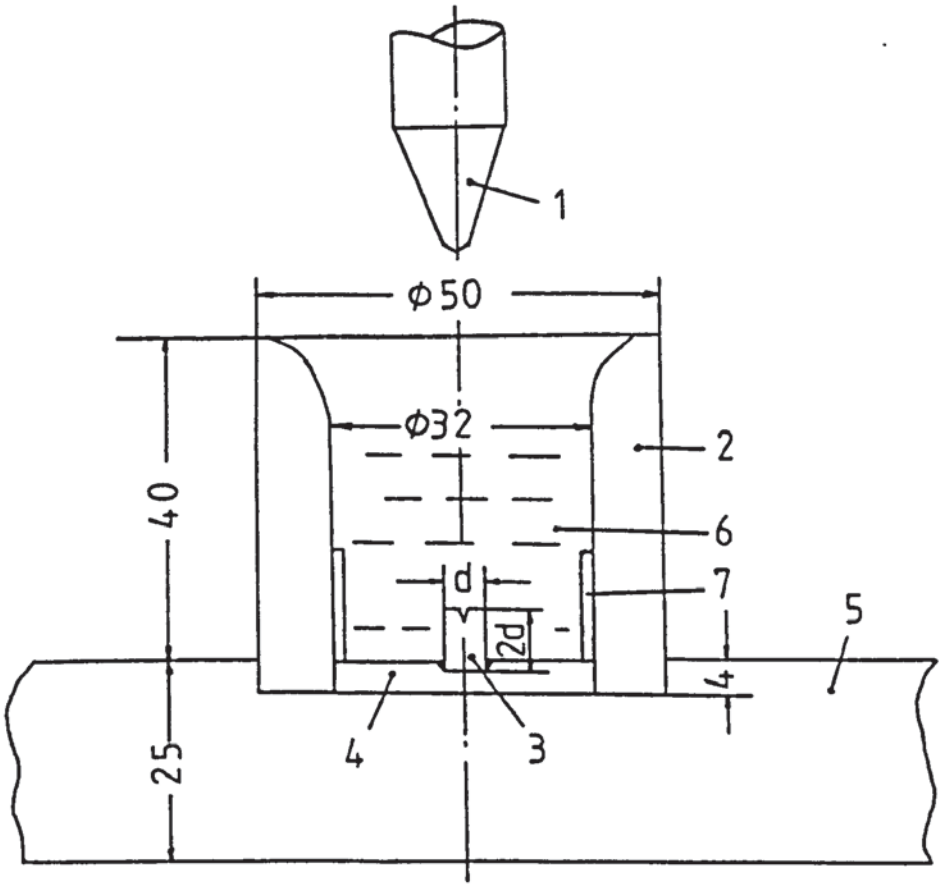

FIGURE 3.3 A set for fracturing the sample in liquid nitrogen
(1) steel wedge;
(2) asbestonite container;
(3) sample;
(4) steel bottom;
(5) asbestonite base plate;
(6) liquid nitrogen
(7) copper liner

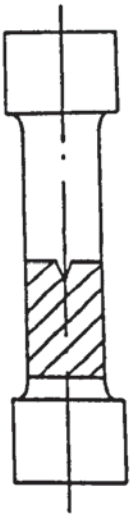

FIGURE 3.4 Longitudinal section prepared for metallographic examination of voids

surfaces from being dirtied by asbestonite, a thin copper lining was laid on the inside of the container. The wedge is made from carbon tool steel and treated by oil quenching and tempering. The whole set is fitted on a manual screw-action press.

Two end surfaces of the sample and its notch were sawed and filed, as shown in Fig. 3.4. Shallow side-grooves sawed might be helpful to guide the fracture surfaces along the centre of the sample. Whole working process was carried out in the stage-pliers, which had lead-shoes on the mouth of the pliers to prevent the sample from forming new plastic deformation. The height/diameter ratio of the sample is about 2.

The process for fracturing the sample is; (i) put a sample on the bottom of the container; (ii) turn the container for centering the wedge and sample notch; (iii) pour liquid nitrogen on the container and keep the sample immersed in liquid nitrogen for about 10 minutes; (iv) fracture the sample by pressing the wedge down rapidly. Plate 3.3 shows a typical fracture surface with voids fractured in liquid nitrogen. Appearance of the voids revealed by this method exhibits much sharper contours. Thus, the accuracy of relative void volume measurement is obviously increased.

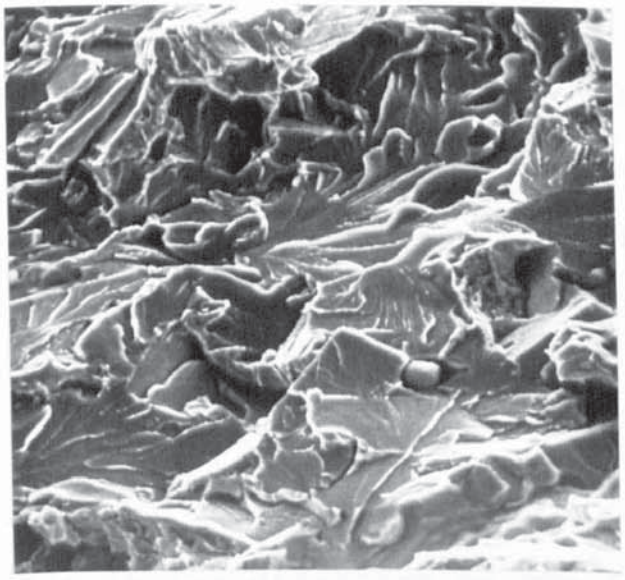

Plate 3.3 Fracture surface sectioned in liquid nitrogen, tensile specimen No. 9T with $\varepsilon^p = 0.093$

3.3 Metallographic Examination

Fracture surfaces were observed by a scanning electron microscope. It has been found that void nucleation predominantly occurs by decohesion of the matrix from inclusions. Plate 3.2 (a) and (b) show that some partial separation begins to form at the interface between the matrix and inclusion. Examining some particles sited in voids by means of x-ray energy spectrometer (KEVEX RAY) shows that nucleation takes place principally at MnS, CaO, and Al_2O_3 inclusions or their mixture, which are usually 2 to 8 μm in diameter. Occasionally, voids also occur at MnO, or the inclusion including cobalt. Plate 3.2 shows some typical inclusions and their compositions.

Additionally, it is found that the observed voids are elongated not only in the direction of the tensile axis, but also in the transverse direction. The voids have extended much more in the direction of the tensile axis than in the transverse direction. Perhaps, it is related to the intergranular micro-stress state in the polycrystal.

3.4 Determination of the Plastic Strain at Void Nucleation

Considering that the spacing between the voids is roughly 40μm in the uniform strained specimens, and the rather

smaller size of the voids, a magnification of about 1000 was chosen to assure that a certain amount of voids may be taken in each photomicrograph. Ten photomicrographs were randomly taken for each specimen. The number of voids per unit area was obtained from each photomicrograph. Then, the average number of voids per unit area corresponding to various plastic shear strain levels was calculated and listed in Table 3.2. Fig 3.5 shows a plot of the cumulative number of voids per unit area versus the plastic shear strain.

Using a least-squares fit to describe this cumulative number of voids, the following equation was obtained:

$$\Sigma N = -0.5\times10^{4}+266\times10^{4}(\bar{\varepsilon}^{p}) \quad \ldots\ldots\ldots\ldots(3.9)$$

where ΣN is the cumulative number of voids per unit area, cm^{-2}; $\bar{\varepsilon}^{p}$ is the plastic shear strain. The sample correlation coefficient, R, is 0.99. Thus, the linear relation between the sample values of ΣN and $\bar{\varepsilon}^{p}$ is very pronounced. Assuming that $\Sigma N = 0$, the plastic strain at void nucleation, $\bar{\varepsilon}^{p}_{o}$, is equal to 0.002. Therefore, voids begin to form at very low plastic strain. Based on the above observations, voids already occur at the plastic shear strain of 0.011. In order to confirm whether the plastic shear strain of 0.002 may be expected as nucleation strain, a few of the smooth tensile specimens were additionally tested. Unfortunately, the minimum value of the plastic shear strain obtained in the experiments

Table3.2: Number of voids per unit area

Specimen No.	Plastic shear strain, $\bar{\varepsilon}^p$	Number of voids per unit area, $10^4/cm^2$	Cumulative number of voids per unit area, $10^4/cm^2$
17T	0.011	2.43	2.43
16T	0.018	1.95	4.38
15T	0.029	1.51	5.89
14T	0.034	2.74	8.63
13T	0.043	3.73	12.36
12T	0.057	2.34	14.70
11T	0.067	2.70	17.40
10T	0.078	3.10	20.50
9T	0.093	3.26	23.76

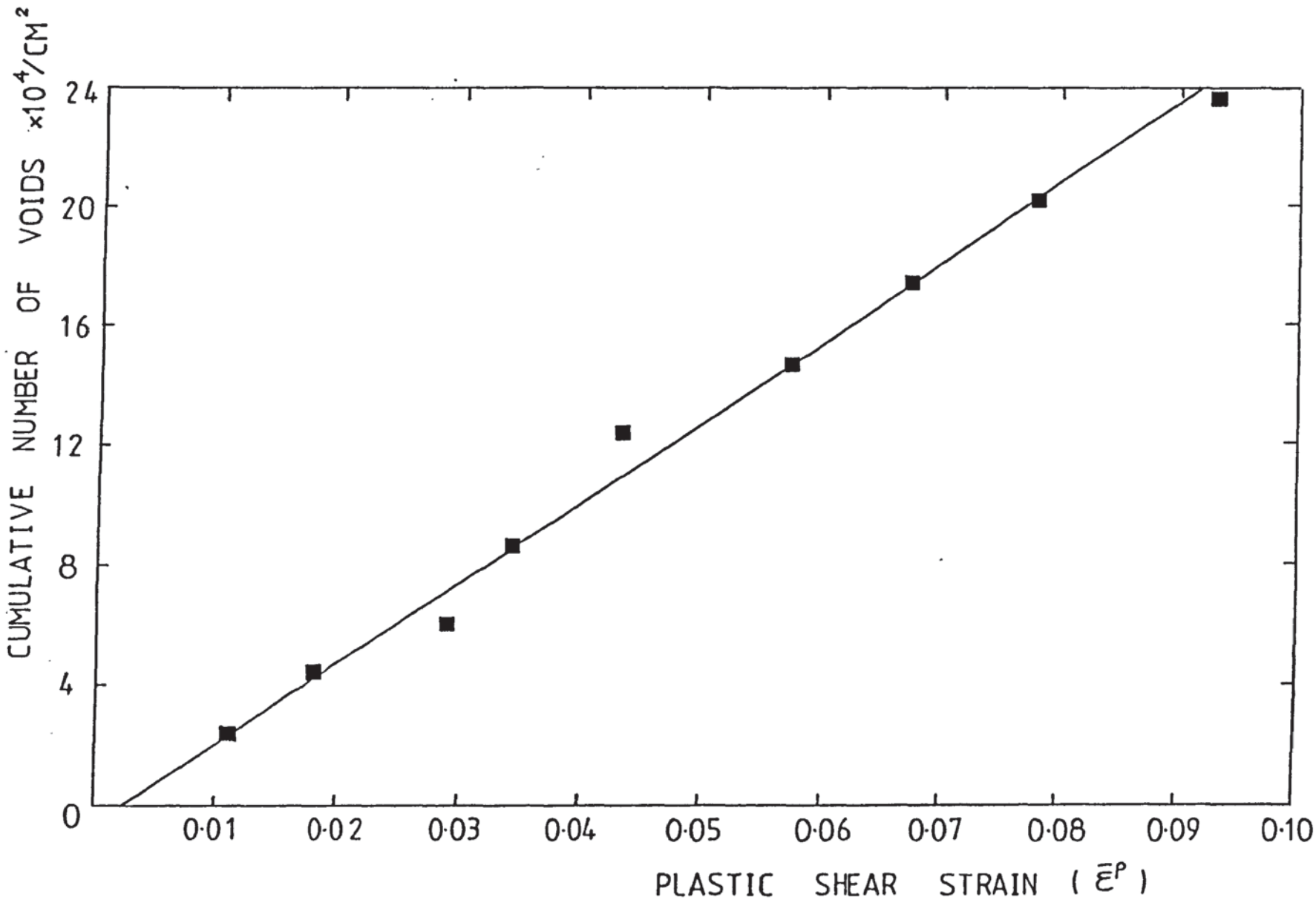

FIGURE 3.5 Cumulative number of voids per unit area versus the plastic shear strain

is 0.003. It is very clear that voids already occur at the plastic shear strain of 0.003, as shown in Plate 3.4. Practically this strain value is only a few times the yield strain. In this case voids only form from some larger inclusions which are sited at the best opportunity for nucleation. In the subsequent computation, the plastic shear strain of 0.002 is still assumed to be the plastic nucleation strain.

3.5 Determination of Relative Void Volume at Void Nucleation

In order to measure the relative void volume, Vv, at the various levels of the plastic shear strain, a point counting method with a regular array of points was chosen. The spacing between the points is greater than the maximum intercept length in the void to be measured. This means that a square grid of 1 cm is used for the SEM photomicrograph with the magnification of about 1000. The grid is randomly superimposed on each photomicrograph 20 times. The number of intersections of the grid, Pv, falling in the void are counted, and compared with the total number of points, P, laid down. Thus, the relative void volume is given by

$$V_v = \frac{P_v}{P} \qquad \text{.....(3.10)}$$

Finding out the arithmatic mean of the relative void volumes randomly measured in one photomicrograph 20 times, and calculating the arithmatic mean for 10 micrographs,

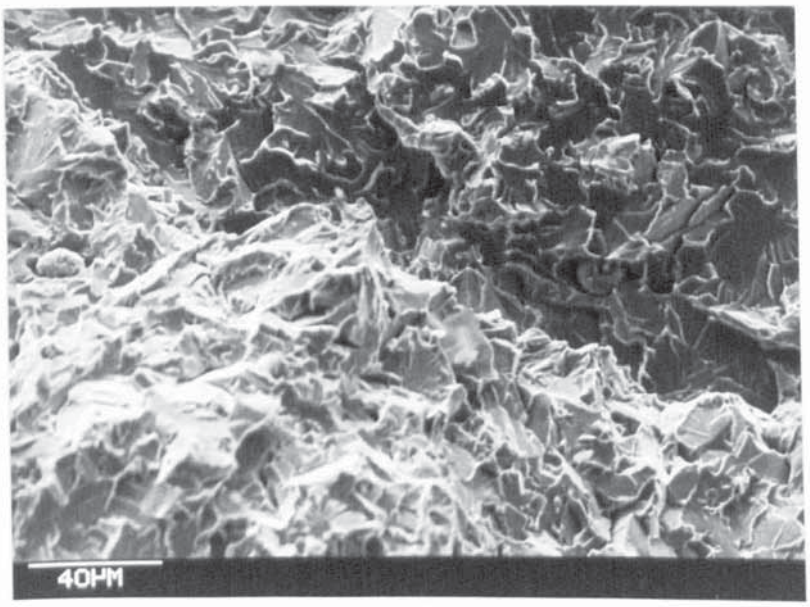

(a) : One (left) occurs at Al-S-Ca inclusions, the other (right) occurs at the inclusion containing cobalt.

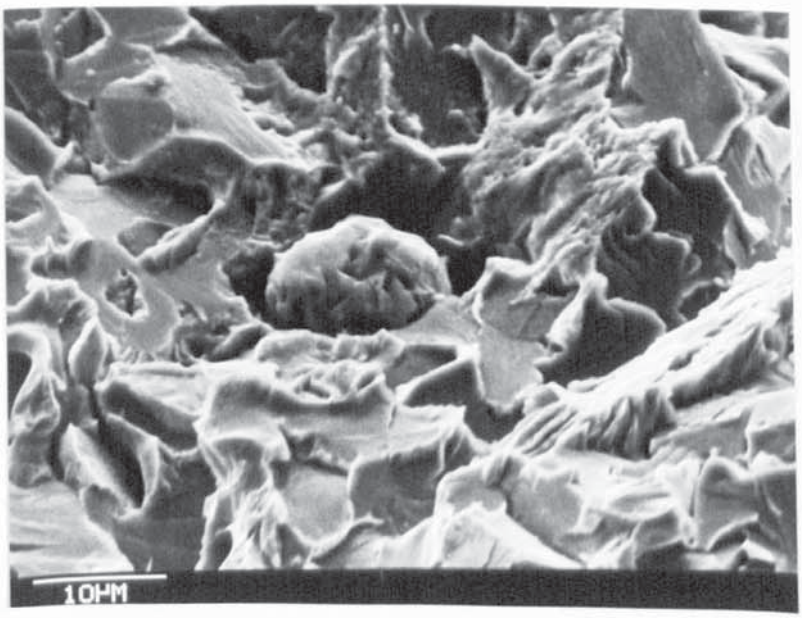

(b) ; Magnified Al-S-Ca inclusion and void, which is the same as (a).

Plate 3.4 : Void nucleation at the plastic shear strain of 0.003 in round tensile specimen No. 21V; horizontal direction in Plates is elongation direction.

the relative void volume for each specimen was obtained and is listed in Table 3.3. Fig 3.6 shows the variation of the relative void volume versus the plastic shear strain. The standard deviation, σ, for the data of the relative void volume can be calculated by

$$\sigma = \sqrt{\frac{\Sigma(V_v-\bar{V}_v)^2}{n-1}} \qquad \text{.....(3.11)}$$

where $\bar{V}_v$ is the mean value of the Vv; n is the number of observations.

Using a linear fit to describe the relationship between the relative void volume and plastic shear strain, the relationship is

$$V_v=0.00177+0.01486(\bar{\varepsilon}^p) \qquad \text{.....(3.12)}$$

Here, the sample correlation coefficient, R, is 0.83. It is assumed that the void formation takes place at a critical nucleation strain, at which the voids will be formed suddenly. Substituting the nucleation strain of 0.002 for $\bar{\varepsilon}^p$ in Eq. (3.12), the relative void volume during nucleation, V_o, will be 0.00180.

Table 3.3: Measured relative void volume by point counting

Specimen No.	Plastic shear strain $\bar{\varepsilon}^p$	Incremental strain, $(\bar{\varepsilon}^p - \bar{\varepsilon}^p_o)$	Relative void volume, V_v	Standard deviation for V_v	$\ell n(V_v/V_o)$
17T	0.011	0.009	0.00215	0.00523	0.17768
16T	0.018	0.016	0.00208	0.00570	0.14458
15T	0.029	0.027	0.00229	0.00552	0.24077
14T	0.034	0.032	0.00200	0.00489	0.10536
13T	0.043	0.041	0.00236	0.00593	0.27087
12T	0.057	0.055	0.00271	0.00550	0.40916
11T	0.067	0.065	0.00229	0.00517	0.24077
10T	0.078	0.076	0.00306	0.00655	0.53063
9T	0.093	0.091	0.00340	0.00660	0.63599

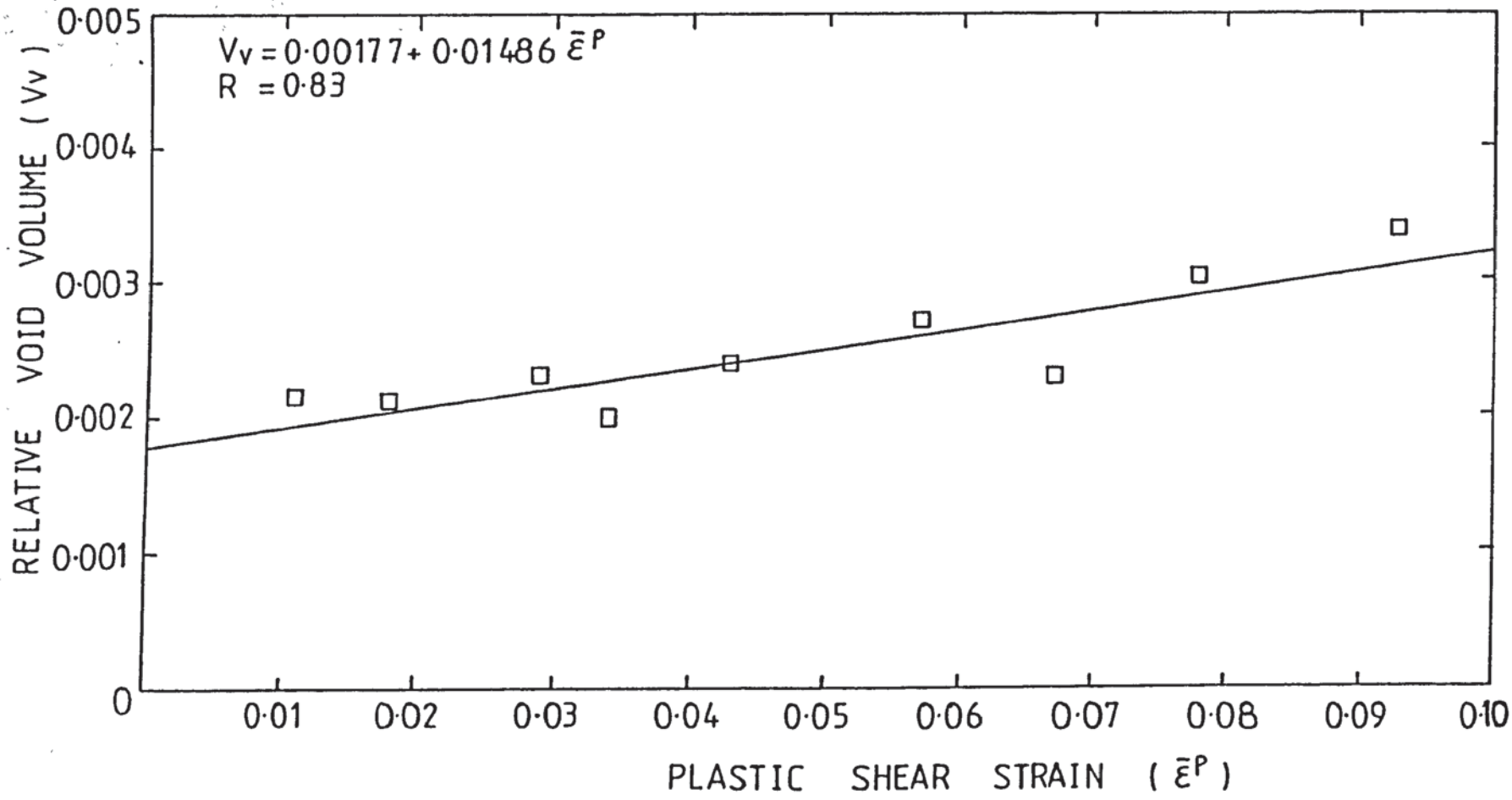

FIGURE 3.6 Relative void volume versus the plastic shear strain, based on statistical measurement

Section 4

VOID GROWTH APPROACH

EPRI report [72] has proposed a linear void growth law based on the experimental observations on a series of smooth and notched tensile specimens. The law is shown in Eq. (1.59). In the original equation, V_o is the specific volume of inclusion. If we have considered V_o as the relative void volume at nucleation and substituted values of nucleation strain and relative void volume at nucleation into Eq. (1.59), the experimental law for void growth becomes

$$V_v = 0.0018 \exp\left[T_1(\bar{\varepsilon}^p - 0.002).\ \frac{\sigma_m}{\bar{\sigma}}\right] \quad \text{.....(4.1)}$$

where σ_m is the mean stress; $\bar{\sigma}$ is the effective stress; V_v is the measured final relative void volume; $\bar{\varepsilon}^p$ is the final plastic shear strain. The present work attempts to determine a dimensionless void growth coefficient, T_1, in the above equation, if it is assumed that this relationship is available in both low stress triaxiality, and severe stress triaxiality.

4.1 Method I for Determining the Void Growth Coefficient - Multiple Tensile Specimen Testing

A series of tensile specimens were pulled at the various interrupted uniform elongations before the neck formation. The details of the experimental procedure and results have already been described in Section 3. The void growth

coefficientwill be calculated using the results obtained in the above section.

In a uniaxial tension test, in which $\sigma_{22}=\sigma_{33}=o$ before neck formation, the mean stress $\sigma_m = \sigma_{11}/3$, and effective stress, $\bar{\sigma}=\sigma_{11}$. Thus the stress triaxiality, $\sigma_m/\bar{\sigma}$ in uniaxial tension is equal to a constant, 0.33, before neck formation.

If a least-squares fit is used to describe the relationship between the $\ell n\ (^{Vv}/Vo)$ and $(\bar{\varepsilon}^p-\bar{\varepsilon}^p_o)$, values of which are given in Table 3.3, it is

$$\ell n(\frac{V_v}{V_o})=0.03303+5.88730(\bar{\varepsilon}^p-\bar{\varepsilon}^p_o) \qquad \text{.....(4.2)}$$

where it is assumed that $\ell n(^{Vv}/Vo)=0$, when $(\bar{\varepsilon}^p-\bar{\varepsilon}^p_o)=0$. The sample correlation coefficient, R, is 0.90. Compared with the Eq. (4.1), the slope in the above fitted line is $(T_1.(^{\sigma}m/\bar{\sigma}))$. Thus, $T_1=17.66$ due to $^{\sigma}m/\bar{\sigma} = 0.33$.

It is found for the relative void volume in Table 3.3 that the standard deviations are larger than the mean values at various strains, and that these results cannot be improved by increasing the number of observations. It has been done that the number of observations for each specimen increases from 200 up to 1000. Unfortunately, the values of the standard deviation hardly change. Thus, it means that the scatter of measured relative void volume is

probably too large, because there is not a large enough number of voids, which can be measured by the point counting technique. For example, the relative void volume is measured 1000 times in tensile specimen No. 9T, which has been stressed at ultimate tensile stress. The distribution proportion for the relative void volume in total 1000 observations is that

$Vv = 0.0$ for 85.6% observations
$Vv = 0.00190$ for 14.0% observations
$Vv = 0.00006$ for 0.4% observations

where the number of grids is 72. Thus, the reliability about the measured Vv values decreases. Furthermore, the reliability of the calculated T_1 value also decreases.

It is known from Table 3.2 that there are about 2.5×10^4 voids/cm^2 in these strained specimens. In order to obtain a large enough number of voids in each photomicrograph, for example, about 20 voids per photomicrograph, the magnification should not be over 300. However, most of the void sizes are often about 2μm to 8μm. If the brittle fracture method is used to prepare the sample surface, the surface will be too rough to observe voids at such low magnification. If the mechanically polished method is used to prepare the sample surface, in which the observed void size is much smaller than its real size, it is very difficult to distinguish voids from inclusions. Furthermore, if the magnification is not large enough, the smaller void size will give difficulty

in point counting.

From the above discussion, the number of voids per unit area is insufficient for a credible statistical treatment. In order to check the validity of the relative void volume based on statistical measurement, it was decided to use a method of directly measuring the area of voids. In fact, this method belongs in a statistical sampling analysis. The measurement was conducted by means of a travelling microscope on photomicrographs. To simplify the calculation of the void area, it was assumed that the voids were in the shape of an oval.

The calculated relative void volume, Vv, is listed in Table 4.1. Using linear regression, the relationship between Vv and $\bar{\varepsilon}^p$ is shown in Fig. 4.1, and given by

$$V_v = 0.00171+0.00705\ (\bar{\varepsilon}^p),\ R = 0.58 \quad \text{.....(4.3)}$$

$$\ln\left(\frac{V_v}{V_o}\right)=0.00368+3.44182(\bar{\varepsilon}^p-\bar{\varepsilon}^p_o),\ R = 0.67 \quad \text{.....(4.4)}$$

Thus, the relative void volume at nucleation, Vo = 0.00172, when $\varepsilon o=0.002$, and the void growth coefficient, $T_1 = 10.3$. It is noted that the datum obtained from specimen No. 13T is remote from its surrounding data. If this datum is omitted, the above expressions become

Table4.1: Measured relative void volume by direct measurement

Specimen No.	Plastic shear strain, $\bar{\varepsilon}^p$	Relative void volume, V_v*	$\ell n(V_v/V_o)$	
			ε_o=0.002, V_o=0.00172	ε_o=0.002, V_o=0.00161 (Omit No.13T)
17T	0.011	0.00178	0.03429	0.10038
16T	0.018	0.00171	-0.00583	0.06026
15T	0.029	0.00183	0.06199	0.12808
14T	0.034	0.00187	0.08361	0.14970
13T	0.043	0.00267	0.43975	0.50584
12T	0.057	0.00190	0.09953	0.16562
11T	0.067	0.00208	0.19004	0.25613
10T	0.078	0.00201	0.15581	0.22190
9T	0.093	0.00254	0.38984	0.45593

*The V_v values were measured directly from photomicrographs by travelling microscope.

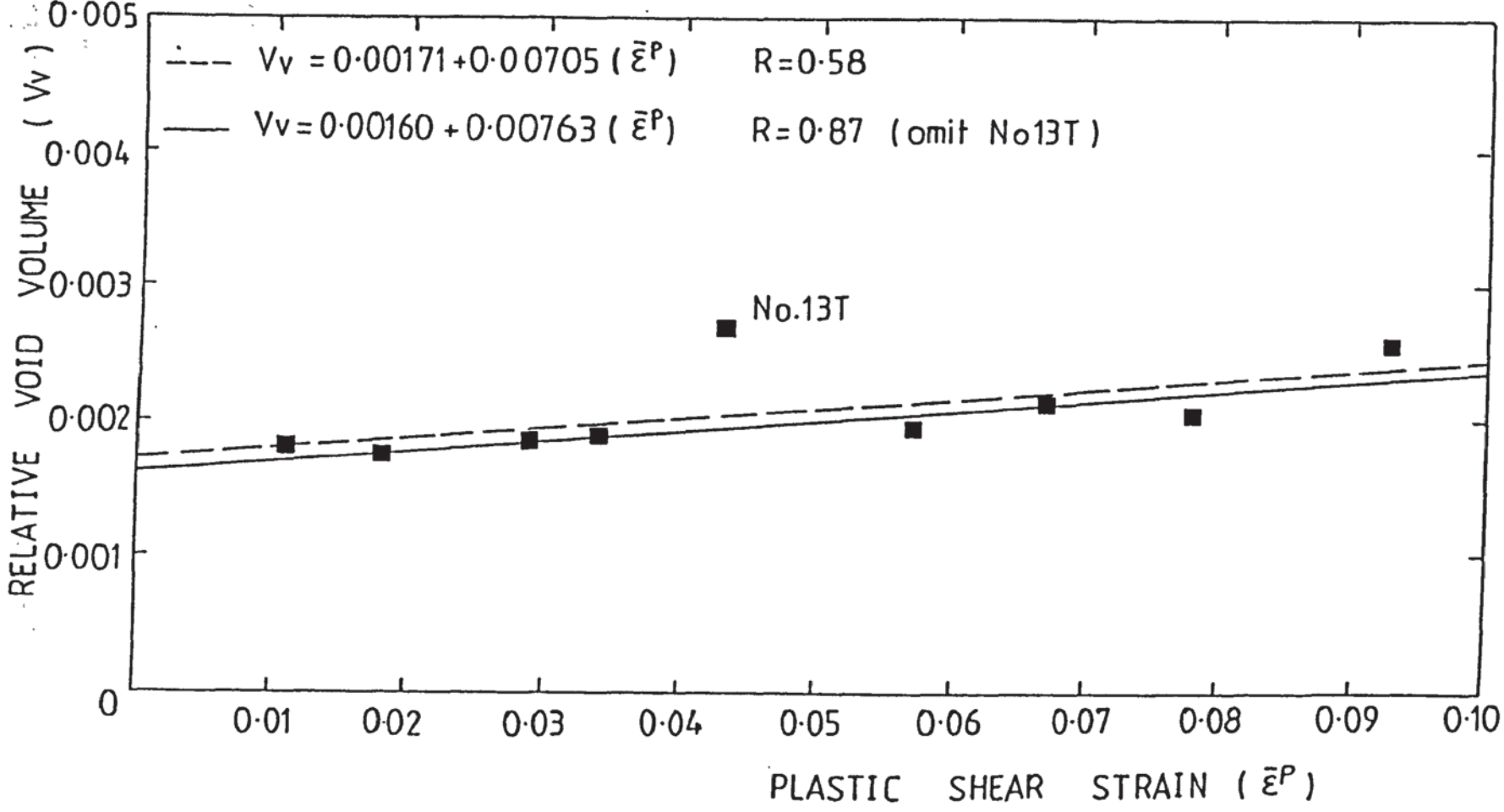

FIGURE 4.1 Relative void volume versus the plastic shear strain, based on direct measurement

$$V_v = 0.00160+0.00763(\bar{\varepsilon}^p), R = 0.87 \quad \text{.....(4.5)}$$

$$\ell n(\frac{V_v}{V_o}) = 0.01407+3.80425(\bar{\varepsilon}^p-\bar{\varepsilon}^p_o), \; R = 0.92 \quad \text{.....(4.6)}$$

Thus, the relative void volume at nucleation, Vo=0.00161, when ε_o=0.002, and the void growth coefficient, T_1= 11.4.

Compared with the results obtained from directly measuring the void area, the statistical measurement basically reports the relationship between the relative void volume and plastic strain level. Although the standard deviation is rather larger for the low void density situation, the point counting technique based on statistics is still used to measure the relative void volume in the subsequent work.

4.2 Method II for Determining the Void Growth Coefficient - Single Tensile Specimen Testing

A round tensile specimen is shown in Fig. 4.2. The orientation of the specimen is along the rolling direction of the test plate. The tensile specimen was pulled in 5000 Kgf Instron testing machine with a loading rate of 0.05 cm/min at 15°C till fracture. Except necking region, the specimen was divided into five parts along the longitudinal direction of the specimen. The change in diameter was measured in these uniform strain regions, and plastic shear strain, $\bar{\varepsilon}^p$, was calculated in each part, separately. Then, each part of the specimen was

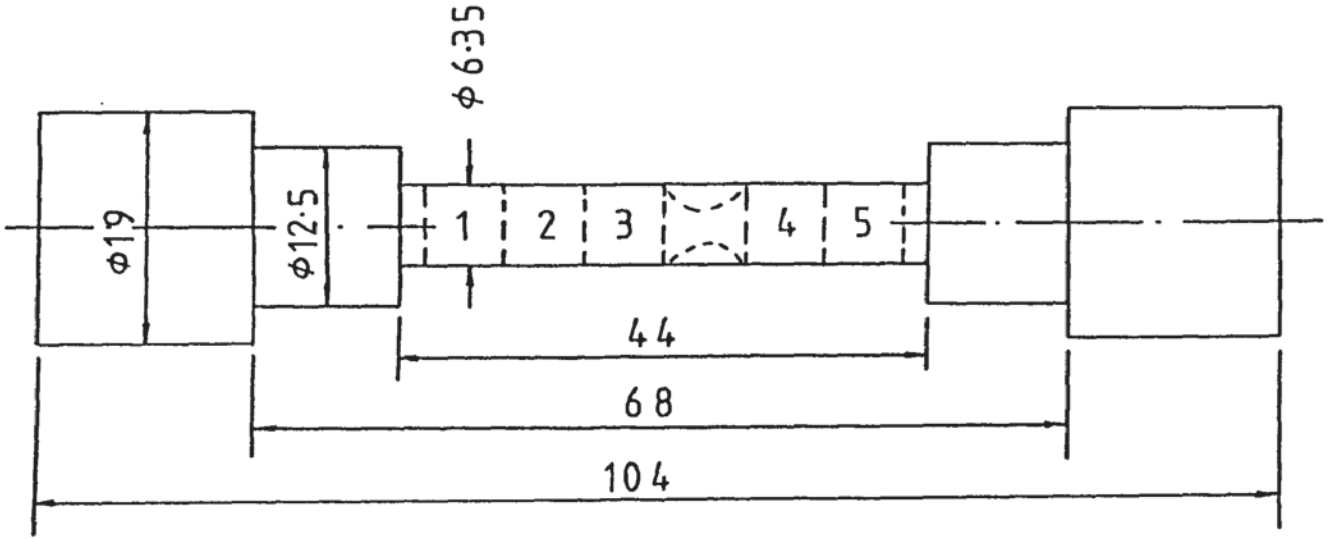

All the dimensions are in mm
Ratio = 1·5 : 1

FIGURE 4.2 Tensile specimen

longitudinally sectioned in liquid nitrogen.

Point counting technique was directly conducted on the screen of scanning electron microscope. A transparent paper with a regular square grid of 1 cm was superimposed on the screen. Magnification of 1000 was chosen to observe the fracture surface. The grid did not move, but the observed location of the specimen moved randomly. Each Vv value was a mean result in 100 observations, as listed in Table 4.2.

Considering that $\ell n(^{Vv}/Vo)=0$, if $(\bar{\varepsilon}^p-\bar{\varepsilon}^p_o) =0$. Thus a regression equation is given by

$$\ell n(^{Vv}/Vo)=0.014+1.363\ (\bar{\varepsilon}^p-\bar{\varepsilon}^p_o) \qquad \text{.....(4.7)}$$

and the sample correlation coefficient, R, is 0.74. Therefore, the void growth coefficient,

$$T_1 = \frac{1.363}{0.33} = 4.13$$

and it is shown in Fig. 4.3.

4.3 Method III for Determining the Void Growth Coefficient - Tensile Testing Combined with Three-Point Bend Testing

The above measurements on the void growth coefficient were conducted under uniaxial stress state. It will

Table 4.2 : Measured plastic strain and relative void volume

Sample number	Initial diameter, do, mm	Final diameter, d, mm	Plastic shear strain, $\bar{\varepsilon}^p$	Relative void volume, Vv	Standard deviation σ	$\ell n(\frac{V_v}{V_o})$	$\bar{\varepsilon}^p - \bar{\varepsilon}^p_o$	$\frac{\ell n(Vv/Vo)}{\bar{\varepsilon}^p - \bar{\varepsilon}^p_o}$
1	6.36	5.73	0.104	0.00200	0.00461	0.10536	0.102	1.033
2	6.36	5.78	0.096	0.00213	0.00472	0.16834	0.094	1.791
3	6.35	5.73	0.103	0.00225	0.00483	0.22314	0.101	2.209
4	6.35	5.65	0.117	0.00200	0.00461	0.10536	0.115	0.916
5	6.36	5.79	0.094	0.00213	0.00472	0.16834	0.092	1.804

a. BS4360 Grade 50D normalized steel; plate number 2A52-1

b. Round tensile specimen was tested with a loading rate of 0.05 $^{cm}/_{min}$ at 15^{o}C

c. It is assumed that $\bar{\varepsilon}^p_o$=0.002, and Vo=0.0018

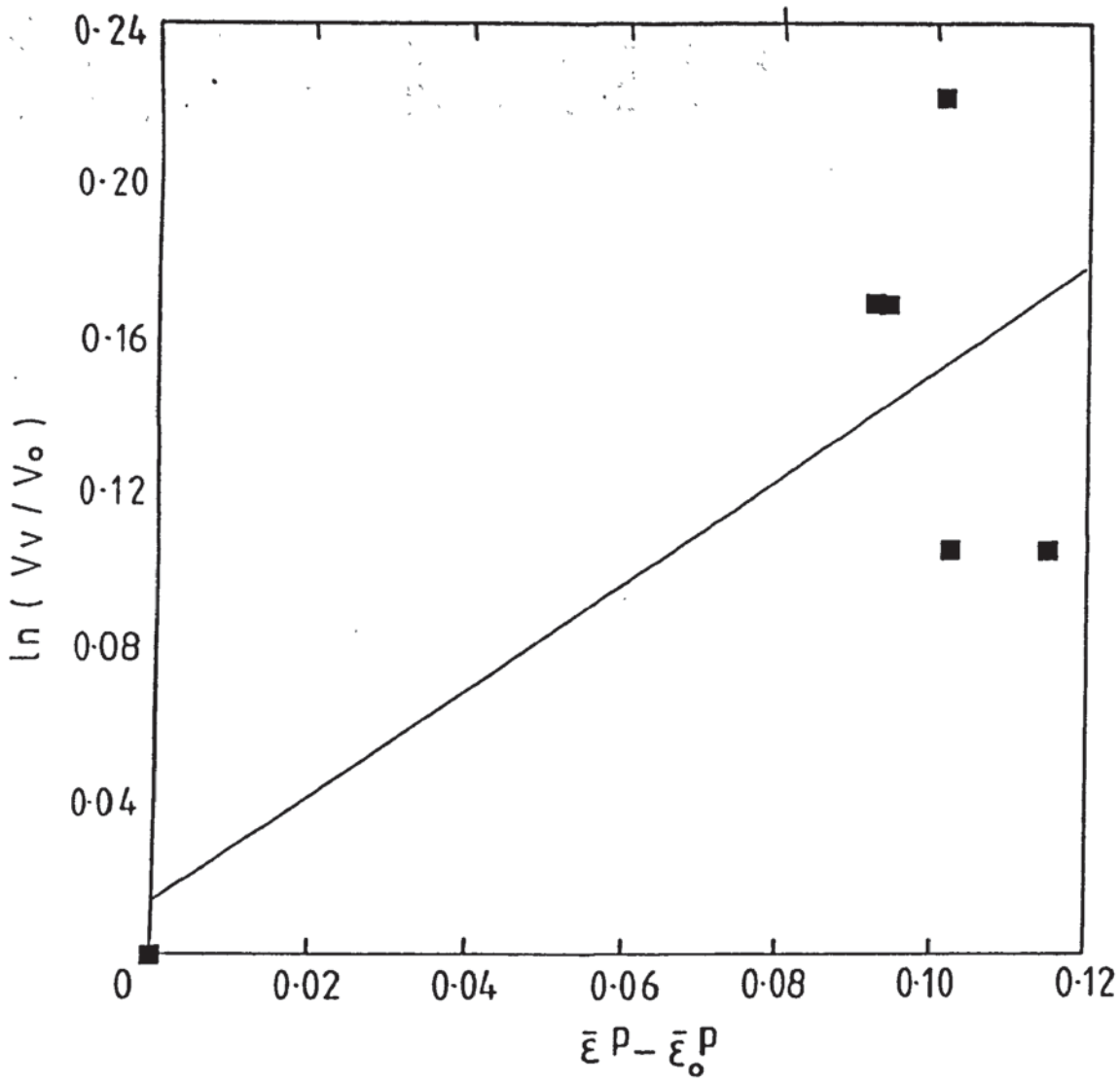

FIGURE 4.3 Relationship between ℓn ($^{Vv}/Vo$) and ($\bar{\varepsilon}^p - \bar{\varepsilon}^p o$), based on single specimen method

be argued whether this coefficient is still available in a rather higher constraint condition. Therefore it is decided to use a pre-cracked side-grooved specimen, as shown in Fig. 5.1. The stress triaxiality ahead of the pre-crack in the specimen is evaluated by the HRR field analysis, and the relative void volume is measured at some specific distance ahead of the crack tip. Then the results are linked by a straight line with the results previously determined by the uniaxial tensile tests, as mentioned in Section 4.2, if it is assumed that a linear relationship between a modified void growth and stress triaxiality exists. In this case, the void growth coefficient expressed by the slope of the straight line probably exhibits a better applicability in a wide range of the constraints.

4.3.1 Experimental Determination of the Plastic Shear Strain and Relative Void Volume Ahead of the Crack Tip

Side-grooved Charpy-size specimens were made from the L-T orientation and fatigue precracked to crack length to specimen depth ratio, $^{a}/_{w} = 0.5$. Three-point slow bend testing was conducted in a 5000 Kgf Instron testing machine at room temperature. In order to determine the plastic shear strain distribution ahead of the crack tip, a gauge length of 1.7 mm across the crack was made by means of microhardness indentations. The plastic strain can be

calculated from a comparison between the original gauge lengths and residual gauge lengths. Then, the bended specimens were sectioned by brittle fracture in liquid nitrogen along the longitudinal mid-thickness. In order to measure the relative void volumes, a point counting technique was directly conducted on the screen of SEM S150. Square grid of 1 cm and magnification of 1000 were used. The observed location was restricted within the region of 0.4 to 0.6 mm ahead of the crack tip. The experimental results on the plastic shear strain and relative void volume in the interesting region are given in Table 5.24. The details will be described in Section 5.

4.3.2. Calculation on the Power Hardening Coefficient

For a material with the cold-worked hardening, its stress-strain behaviour may be taken in the form of a pure power hardening relation suggested by Ilyushin [80] so that in simple tension, $\varepsilon/\varepsilon_o=\alpha(\sigma/\sigma_o)^n$, where α is a dimensionless material constant, and ε_o and σ_o are reference values of the strain and stress, which may be associated with the yield strain and stress of the material. The connection is that $\sigma_o=E\varepsilon_o$, where E is Young's modulus. n is the power hardening coefficient. n=1 corresponds to the elastic condition and $n=\infty$ to the ideally plastic condition.

Based on the values of true stress and true strain obtained in the round tensile specimens, as given in Table 3.1. Considering that σ_o=349MPa in the test material, and $\varepsilon_o=\sigma o/E=0.002$, a best fit relationship is given by

$$\frac{\varepsilon}{\varepsilon_o}=5.692\left(\frac{\sigma}{\sigma_o}\right)^{4.325} \qquad \text{.....(4.8)}$$

If the best fit is based on Ramberg-Osgood relation, it is shown as follows

$$\frac{\varepsilon}{\varepsilon_o}=\frac{\sigma}{\sigma_o}+5.016\left(\frac{\sigma}{\sigma_o}\right)^{4.502} \qquad \text{.....(4.9)}$$

The above relations apply to uniaxial or equivalent stress equivalent strain relations.

It might be noted that the α values are much larger than 0.02 corresponding to a usual engineering definition of yield [38] or 3/7 corresponding to A533B steel [41]. These results may be related to the apparent discontinuous yielding generated during tensile test. In the yielding terrace, the strain ratio, $(\varepsilon/\varepsilon_o)$, varied from 3.5 to 9.0, corresponds to almost same stress ratio, (σ/σ_o), of about 1.1. However, these data sited on the yielding terrace were excluded, when the regression relationships were established.

4.3.3 Estimation of the Stress Triaxiality Ahead of the Crack Tip by the HRR Field Analysis

The distribution of the stress and strain at the tip of the crack under yielding conditions varying from small-scale to fully plastic for infinite bodies is given by Eq. (1.30). After some manipulation, Eq (1.30) can be rewritten in the form

$$J=\alpha\sigma_o\varepsilon_o\left[\frac{\sigma_{ij}(r,\theta)}{\sigma_o\,\tilde{\sigma}_{ij}(\theta,n)}\right]^{n+1}.r.In \qquad .....(4.10)$$

where $\sigma_{ij}(r.\theta)$ is the near tip stress field, expressed by polar co-ordinates, r and θ, centred at the crack tip. $\tilde{\sigma}_{ij}(\theta,n)$ is a dimensionless function, and In is an integration constant. Both $\tilde{\sigma}_{ij}(\theta,n)$ and In values can be estimated from Hutchinson's paper [39]. σ_o and ε_o are the yield stress and yield strain of the material, separately. n is the strain hardening exponent in Ramberg-Osgood relation. α is a material constant.

Recently, the fully plastic crack solutions for common fracture toughness test specimen configurations were presented in the EPRI report NP-1931 [81]. For the single edge cracked bend bar (SECBB) loading in three-point bending, the crack parameter in the fully plastic state is expressed as follows

$$J=\alpha\sigma_o\varepsilon_o ch_1(a/b,n)(P/Po)^{n+1} \qquad .....(4.11)$$

where P is the load per unit thickness, and c=b-a is the remaining ligament, as shown in Fig. 4.4. $h_1(a/b,n)$ is the fully plastic solutions corresponding to J for the test specimen configuration. h_1 values were presented in the EPRI report NP-1931. Po is the limit load per unit thickness. For plane strain Po is given by the Green and Hundy solution

$$Po = 0.728\sigma_o C^2/L \qquad \text{.....(4.12)}$$

where L is the half length of the specimen.

If we connect Eq. (4.10) with Eq. (4.11), the near tip stress field in our interesting finite body may be expressed by [82]

$$\sigma_{ij}(r,\theta)=\sigma_o\tilde{\sigma}_{ij}(\theta,n)\left[\frac{ch_1(a/b,n)}{r.In}\right]^{\frac{1}{n+1}}\left(\frac{P}{Po}\right) \qquad \text{.....(4.13)}$$

At the angle θ=o the $\sigma_{yy}=\sigma_{\theta\theta}$, and the$\sigma_{xx}=\sigma_{rr}$. The through thickness stress $\sigma_{zz}=0.5(\sigma_{xx}+\sigma_{yy})$ for plane strain deformation. After some manipulation, a following equation can be obtained to evaluate the ratio of the mean normal stress to the effective stress in the yielded region at some specific distance ahead of the crack tip

$$\frac{\sigma_m}{\bar{\sigma}} = \frac{1}{2}\left[\frac{\tilde{\sigma}_\theta+\tilde{\sigma}_r}{\sigma e}\right] \qquad \text{.....(4.14)}$$

where the θ-variations of stresses at the crack tip for plane strain may be estimated from the Hutchison's paper[39].

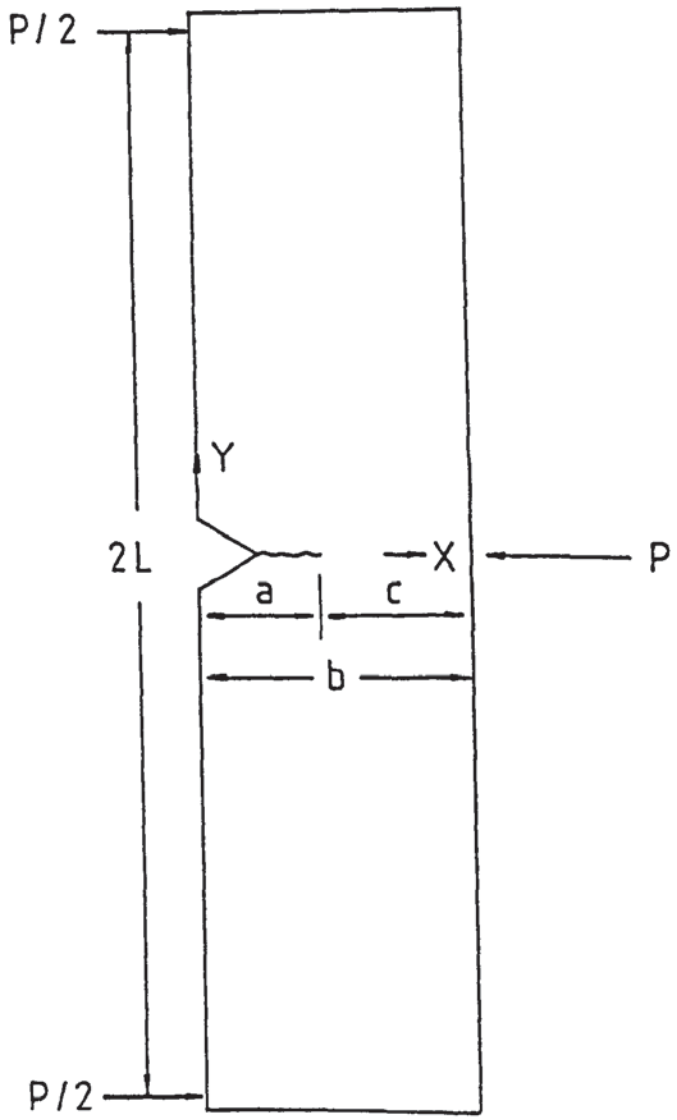

FIGURE 4.4 Schematic of a single-edge cracked bend bar

For a pre-cracked side-grooved Charpy-size specimen, general yielding condition is formed during the crack initiation in bending test. Additionally, it is assumed that the crack tip is under the condition of plane strain. As the power hardening co-efficient n=4.5 for the interesting material, the corresponding values of the scaling factors are approximately evaluated by interpolation for $\theta=0$, as follows

$\tilde{\sigma}_{ij}(\theta,n)$	n=3	n=4.5	n=13
$\tilde{\sigma}_{\theta}$	1.93	2.03	2.60
$\tilde{\sigma}_{r}$	1.66	1.67	1.75
$\tilde{\sigma}_{e}$	0.24	0.31	0.71

The stress triaxiality at some distance ahead of the crack tip is calculated by

$$\frac{\sigma_m}{\bar{\sigma}} = \frac{1}{2}\left(\frac{2.03+1.67}{0.31}\right) = 5.97$$

It should be noted for plane strain that the stress triaxiality calculated by the above procedure at some distance ahead of the crack tip is only dependent on n, if $\theta=0$, but independent of the distance, r.

4.3.4 Determination of the Void Growth Coefficient

Table 4.3 summarizes some results about the void growth scaled by the increment of the plastic shear strain and stress trixiality for the round tensile specimen and pre-cracked side-grooved Charpy-size specimen. The experimental procedure in detail is described in Section 4.2 and Section 5.3. Based on these results, a best fit equation is given by

$$\frac{\ell n(Vv/Vo)}{(\bar{\varepsilon}^p - \bar{\varepsilon}^p_o)} = 0.29 + 3.83\ (\frac{\sigma_m}{\bar{\sigma}}) \qquad \text{.....(4.15)}$$

$$R = 0.99$$

Therefore, the void growth coefficient T_1 of 3.83 is determined by means of the two groups of terminal values, which have very different stress triaxialities.

Table 4.3 Summary of the observed void growth and calculated stress triaxiality.

Sample number	$\frac{\sigma_m}{\bar{\sigma}}$	$\frac{\ell n(V_v/V_o)}{\bar{\varepsilon}^p - \bar{\varepsilon}^p_o}$
ROUND TENSILE SPECIMEN		
1	0.33	1.033
2		1.791
3		2.209
4		0.916
5		1.804
PRE-CRACKED SIDE-GROOVED BEND SPECIMEN		
S13v	5.97	24.682
S19v		21.568

Section 5

CALIBRATION OF NOTCH AND CRACK OPENING DISPLACEMENT AND ESTIMATION OF THE CONSTRAINT IN CHARPY-SIZE SPECIMENS

5.1 Introduction

The standard Charpy specimen with the 0.25 mm radius V-notch, as covered in BS.131 or ASTM E23, represents well-known specimen geometry. In the past, the specimen has been used most widely in the impact mode of loading for testing lower and intermediate strength grades of steel. Using the Charpy specimen as a quality control test for correlating with or estimating the fracture toughness of materials exhibits several advantages which derive primarily from the small overall size of the specimen (which means a small test material volume requirement), the flexibility for examining various test orientations, the relatively low specimen preparation cost, and the ease in testing at various temperatures. In addition, its long use history means that testing personnel generally are familiar with the specimen and the test [83]. Recently, considerable effort has been devoted to testing a side-grooved modification of the Charpy specimen, which could be readily utilised in reactor surveillance programmes, for estimating the fracture toughness at crack initiation in nuclear pressure vessel steels [84]. The test utilises Charpy V-notch three-point bend specimens

fatigue-pre-cracked to a crack length-to-width ratio ($^{a}/W$) of 0.5; side-grooves of varying depth are then machined with 0.25 mm root radii and 45° V-notches. Side-grooves increase constraint, that is, they effectively thicken the specimen by restricting or eliminating regions of through-thickness deformation, thus inducing a straight crack front. It has also been found for the compact specimen that the presence of side-grooves promoted flat fracture and suppressed shear lips [13]. However, as many small specimen fracture toughness techniques, the results must only be regarded as estimates since the analysis is difficult to fully justify on strict fundamental grounds. For example, an assumption of purely plane strain deformation is not certain since it is not known how the presence of side-grooves influences the slip-line fields at the base of the notch. The precise influence of side-grooves on the state of stress at the notch root cannot be fully clarified until a three-dimensional elastic-plastic stress analysis is performed for the specimen containing side grooves.

Current investigations have pointed out that toughness is structure and stress-state dependent. In 1969, Rice and Tracey [71] showed a theoretical law for void growth in a non-hardening material. Based on the experimental observations of A533B pressure vessel steel, EPRI [72] has proposed a linear law for studying the relationship among

the void growth, plastic shear strain, and stress triaxiality. In order to investigate this linear relationship of BS.4360 Grade 50D steel, the void growth coefficient, critical plastic strain, and relative void volume during nucleation have been determined in the Sections 3, and 4.

The present work attempts to calibrate the constraint of the side-grooved specimen by means of the void growth studies, comparing with the standard Charpy specimen. The three-point bending specimens were photographed periodically during the tests to record the strain histories in the vicinity of the notch- or crack-tip, and to establish the relationship between the notch or crack opening displacement and load-point deflection. Sectioned specimen surfaces were observed with a scanning electron microscope. Point counting method was used to measure the relative void volume.

5.2 Nonside- and Side-Grooved Charpy Specimens

5.2.1 Experimental Procedure

Standard Charpy V-notch specimen and side-grooved Charpy V-notch specimen were investigated. The side-grooved specimens exhibited standard Charpy dimensions, as shown in Fig. 5.1. The side-grooves of tapering depth were machined with 0.25 mm root radii and 45° V-notches. The

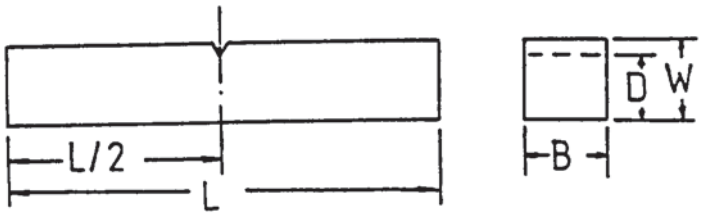

(a) CVN specimen

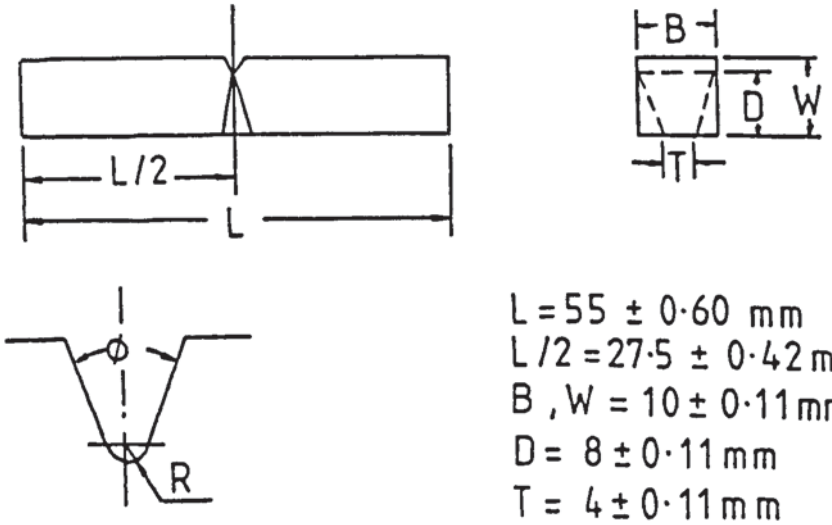

(b) Side-grooved CVN specimen

$L = 55 \pm 0{\cdot}60$ mm
$L/2 = 27{\cdot}5 \pm 0{\cdot}42$ mm
$B, W = 10 \pm 0{\cdot}11$ mm
$D = 8 \pm 0{\cdot}11$ mm
$T = 4 \pm 0{\cdot}11$ mm
$R, R_S = 0{\cdot}25 \pm 0{\cdot}025$ mm
$\phi, \phi_S = 45 \pm 2^{\circ}$

FIGURE 5.1 Dimensions for Charpy-size specimens (Subscript S denotes the root size of the side-grooves)

total maximum side-groove depth was 6 mm on the surface opposite the main notch. The specimens were cut from a 50 mm thickness plate of BS.4360 Grade 50D steel (2A52-1). The longitudinal direction of the specimens was along the principal direction of rolling and the axis of the notch was perpendicular to the rolled surface of the plate. Sampling location is shown in Fig. 5.2. 'T' and 'V' are the symbols of the sampling location. Dimensions in cross section of the specimens were measured using a Micrometer, and dimensions in notch geometry were measured by Vickers Fifty-Five Microscope with the magnification of 50 x. The side-groove geometry was measured on the surface opposite the main notch. The actual dimensions of the specimens are listed in Table 5.1.

The three-point bending test was carried out using a 5000 Kg Instron testing machine under displacement control at room temperature. The load range of 2000 kg was chosen. All the specimens were tested with a span of 4 W(W = 10 mm). The testing arrangement is shown in Plate 5.1. The bend test fixture was designed according to BS.5762. The diameter of the rolls and of the centre loading point was chosen as 6 mm. The rolls were made from a high-speed tool steel. A support was made of a Thermo-die (hotwork die steel) steel. This is given in Plate 5.2.

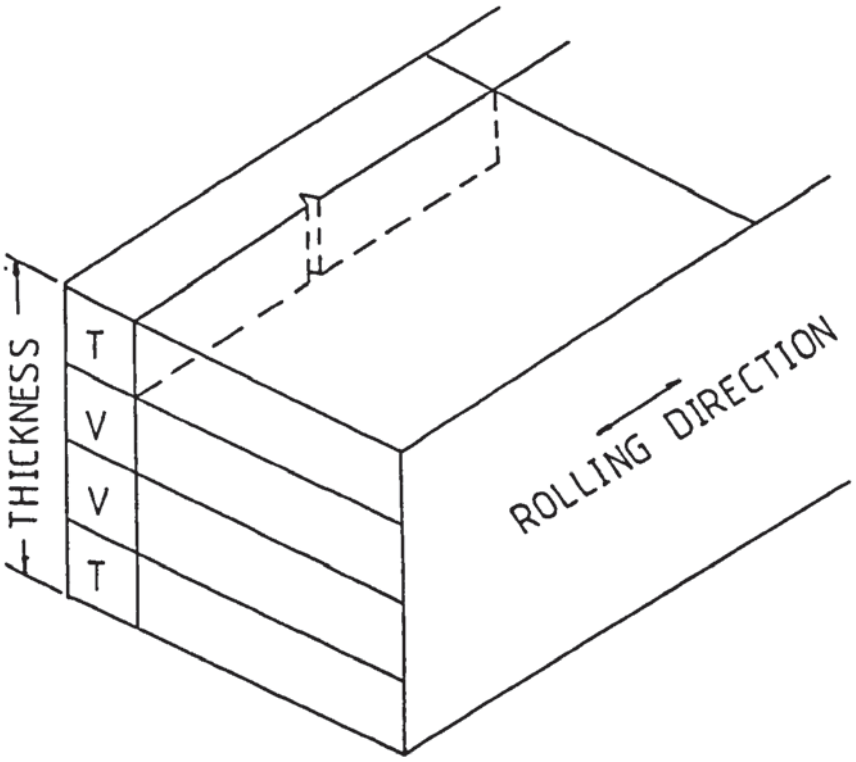

FIGURE 5.2 Sampling location of Charpy-size specimens

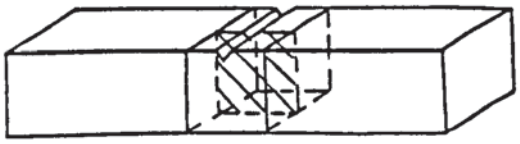

FIGURE 5.11 Mid-thickness section prepared for metallographic examination of voids

Table5.1: Measured dimensions of the CVN specimens

Specimen No.	L	L/2	B	W	D	T	R	R_{S1}	R_{S2}	ϕ	ϕ_{S1}	ϕ_{S2}
NONSIDE-GROOVED SPECIMEN												
B1T	55.6	27.8	9.98	9.98	8.00		0.22			46.0		
B2T	55.8	28.0	9.99	9.98	8.02		0.22			45.5		
B3T	55.8	27.7	9.97	9.98	8.05		0.22			44.5		
B4T	55.8	27.7	9.99	9.98	8.00		0.21			42.0		
SIDE-GROOVED SPECIMEN												
S2T	55.8	28.1	10.00	9.99	8.07	3.93	0.28	0.23	0.22	44.0	43.0	41.5
S6T	55.6	27.8	9.98	10.00	7.98	3.98	0.22	0.23	0.20	46.5	43.3	42.9
S7T	55.8	28.0	9.98	10.00	8.02	3.95	0.25	0.22	0.23	47.0	43.0	42.0
S8T	55.7	27.9	9.97	10.01	8.02	3.98	0.26	0.23	0.25	47.5	41.5	41.5

a. The notations used for the dimensions are shown in Fig. 5.1;

b. All dimensions are in millimetres or degrees;

c. The side-groove geometry was measured on the surface opposite the main notch.

Plate 5.1 : Testing Machine

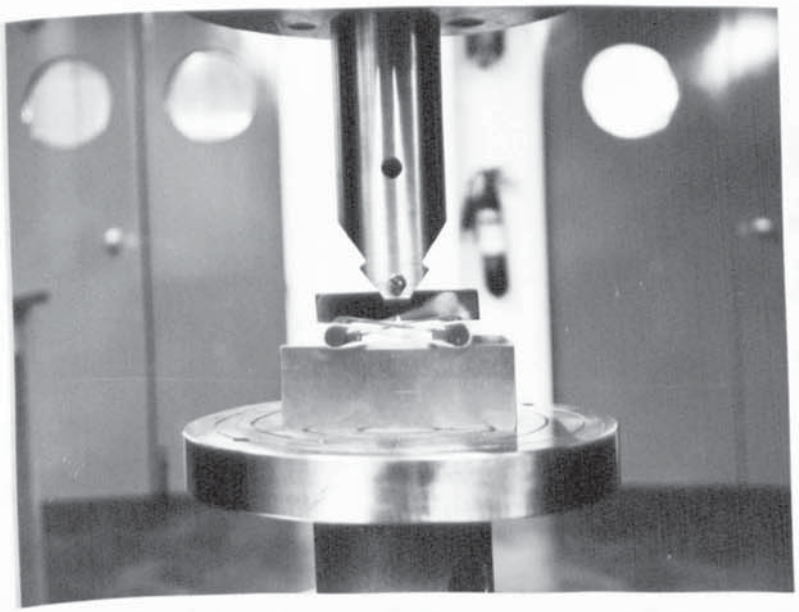

Plate 5.2 : Bend test fixture design

Load was recorded versus load-point displacement by a Farnell Model W211 X-Y Plotter. Load versus load-point displacement curves and load versus plastic deflection curves for nonside- and side-grooved three-point bend specimens are shown in Figs.5.3 and 5.4, respectively. It can be seen that the small increase in load after yielding in these specimens is accompanied by a relatively large increase in displacement or strain to instability. It has been found that these curves for side-grooved Charpy specimen are below that for nonside-grooved specimen. Additionally, the displacement point corresponding to the maximum load was shifted left by the side-grooves. It may be thought that this is because the side grooves decrease the effective section of the specimen. In all cases, general yielding in the calibration specimens at ambient temperature occurred before the crack initiation.

Specimens were loaded at a rate of 0.02 cm/min. The rate of increase of load during the initial elastic deformation was measured to be 65.5 N/sec for standard Charpy specimen, and 59.7 N/sec for side-grooved Charpy specimen. It is obvious that the elastic compliance of the side-grooved specimen increases due to the decrease of the specimen section.

The standard and side-grooved Charpy specimens were loaded to the same level of the notch root opening displacement (NROD) so as to make a comparison of the strain states

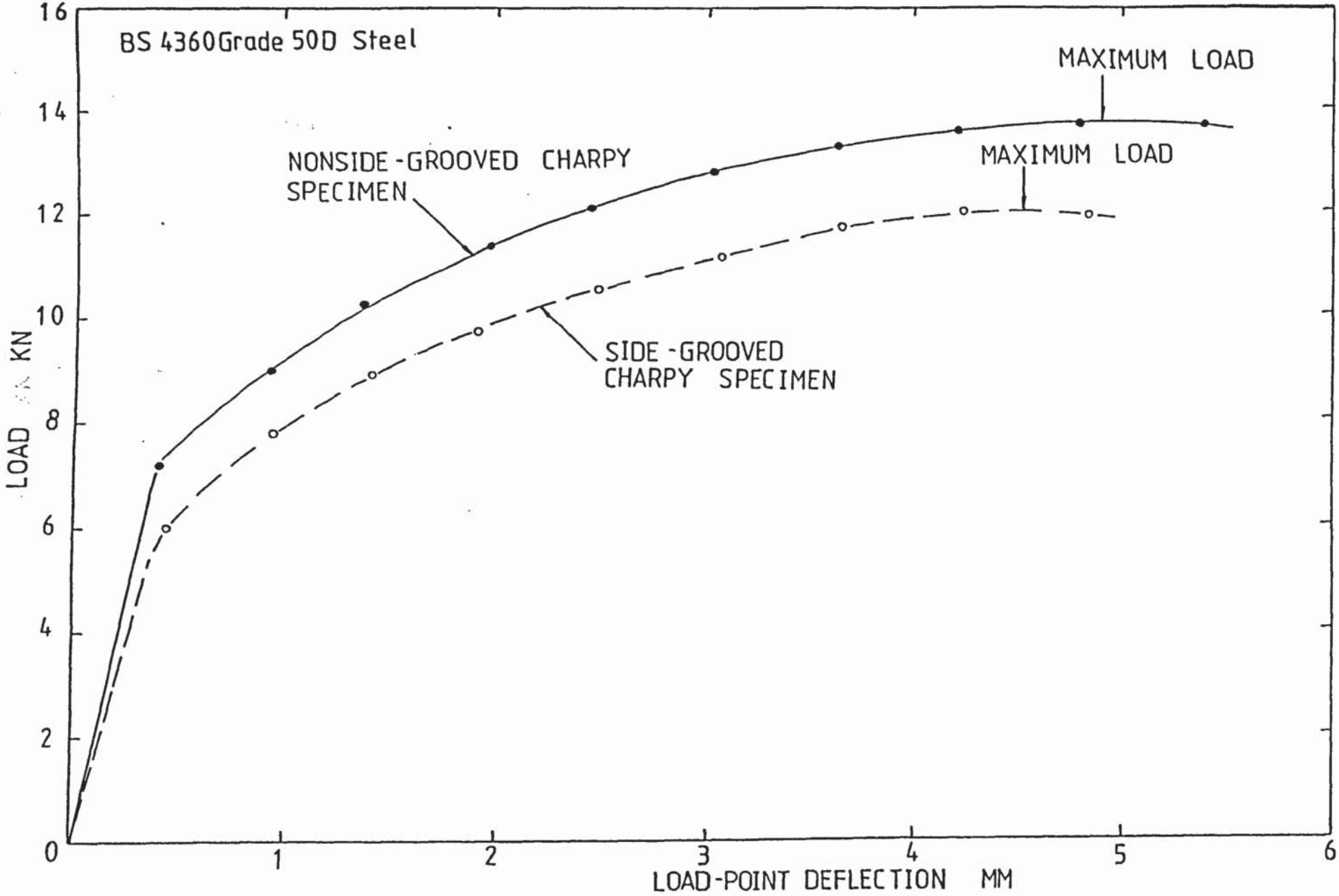

FIGURE 5.3 Load versus load-point displacement curves for nonside- and side-grooved three-point bend specimens

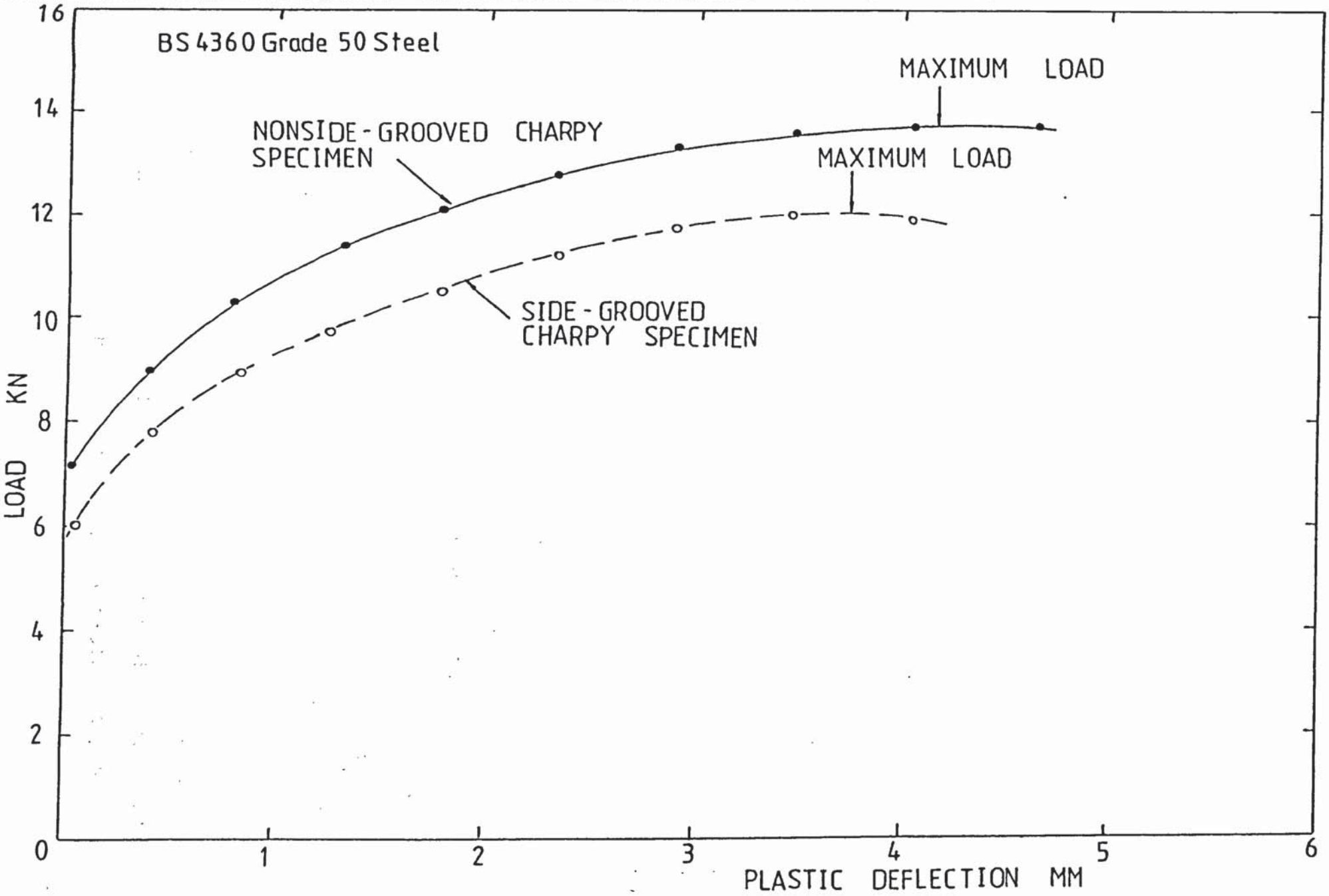

FIGURE 5.4 Load versus plastic deflection curves for non side- and side-grooved three-point bend specimens

and stress triaxialities ahead of the notch root between the two kinds of specimens. The plastic shear strain at the notch root can be obtained from the notch root opening displacement after unloading. Since a deformed notch root stretches beyond the original notch root position, here it is provided that the notch root opening displacement should be defined as the displacement at the original root position [85].

5.2.2 Calibration of Notch Root Opening Displacement

In order to determine the notch root opening displacement of the Charpy specimens, it was decided to use a photographic calibration technique [24, 25]. At the same time, this technique could be used to obtain the data about the longitudinal strain field ahead of the notch root.

The side surface of the specimen was metallographically ground up to grinding paper No.1200. Microhardness indentations were made on the two sides of the notch with the gauge length of 0.80 mm. The indentation spacing on each side was 0.1 mm. A Leitz Miniload microhardness tester was used with a 300 g. load. A typical specimen prepared in this manner is shown in Plate 5.4(a). During the three-point bend testing, photographs were periodically taken of the notch root area using a microscope, camera, and other attachment with a magnification of 15 x. This arrangement is shown in Plate 5.3. Intralux 150H Volpi

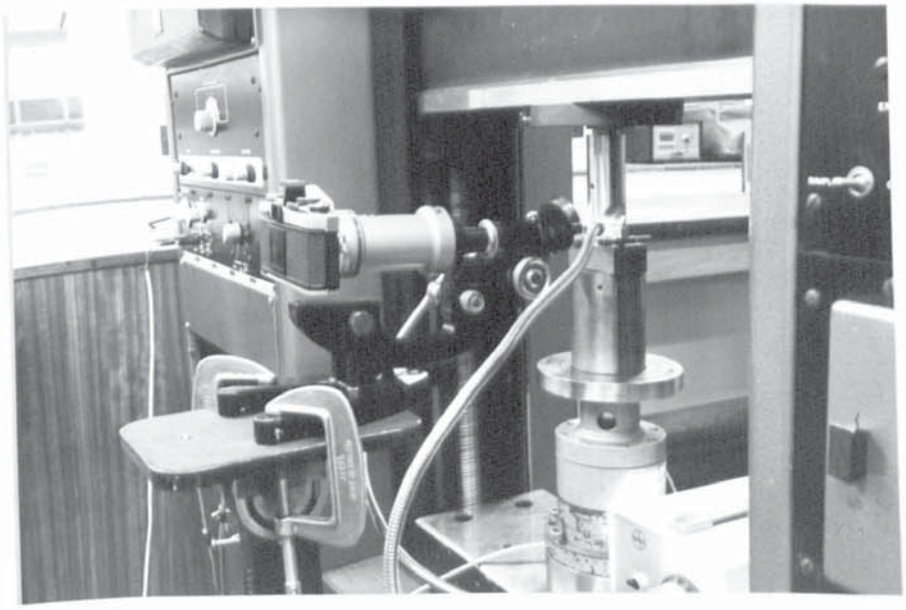

Plate 5.3 : Arrangement of photographic calibration technique.

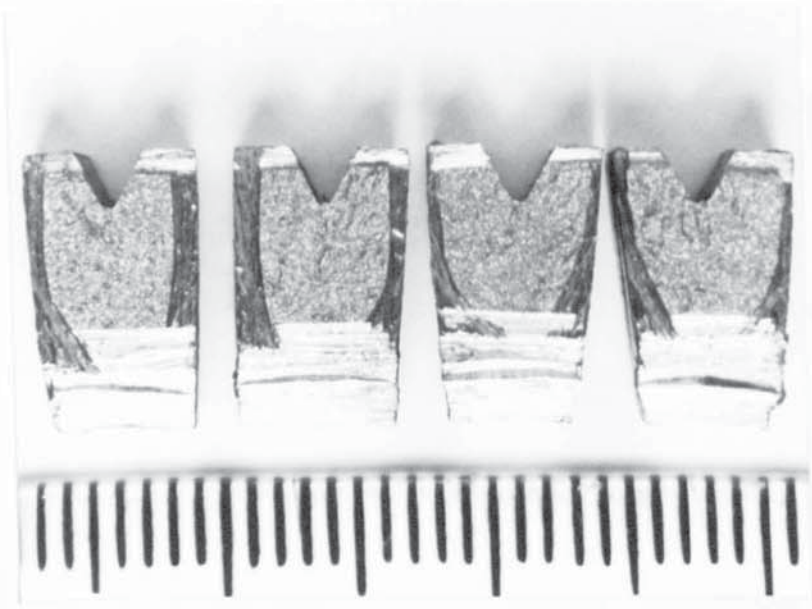

Plate 5.6 : Fracture surfaces in the mid-thickness section of the nonside- and side-grooved specimens (No. B4T on the right; No. S6T on the left).

with two optical fibres was used to illuminate the specimen. The record chart was marked to show the time at which the photographs were taken. Two typical series of the photographs are shown in Plates 5.4 and 5.5 for the nonside- and side-grooved specimens, respectively. The corresponding load-deflection values are listed in Tables 5.2 and 5.3. It can be seen from the two series of photographs that some indentation marks at the notch root tend to be obscured as the test proceeds due to severe plastic flow. In this case, the displacement value must be estimated by extra-polating the other values.

The initiation and spread of plastic zone ahead of the notch root with increasing the load-point displacement are also schematically given in the two series of photographs. It may be noted from the white obscure regions that the schematical extent of the plastic zone is smaller in the side-grooved Charpy specimen than in the standard Charpy specimen, when the crack initiates. For the standard Charpy specimen, the initial growth of the crack occurs at the two corners in the notch root and has an angle of about 45° with loading direction. However, for the side-grooved Charpy specimen the initial growth of the crack occurs along the side-grooves. The side-grooves may serve as crack guides. Making a comparison between the Plates 5.4 (j) and 5.5 (i), which near the maximum bending load, the crack growth is obviously longer in the side-grooved specimen than in the standard Charpy

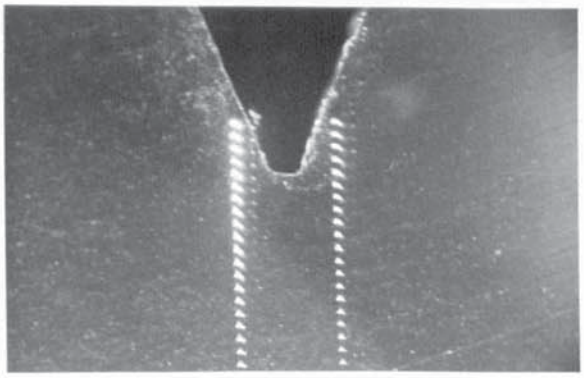

(a)

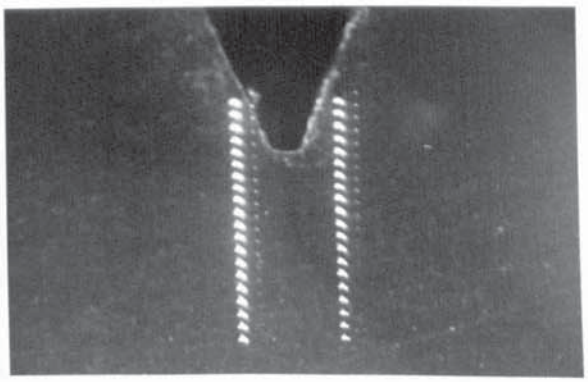

(b)

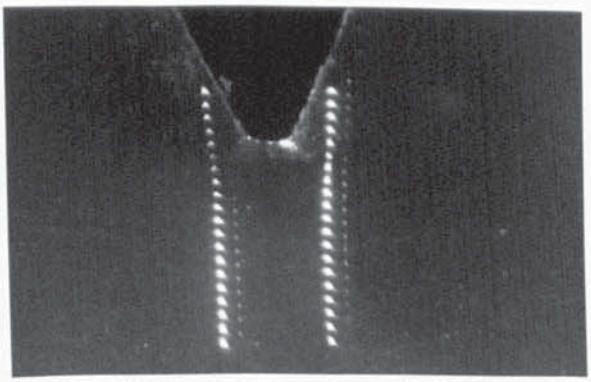

(c)

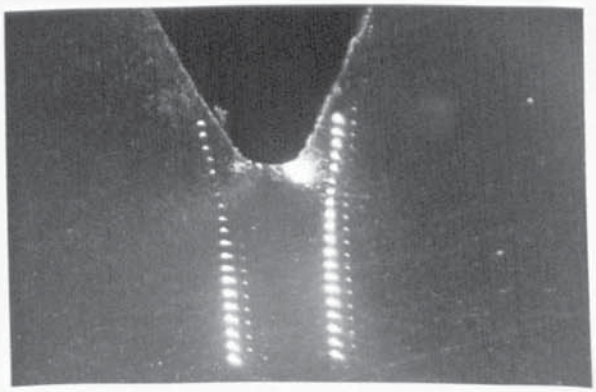

(d)

Plate 5.4 : Calibration series of nonside-grooved Charpy specimen, 17.5 x.

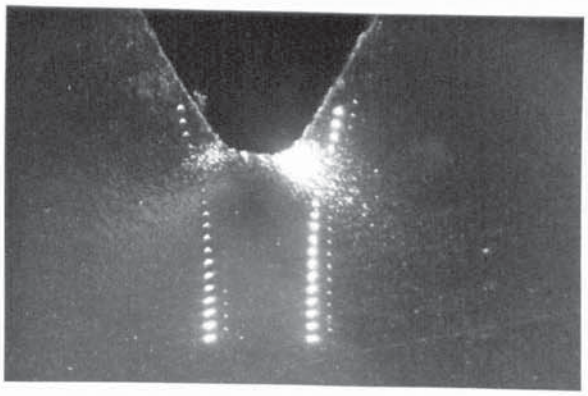

(e)

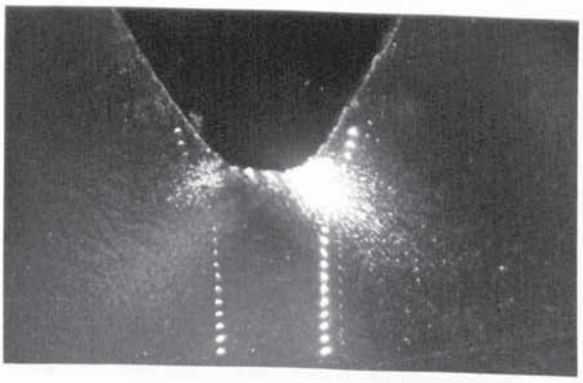

(f)

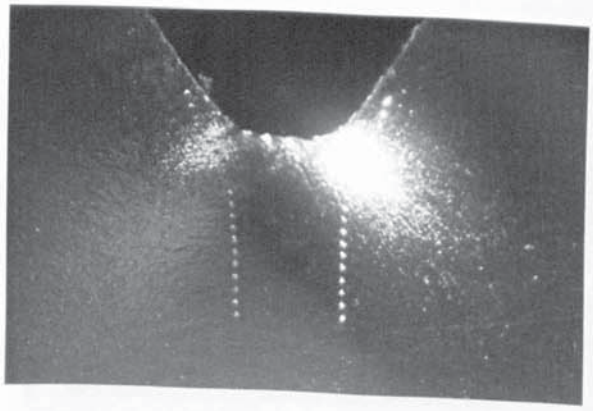

(g)

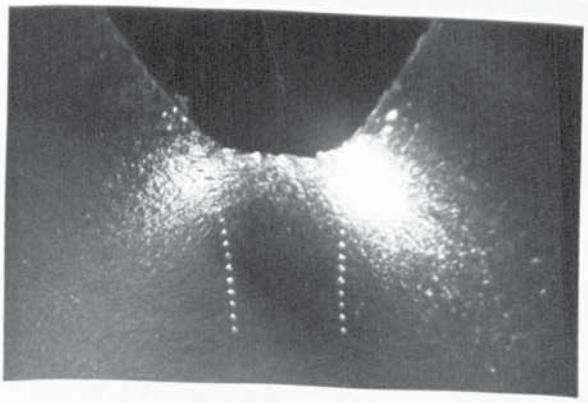

(h)

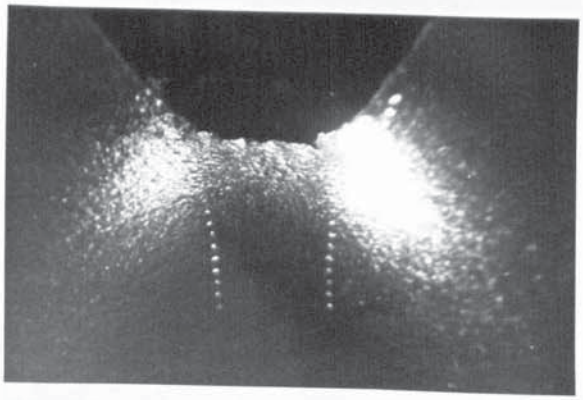

(i)

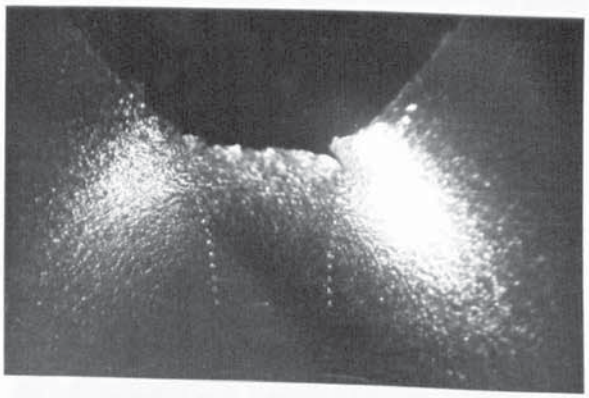

(j)

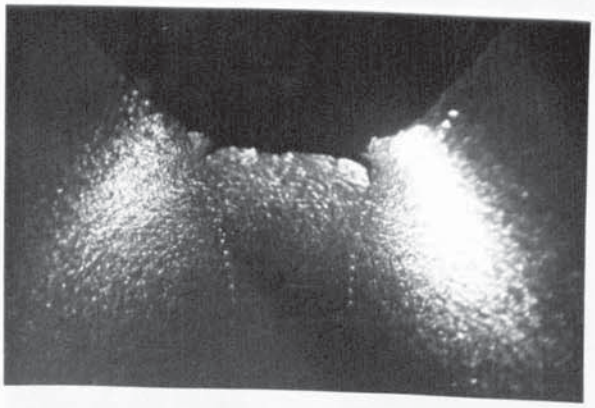

(k)

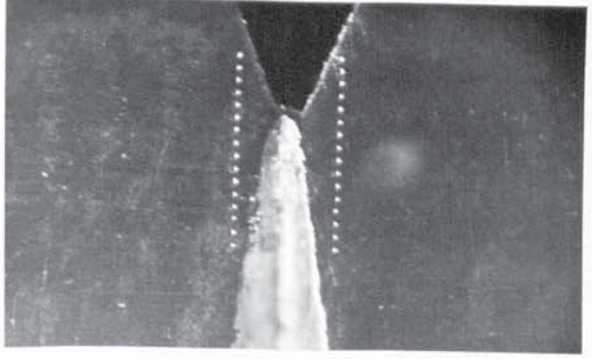

(a)

(b)

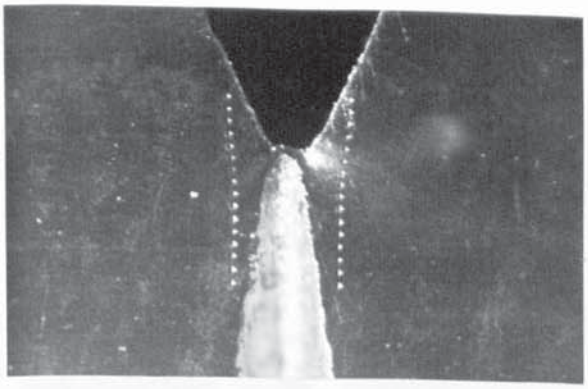

(c)

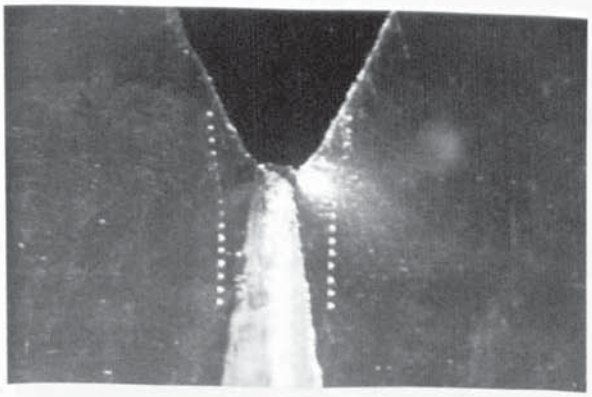

(d)

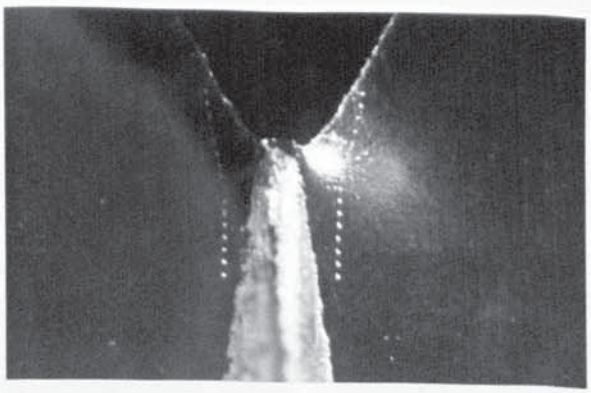

(e)

Plate 5.5 : Calibration series of side-grooved Charpy specimen, 17.5 x.

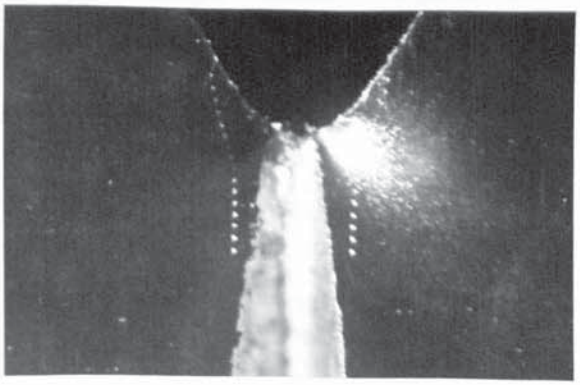

(f)

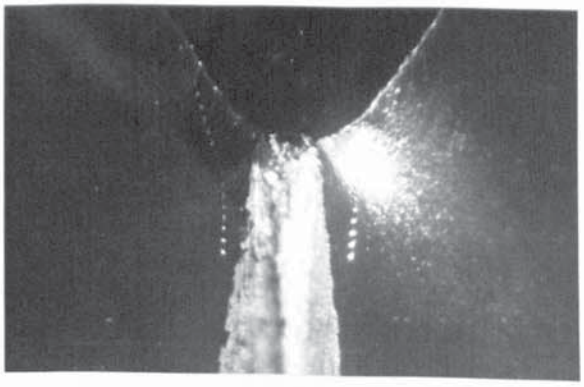

(g)

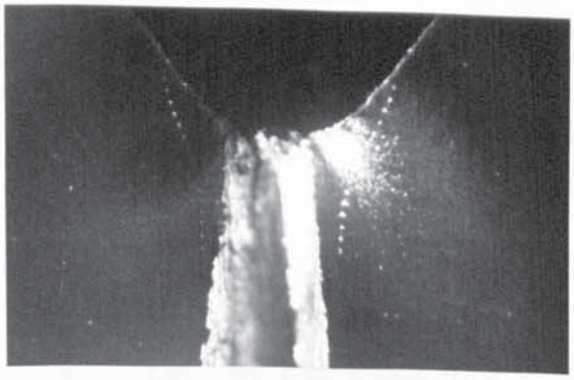

(h)

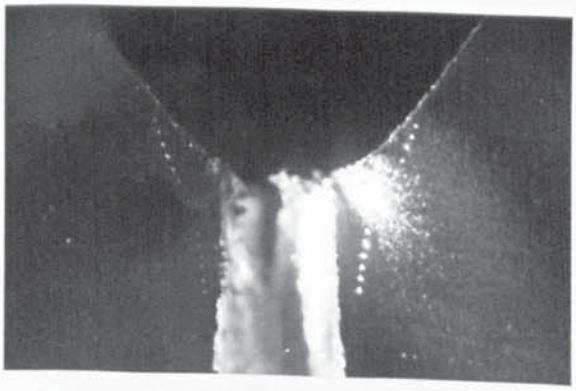

(i)

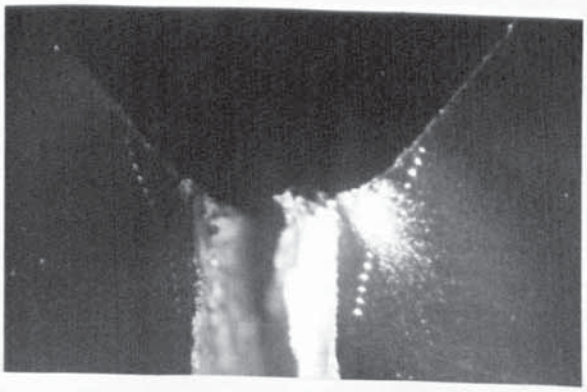

(j)

Table5.2: Results obtained for nonside-grooved three-point bend specimen, No. B3T

Load (KN)	7.2	9.0	10.3	11.4	12.1	12.8	13.3	13.6	13.7	13.8 (P_{max})	13.7
Load-point displacement (mm)	0.40	0.88	1.36	1.95	2.43	3.02	3.61	4.20	4.79	4.92	5.39
Plastic deflection (mm)	0.02	0.38	0.79	1.32	1.77	2.32	2.88	3.46	4.04	4.17	4.63
Photograph No. in Plate 5.4	(b)	(c)	(d)	(e)	(f)	(g)	(h)	(1)	(j)	-	(k)

* Crosshead speed = 0.02 cm/min; test temperature = 17°C

Table5.3: Results obtained for side-grooved three-point bend specimen, No. S2T

Load (KN)	6.0	7.8	8.9	9.7	10.5	11.2	11.7	12.0	12.0 (P_{max})	11.9
Load-point displacement (mm)	0.44	0.92	1.39	1.89	2.46	3.05	3.64	4.23	4.55	4.83
Plastic deflection (mm)	0.04	0.40	0.81	1.25	1.77	2.32	2.88	3.44	3.73	4.03
Photograph No. in Plate 5.5	(b)	(c)	(d)	(e)	(f)	(g)	(h)	(i)	-	(j)

*Crosshead speed = 0.02 cm/min; test temperature = 19°C

specimen.

The notch opening displacement and the longitudinal displacement field in the vicinity of the notch root were measured from the images with the magnification of 72 x using an Envoy enlarger. In this way, the displacement could be measured to an accuracy of $\pm$ 0.5 x 10^{-2}mm. The notch opening displacement (NOD) was calculated from:

$$NOD = \ell - \ell o \qquad \text{.....(5.1)}$$

where ℓo is the original gauge length; ℓ is the instantaneous gauge length at the instantaneous load. The notch opening displacement values are listed in Tables 5.4 and 5.5 for the nonside- and side-grooved specimens, separately. Then the notch opening displacement values obtained were calibrated against the specimen deflection, as shown in Figs. 5.5 and 5.6, respectively.

The relationship between the notch opening displacement values at the notch root and load-point displacement values were described by a polynomial curve fit. They are given by:

$$y = -0.0006 + 0.1133x - 0.0015x^2 + 0.0046x^3 \qquad \text{....(5.2)}$$

for the nonside-grooved specimen, and

Table 5.4: Notch root opening displacement and longitudinal displacement in the vicinity of the notch root for nonside-grooved Charpy specimen, No.B3T

DFNR / LPD	-0.4	-0.3	-0.2	-0.1	0.0	+0.1	+0.2	+0.3	+0.4	+0.5	+0.6	+0.7	+0.8	+0.9	+1.0	+1.1	+1.2	+1.3	+1.4	+1.5
0.40	0.04	0.03	0.02	0.02	0.01	0.00	0.00	0.00	0.00	0.00	0.00	0.00	0.00	0.00	0.00	0.00	0.00	0.00	0.00	0.00
0.88	0.15	0.14	0.13	0.10	0.10	0.07	0.03	0.02	0.02	0.02	0.02	0.02	0.02	0.01	0.01	0.01	0.01	0.01	0.01	0.01
1.36	0.29	0.26	0.23	0.18	0.16	0.11	0.08	0.08	0.05	0.05	0.03	0.03	0.02	0.02	0.02	0.02	0.01	0.01	0.01	0.01
1.95	0.44	0.40	0.36	0.30	0.26	0.21	0.15	0.10	0.08	0.08	0.06	0.04	0.03	0.03	0.03	0.02	0.01	0.01	0.01	0.01
2.43	0.58	0.53	0.47	0.41	0.34	0.21	0.16	0.12	0.11	0.08	0.06	0.05	0.05	0.04	0.04	0.03	0.02	0.02	0.02	0.02
3.02	0.79	0.72	0.66	0.55	0.45	0.30	0.25	0.18	0.17	0.14	0.10	0.09	0.07	0.06	0.06	0.05	0.03	0.03	0.03	0.03
3.61	1.01	0.91	0.81	0.66	0.58	0.45	0.36	0.29	0.25	0.21	0.16	0.14	0.11	0.09	0.08	0.07	0.04	0.04	0.04	0.04
4.20	1.24	1.15	1.05	0.90	0.80						0.22	0.19	0.17	0.15	0.11	0.10	0.08	0.07	0.06	0.05
4.79	1.49	1.40	1.32	1.20	1.03						0.30	0.26	0.25	0.22	0.17	0.14	0.11	0.09	0.08	0.07
5.38	1.77	1.65	1.53	1.41	1.27					0.51	0.44	0.38	0.33	0.28	0.24	0.19	0.16	0.13	0.12	0.10

a. Gauge length = 0.80 mm

b. Tested at 17°C with loading rate of 0.02 cm/min.

c. All units are in millimetres.

d. DFNR is distance from notch root

e. LPD is load-point deflection.

Table 5.5: Notch root opening displacement and longitudinal displacement in the vicinity of the notch root for side-grooved Charpy specimen, No. S2T.

distance from notch root / Load-point deflection	-0.4	-0.3	-0.2	-0.1	0.0	+0.1	+0.2	+0.3	+0.4	+0.5	+0.6	+0.7	+0.8	+0.9	+1.0	+1.1
0.44	0.03	0.02	0.02	0.01	0.01	0.00	0.00	0.00	0.00	0.00	0.00	0.00	0.00	0.00	0.00	0.00
0.92	0.15	0.14	0.13	0.11	0.09	0.07	0.05	0.04	0.03	0.03	0.03	0.03	0.03	0.03	0.03	0.03
1.39	0.30	0.27	0.25	0.22	0.19	0.15		0.07	0.07	0.07	0.07	0.07	0.07	0.07	0.07	0.07
1.89	0.44	0.40	0.36	0.32	0.27	0.22			0.12	0.11	0.10	0.10	0.10	0.10	0.10	0.09
2.46	0.60	0.55	0.50	0.44	0.35	0.34	0.28	0.23	0.19	0.16	0.16	0.15	0.14	0.14	0.14	0.14
3.05	0.81	0.74	0.67	0.61	0.54	0.47	0.39	0.33	0.28	0.25	0.25	0.24	0.24	0.24	0.22	0.21
3.64	1.00	0.95	0.88	0.82	0.74	0.65	0.54	0.47	0.44	0.39	0.37	0.36	0.33	0.32	0.30	0.29
4.23	1.26	1.19	1.12	1.04	0.96	0.86	0.78	0.69	0.65	0.58	0.55	0.52	0.49	0.47	0.45	0.42
4.82	1.53	1.45	1.36	1.29	1.20	1.12				0.81	0.77	0.74	0.71	0.68	0.65	0.62

a. Gauge length = 0.80 mm;

b. Tested at 19°C with loading rate of 0.02 cm/min;

c. All units are in millimetres.

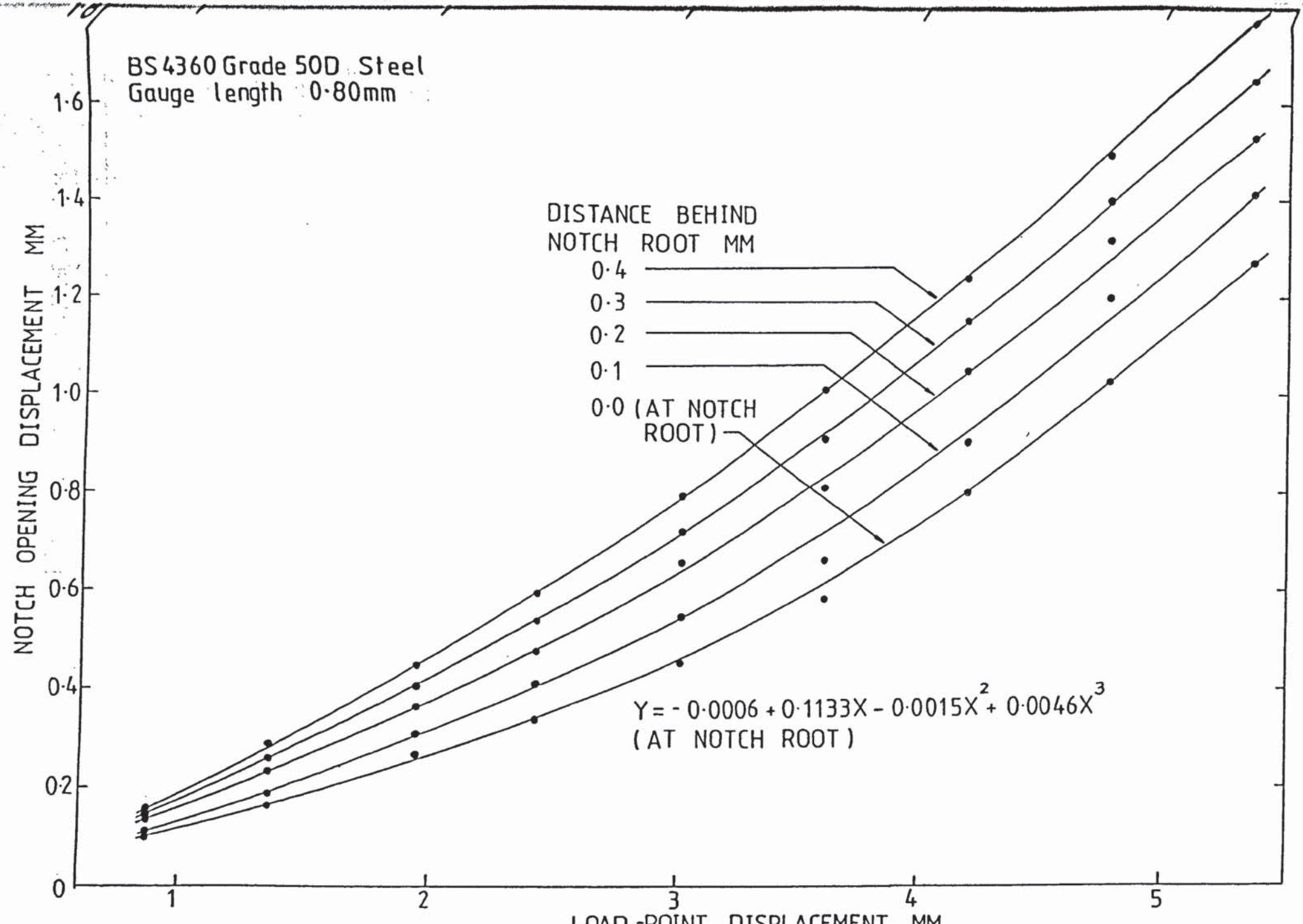

FIGURE 5.5 Notch opening displacement calibration for nonside-grooved Charpy specimen

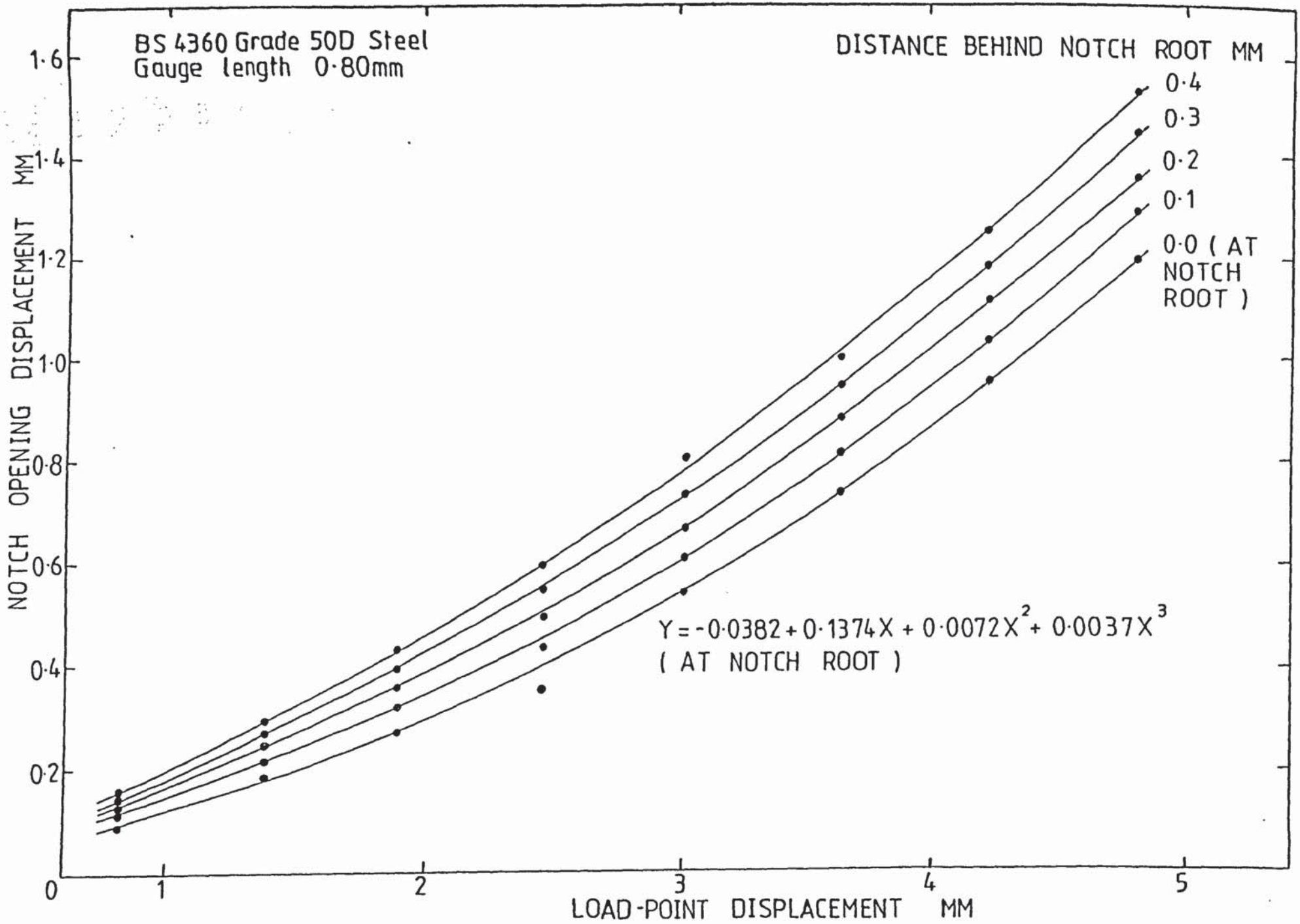

FIGURE 5.6 Notch opening displacement calibration for side-grooved Charpy specimen

$$y = -0.0382 + 0.1374x + 0.0072x^2 + 0.0037x^3 \quad ...(5.3)$$

for the side-grooved specimen. Here the y represents the notch root opening displacement; the x represents the load-point displacement. Calculating the differences between the observed value y_i and the correspondingly fitted value $\hat{y}_i$ for each observation, we have found that residuals are 0.01 mm or so. Thus the regression functions are accurate enough.

These calibration curves will be valid on all the specimens which have the same sizes and the same geometries. Two specimens of each geometry were used to check the regression curves. The data obtained are listed in Table 5.6. These results show that the checking data appear to agree fairly well with the regression curves. The maximum relative error of the notch root opening displacements for the checking test specimens against the calibration curves is less than 5%.

It should be noted that the stiffness of the testing machine and the gauge length of the specimen have an influence upon the calibration curve, when the specimen is tested in three-point bending in an Instron tensile machine. Although the Charpy-size specimen is small, the crosshead movement is related to the compliance of the testing machine including bend test fixture. The calibration curve will not be valid, if another testing machine or fixture is used to carry out the three-point

Table5.6 : Results obtained from checking tests of notched specimens

Specimen No.	Load-point displacement, mm	Plastic deflection, mm	Calculated NROD, mm	Measured NROD, mm	Interrupted Load, KN
NONSIDE-GROOVED SPECIMEN					
B2T	3.96	3.35	0.71	0.73	13.5
B1T	3.96	3.28	0.71	0.74	13.4
SIDE-GROOVED SPECIMEN					
S7T	3.58	2.94	0.72	0.74	11.8
S8T	3.58	2.92	0.72	0.71	12.1

*NROD = notch root opening displacement

bending test. George Succop et al [86] have proposed that the influence of the tensile machine compliance for practical purposes may be neglected, if the deflection is obtained from measurement made directly on the specimen. However, we did not go further into this question. The influence of the gauge length will be discussed in the Section 5.3.

During the calibration of the notch opening displacement versus the specimen deflection, the longitudinal displacement distribution in the vicinity of the notch root was also determined. The results obtained for the two kinds of specimens are listed in Tables 5.4 and 5.5. The variations of the longitudinal displacement fields with the increase of the load-point displacement are presented in Figs. 5.7 and 5.8 for the nonside- and side-grooved specimens respectively. It can be seen from these figures that the shape of the curves in the notch part also represents the instantaneous appearance of the notch edges.

Based on an assumption that a series of the tensile specimens with a gauge length of 0.80 mm exist ahead of the notch root, the longitudinal shear strain, γ, at the instantaneous load can be calculated by:

$$\gamma = \tfrac{1}{2}\ell n\left(\frac{\ell}{\ell o}\right) = \tfrac{1}{2}\ell n\left(\frac{\ell o + u}{\ell o}\right) \qquad \text{.....(5.4)}$$

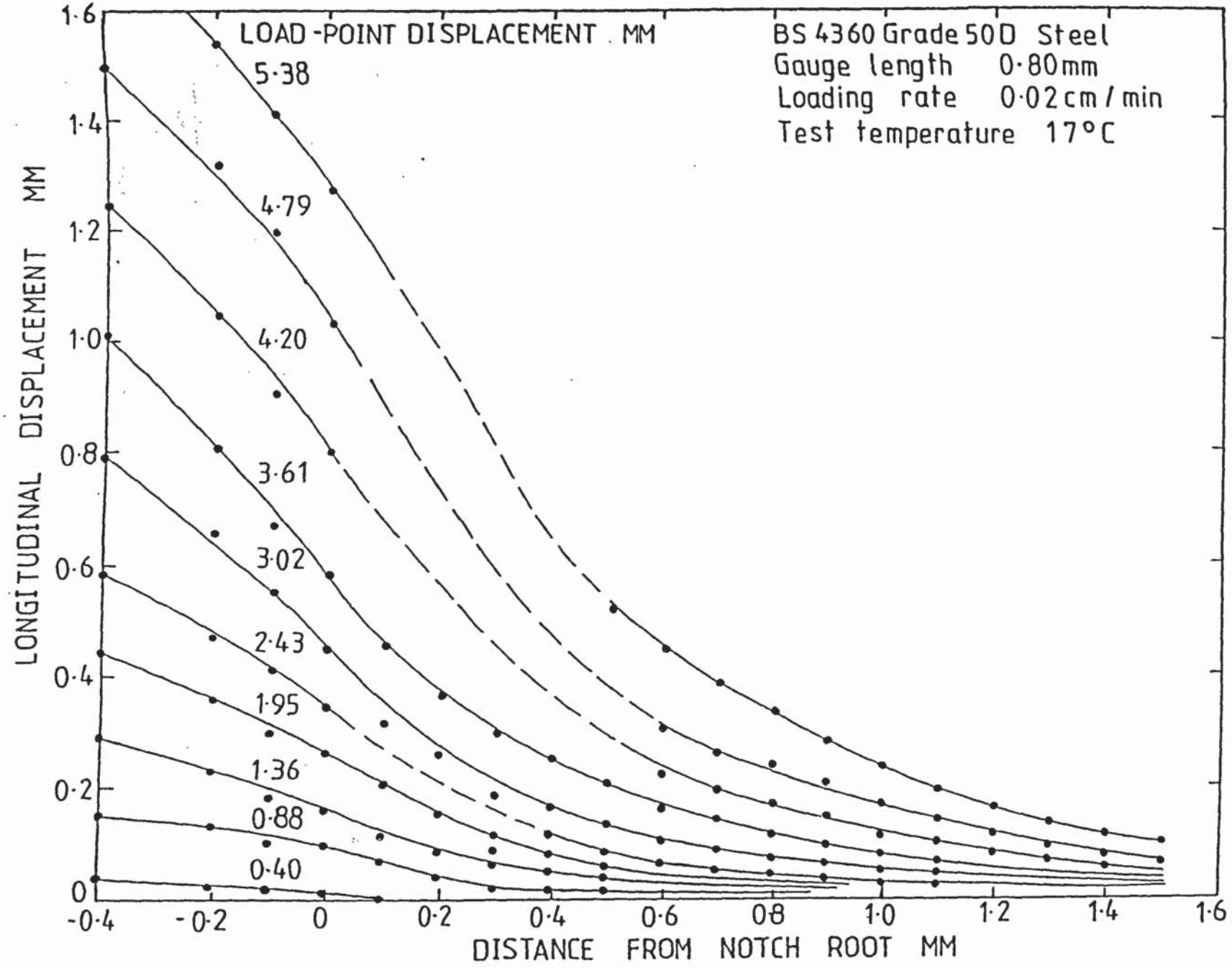

FIGURE 5.7 The variations of the longitudinal displacement fields for nonside-grooved Charpy specimen, No. B3T

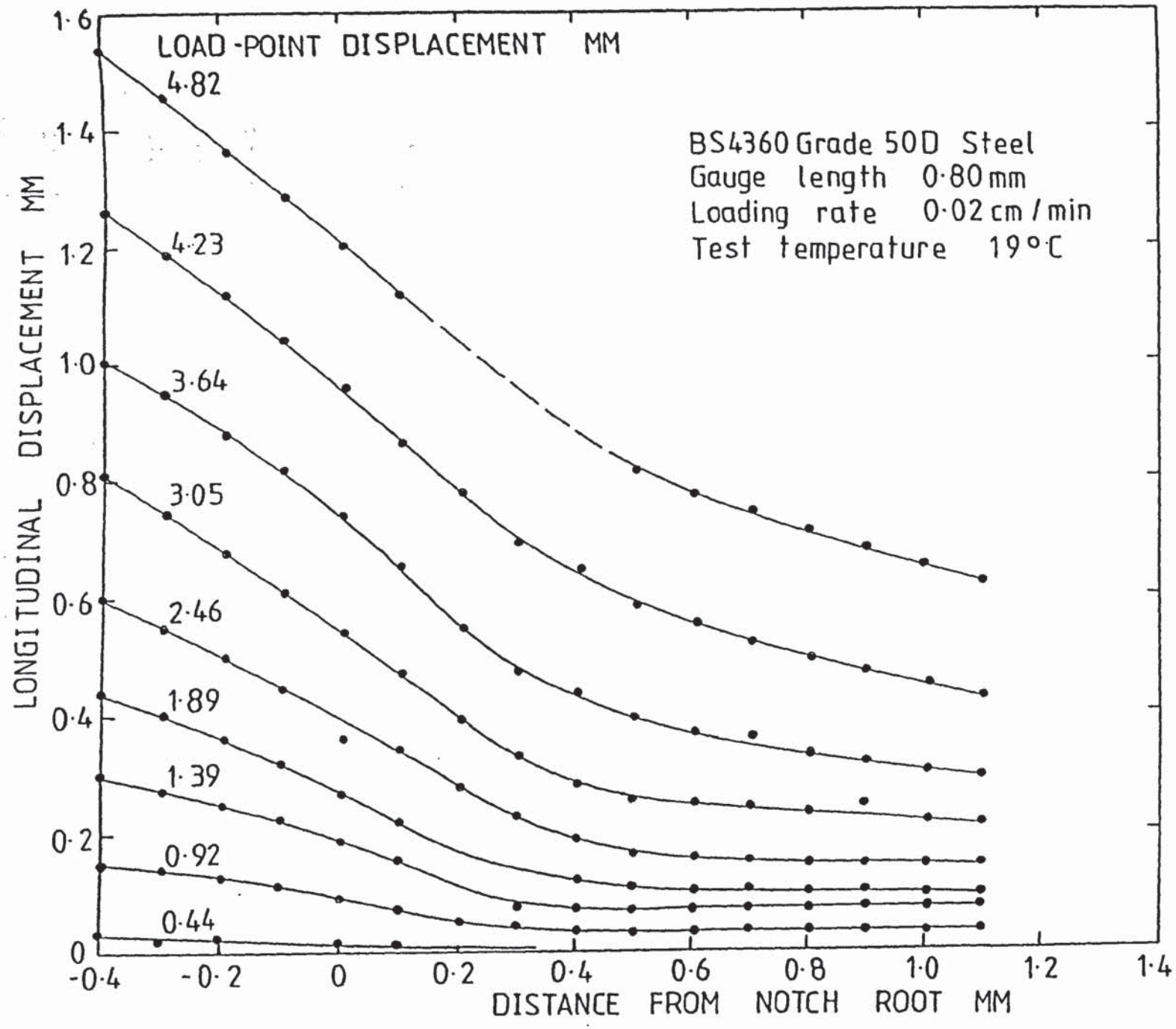

FIGURE 5.8 The variations of the longitudinal displacement fields for side-grooved Charpy specimen No. S2T

where u is the measured longitudinal displacement; ℓ_o is the original gauge length; ℓ is the instantaneous gauge length at the instantaneous load.

This instantaneous shear strain consists of elastic shear strain and plastic shear strain. The results calculated for the two kinds of specimens are listed in Tables 5.7 and 5.8, separately. Figs. 5.9 and 5.10 show the variations of the longitudinal shear strain fields with the increase of the load-point displacement. It has been found that a steeper descent of the shear strain exists ahead of the notch root in the nonside-grooved specimen than in the side-grooved specimen. This characteristic distribution must be of great concern to measuring the relative void volume under the notch root.

The question is as to whether the longitudinal displacement fields and shear strain fields measured at the side surface using gauge marks are the same as that which occur at the centre of the specimen. In order to examine this, six interrupted specimens used for checking the calibration curves were fractured in liquid nitrogen along the mid-thickness perpendicular to the specimen notch, as shown in Fig. 5.11. Plate 5.6 shows the fracture surfaces in the mid-thickness section of the nonside- and side-grooved specimens. The contours of the notch root were traced out on the screen of the optical microscope, Vickers Fifty-Five, with the

Table5.7: Longitudinal shear strain at the instantaneous load for nonside-grooved Charpy specimen, No. B3T

DFNR / LPD	0.0	0.1	0.2	0.3	0.4	0.5	0.6	0.7	0.8	0.9	1.0	1.1	1.2	1.3	1.4	1.5
0.40	0.006	0.000	0.000	0.000	0.000	0.000	0.000	0.000	0.000	0.000	0.000	0.000	0.000	0.000	0.000	0.000
0.88	0.060	0.042	0.019	0.013	0.013	0.013	0.013	0.013	0.013	0.006	0.006	0.006	0.000	0.000	0.000	0.000
1.36	0.092	0.065	0.048	0.048	0.031	0.031	0.019	0.019	0.013	0.013	0.013	0.013	0.006	0.006	0.006	0.006
1.95	0.142	0.118	0.087	0.060	0.049	0.049	0.037	0.025	0.019	0.019	0.019	0.013	0.006	0.006	0.006	0.006
2,43	0.179	0.118	0.092	0.071	0.066	0.049	0.037	0.031	0.031	0.025	0.025	0.019	0.013	0.013	0.013	0.013
3.02	0.225	0.161	0.138	0.103	0.099	0.083	0.060	0.055	0.043	0.037	0.037	0.031	0.019	0.019	0.019	0.019
3.61	0.275	0.225	0.188	0.156	0.139	0.119	0.093	0.083	0.066	0.055	0.049	0.043	0.025	0.025	0.025	0.025
4.20	0.035						0.124	0.109	0.099	0.088	0.066	0.060	0.048	0.042	0.037	0.031
4.79	0.417						0.163	0.144	0.139	0.124	0.099	0.083	0.065	0.054	0.048	0.042
5.38	0.479					0.252	0.224	0.198	0.176	0.153	0.134	0.109	0.092	0.076	0.071	0.060

a. Gauge length = 0.80mm;

b. Tested at 17°C with loading rate of 0.02 cm/min.

c. DFNR is distance from notch root

d. LPD is load-point deflection

Table5.8: Longitudinal shear strain at the instantaneous load for side-grooved Charpy specimen, No. S2T

Distance from notch root / Load-point deflection	0.0	0.1	0.2	0.3	0.4	0.5	0.6	0.7	0.8	0.9	1.0	1.1
0.44	0.006	0.000	0.000	0.000	0.000	0.000	0.000	0.000	0.000	0.000	0.000	0.000
0.92	0.053	0.042	0.030	0.024	0.019	0.019	0.019	0.019	0.019	0.019	0.019	0.019
1.39	0.107	0.086		0.042	0.042	0.042	0.042	0.042	0.042	0.042	0.042	0.042
1.89	0.145	0.121			0.071	0.065	0.060	0.060	0.060	0.060	0.060	0.055
2.46	0.182	0.177	0.150	0.126	0.108	0.092	0.092	0.087	0.083	0.083	0.083	0.083
3.05	0.258	0.231	0.199	0.173	0.152	0.138	0.138	0.133	0.133	0.133	0.124	0.119
3.64	0.328	0.297	0.258	0.231	0.221	0.201	0.192	0.188	0.176	0.172	0.163	0.158
4.23	0.394	0.365	0.340	0.311	0.300	0.275	0.264	0.253	0.244	0.236	0.228	0.215
4.82	0.458	0.438				0.353	0.340	0.331	0.324	0.313	0.303	0.293

a. Gauge length = 0.80mm;

b. Tested at 17°C with loading rate of 0.02 cm/min.

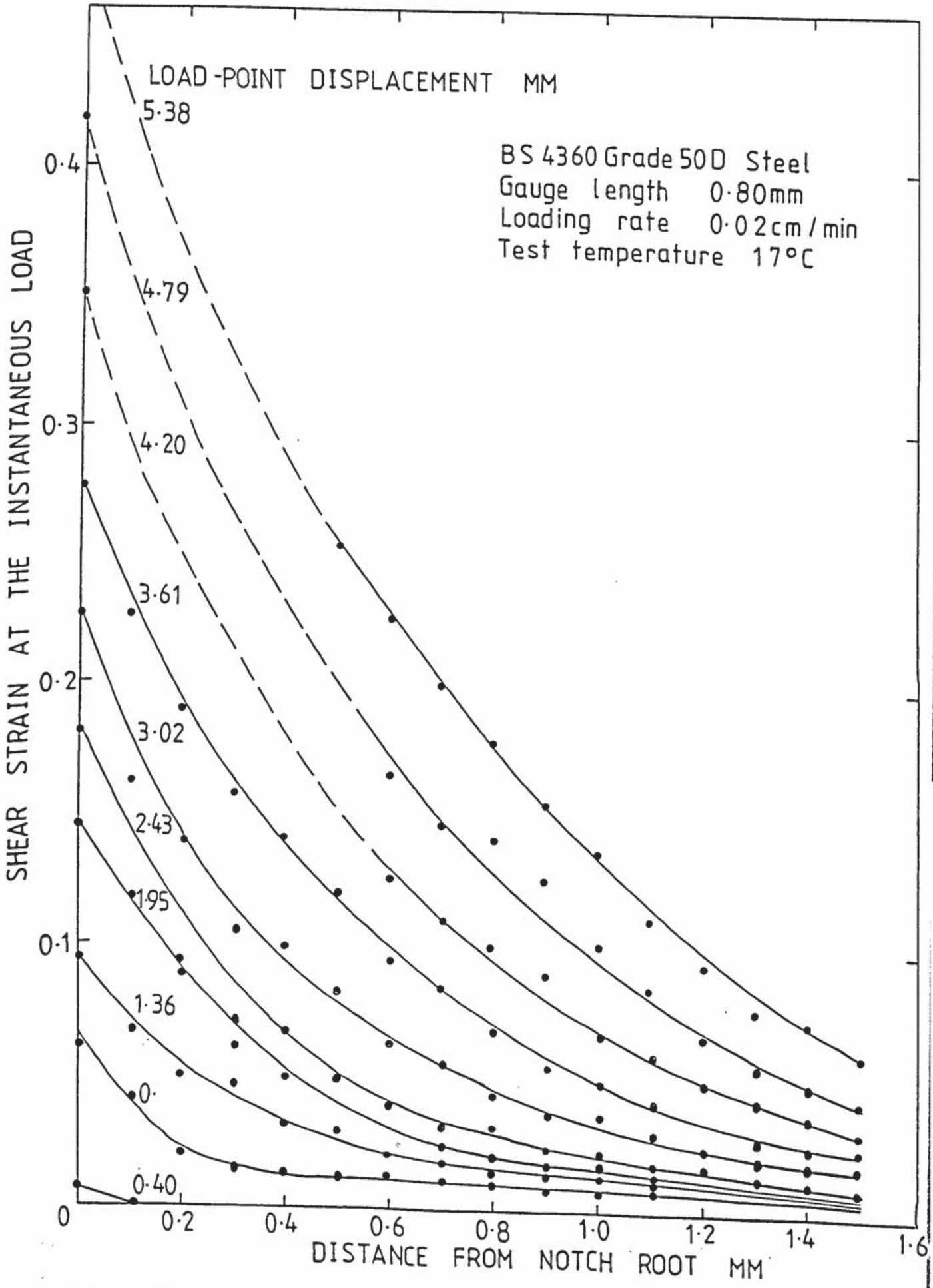

FIGURE 5.9 The variations of the longitudinal shear strain fields for nonside-grooved Charpy specimen, No. B3T

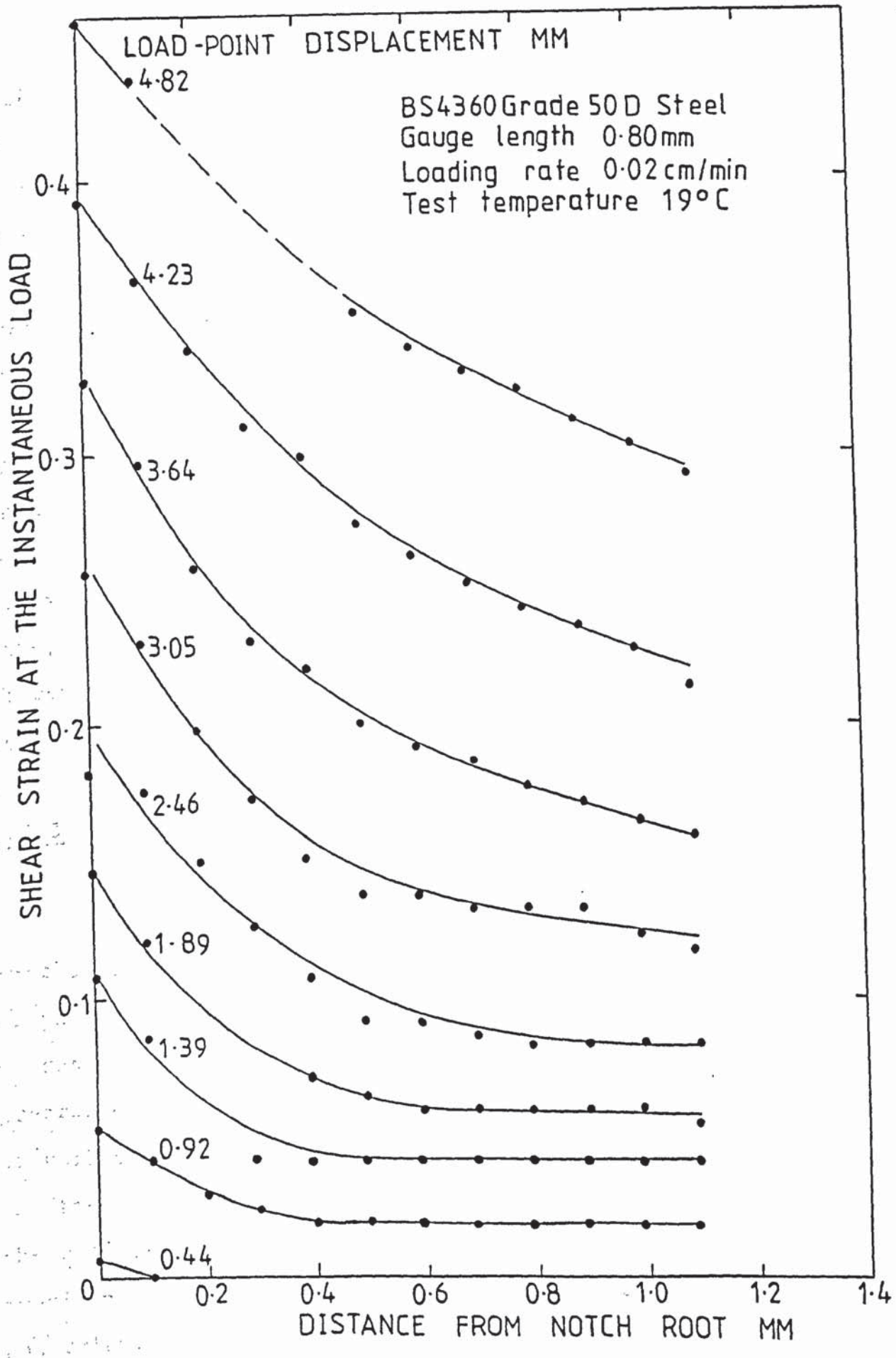

FIGURE 5.10 The variations of the longitudinal shear strain fields for side-grooved Charpy specimen, No. S2T

magnification of 50 x. The contours of the notch root of two specimens among them are shown in Fig. 5.12. In order to carefully compare the difference of the notch root geometry measured in the side surface and mid-thickness section, the notch root radius and notch opening angle were calculated from these traces and listed in Table 5.9. It has been found that the notch opening angles are almost the same, but the notch root radii measured are larger from the side surface than from the mid-thickness section. However, the maximum relative error of the root radius measured in the side surface and mid-thickness section is less than 18%. Thus, the inaccuracy of the notch root opening displacement introduced by making this measurement may be assumed to be acceptable.

5.2.3 Estimation of Stress State Ahead of the Notch Root

Shockey et al [72] have proposed that the same mechanism of the void growth controls the ductile fracture process for round tensile specimen and other notched or precracked specimens in spite of differences in the states of stress and strain. Therefore, the experimental law for the void growth in Eq. (4.1) can be used to investigate the void growth relation for the two kinds of the notched specimens. Once the values of the plastic shear strain and relative void volume are obtained in a specific region ahead of the notch root, the level of the stress triaxiality in each kind of the specimen can be estimated

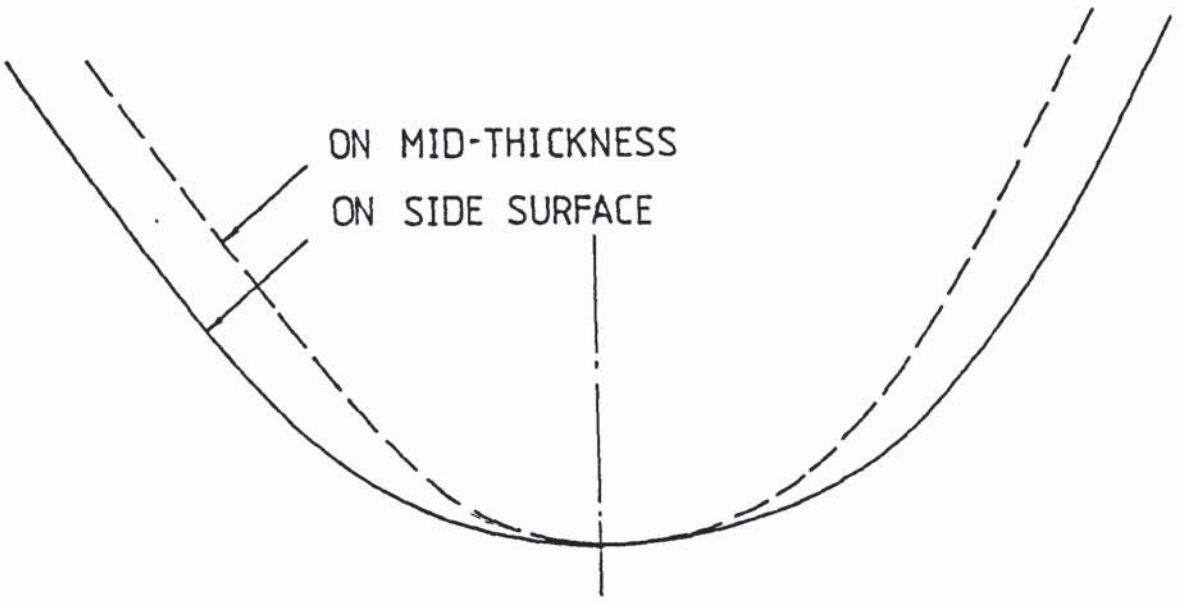

(a) Nonside-grooved specimen No. B1T

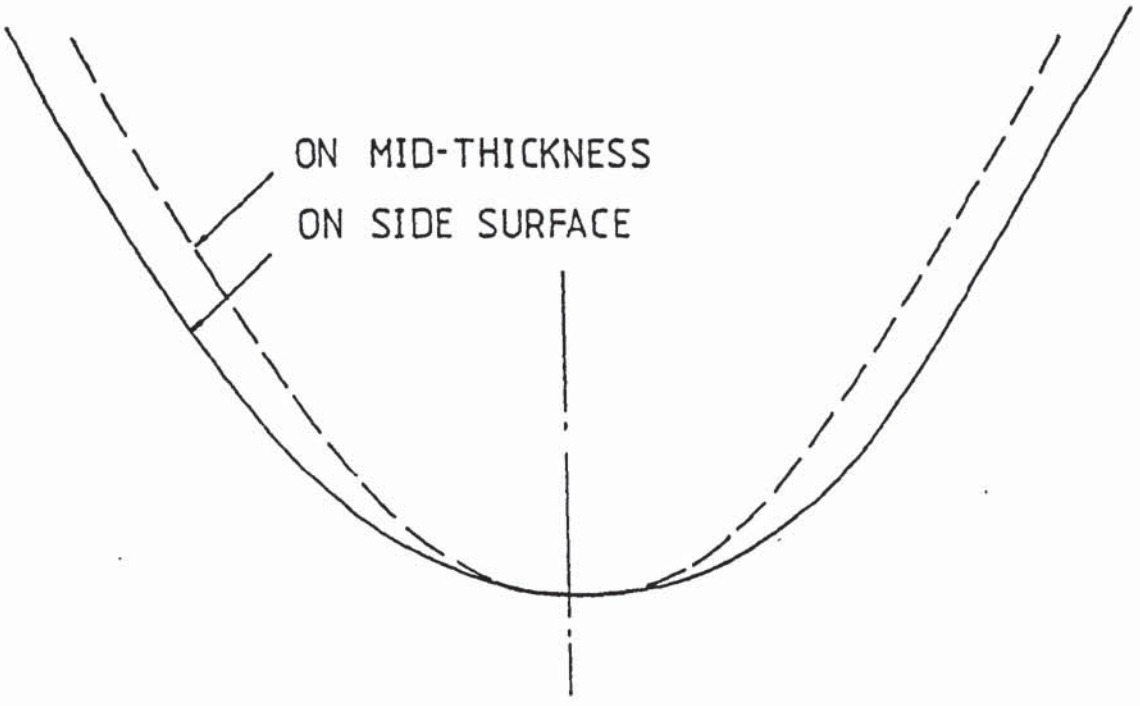

(b) Side-grooved specimen No. S8T

FIGURE 5.12 Traced contours of the notch root after three-point bending test, 50x.

Table5.9: Notch geometry measured after unloading

Specimen No.	On side surface		In mid-thickness section		Relative error of the root radius* %
	Root radius mm	Notch angle degree	Root radius mm	Notch angle degree	
NONSIDE-GROOVED SPECIMEN					
B4T	0.90	54.0	0.77	53.0	16.9
B2T	1.46	70.5	1.27	64.0	15.0
B1T	1.41	65.0	1.20	65.0	17.5
SIDE-GROOVED SPECIMEN					
S6T	0.78	54.5	0.72	53.0	8.3
S7T	1.23	66.5	1.08	62.0	13.9
S8T	1.24	63.0	1.09	64.5	13.8

* It is the relative error of the root radius measured from the mid-thickness section to that measured from the side surface. It is calculated by

$$\text{Relative error} = \frac{\text{Value on side surface - Value in mid-thickness}}{\text{Value in mid-thickness}}$$

using the void growth coefficient, T_1, determined previously.

In order to easily compare the levels of triaxiality ahead of the notch root for the nonside- and side-grooved specimens, that is, to determine the effect of the side-grooves on the constraint of the notched bar specimen, the regions ahead of the notches should be taken to the same level of the plastic strains during the three-point bending test. It is known from the calibration curves that the requirements of the load-point deflection are different for the nonside- and side-grooved specimens so as to obtain the same notch root opening displacement or the same plastic strain at the notch root. Furthermore, it is necessary for the point counting technique that a large enough number of voids exists ahead of the notch root. Thus, the specimen should be loaded to crack initiation. If the notch root opening displacement of 0.72 mm is expected, we should load the specimens to the load-point deflections of 3.96 mm and 3.58 mm for the nonside- and side-grooved specimens, separately, according to the calculation of the polynominal fit equations (5.2) and (5.3). For each specimen geometry, the same experimental condition should be repeated. When the Eq. (4.1) is used to calculate the level of triaxiality, an average of the two tests is assured. Plate 5.7 shows a view of the two kinds of Charpy specimens after the three-point bending test.

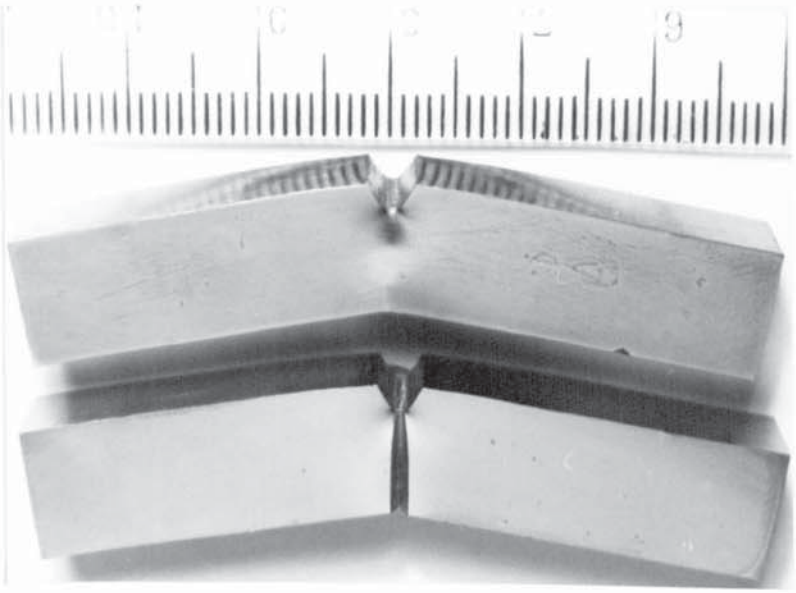

Plate 5.7 : View of specimens after three-point bending test (No. B1T at the top; No. S8T at the bottom).

Plate 5.12 : Fracture surfaces in the mid-thickness section of the pre-cracked nonside- and side-grooved specimens; No.B19V (left), No. S19V (right).

The notch opening displacement and longitudinal displacement in the vicinity of the notch root are measured by photographic technique and listed in Tables 5.10 and 5.11 for the two kinds of specimens, respectively. In order to determine the values of the plastic shear strain ahead of the notch root, the change of the indentation spacing was also measured after unloading. It has been found from the experimental results that the amount of the elastic recovery of the specimens is very small. The maximum value of the elastic recovery is less than 6% of the total elastic-plastic opening displacement at the notch root.

The plastic shear strain, $\bar{\varepsilon}^p$, at the notch root is calculated by:

$$\bar{\varepsilon}^p = \tfrac{1}{2} \ell n \left(\frac{\ell res}{\ell o}\right) = \tfrac{1}{2} \ell n \left(\frac{\ell o + Ures}{\ell o}\right) \qquad .....(5.5)$$

where ℓo is the original gauge length; ℓres and Ures are residual gauge length and longitudinal displacement after unloading. The longitudinal shear strains calculated ahead of the notch root are listed in Tables 5.12 and 5.13 for the nonside-and side-grooved specimens, respectively.

On the basis of the information obtained in this investigation it is apparent that the longitudinal strain distribution is not uniform ahead of the notch root. The more approximate to the notch root the measure

Table5.10: Notch opening displacement and longitudinal displacement ahead of the notch root for nonside-grooved Charpy specimens

Distance from notch root	-0.4	-0.3	-0.2	-0.1	0.0	+0.1	+0.3	+0.5	+0.7	+0.9	+1.1
SPECIMEN No. B1T											
Longitudinal displacement at the instantaneous load, u	1.16	1.10	1.01	0.87	0.74	0.66	0.48	0.35	0.20	0.14	0.10
Longitudinal displacement after unloading, u_{res}	1.12	1.06	0.98	0.84	0.71	0.64	0.41	0.27	0.19	0.13	0.10
SPECIMEN No. B2T											
Longitudinal displacement at the instantaneous load, u	1.11	1.04	0.94	0.85	0.73	0.62	0.41	0.24	0.18	0.10	0.08
Longitudinal displacement after unloading, $u_{res.}$	1.09	1.01	0.92	0.82	0.69	0.59	0.39	0.23	0.17	0.10	0.08

a. Gauge length = 0.80mm;

b. Specimen No. B1T was tested at $15^{o}C$; specimen No. B2T was tested at $19^{o}C$

c. Loading rate = 0.02 cm/Min;

d. Load-point deflection at the instantaneous load was 3.96mm;

e. All units are in millimetres.

Table 5.11: Notch opening displacement and longitudinal displacement ahead of the notch root for side-grooved Charpy specimens

Distance from notch root	-0.4	-0.3	-0.2	-0.1	0.0	+0.1	+0.3	+0.5	+0.7	+0.9	+1.1
Specimen No. S7T											
Longitudinal displacement at the instantaneous load, u	1.03	0.97	0.91	0.83	0.74	0.67	0.53	0.45	0.39	0.36	0.33
Longitudinal displacement after unloading, $u_{res.}$	1.00	0.94	0.88	0.80	0.72	0.63	0.49	0.43	0.38	0.35	0.33
Specimen No. S8T											
Longitudinal displacement at the instantaneous load, u	1.01	0.92	0.87	0.80	0.71	0.60	0.49	0.40	0.31	0.30	0.28
Longitudinal displacement after unloading, $u_{res.}$	0.99	0.89	0.84	0.77	0.68	0.56	0.42	0.37	0.30	0.29	0.28

a. Gauge length = 0.80mm;

b. Specimen No. S7T was tested at 19°C specimen No. S8T was tested at 15°C;

c. Loading rate = 0.02 cm/min;

d. Load-point deflection at the instantaneous load was 3.58mm;

e. All units are in millimetres.

Table5.12: Longitudinal shear strains for nonside-grooved Charpy specimens

Distance from notch root	0.0	0.1	0.3	0.5	0.7	0.9	1.1
SPECIMEN No. B1T							
Longitudinal shear strain at the instantaneous load, γ	0.327	0.301	0.235	0.182	0.112	0.081	0.059
Longitudinal shear strain after unloading, $\bar{\varepsilon}^p$	0.318	0.294	0.207	0.145	0.107	0.075	0.059
SPECIMEN No. B2T							
Longitudinal shear strain at the instantaneous load, γ	0.324	0.287	0.207	0.131	0.102	0.059	0.048
Longitudinal shear strain after unloading, $\bar{\varepsilon}^p$	0.311	0.276	0.199	0.126	0.096	0.059	0.048

a. Gauge length = 0.80mm;

b. Specimen No. B1T was tested at 15°C; specimen No. B2T was tested at 19°C;

c. Loading rate = 0.02 cm/min;

d. Load-point deflection at the instantaneous load was 3.96mm.

Table5.13: Longitudinal shear strains for side-grooved Charpy specimens

Distance from notch root	0.0	0.1	0.3	0.5	0.7	0.9	1.1
SPECIMEN No. S7T							
Longitudinal shear strain at the instantaneous load, γ	0.328	0.304	0.254	0.223	0.199	0.186	0.173
Longitudinal shear strain after unloading, $\bar{\varepsilon}^p$	0.321	0.290	0.239	0.215	0.194	0.182	0.173
SPECIMEN No. S8T							
Longitudinal shear strain at the instantaneous load, γ	0.318	0.280	0.239	0.203	0.164	0.159	0.150
Longitudinal shear strain after unloading, $\bar{\varepsilon}^p$	0.308	0.265	0.211	0.190	0.159	0.155	0.150

a. Gauge length = 0.80mm;

b. Specimen No. S7T was tested at 19°C; specimen No. S8T was tested at 15°C;

c. Loading rate = 0.02 cm/min;

d. Load-point deflection at the instantaneous load was 3.58mm.

location is, the larger the longitudinal strain is. Furthermore, the singularity of the longitudinal strain distribution is much stronger in the nonside-grooved specimen than in the side-grooved specimen.

Ductile crack initiation is usually assumed to be that the blunting notch root coalesces with the growing void nearest to the notch root. Since the constraint stresses are generated by geometrical constraint the notch-plane stress and through-thickness stress tend to follow the longitudinal singular stress, and they must be zero at the free surface of the notch root. Therefore the stress triaxiality is developed at a specific distance ahead of the notch root. Finite element analysis on the CVN impact specimen indicates that the maximum value of the stress triaxiality is developed at about 0.5 mm ahead of the notch root [97]. To make a comparison of the stress state in the standard CVN and side-grooved CVN specimens, a region of 0.4 to 0.6 mm ahead of the notch root is chosen to investigate the void growth. In this specific region the plastic strain is still large and the stress triaxiality is developed sufficiently.

In order to perform the metallographic examination on the notch root, the bended specimens were sectioned along the longitudinal mid-thickness, as indicated in Fig. 5.11. The method and set used for sectioning the specimens in liquid nitrogen were in the same way as shown in Fig. 3.3.

Fracture surfaces were observed by scanning electron microscope. Typical fractographys with voids in the observed region are shown in Plates 5.8 and 5.9 for the standard CVN and the side-grooved CVN specimens, respectively. The main sources of these voids are still MnS, Al_2O_3 and CaO inclusions. The voids are typically 2 to 10 μm in diameter. Compared with the round tensile tests, the density of voids and the size of individual voids are somewhat similar to that at the strain corresponding to the ultimate tensile strength. Basically, the voids maintain a roughly spherical or oval shape.

Point counting technique was directly conducted on the screen of scanning electron microscope. A transparent paper with a regular square grid of 1 cm was superimposed on the screen. Magnification of 1000 was chosen to observe the fracture surface. The grid did not move, but the observed location of the specimen moved randomly in the region of 0.2 mm (along the notch direction) x 1.0 mm at 0.5 mm ahead of the notch root. Relative void volume for each specimen is the average value in total 100 observations, and are listed in Table 5.14. The standard deviations for the data of the relative void volume are also given in Table 5.14. It has been found that the standard deviations are still larger than the mean values for the relative void volume.

If the void growth coefficient is considered to be 3.83

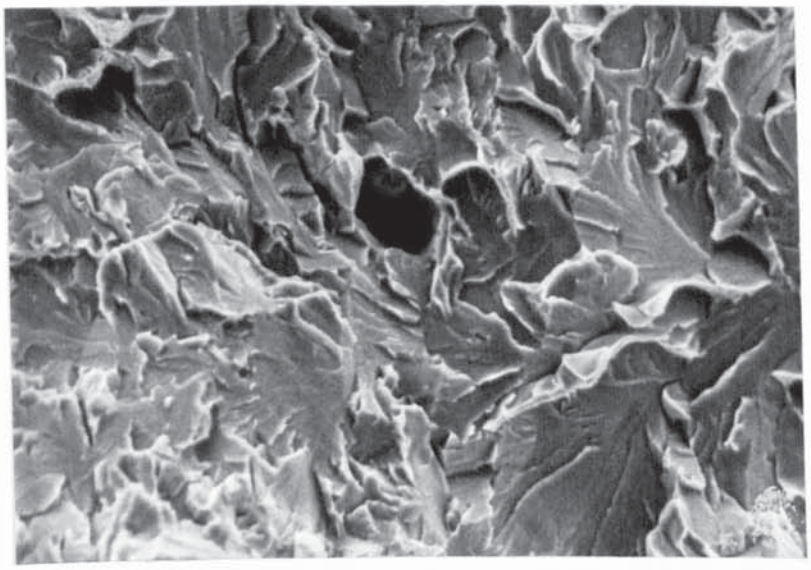

(a) : Specimen No. B1T; observation is in 0.4 mm ahead of the notch root.

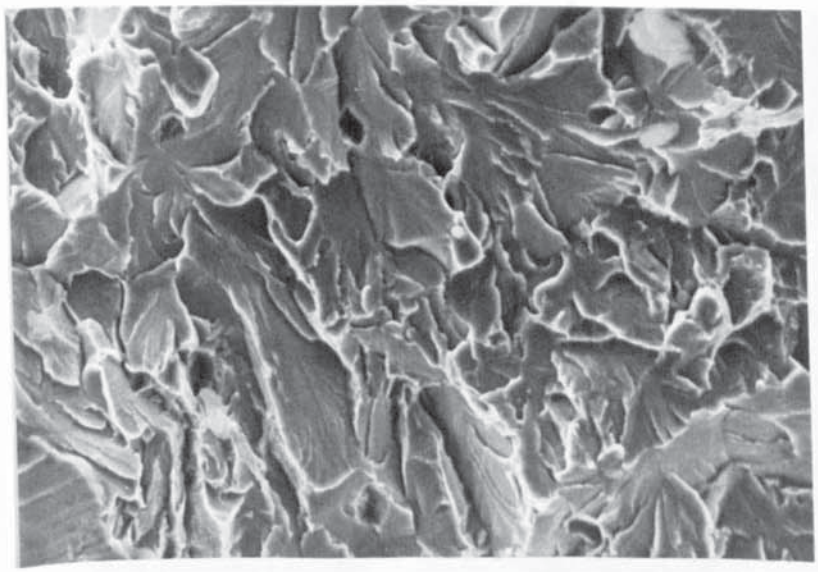

(b) : Specimen No. B1T; observation is in 0.5 mm ahead of the notch root.

Plate 5.8 Fractographs with voids for nonside-grooved specimen; horizontal direction in Plates is loading direction of specimen.

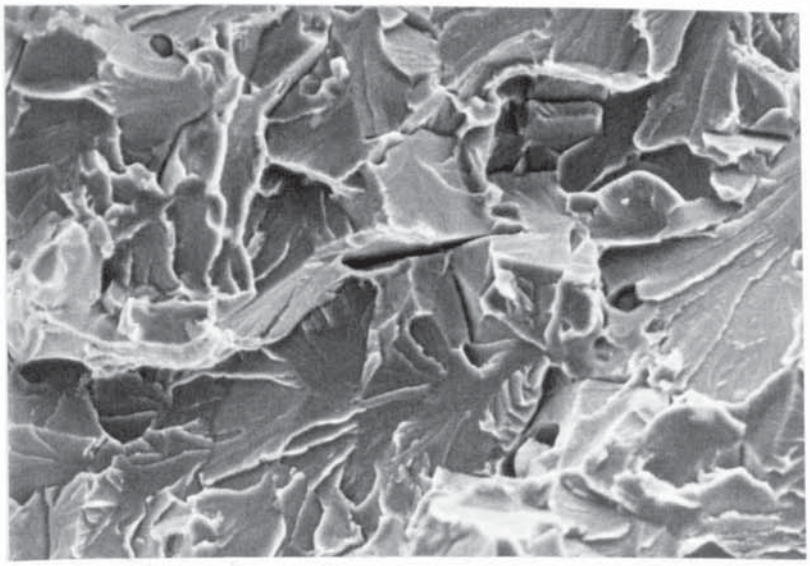

(a) : Specimen No. S8T; observation is in 0.3 mm ahead of the notch root.

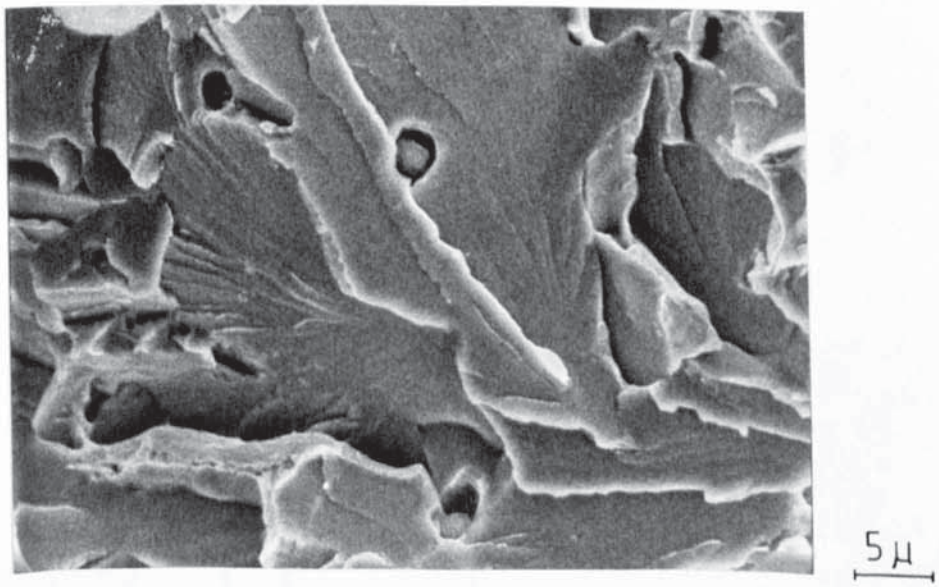

(b) : Specimen No. S7T; observation is in 0.4 mm ahead of the notch root.

Plate 5.9 : Fractographs with voids for side-grooved specimen; horizontal direction in Plates is loading direction of specimen.

Table 5.14: Measured relative void volume and calculated triaxiality ahead of the notch root for nonside- and side-grooved specimens

Specimen No.	Relative void volume, Vv	Standard deviation, σ	Plastic shear strain at 0.5mm ahead of the root, $\bar{\varepsilon}^p$	$\frac{\ell n(Vv/Vo)}{\bar{\varepsilon}^p - \bar{\varepsilon}^p_o}$	$\sigma_m/\bar{\sigma}$	
					T_1=3.83	T_1=4.13
NONSIDE-GROOVED SPECIMEN						
B1T	0.00313	0.00673	0.145	3.869	1.01	0.94
B2T	0.00275	0.00520	0.126	3.418	0.89	0.83
SIDE-GROOVED SPECIMEN						
S7T	0.00463	0.00725	0.215	4.436	1.16	1.07
S8T	0.00438	0.00649	0.190	4.730	1.24	1.15

(from Method III), the average levels of stress triaxiality ahead of the notch root, $\sigma_m/\bar{\sigma}$, are 0.95 for the nonside-grooved specimen and 1.20 for the side-grooved specimen. The calculating results are listed in Table 5.14. This table also shows the calculating results at the void growth coefficient of 4.13 (from Method II). It might be thought that the triaxiality at 0.5 mm ahead of the notch root in the mid-thickness of the Charpy-size specimens has already attained the state of the plane strain. The through-thickness stress starts forming. Furthermore, the side-grooves slightly increase the constraint ahead of the notch root.

5.3 Nonside and Side-Grooved Charpy Specimens with Pre-Fatigue Crack

5.3.1 Experimental Procedure

In this test, two series of specimens are still nonside- and side-grooved specimens, but a sharp crack is developed by fatigue, from the notch root. Therefore, we can research on the triaxial stress state ahead of the crack tip in the Charpy-size specimen of mild steel, and the effect of the side-grooves on the constraint of the pre-cracking specimens.

In order to develop a fatigue crack from the notch root, the stress ratio, R= +0.1 ($R=P_{min}/P_{max}$) was used. Based

on the requirements of BS.5762:1979, the stress intensity level during fatigue, K_f was limited as follows:

$$K_f < 0.63\ \sigma_{ys}.B^{\frac{1}{2}} \qquad \text{.....(5.6)}$$

$$= 0.63 \times 349 \times 0.01^{\frac{1}{2}}$$

$$= 22\ \text{MN m}^{-3/2}$$

Value of fatigue pre-cracking force, P_f, was calculated using the following equation:

$$P_f < \frac{K_f.B.W^{\frac{1}{2}}}{Y} \qquad \text{.....(5.7)}$$

when $\frac{a}{W} = 0.2$, $Y = 4.66$

Thus, $$P_f < \frac{22 \times 0.01 \times 0.01^{\frac{1}{2}}}{4.66} = 4721\text{N}$$

In order to ensure that K_f does not rise above the maximum permissible value during propagation of the fatigue crack, the pre-cracking force, P_f, should be reduced. For example, when the ratio of the overall length of notch plus fatigue crack/specimen depth attains about 0.45, the maximum permissible force, $(P_f)_{max}$, should be reduced to 2418 or less.

In order to estimate whether or not the K_f value of 22 $MN.m^{-3}/2$ is larger than the value of fatigue-crack-

initiation threshold, under three-point bending, the values of fatigue-crack-initiation threshold can be predicted by the following equations [2]:

$$\Delta K_I)_{th} = 0.9 \cdot \sigma_{UTS} \cdot \rho^{\frac{1}{2}} \quad \text{.....(5.8)}$$

$$= 0.9 \times 542 \times 0.00025^{\frac{1}{2}}$$

$$= 7.71 \text{ MN.m}^{-3/2}$$

$$\Delta K_I)_{th} = 5 \cdot (\sigma_{ys})^{\frac{2}{3}} \cdot \rho^{\frac{1}{2}} \quad \text{.....(5.9)}$$

$$= 5 \times \left(\frac{349}{6.895}\right)^{\frac{2}{3}} \times \left(\frac{0.25}{25.4}\right)^{\frac{1}{2}} \times 1.099$$

$$= 7.45 \text{ MN.m}^{-\frac{3}{2}}$$

where ρ is the notch root radius. Corresponding pre-cracking forces, ΔP_f, are 1655 N and 1599 N for the above equations.

During the fatigue pre-cracking, 2800 N/200 N (corresponding to P_{max}/P_{min}) were chosen as the actual fatigue pre-cracking forces at the preliminary stage. Usually, the crack initiated after 2×10^5 fatigue cycles. Then, the crack might propagate about 1 mm passing 10^5 cycles. After that, the forces were reduced to 2200 N/200 N. Passing (2.5 to 3) $\times 10^5$ cycles, the a/W ratio might attain to about 0.5. Fatigue pre-cracking was carried out using a 2 ton Amsler fatigue testing machine. A loading span to specimen width ratio of 4:1 was used for the three-point bending fatigue. As a preliminary check, the length of the propagated crack

on the ground side-surfaces was monitored by a magnifying-glass. After the three-point bending test or void counting, the fatigue crack length was measured from the fracture surface, by means of a travelling microscope. Three measuring positions were 25% B, 50% B, 75% B, respectively. Then, the average crack length was obtained.

In the case of side-grooved specimen, once the crack initiates in the notch root, the effective specimen thickness in which the crack front situates becomes small. In addition, the constraint of the crack front increases. Therefore, the crack will propagate at a high speed following the crack initiation. In this case, it is difficult to control the $^{a}/W$ ratio required. In order to improve this situation, a smaller pre-cracking forces at the preliminary stage, for example 2400 N/200 N, can be used. The forces will be reduced to 2000 N/200 N as soon as the crack initiates.

The actual dimensions of the two series of specimens are listed in Table 5.15. Three-point bending test was carried out using a 5000 Kgf Instron testing machine at room temperature. The load range of 2000 Kgf was chosen. The testing arrangement was the same as that during testing the notched specimens without pre-cracking. Specimens were loaded at a rate of 0.02 cm/min. Because the rate of increase of load during the initial elastic deformation was measured to be 38.5 N/sec. for the nonside-grooved specimen with the $^{a}/W$ ratio of 0.525, thus the rate of

Table 5.15: Measured dimensions of the CVN specimens with pre-cracking

Specimen	L	L/2	B	W	D	T	R	R_{S1}	R_{S2}	ϕ	ϕ_{S1}	ϕ_{S2}	a/w	T^1
NONSIDE-GROOVED SPECIMEN														
B19V	55.6	27.9	10.00	10.00	8.08		0.232			41.5			0.524	
B21V	55.6	27.6	9.98	10.00	8.05		0.237			43.5			0.525	
B23V	55.6	27.8	9.99	9.99	8.02		0.212			42.0			0.524	
SIDE-GROOVED SPECIMEN														
S13V	55.6	27.5	9.98	10.00	7.98	4.03	0.211	0.223	0.226	47.0	43.8	42.0	0.527	7.56
S17V	55.9	27.7	9.99	10.00	8.05	4.00	0.250	0.225	0.235	46.1	43.5	42.2	0.546	7.38
S19V	55.8	28.3	9.97	10.00	8.02	3.98	0.252	0.216	0.246	47.1	43.5	41.9	0.589	7.05

a. The notations used for the dimensions are shown in Fig.5.1;

b. T^1 is the calculated distance between side-grooved roots at the pre-crack front;

c. All dimensions are in millimetres or degrees;

d. The side-grooved geometry was measured on the surface opposite the main notch,

increase of stress intensity factor was calculated to be 14.0 $N.mm^{-\frac{3}{2}}/sec$. In the case of the side-grooved specimen with the $^{a}/_{W}$ ratio of 0.546, the rate of increase of load was 29.1 N/sec. Thus, the side-grooved specimen exhibited a slightly low rate of increase of stress intensity factor. Load versus load-point displacement curves and load versus plastic deflection curves for nonside- and side-grooved specimens with pre-cracking are shown in Figs. 5.13 and 5.14, respectively. It has been found that both the pre-cracked specimens promote attaining maximum load or fracture instability, compared with the notched specimens. Furthermore, for pre-cracked side-grooved specimen, the attainment of maximum load is at much smaller displacement than for pre-cracked nonside-grooved specimen.

5.3.2 Calibration of Crack Tip Opening Displacement

In order to determine the crack tip opening displacement of the pre-cracked Charpy specimens a photographic calibration technique the same as previously used was employed. Microhardness indentations were made on the two sides of the crack with the gauge length of 1.7 mm, as the same gauge length might easily make a comparison between the two series of specimens. The indentation spacing on each side was 0.2 mm. During the three-point bending test, photographs were taken of the crack tip area. Two typical series of the photographs are shown in Plates 5.10 and

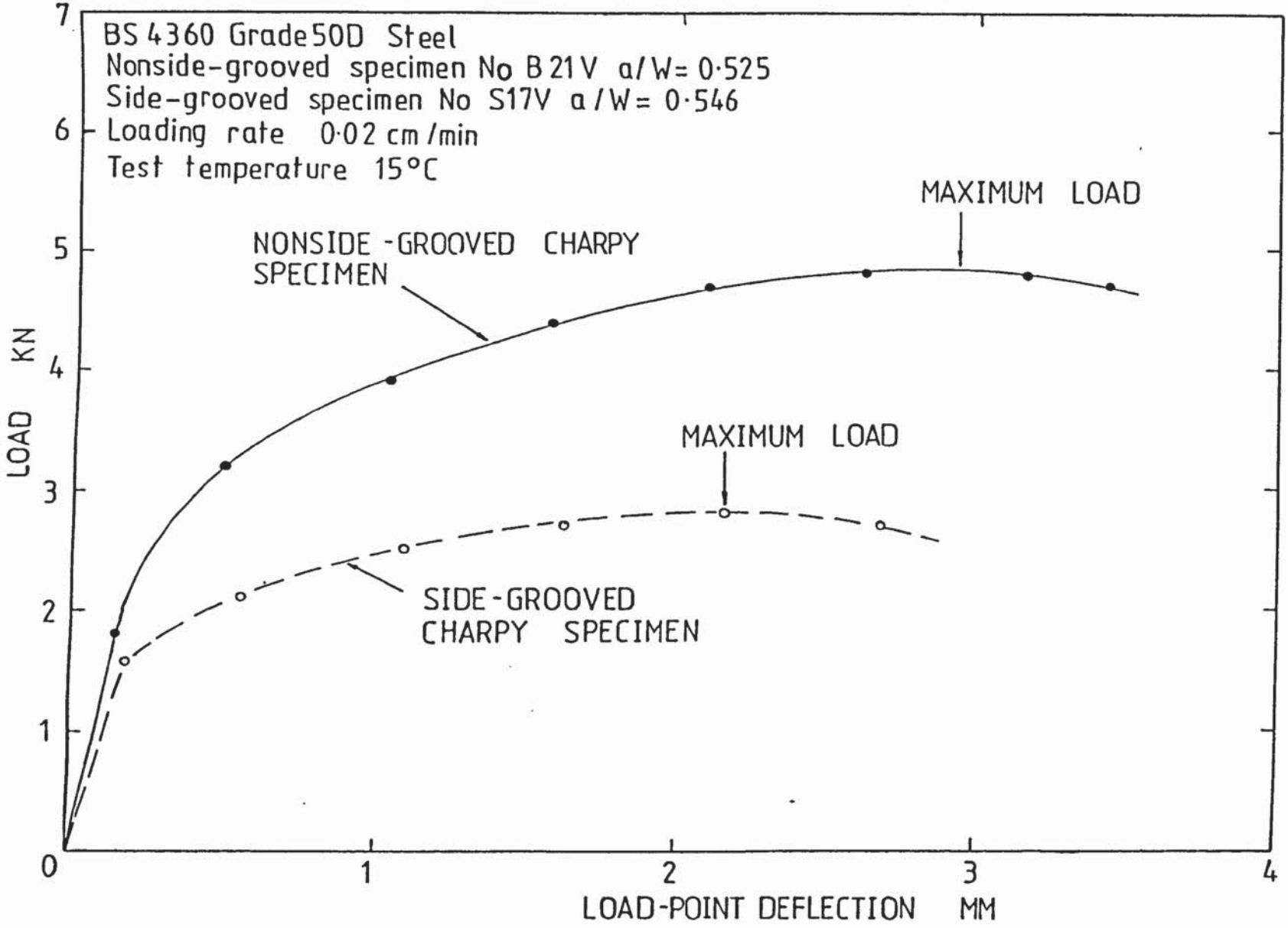

FIGURE 5.13 Load versus load-point displacement curves for nonside- and side-grooved three-point bend specimens with pre-fatigue crack

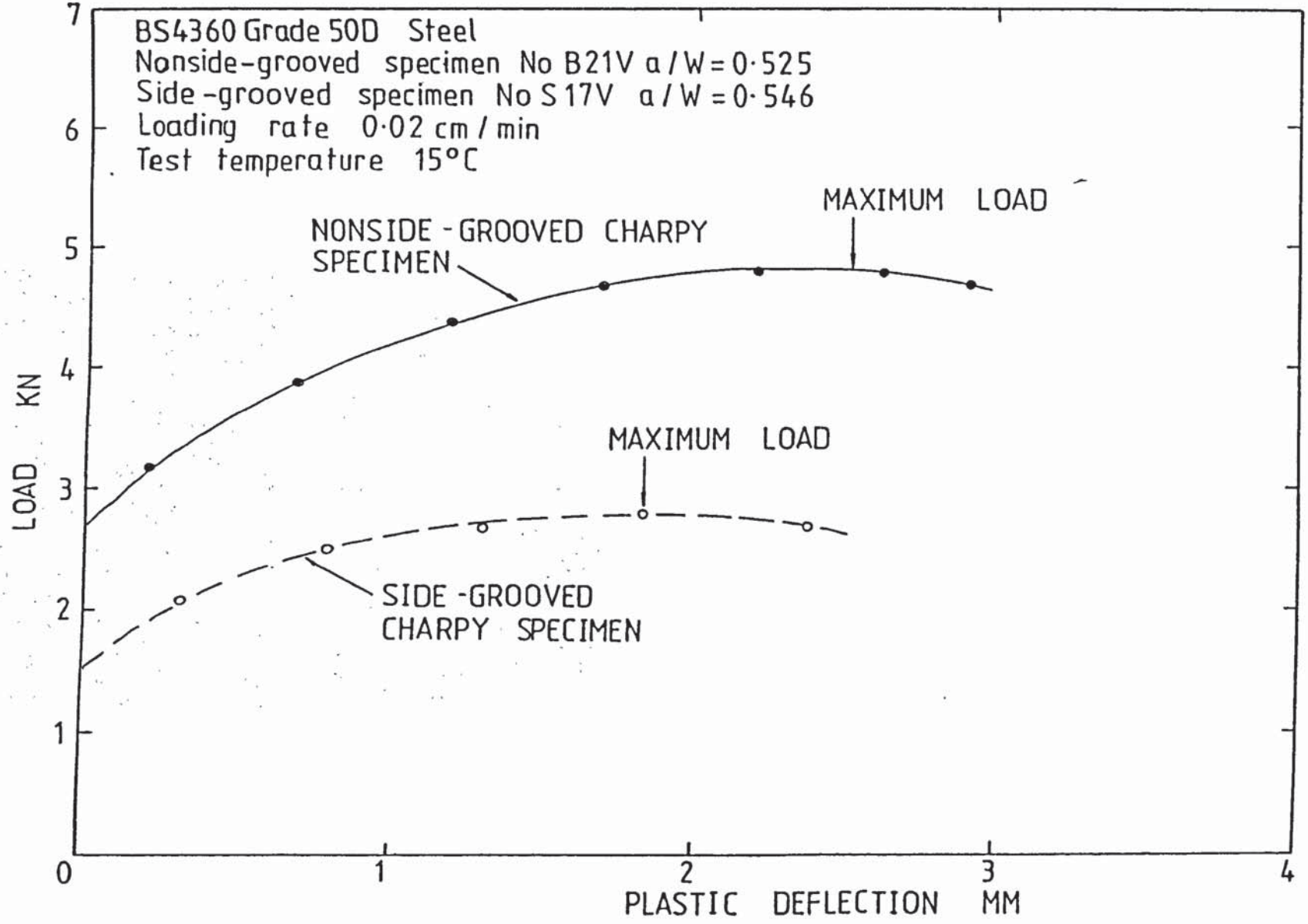

FIGURE 5.14 Load versus plastic deflection curves for nonside- and side-grooved three-point bend specimens with pre-fatigue crack

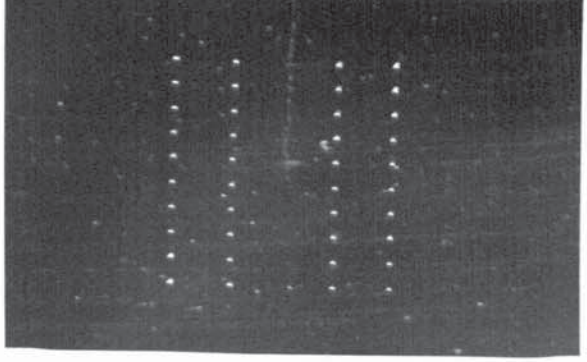

(a)

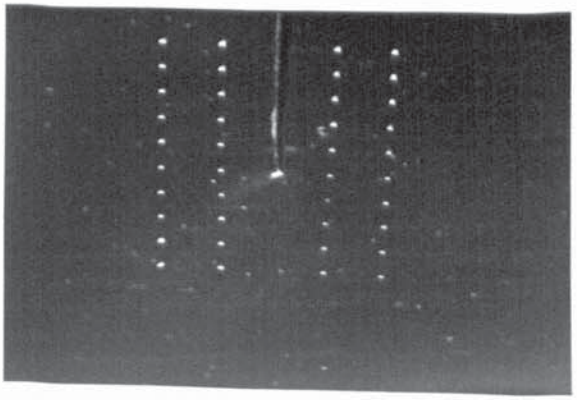

(b)

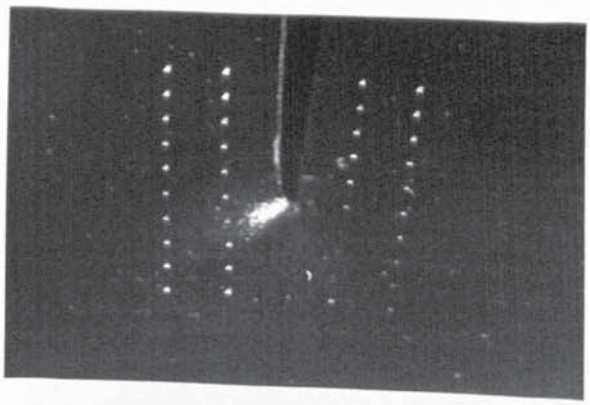

(c)

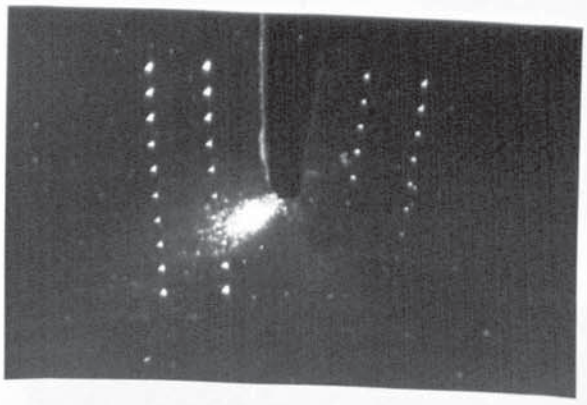

(d)

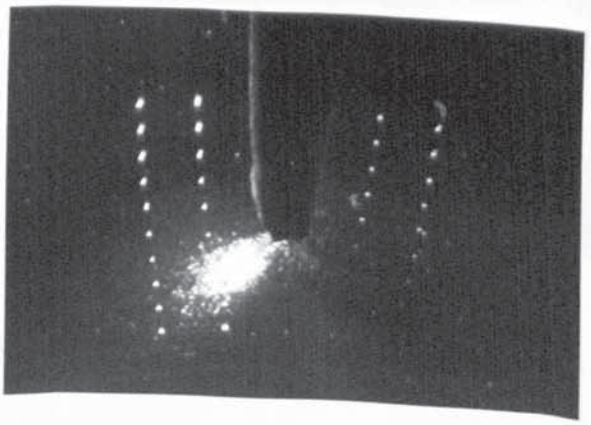

(e)

Plate 5.10:: Calibration series of pre-cracked non-side-grooved Charpy specimen, 17.5 x. Photograph (i) was taken after unloading.

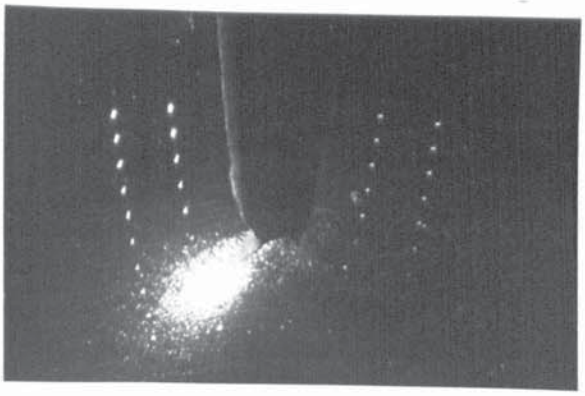

(f)

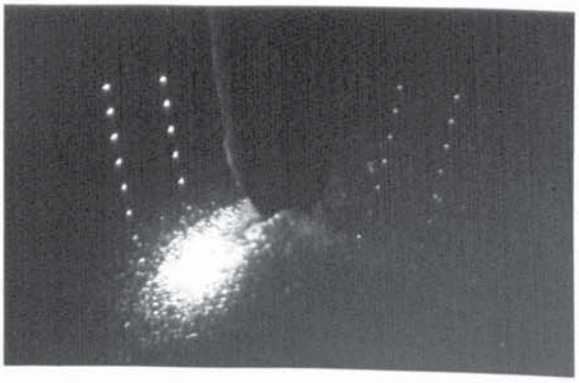

(g)

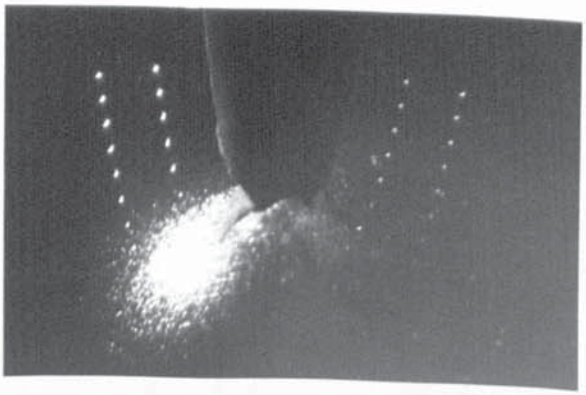

(h)

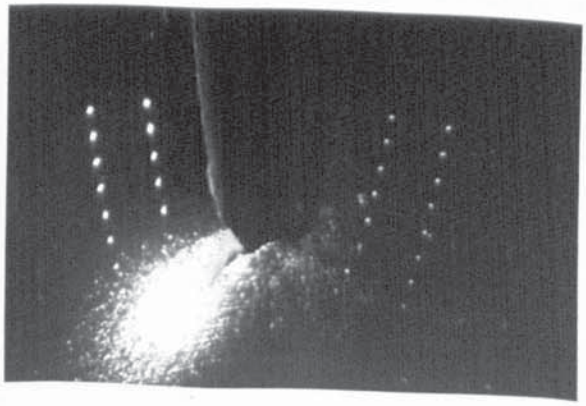

(i)

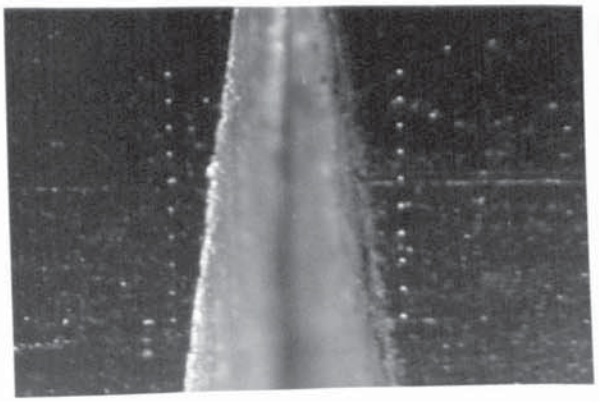

(a)

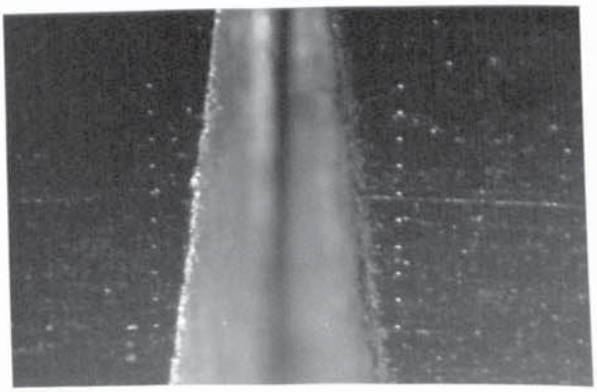

(b)

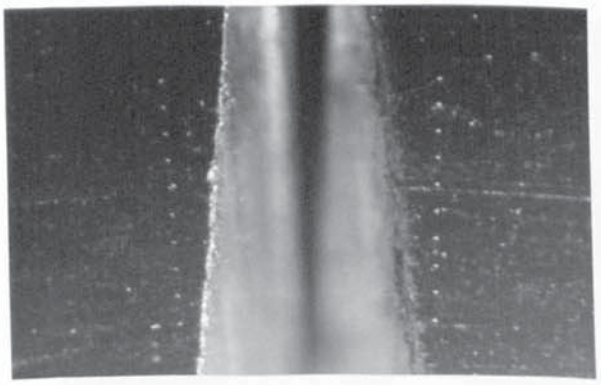

(c)

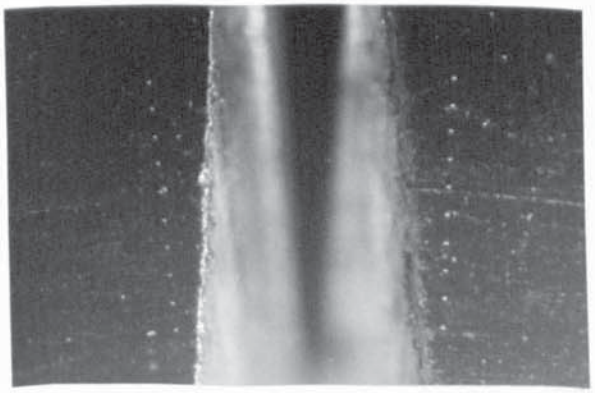

(d)

Plate 5.11 : Calibration series of pre-cracked side-grooved Charpy specimen, 17.5 x; Photograph (g) was taken after unloading.

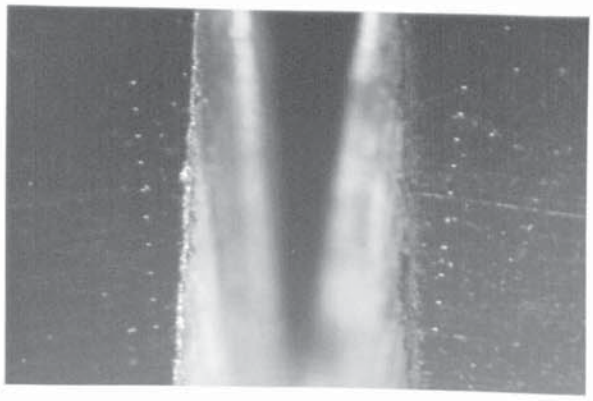

(e)

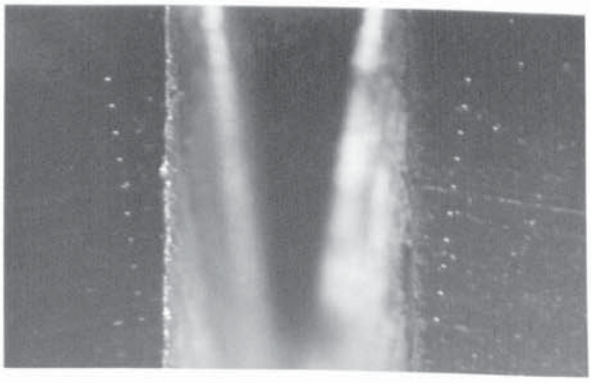

(f)

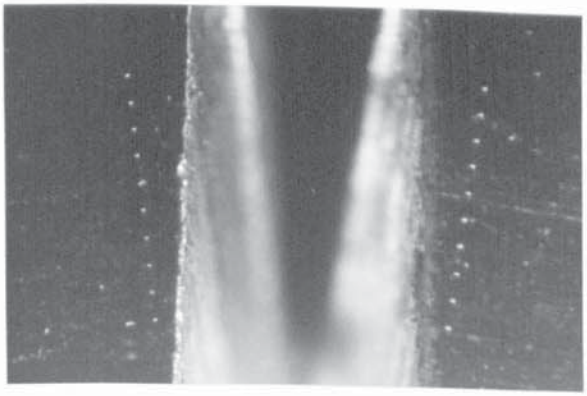

(g)

5.11 for the pre-cracked nonside- and side-grooved specimens, respectively. The corresponding load-deflection values are listed in Tables 5.16 and 5.17.

Compared with the notched specimens, the extent of the plastic zone observed on the lateral surfaces of the specimen is smaller, as shown in Plate 5.10 (f) and (g), during instability of the pre-cracked specimen. The crack initiation occurs after obviously blunting of the crack tip. The initial crack growth has an angle of about 45^{o} with the loading direction, and it is the same with the standard CVN bending test. For the pre-cracked side-grooved specimen, white obscure regions cannot be found on the lateral surfaces of the specimen during instability, as shown in Plate 5.11. It is also indicated that the severe plastic deformation which usually exists in the region of the near lateral surfaces does not occur.

The crack opening displacement (COD) and longitudinal displacements (u) in the vicinity of the crack tip are calculated from:

$$\text{COD (or u)} = \ell - \ell o \qquad \text{.....(5.10)}$$

where ℓo is the original gauge length; ℓ is the instantaneous gauge length at the instantaneous load. These calculated results are listed in Tables 5.18 and 5.19,

Table5.16: Results obtained for nonside-grooved three-point bend specimen with pre-fatigue crack, No. B21V

Load (KN)	3.2	3.9	4.4	4.7	4.8	4.8 (P_{max})	4.8	4.7
Load-point displacement (mm)	0.49	1.02	1.56	2.09	2.62	2.93	3.16	3.44
Plastic deflection (mm)	0.21	0.68	0.18	1.68	2.20	2.51	2.62	2.91
Photograph No. in Plate 5.10	(b)	(c)	(d)	(e)	(f)	-	(g)	(h)

* a/w = 0.525

** Crosshead speed = 0.02 cm/min; test temperature = 15°C

Table5.17: Results obtained for side-grooved three-point bend specimen with pre-fatigue crack, No. S17V

Load (KN)	2.1	2.5	2.7	2.8 (P_{max})	2.7
Load-point displacement (mm)	0.55	1.08	1.61	2.15	2.68
Plastic deflection (mm)	0.31	0.79	1.29	1.82	2.37
Photograph No, in Plate 5.11	(b)	(c)	(d)	(e)	(f)

a.. a/w = 0.546

b. Crosshead speed = 0.02 cm/min; test temperature = 15°C

Table 5.18: Crack tip opening displacement and longitudinal displacement in the vicinity of the crack tip for nonside-grooved Charpy specimen with pre-fatigue crack, No. B21V

Distance from crack tip / Load-point displacement	-1.05	-0.85	-0.65	-0.45	-0.25	-0.05	0.0[a]	+0.15	+0.35	+0.55	+0.75
0.49	0.10	0.09	0.08	0.07	0.05	0.04	0.037	0.03	0.02	0.00	0.00
1.02	0.26	0.25	0.23	0.20	0.17	0.14	0.134	0.12	0.08	0.05	0.03
1.56	0.44	0.40	0.37	0.33	0.30	0.25	0.241	0.19	0.14	0.10	0.05
2.09	0.62	0.58	0.53	0.48	0.42	0.36	0.347	0.29	0.21	0.15	
2.62	0.82	0.76	0.71	0.64	0.57	0.48	0.463	0.40	0.30	0.21	
3.16	1.03	0.96	0.87	0.80	0.72	0.62	0.600	0.53	0.41	0.30	
3.44	1.12	1.05	0.97	0.89	0.80	0.71	0.689	0.59	0.48	0.37	
After unloading	1.08	1.03	0.95	0.87	0.78	0.69	0.670	0.59	0.47		

a. This column of values was obtained by means of extrapolation;

b. Gauge length = 1.7mm;

c. Tested at 15°C with loading rate of 0.02 cm/min;

d. All units are in millimetres.

Table 5.19: Crack tip opening displacement and longitudinal displacement in the vicinity of the crack tip for side-grooved Charpy specimen with pre-fatigue crack, No. S17V

Distance from crack tip / Load-point displacement	-1.26	-1.06	-0.86	-0.66	-0.46	-0.26	-0.06	0.0[a]	+0.14	+0.34	+0.54
0.55	0.15	0.14	0.13	0.12	0.11	0.10	0.09	0.087	0.08	0.07	0.07
1.08	0.34	0.32	0.30	0.28	0.26	0.24	0.22	0.214	0.20	0.18	0.15
1.61	0.54	0.51	0.48	0.44	0.41	0.37	0.35	0.340	0.31	0.28	0.24
2.15	0.74	0.69	0.65	0.60	0.56	0.52	0.48	0.467	0.44	0.39	0.34
2.68	0.95	0.89	0.84	0.78	0.73	0.67	0.62	0.604	0.56	0.51	0.44
After unloading	0.92	0.86	0.80	0.76	0.70	0.65	0.60	0.565	0.54	0.48	0.43

a. This column of values was obtained by means of extrapolation;

b. Gauge length = 1.7mm;

c. Tested at 15°C with loading rate of 0.02 cm/min;

d. All units are in millimetres.

and shown in Figs. 5.15 and 5.16 for the pre-cracked nonside- and side-grooved specimens, separately. After determining the pre-crack length, the crack opening displacement at the crack tip (CTOD) was calculated by means of an extrapolation of the measured crack opening displacements. It is apparent from this investigation that the longitudinal displacement or strain field ahead of the crack tip falls less steeply, compared with the two series of notched specimens. It is also indicated that the notch acuity has a significant influence upon the singularity of the strain field ahead of the notch tip.

The crack opening displacement values obtained were calibrated against the specimen deflection, as shown in Figs. 5.17 and 5.18, for pre-cracked nonside- and side-grooved specimens, respectively. The relationship between the crack tip opening displacement and the load-point displacement were described by a polynomial curve fit. They are given by:

$$Y = -0.0658 + 0.2183x - 0.0267x^2 + 0.0078x^3 \quad ....(5.11)$$

for the pre-cracked nonside-grooved specimen, and

$$Y = -0.0574 + 0.2772x - 0.0312x^2 + 0.0074x^3 \quad ....(5.12)$$

for the pre-cracked side-grooved specimen, where the Y

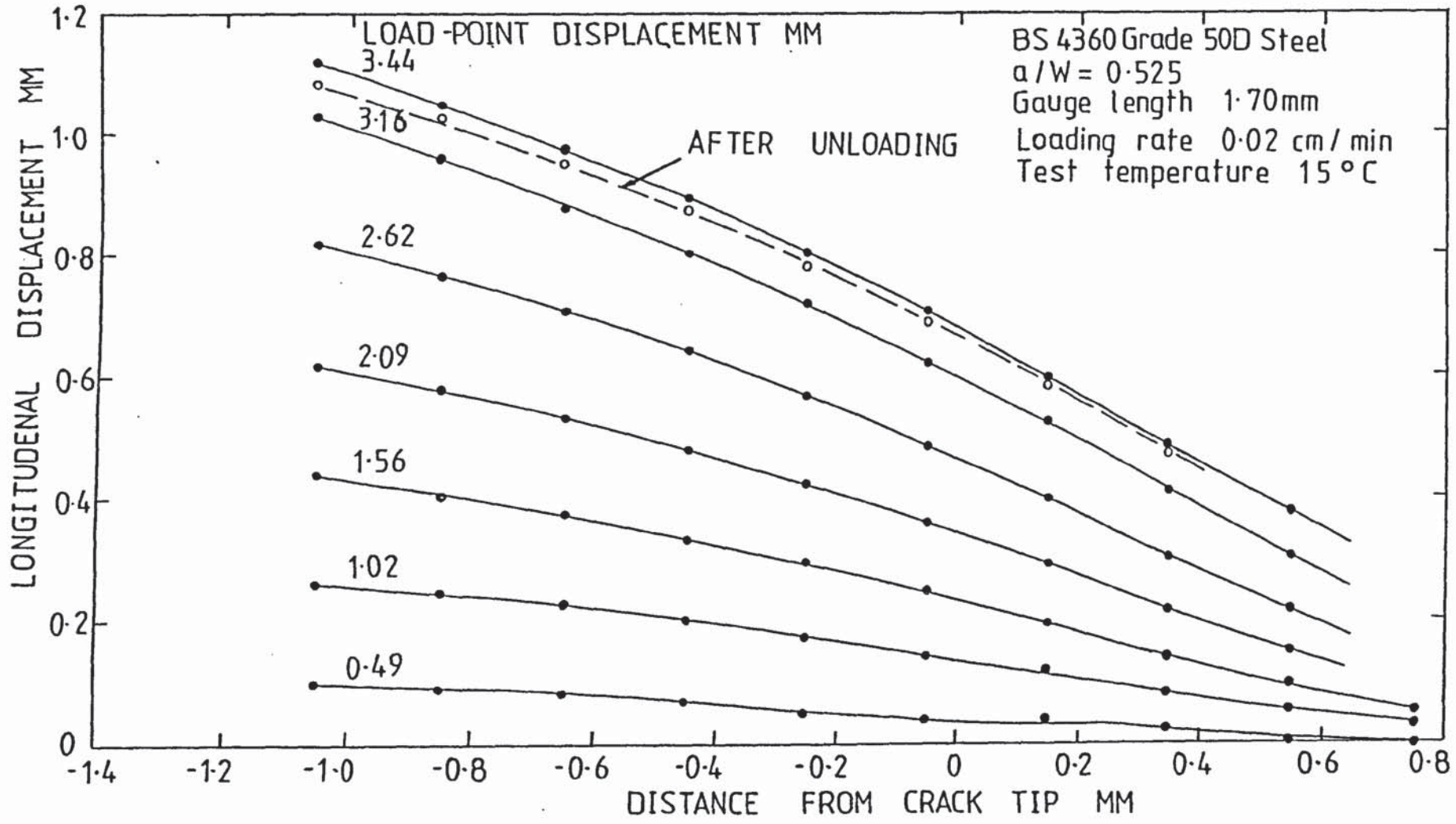

FIGURE 5.15 The variations of the longitudinal displacement fields for nonside-grooved Charpy specimen with pre-fatigue crack, No. B21V

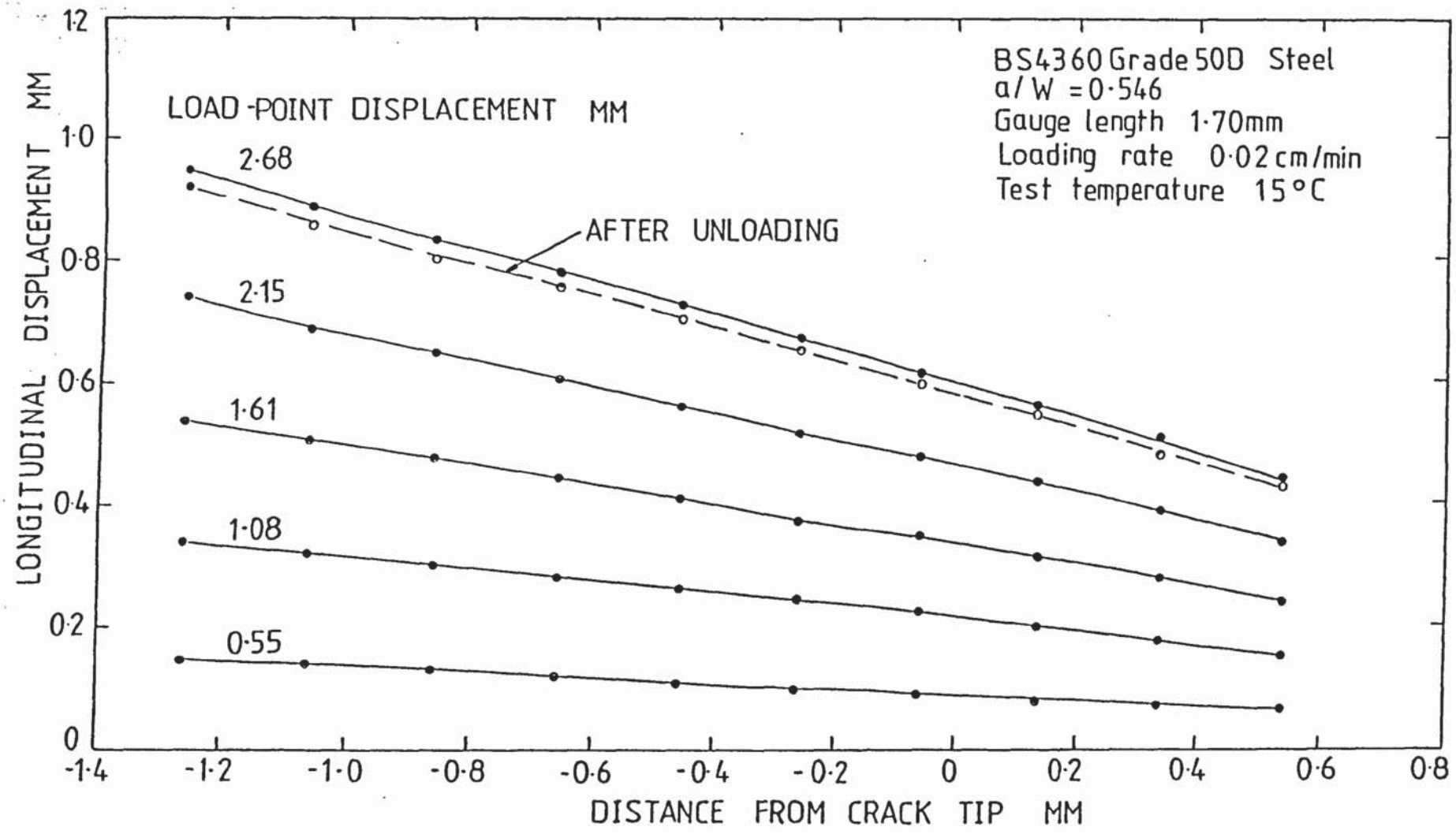

FIGURE 5.16 The variations of the longitudinal displacement fields for side-grooved Charpy specimen with pre-fatigue crack, No. S17V

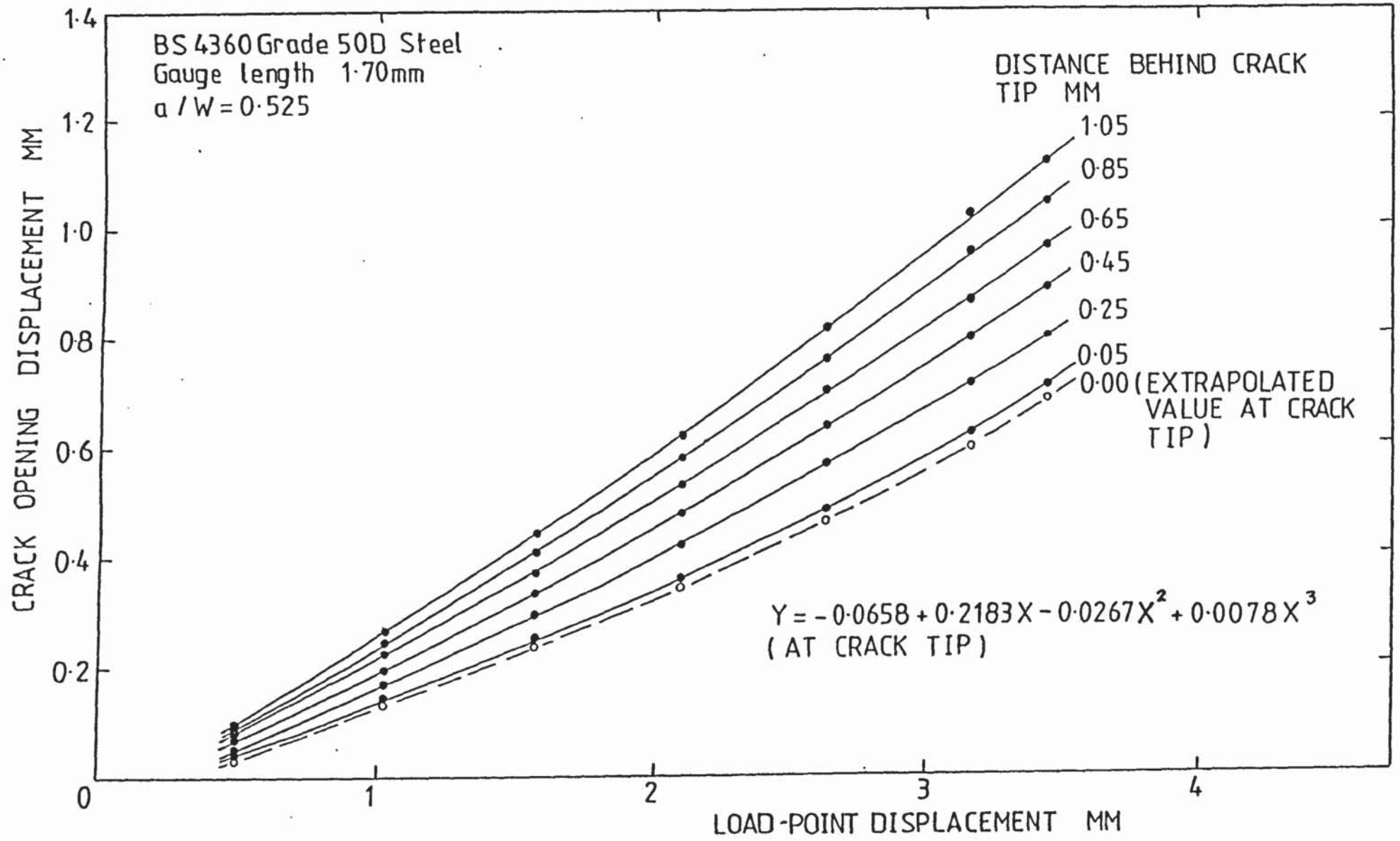

FIGURE 5.17 Crack opening displacement calibration for nonside-grooved Charpy specimen with pre-fatigue crack

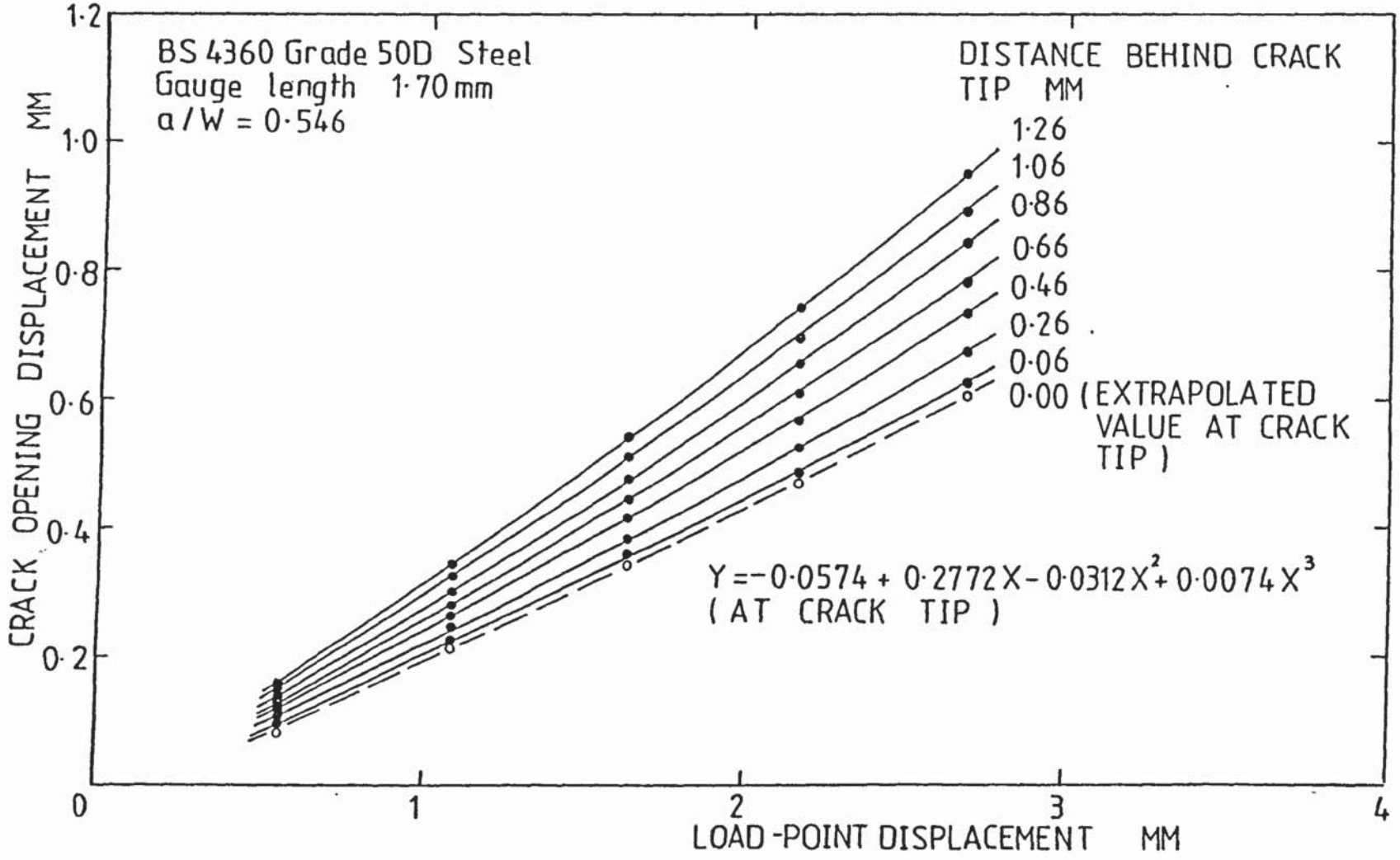

FIGURE 5.18 Crack opening displacement calibration for side-grooved Charpy specimen with pre-fatigue crack

represents the crack tip opening displacement; the x represents the load-point displacement.

Two specimens of each geometry were used to check the regression curves. The results are listed in Table 5.20. The maximum relative error of the crack tip opening displacement to the expected value is less than 6% for the pre-cracked nonside-grooved specimen. However, the maximum relative error for the pre-cracked side-grooved specimen approach to 17% (corresponding to the maximum absolute error of 0.08 mm).

These calibration curves might be thought to be valid on all specimens which have the same sizes and the same geometries, and which are tested in the same machine stiffness. However, the question is as to whether the measured gauge length will have an influence upon the calibration curves. Therefore, the different gauge lengths were decided to measure the crack opening displacement and longitudinal displacement field on the same nonside-grooved specimen. The gauge lengths of 1.7 mm and 0.8 mm were used simultaneously, as shown in Plate 5.10(a). The measured results are listed in Tables 5.18 and 5.21 for the gauge length of 1.7 mm and 0.8 mm respectively. As for the values of crack tip opening displacement, maximum absolute error and maximum relative error are 0.02 mm, and 9%, separately. Thus it might be thought that the influence of the measured gauge length is small.

Table 5.20: Results obtained from checking tests of pre-cracked specimens

Specimen No.	Load-point displacement mm	Plastic deflection mm	Calculated CTOD mm	Extrapolated CTOD from test, mm	Interrupted load KN	$\frac{a}{w}$
PRE-CRACKED NONSIDE-GROOVED SPECIMEN						
B19V	2.64	2.24	0.47	0.48	5.0	0.524
B23V	2.64	2.25	0.47	0.50	4.6	0.524
PRE-CRACKED SIDE-GROOVED SPECIMEN						
S13V	2.15	1.78	0.47	0.39	3.2	0.527
S19V	2.15	1.85	0.47	0.40	2.2	0.589

a. CTOD = crack tip opening displacement;

b. Test temperature = $12^{o}C$.

Table5.21: Crack tip opening displacement and longitudinal displacment in the vicinity of the crack tip for the same specimen as shown in Table 5.18, with the gauge length of 0.8mm

Distance from crack tip / Load-point displacement	-1.05	-0.85	-0.65	-0.45	-0.25	-0.05	0.0*	+0.15	+0.35	+0.55	+0.75
0.49	0.09	0.08	0.07	0.07	0.06	0.04	0.038	0.02	0.00	0.00	0.00
1.02	0.26	0.24	0.23	0.20	0.18	0.13	0.124	0.07	0.05	0.01	0.00
1.56	0.44	0.41	0.38	0.34	0.29	0.23	0.220	0.17		0.04	0.00
2.09	0.62	0.58	0.54	0.49	0.43	0.34	0.326	0.21	0.13	0.05	0.01
2.62	0.82	0.77	0.72	0.65	0.57	0.47	0.453	0.34	0.25		
3.16	1.02	0.97	0.89	0.82	0.73	0.61	0.590				
3.44	1.13	1.07	1.00	0.91	0.81	0.69	0.668				
After unloading	1.10	1.04	0.96	0.88	0.79	0.67	0.649				

* This column of values was obtained by means of extrapolation.

5.3.3 Estimation of Stress State Ahead of the Crack Tip

In order to estimate the level of triaxiality ahead of the crack tip in two series of pre-cracked Charpy specimens, Eq. (4.1), mentioned on a previous occasion, was used to research on the relationship among the void growth, plastic shear strain and triaxial stress state. Based on a similar consideration to the notched Charpy specimens, pre-cracked nonside- and side-grooved specimens were loaded to the load-point deflection of 2.64 mm and 2.15 mm, separately, according to the calculation of the polynomial curve fit Eqs. (5.11) and (5.12), if the crack tip opening displacement of 0.47 mm was expected. In order to obtain more reliable results, we made use of an average of the two specimens which underwent the same experimental condition.

The crack opening displacement and longitudinal displacement in the vicinity of the crack tip are measured by photographic technique, and listed in Tables 5.22 and 5.23 for the two kinds of the specimens, respectively. The values of the longitudinal plastic shear strain are calculated from the residual gauge lengths after unloading. The residual gauge lengths are also listed in the above tables. According to the calculation of Eq. (5.5), the plastic shear strains of the two kinds of the specimens are given in Tables 5.24 and 5.25 respectively.

Table5.22: Crack opening displacement and longitudinal displacement in the vicinity of the crack tip for pre-cracked nonside-grooved specimens.

SPECIMEN No. B19V											
Distance from crack tip	-1.04	-0.84	-0.64	-0.44	-0.24	-0.04	0.0[f]	+0.16	+0.36	+0.56	+0.76
Longitudinal displacement at the instantaneous load, u	0.83	0.76	0.70	0.63	0.58	0.49	0.48	0.41	0.32	0.23	0.15
Longitudinal displacement after unloading, u_{res}	0.79	0.73	0.67	0.60	0.53	0.46	0.45	0.38	0.28	0.21	0.14
SPECIMEN No.B23V											
Distance from crack tip	-1.04	-0.84	-0.64	-0.44	-0.24	-0.04	0.0[f]	+0.16	+0.36	+0.56	+0.76
Longitudinal displacement at the instantaneous load, u	0.85	0.78	0.73	0.67	0.58	0.51	0.50	0.43	0.33	0.26	
Longitudinal displacement after unloading, u_{res}	0.80	0.76	0.69	0.64	0.57	0.49	0.48	0.41	0.31		

a. Gauge length = 1.7mm;

b. Specimens were tested at 12°C;

c. Loading rate = 0.02 cm/min;

d. $\frac{a}{w}$ = 0.524 for both specimens;

e. Loading-point deflection at the instantaneous load was 2.64mm;

f. This column of values was obtained by means of extrapolation;

g. All units are in millimetres.

Table5.23 : Crack opening displacement and longitudinal displacement in the vicinity of the crack tip for pre-cracked side-grooved specimens.

SPECIMEN No. S13V											
Distance from crack tip	-1.07	-0.87	-0.67	-0.47	-0.27	-0.07	0.0[f]	+0.13	+0.33	+0.53	+0.73
Longitudinal displacement of the instantaneous load, u	0.62	0.58	0.53	0.48	0.44	0.40	0.39	0.36	0.31	0.28	0.23
Longitudinal displacement after unloading, u_{res}	0.58	0.54	0.50	0.46	0.42	0.39	0.38	0.34	0.29	0.26	0.21
SPECIMEN No. S19V											
Distance from crack tip	-1.29	-1.09	-0.89	-0.69	-0.49	-0.29	-0.09	0.0[f]	+0.11	+0.31	+0.50[f]
Longitudinal displacement at the instantaneous load, u	0.69	0.64	0.59	0.55	0.50	0.47	0.42	0.40	0.38	0.34	0.31
Longitudinal displacement after unloading, u_{res}	0.64	0.60	0.56	0.52	0.48	0.44	0.39	0.37	0.35	0.32	0.28

a. Gauge length = 1.7mm;

b. Specimens were tested at 12°C;

c. Loading rate = 0.02 cm/min;

d. $\frac{a}{w}$ = 0.527 for No. S13V; $\frac{a}{w}$ = 0.589 for No. S19V;

e. Loading-point deflection at the instantaneous load was 2.15mm;

f. This column of values was obtained by means of extrapolation;

g. All units are in millimetres.

Table 5.24: Longitudinal shear strains for pre-cracked nonside-grooved Charpy specimens

Distance from crack tip, mm	0.0[f]	0.16	0.36	0.50[f]	0.56	0.76
SPECIMEN NO. B19V						
Longitudinal shear strain at the instantaneous load, γ	0.124	0.108	0.086	0.071	0.064	0.042
Longitudinal shear strain after unloading, $\bar{\varepsilon}^p$	0.117	0.101	0.076	0.063	0.058	0.040
SPECIMEN NO. B23V						
Longitudinal shear strain at the instantaneous load, γ	0.129	0.113	0.089	0.076	0.071	
Longitudinal shear strain after unloading, $\bar{\varepsilon}^p$	0.124	0.108	0.084	0.067		

a. Gauge length = 1.7 mm;
b. Specimens were tested at 12°C;
c. Loading rate = 0.02 cm/min;
d. Loading-point deflection at the instantaneous load was 2.64 mm;
e. a/W = 0.524 for both specimens;
f. These columns of values were obtained by means of extrapolation.

Table 5.25: Longitudinal shear strains for pre-cracked side-grooved Charpy specimens.

SPECIMEN NO. S13V						
Distance from crack tip, mm	0.0[f]	0.13	0.33	0.50[f]	0.53	0.73
Longitudinal shear strain at the instantaneous load, γ	0.103	0.096	0.084	0.077	0.076	0.064
Longitudinal shear strain after unloading, $\bar{\varepsilon}^p$	0.101	0.091	0.079	0.072	0.071	0.058
SPECIMEN NO. S19V						
Distance from crack tip, mm	0.0[f]	0.11	0.31	0.50[f]		
Longitudinal shear strain at the instantaneous load, γ	0.106	0.101	0.092	0.083		
Longitudinal shear strain after unloading, $\bar{\varepsilon}^p$	0.099	0.094	0.085	0.076		

a. Gauge length = 1.7 mm;
b. Specimens were tested at 12°C;
c. Loading rate = 0.02 cm/min;
d. Loading-point deflection at the instantaneous load was 2.15 mm;
e. a/w=0.527 for No. S13V; a/w=0.589 for No. S19V;
f. These columns of values were obtained by means of extrapolation.

The method, mentioned on a previous occasion, was used to section the bended specimens along the mid-thickness. The fracture surfaces are shown in Plate 5.12. Based on a similar consideration to the notched Charpy specimens, the observed location was restricted within the area of 0.4 to 0.6 mm ahead of the crack tip. Typical fractography with voids in the observed areas is shown in Plate 5.13 and 5.14 for the nonside- and side-grooved specimens, respectively.

It has been found that there are some smaller voids in the fractography. These submicrometer voids in diameter of 0.1 to 2 μm might be nucleated from the tiny iron carbide particles [72]. At the same time, the size of voids, nucleated at MnC, Al_2O_3 or CaO inclusions, apparently increased. Much larger increase in the size of some voids was produced in pre-cracked side-grooved specimen, compared with the notched specimens. A typical fractography is shown in Plate 5.15.

Point counting techniques was directly conducted on the screen of scanning electron microscope. Regular square grid of 1 cm and magnification of 1000 x were chosen to count and measure voids on the fracture surfaces. The relative void volumes and standard deviations for each specimen are listed in Table 5.26. It has been found that the standard deviations are the values approximate to the mean values for the relative void volumes.

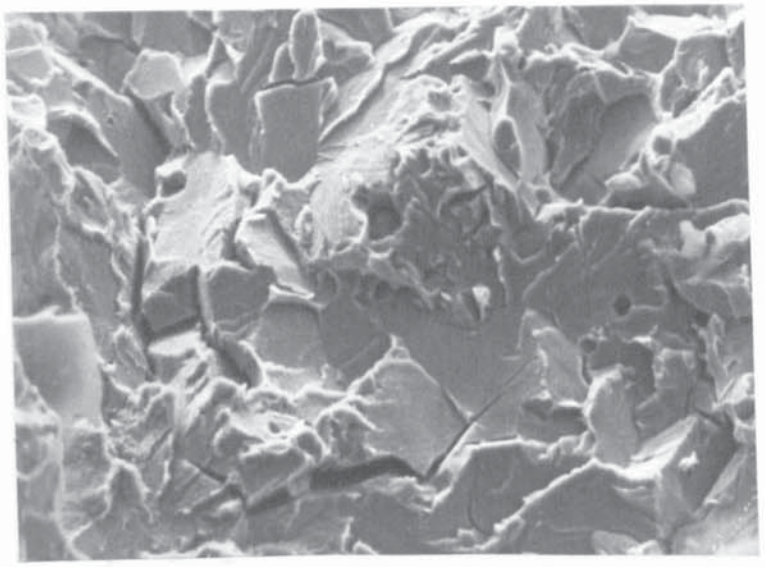

(a) : Specimen No. B19V; observation is in 0.35 mm ahead of the crack tip; horizontal direction in Plate is loading direction of specimen.

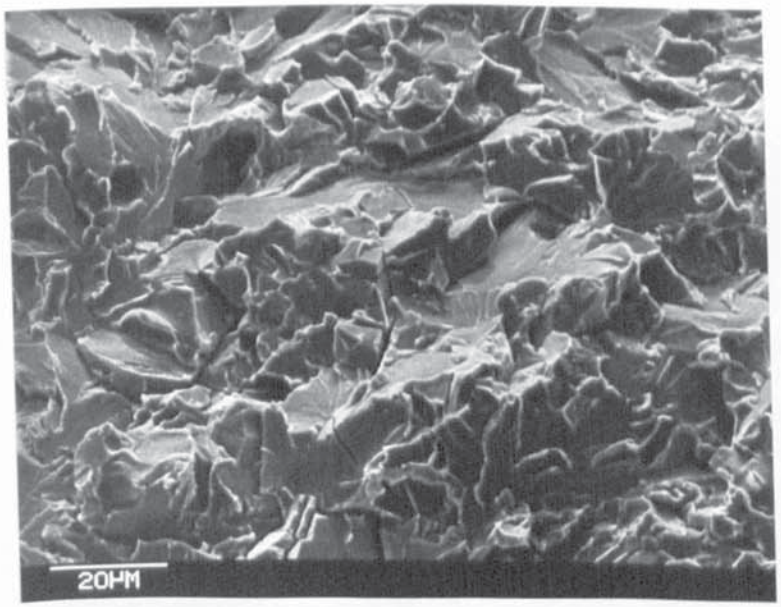

(b) : Specimen No. B19V; observation is in 0.50 mm ahead of crack tip; upright direction in Plate is loading direction of specimen.

Plate 5.13: Fractographs with voids for pre-cracked nonside-grooved Charpy specimen.

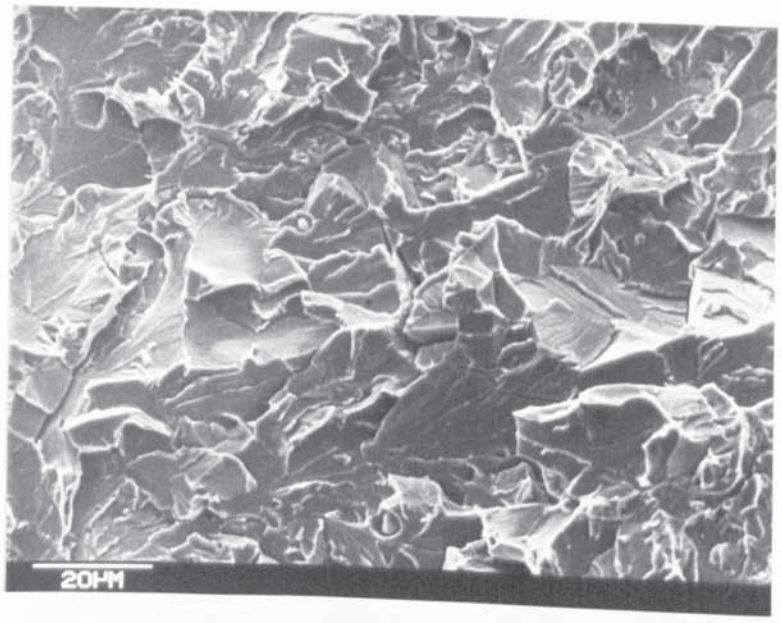

(a) : Specimen No.S13V; observation is in 0.40 mm ahead of the crack tip.

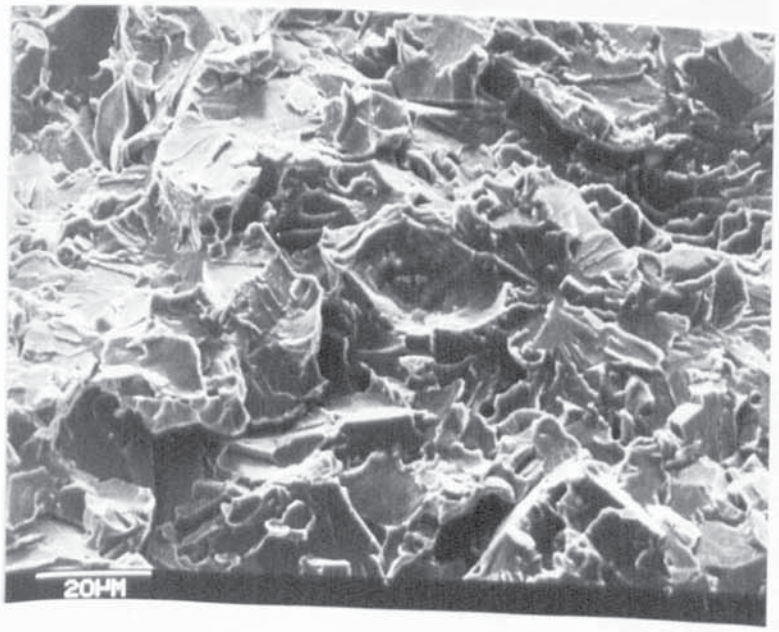

(b) : Specimen No. S19V, observation is in 0.45 mm ahead of the crack tip.

Plate 5.14: Fractographs with voids for pre-cracked side-grooved Charpy specimens; upright direction in Plates is loading direction of specimens.

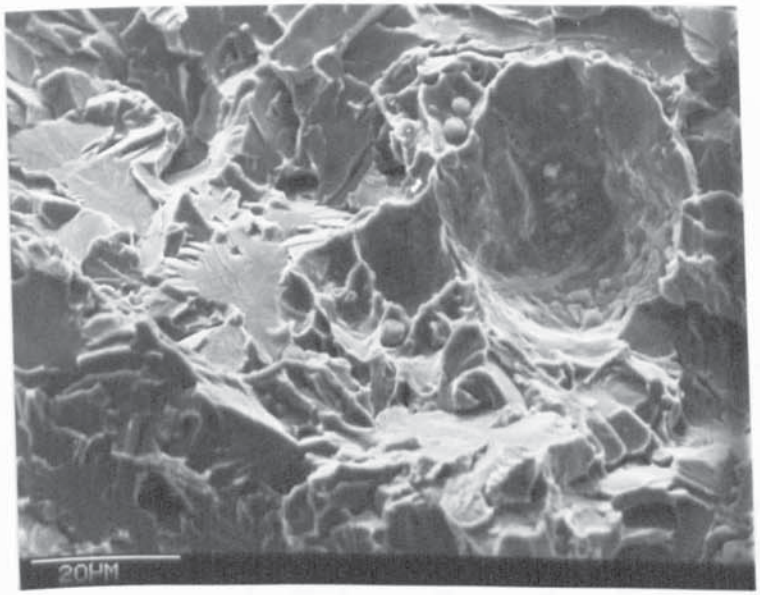

Plate 5.15 : Larger increase in the size of voids in pre-cracked side-grooved specimen No. S19V; observation is in 0.25 mm ahead of the crack tip; horizontal direction in Plate is loading direction of specimen.

Table 5.26 : Measured relative void volume and calculated triaxiality ahead of the pre-crack tip for nonside- and side-grooved specimens.

Specimen No.	Relative void volume, Vv	Standard deviation, σ	Plastic shear strain at 0.5mm ahead of the crack tip, $\bar{\varepsilon}^p$	$\frac{\ell n(Vv/Vo)}{\bar{\varepsilon}^p - \bar{\varepsilon}^p{}_o}$	$\sigma_m/\bar{\sigma}$	
					T_1=3.83	T_1=4.13
PRE-CRACKED NONSIDE-GROOVED SPECIMEN						
B19V	0.00538	0.00716	0.063	17.949	4.69	4.35
B23V	0.00475	0.00770	0.067	14.929	3.90	3.62
PRE-CRACKED SIDE-GROOVED SPECIMEN						
S13V	0.01013	0.01061	0.072	24.682	6.44	5.98
S19V	0.00888	0.00856	0.076	21.568	5.63	5.22

According to the Eq. (4.1), the average levels of the stress triaxiality at 0.5 mm ahead of the crack tip, $\sigma_m/\bar{\sigma}$, are 4.30 for nonside-grooved specimens, and 6.04 for side-grooved specimens, if the void growth coefficient is thought to be 3.83 (from Method III). It might be considered that the stress triaxiality ahead of the pre-crack tip in the Charpy-size specimens is much higher than that ahead of the notch root. At the same time, the tapered side-grooves apparently increased the constraint ahead of the crack tip.

Section 6

FRACTURE TOUGHNESS IN THE DUCTILE - BRITTLE TRANSITION REGION OF STRUCTURAL STEEL

6.1 Charpy V-Notch Impact Test

6.1.1. Experimental Procedure

Impact toughness tests were carried out using an Impact machine with a striker energy of 300 Joules and a linear velocity at the point of impact of 5^m/sec. Standard test pieces were used, as shown in Fig. 5.1(a). The specimens were cut parallel to the principal direction of rolling and the axis of the notch was perpendicular to the rolled surface of the plate. Specimen dimensions in cross section were measured using a Micrometer, and dimensions in notch geometry were measured by Vickers Fifty-Five Microscope. It was found that all dimensions were in the desired range.

Impact tests were made at -100^oC, -50^oC, 0^oC, $+50^oC$, and $+100^oC$, separately. In order that the test pieces be brought to a desired temperature by immersion in a bath, some liquid mediums were used. Methylated spirit with liquid nitrogen was used at -100^oC and -50^oC. Ice with water was used at 0^oC. Hot and boiled water were used at $+50^oC$ and $+100^oC$. In all cases the periods of immersion of the specimens were not less than 15 minutes and the specimens were removed from bath and broken within 6 seconds.

6.1.2 Results of the Standard CVN Impact Test

For each specimen, the energy absorbed during fracture was directly recorded on a dial gauge. The relative amount of the shear area in the fracture surface of broken Charpy specimen was measured using an empirical method described in ASTM A370 [87]. The lateral contraction at the notch root and lateral expansion on the back of the specimen were measured by a travelling microscope. All the test results covering the temperature range from -100°C to +100°C are given in Table 6.1. The evolution of the impact toughness as a function of temperature is shown in Figs. 6.1 through 6.3, named as energy transition, fracture transition, and ductility transition, separately.

At low temperature, fracture occurs principally by cleavage or quisa-cleavage, as shown in Plate 6.1. In the temperature range investigated, unfortunately, we do not find the nil-ductility temperature (NDT), at which the fracture occurs entirely by cleavage. Because the NDT indicates the lower limitation temperature of the transition region, thus all the test results investigated are in the transition and upper shelf temperature regions. In the transition region, the fracture is initiated by fibrous tearing at the notch root. Thus the lateral contraction at the notch root is essentially similar to that formed in the neck region of the tensile specimen. After the final fracture

Table 6.1: Results of Charpy V-notch impact tests for ductile-brittle transition behaviour

Specimen No.	Test Temperature °C	Energy absorbed, J	Shear fracture area, %	Lateral contraction, %	Lateral expansion, mils	Comments
C20	-100	56	17	10.1	27	broken
C21	-100	22	6	3.2	7	unbroken
C22	-100	66	29	10.8	31	"
C3	-100	28	6	5.5	15	broken
C23	-50	208	99	19.6	77	unbroken
C24	-50	100	55	16.0	52	"
C25	-50	169	61	21.7	83	"
C26	-50	53	36	8.1	36	"
C27	-50	174	66	22.6	85	"
C1	-50	168	62	16.3	87	"
C2	-50	152	37	20.0	85	"
C5	0	230	99	20.5	93	"
C6	0	262	99	22.1	85	"
C7	+50	240	99	23.5	89	"
C8	+50	256	99	25.9	84	"
C9	+100	241	99	22.9	89	"
C10	+100	231	99	25.7	109	"

a. BS4360 Grade 50D normalized steel; plate number 2A52-1
b. Specimen length is parallel to rolling direction
c. Shear fracture area was determined by ASTM E23-81
d. Striker energy=300 Joules; Linear Velocity at the point of impact=5^{m}/sec.

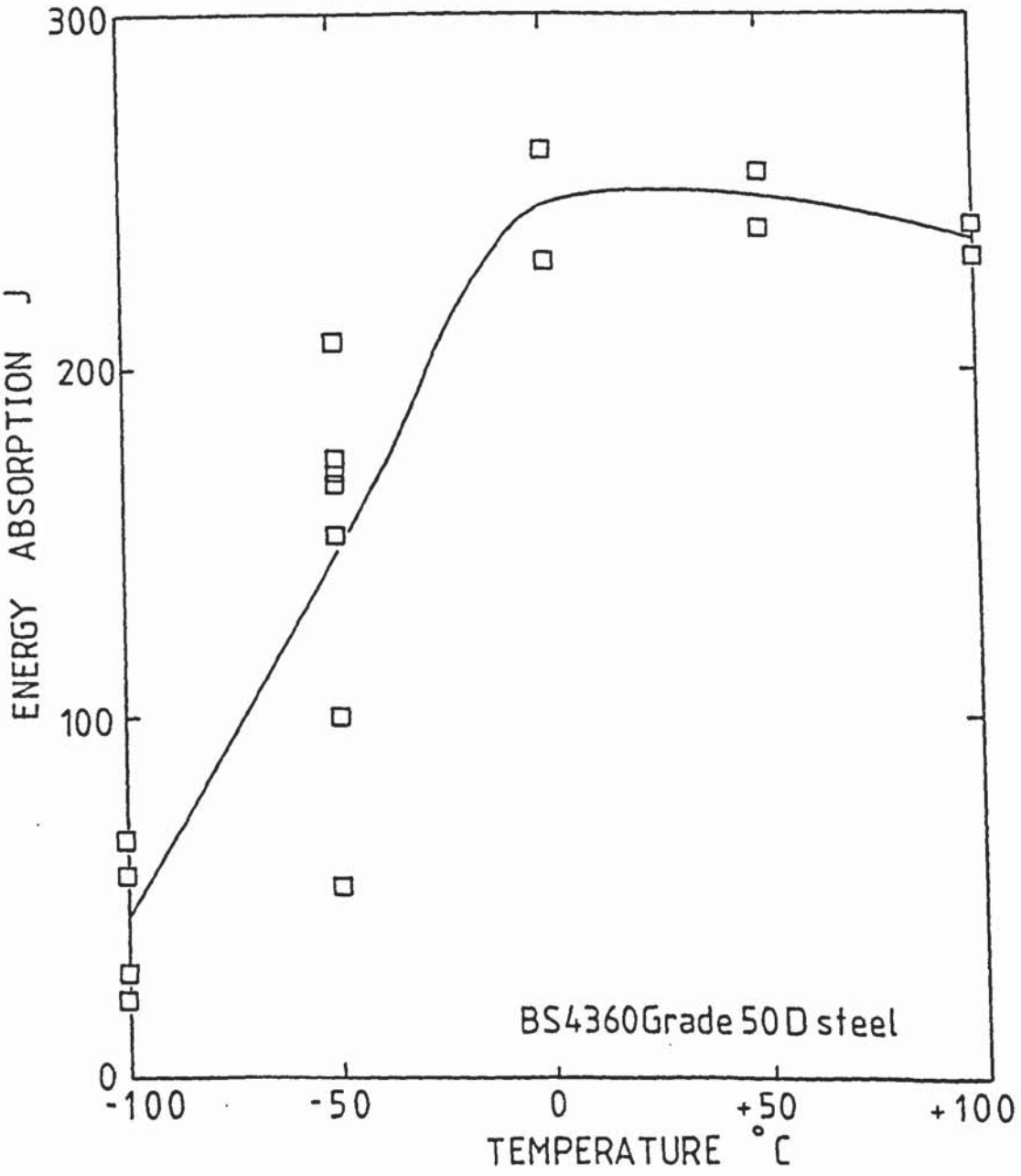

FIGURE 6.1 Energy transition with temperature for Charpy V-notch impact tests.

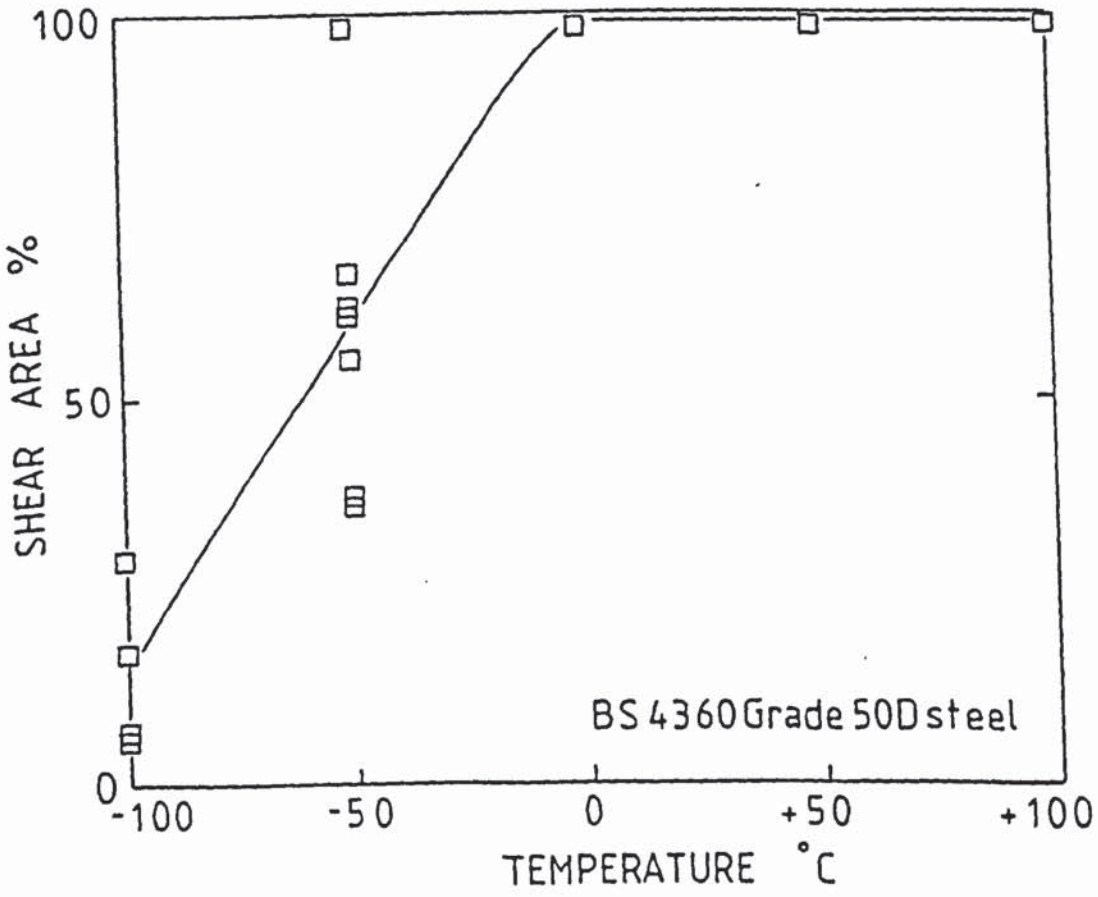

FIGURE 6.2 Fracture transition with temperature for Charpy V-notch impact tests

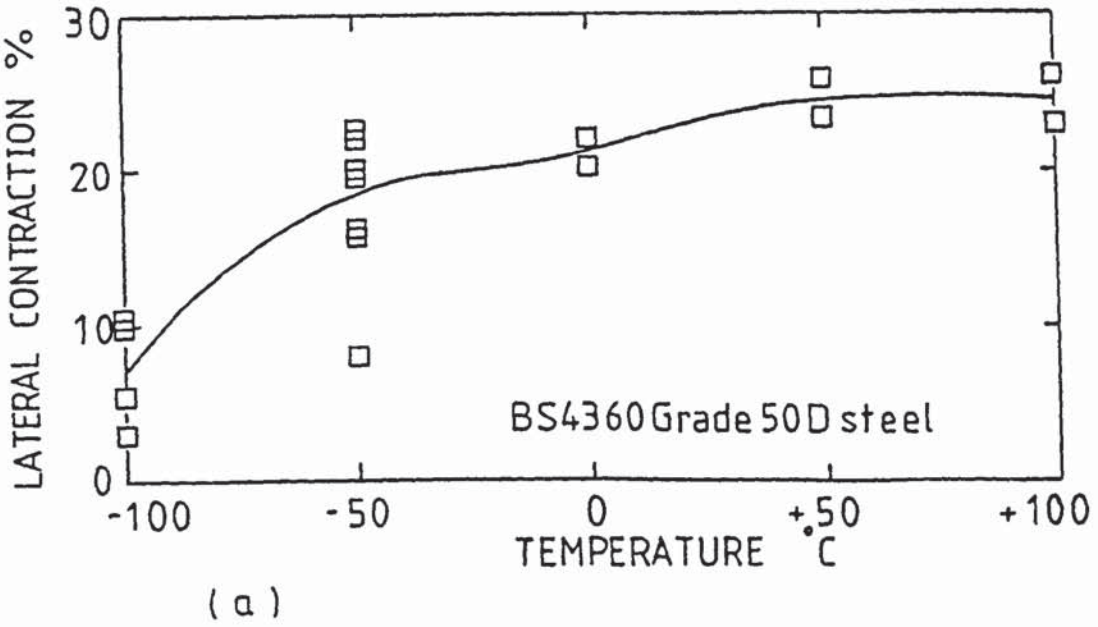

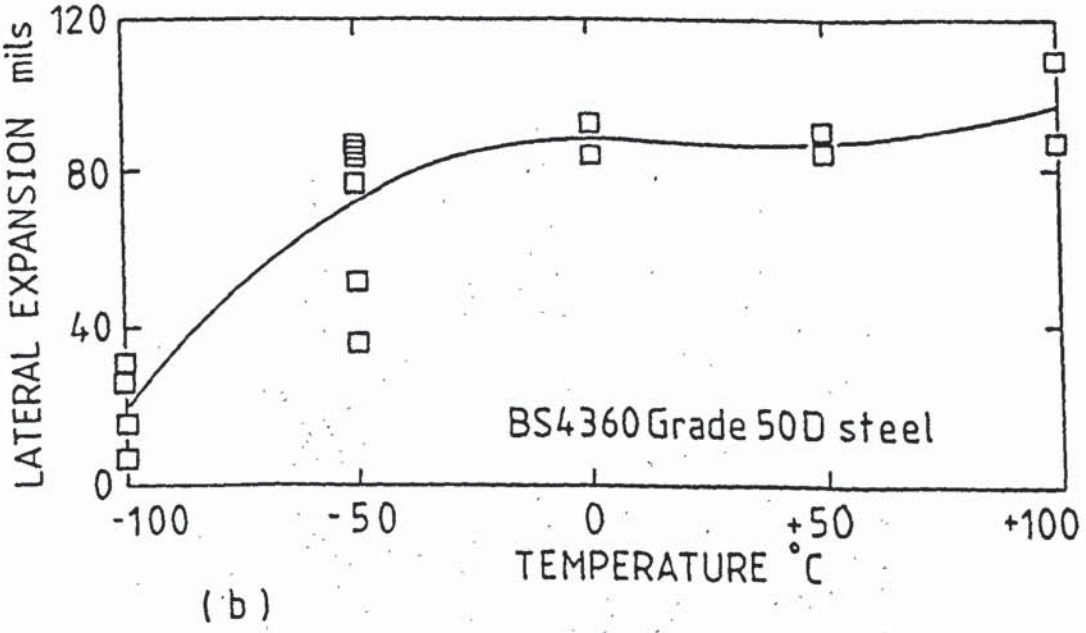

FIGURE 6.3 Ductility transition with temperature for Charpy V-notch impact tests

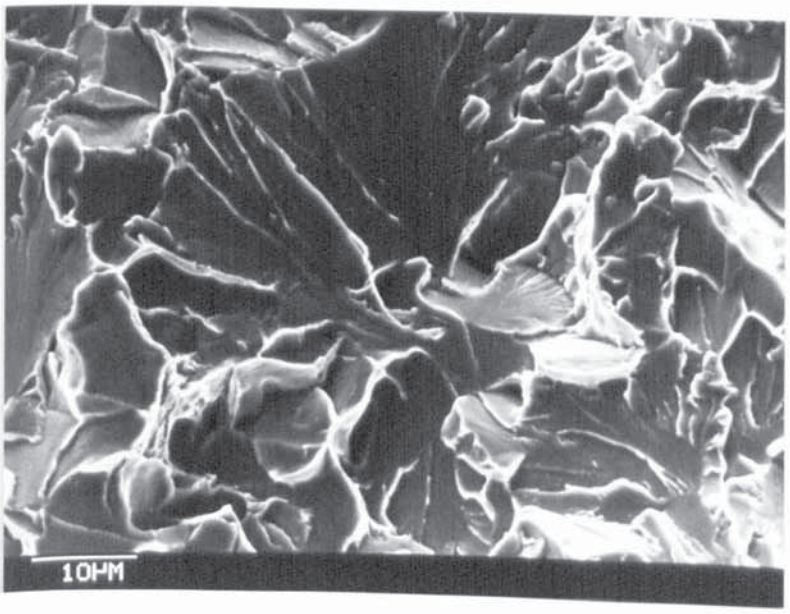

Plate 6.1 : SEM micrograph of the fracture surface of a Charpy impact specimen, tested at -100°C.

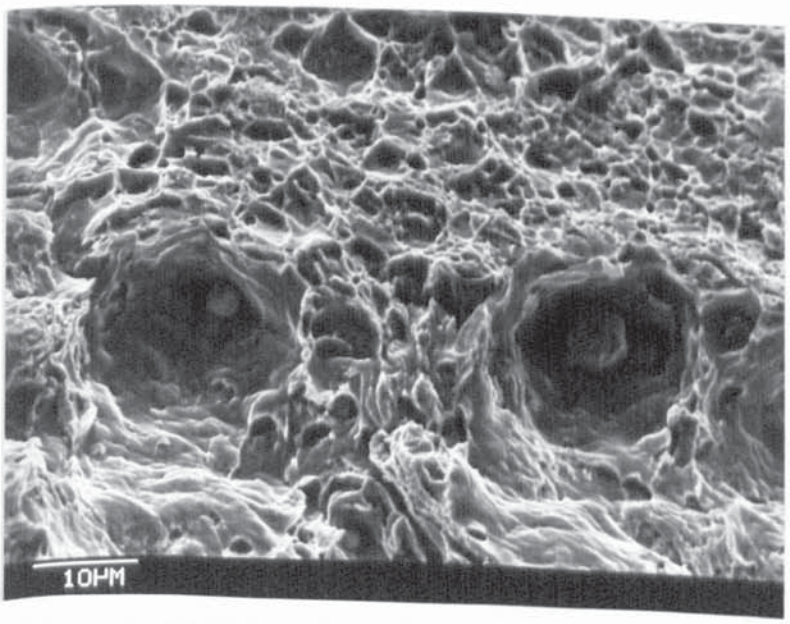

Plate 6.2 : SEM micrograph of the fracture surface of a Charpy impact specimen, tested at 0°C.

the shear lip formation can be found in the sides and back of the specimen. Because the energy absorbed in the shear fracture is much greater than the energy absorbed in cleavage, the impact energy increases as the proportion of shear fracture increases. If a 50% of shear area is used to express fracture appearance transition temperature (FATT), the transition temperature is about -60°C. At the same time, CVN test results indicate that there is a considerable scatter in the transition temperature region. Eventually, a temperature is reached at which the fracture becomes 100% shear fracture. This temperature is about 0°C, which is known as the upper shelf temperature. At temperatures above this temperature the impact energy is essentially independent of temperature.

6.1.3 Fracture Surface Observations at the Upper Shelf Region

Fracture surfaces of broken Charpy specimens showed ductile fracture with near hemispherical dimples at upper shelf temperatures, as shown in Plate 6.2. The larger dimples were tens of micrometers in diameter and often contained regularly spherical particles. Areas between the larger dimples exhibited a lot of much smaller hemispherical dimples, typically from a few tenths of micrometer to several micrometers in diameter. The particle in the larger dimples were present as inclusions in this steel and were identified by x-ray

energy spectrometer (KEVEX RAY) as mainly MnS, Al_2O_3, and CaO. The smaller dimples are usually thought to be associated with submicrometer Fe_3C particles. Generally dimples are thought to be halves of voids which have formed in the material under applied load. Thus, the fracture surface observations show that voids are nucleated predominantly at included particles in the steel and growth by means of local plastic flow to maintain an approximately spherical shape. The mechanism of fracture in Charpy specimens of BS4360 Grade 50D steel at upper shelf temperatures appears to consist of nucleation, growth, and coalescence of voids.

6.1.4 Effect of Side-Grooves on the Transition Behaviour in CVN Impact Test

In order to investigate the effect of the side-grooves on the ductile-brittle transitions in CVN impact test, it was decided to use the tapered side-grooved specimens, as shown in Fig. 5.1(b). The experimental procedure was the same with the standard CVN impact test. The test results are given in Table 6.2. Similarly, the curves of the energy transition, fracture transition, and ductility transition are shown in Figs. 6.4 through 6.6. It should be noted that the ratio of the shear area in the fracture surface was estimated by real measurement, due to the non-standardization of the side-grooved specimens.

For side-grooved specimens, the 50% of FATT and the 100%

Table 6.2 : Results of side-grooved Charpy V-notch impact tests for ductile-brittle transition behaviour

Specimen No.	Test Temperature °C	Energy absorbed, J	Shear fracture area, %	Lateral contraction, %	Lateral expansion, mils
CS1	-100	41	8	4.3	10.8
CS2	-100	53	20	4.8	14.2
CS10	-100	51	16	5.6	13.4
CS3	-50	78	32	6.4	23.8
CS5	-50	78	29	6.3	23.0
CS6	-50	48	23	5.8	12.6
CS4	0	122	100	6.2	43.7
CS7	0	127	100	7.1	41.9
CS14	0	100	52	5.4	33.1
CS11	+50	118	100	8.5	46.5
CS12	+50	121	100	8.0	48.2
CS8	+100	126	100	8.2	53.0
CS9	+100	124	100	8.3	58.3

a. BS4360 Grade 50D normalized steel; plate number 2A52-1,

b. Specimen length is parallel to rolling direction,

c. Shear fracture area was estimated by real measurement,

d. All the specimens were broken except for specimen No. CS5,

e. Striker energy = 300 Joules; Linear velocity at the point of impact = 5 m/sec,

f. mils are equal to thousandths of an inch.

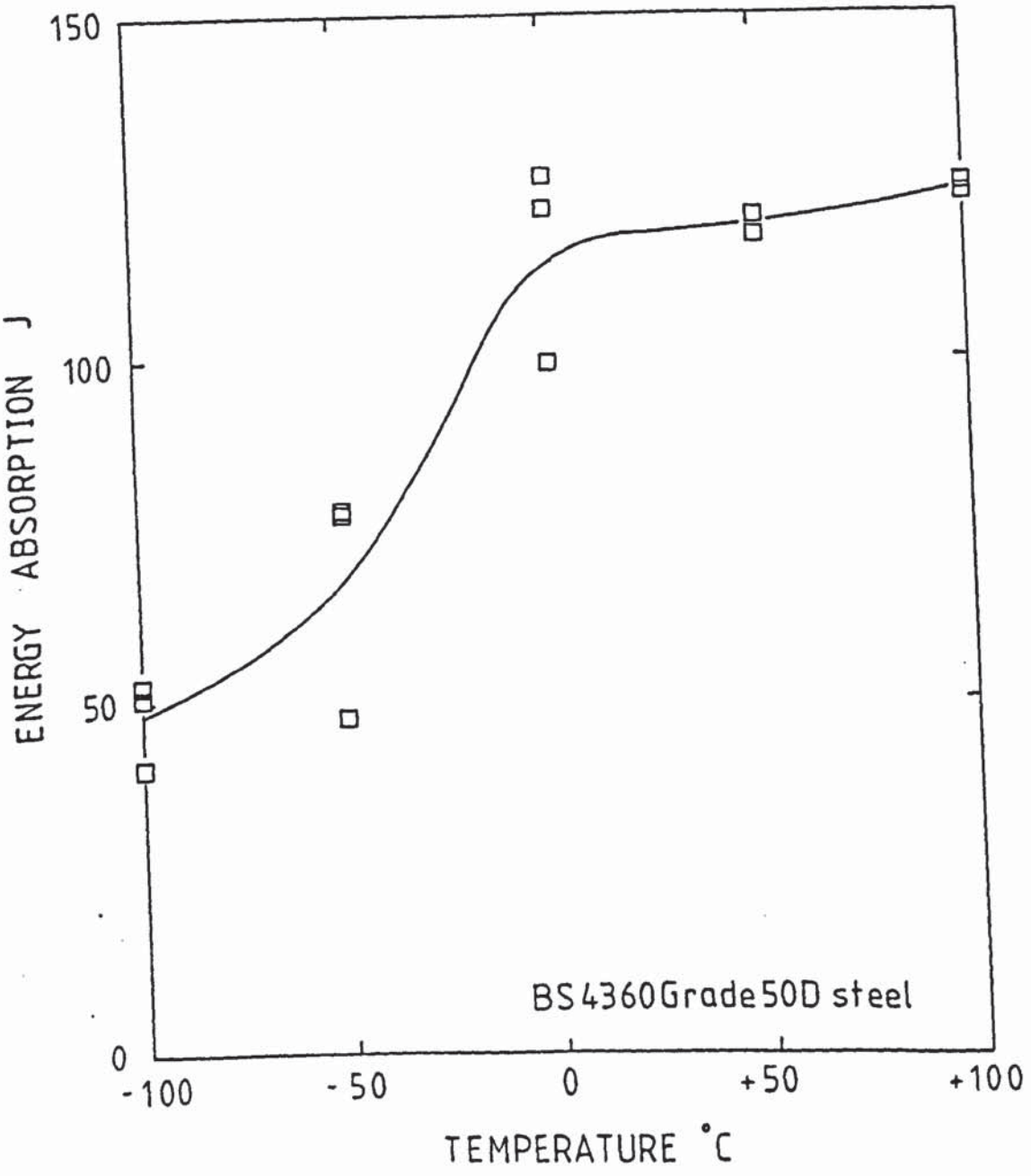

FIGURE 6.4 Energy transition with temperature for side-grooved Charpy V-notch impact tests

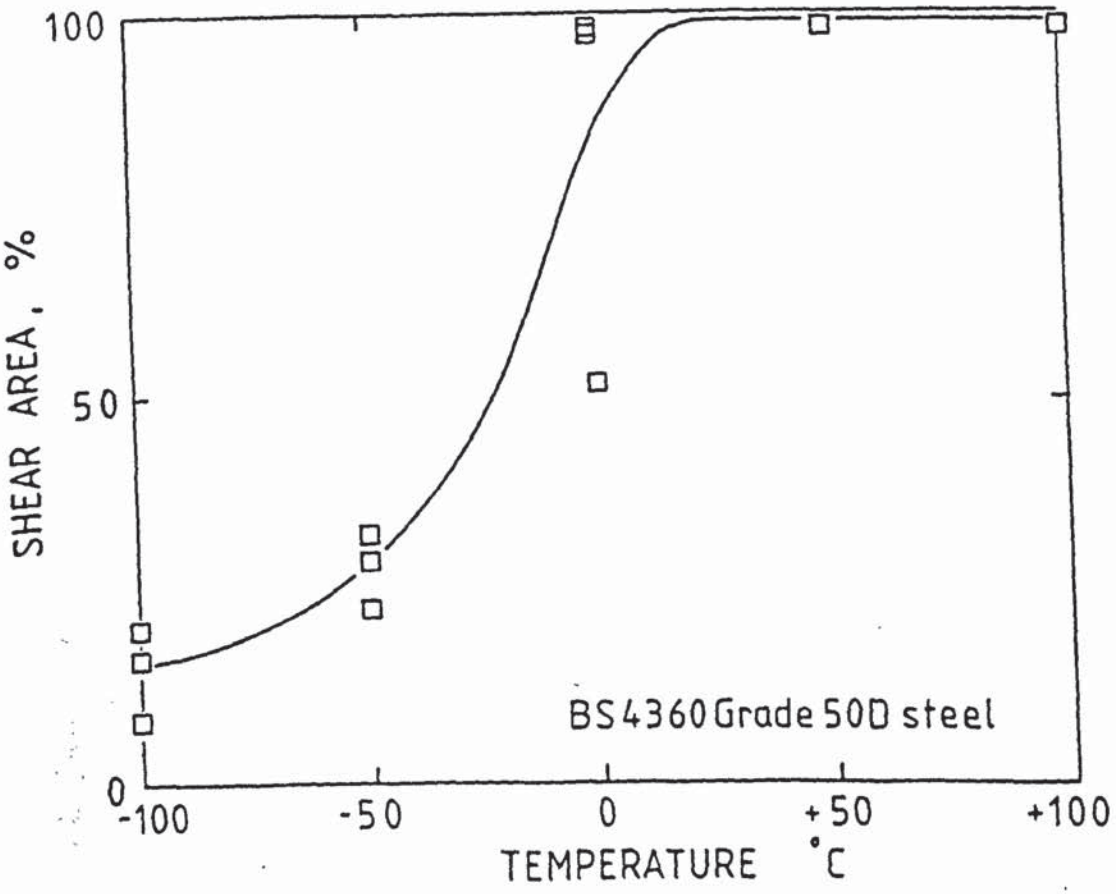

FIGURE 6.5 Fracture transition with temperature for side-grooved Charpy V-notch impact tests

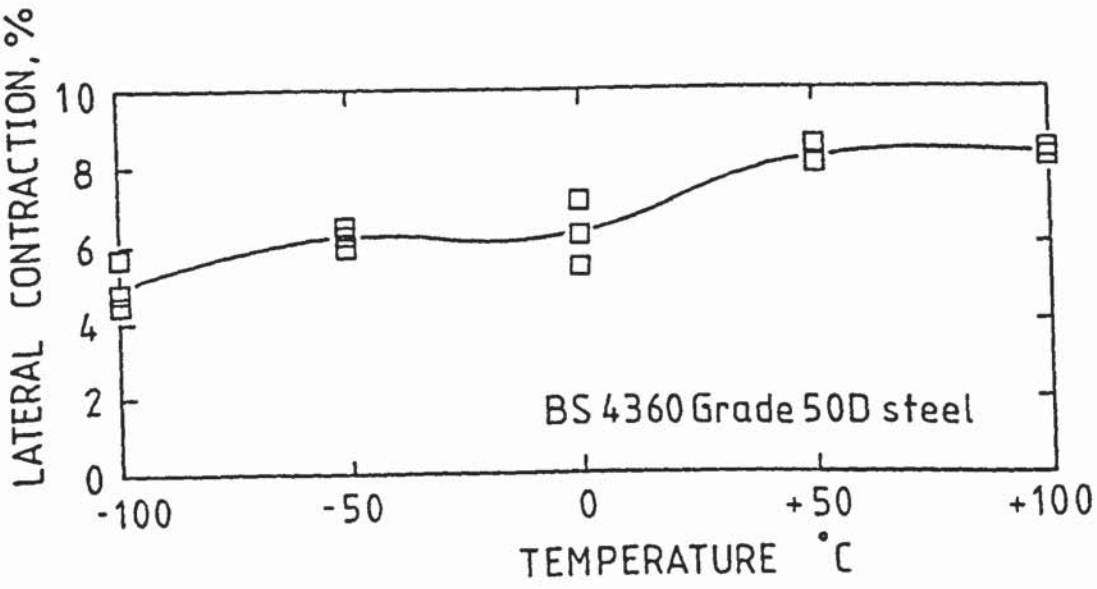

(a)

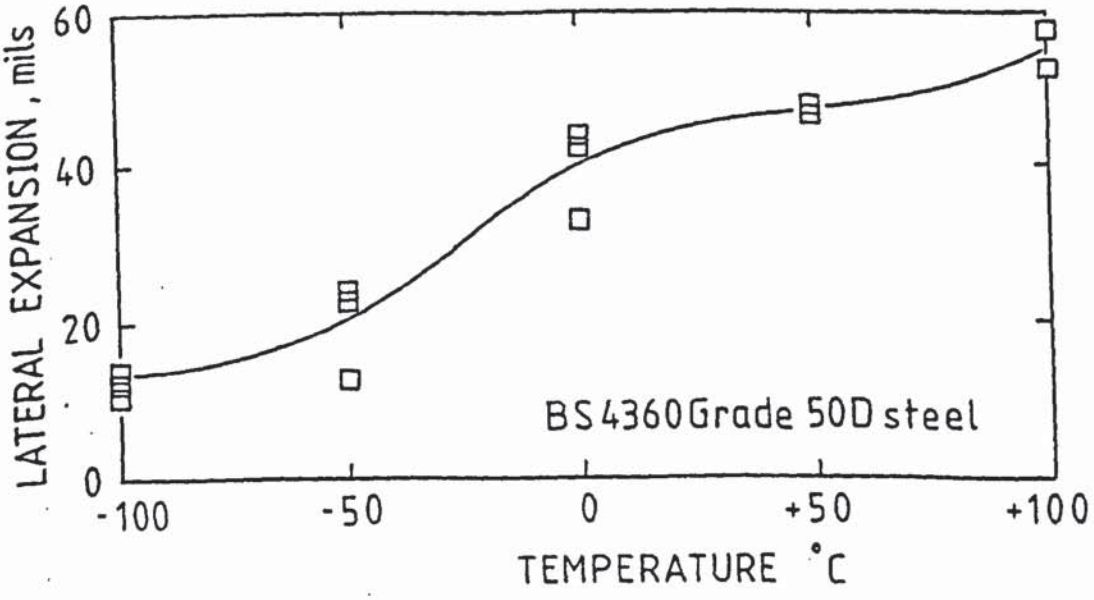

(b)

FIGURE 6.6 Ductility transition with temperature for side-grooved Charpy V-notch impact tests

ductile fracture appearance temperature are shifted to about-23°C and +20°C, separately. There is also a major reduction in upper shelf energy. Thus it is clear that the side-grooves cause the increase of the specimen constraint, subsequently shift the transition temperature to higher temperature.

In the upper shelf and transition temperature regions, the side-grooves make the energy absorbed in propagating a crack through the whole section of the specimen decreases. It might be thought that it is because the cross-section area in the side-grooved specimen is only 70% of that in the standard Charpy specimen. However, in the temperature near lower shelf no obvious change in the energy absorbed between side-grooved specimen and standard Charpy specimen has been found.

6.2 Slow Bend Charpy-Size Bar Testing

Common structural steels display the well-known ductile to brittle fracture transition with decreasing temperature, as discussed in the above impact testing. Various investigators have shown that there exists an important effect of specimen size and geometry on fracture toughness for structural steels in the ductile-brittle transition region. The elastic-plastic fracture toughness, evaluated from small specimens is often in excess of the scatter band of the linear elastic fracture toughness, evaluated from large or valid specimens [88]. Additionally, with decreasing specimen thickness, the

transition from cleavage to dimple fracture made is observed [89]. This is equivalent to a lowering of the ductile-brittle transition temperature with decreasing specimen thickness. This behaviour is usually explained in terms of a loss of constraint [90]. The loss of crack tip constraint explanation implies that small specimens cannot be used to characterize the toughness of large structural steel components in the transition region.

An alternative explanation for the size effect on fracture toughness has been advanced by Landes and Shaffer [14]. Due to the toughness nonuniformity in material, the fracture toughness of any specimen is controlled by the point or region of lowest toughness along the crack front. In a small specimen the amount of material adjacent to the crack tip is less than in a large specimen. Thus, small specimens, correspondingly, sample less of the variation in toughness and on the average should exhibit higher toughness. Using Weibull statistics Landes and Shaffer attempted to predict large specimen behaviour from small specimen tests.

This objective is to investigate the effect of side-grooves on the fracture behaviour of a C-Mn steel in the ductile-brittle transition region, using a CTOD evaluation method.

6.2.1 Experimental Procedure

Three kinds of Charpy-size specimens were used for investigating the ductile-brittle transition behaviour. They were nonside-grooved specimens, side-grooved specimens, and pre-cracked side-grooved specimens. It was found from measurement that all dimensions of the specimens were in the designed range. The crack length to width ratio was about 0.5 in the pre-cracked side-grooved specimens. Three-point bending test was carried out using a 5000 Kgf Instron testing machine at a loading rate of 0.05 cm/min. The tests were performed in the temperature range of -124^{o}C to room temperature in a specially designed cooler. Load was recorded versus load-point displacement. Then CTOD values were obtained from Eqs. (5.2), (5.3) and (5.12), which were established from the photographic calibration technique. The point of stable crack initiation was detected by an electrical potential method. Sectioned fracture surfaces of some specimens were examined under the scanning electron microscope. Void growth rate against COD was measured by the point counting technique.

6.2.1.1. Cooling Method

During three-point bending test, specimens were cooled with a specially designed cooler spraying liquid nitrogen, as shown in Fig. 6.7(a). In order to keep the specimen in a constant temperature, a simple automatic adjustment system was used, as shown in Fig. 6.8. Liquid nitrogen

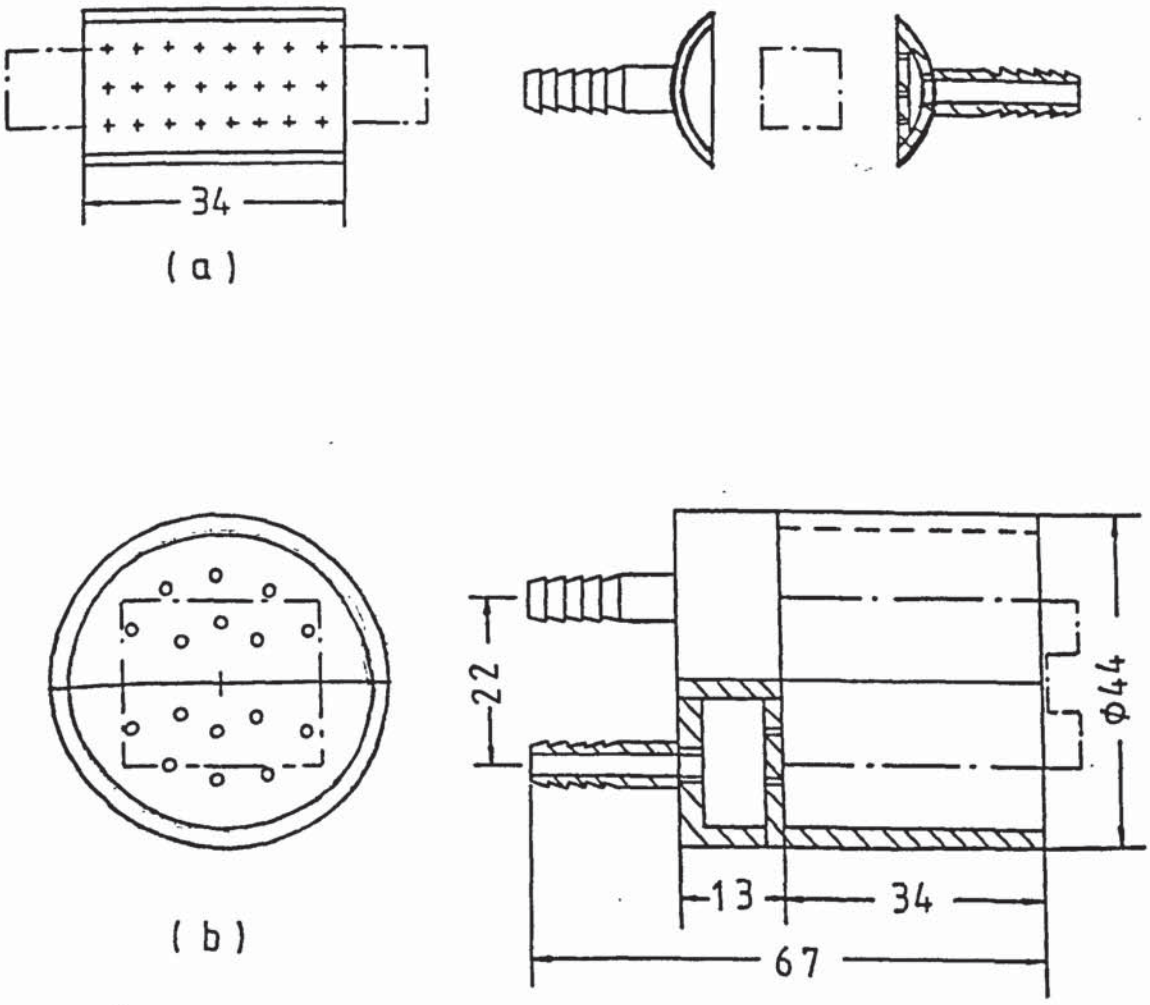

1 MATERIAL : BRASS
2 ALL JOINTS ARE WELDED BY Ag-Cu SOLDER
3 ALL DIMENSIONS ARE IN MM
4 SMALL HOLES : φ 1 MM

FIGURE 6.7 Cooler (a) for Charpy-size specimen; (b) for short bar specimen

FIGURE 6.8 : Measuring set-up for D.C.potential drop of the crack initiation and controlling set-up for cooling specimen. (1) specimen; (2) copper-constantan thermo-couple; (3) cooling jacket; (4) ETHER TRANSITROL Type No. 991; (5) electro-magnetic valve ASCO Model liquid nitrogen; (6) air pump MORRIS and INGRAM Model 662771; (7) foot-switch; (8) liquid nitrogen vessel KELVEN; (9) constant current power supply FARNELL Model H60/50; (10) D C potential drop vs time recorder TEKMAN TE 200; (11) D C voltage calibrator Type 2003S, 0.02% Grade; (12) temperature(mV) vs time recorder TEKMAN, SERIAL No.220A/126.

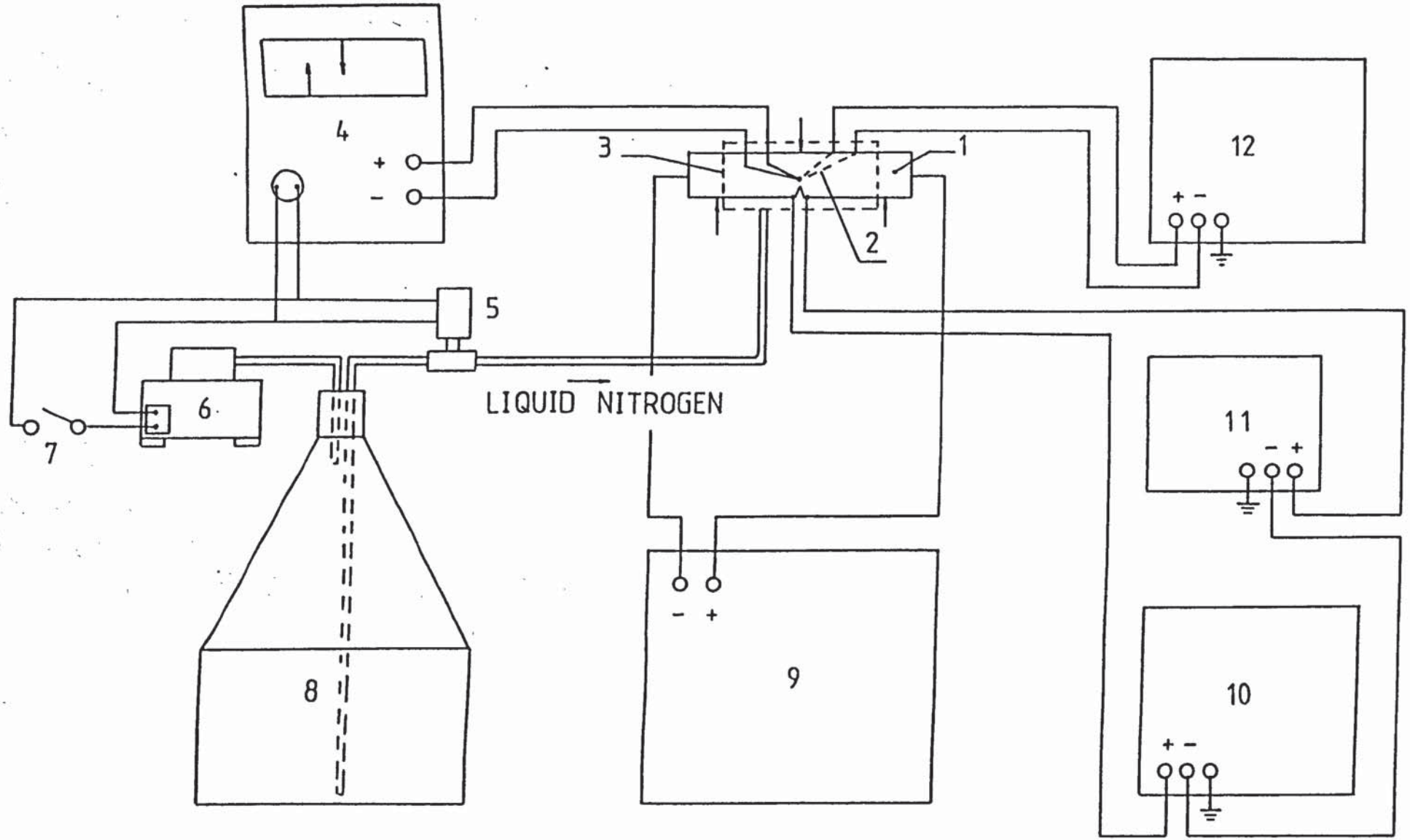

FIGURE 6.8

was stored in a Kelvin vessel. Due to the compressed-air pressure, liquid nitrogen passed through nylon tube, electromagnetic valve and cooling jacket, finally sprayed toward the specimen. The specimen temperature was monitored by a copper-constantan thermo-couple of 0.2 mm diameter, which was spot-welded in the range of 2 mm far from the edge at the open end of the notch. When the specimen temperature was lower than the temperature required or pre-set during spraying liquid nitrogen, the automatic temperature controller Ether Transitrol acted. Then the electromagnetic valve and small air compressor were shut down. Subsequently, the spraying liquid nitrogen stopped. In this period, the specimen temperature started to increase because of the heat exchange between the specimen and ambient (specially, clad copper clamps for the D.C. potential drop technique and bend test fixture). When the specimen temperature was higher than the pre-set temperature by a certain deviation, the automatic temperature controller acted. Then the electromagnetic valve was switched on and spraying liquid nitrogen started again. Meanwhile, the air compressor was switched on and started to pump air into the liquid nitrogen vessel. This process would carry on repeatedly.

In the initial stages of this cooling process, the recorded temperature fluctuation of the specimen was quite large. However, a dynamic equilibrium condition with very small temperature fluctuation could be attained in about 20 minutes. Usually, the temperature deviation of the

specimen was about ±1°C at the lowest testing temperature of -124°C. In this equilibrium condition, the specimen was begun to load.

6.2.1.2. Evaluation of Certain Values of the CTOD

BS5762 identifies four possible points on load versus load-point displacement records which may be taken as measurement points.

If a cleavage crack initiates and leads to complete failure of the specimen, or to an arrested brittle crack or pop-in, the CTOD is defined as δ_c. The behaviour subsequent to pop-in is related to the suddenly propagated crack. In the instant of crack extension the load must drop with an audible "pop", because a finite time is required to accelerate the testing machine ram and the specimen bars. For ductile materials, records may be obtained with the load passing through a smooth maximum value. The CTOD at which slow crack growth initiates is defined as δ_i, and that at first attainment of maximum load plateau as δ_m. Sometimes, cleavage instability may be preceded by stable tearing. In this case, the CTOD at tear initiation is also δ_i, but the CTOD at cleavage instability is defined as δ_u.

Although easy to measure, δ_m can be varied by altering the specimen dimensions. This is because δ_m refers to the instability in a generally yielded specimen, which has occurred after some crack growth. This can lead to

an apparent excessive fracture toughness value, if the ductile crack growth is not recognised. Furthermore, the instability in the specimens with the different size or geometry may occur after the different amount of crack growth. For example, side grooves may be used to promote instability at crack initiation [12]. A more consistent CTOD value is that at the initiation of fracture, δ_i, which is independent of specimen geometry and can be related to the microstructure behaviour of the material [21]. However, the Welding Institute [91] has for a number of years held that the use of δ_i is unnecessarily conservative and it has almost invariably been Institute practice to use δ_u or δ_m, based on experience with large scale tests rather than on any rigorous analysis.

In this work, all the four possible points on the load versus load-point displacement records for most of the specimens tested were reported.

6.2.1.3 Detection of Slow Crack Initiation Using an Electrical Potential Method

There are now available several techniques for detecting the initiation point, when a crack starts to grow by ductile mechanisms. In general, for ductile materials, it is better to determine the initiation toughness from a resistance curve generated from a number of specimens

loaded to produce different amounts of crack extension by extrapolating the data to zero crack growth. However, the waste of specimens is considerable, specially if the ductile-brittle transition of a structural steel is investigated.

The use of the electrical potential method is successful to fatigue investigations and to linear elastic fracture mechanics tests in which fracture occurs when small notch tip strains and displacements are attained. These small displacements are not expected to influence the potential fields. However, the electrical potential method has still been reported to monitor the initiation point during the COD tests [22, 23]. In this case, the greater displacement, even in the absence of ductile tearing, may influence the potential field because of the effective change in geometry of the specimen. The problem centres around how to distinguish the effect of crack extension from plastic zone effect on the potential change. In this experimental work, the following procedure was used.

A direct current of 20 Amp was passed through the test specimen using clad copper clamps for electrical connection at the both ends. The potential pick-up leads of 0.006" Nichrome wires were spot-welded in the middle of the specimen thickness and on the edges at the open end of the notch. The initial potential voltage of the notched specimen was balanced to zero or near zero by an accurate potential source, D.C. Voltage Calibrator Type 2003S,

0.02% Grade. The small voltage changes due to plastic deformation or crack growth were amplified and recorded by a time base chart plotter, TEKMAN TE200. Fig. 6.8 shows a set-up used for the electrical potential drop measurement.

All the plots of potential change against time in the nonside-grooved specimens are of the form exemplified in Fig. 6.9(a). The figure shows an initial linear change in potential (BC). Thereafter the potential changes at an increasing rate (CD). A specimen was unloaded just beyond the deviation from linearity (point C), and heat-tinted (400°C for 2 hr.), subsequently, fractured at -196°C. The specimen showed evidence of small ductile tears. The maximum tear length observed was less than 0.1 mm. If the potential starts to deviate the linear BC or its extension line, it is assumed that this deviation position corresponds to the crack initiation point. Because there is no sharp deviation on the potential trace in the blunting notched specimens, the difficulty of obtaining an unambiguous value of δ_i is apparent. The other possible reason generating measurement error is related to the test temperatures. On the basis of the information obtained in this investigation, it is apparent that the potential drop decreases with decreasing the test temperature. Therefore, the same significant deviation from linearity at the different test temperatures may represent the different crack lengths.

The above procedure may be a reference to detect slow

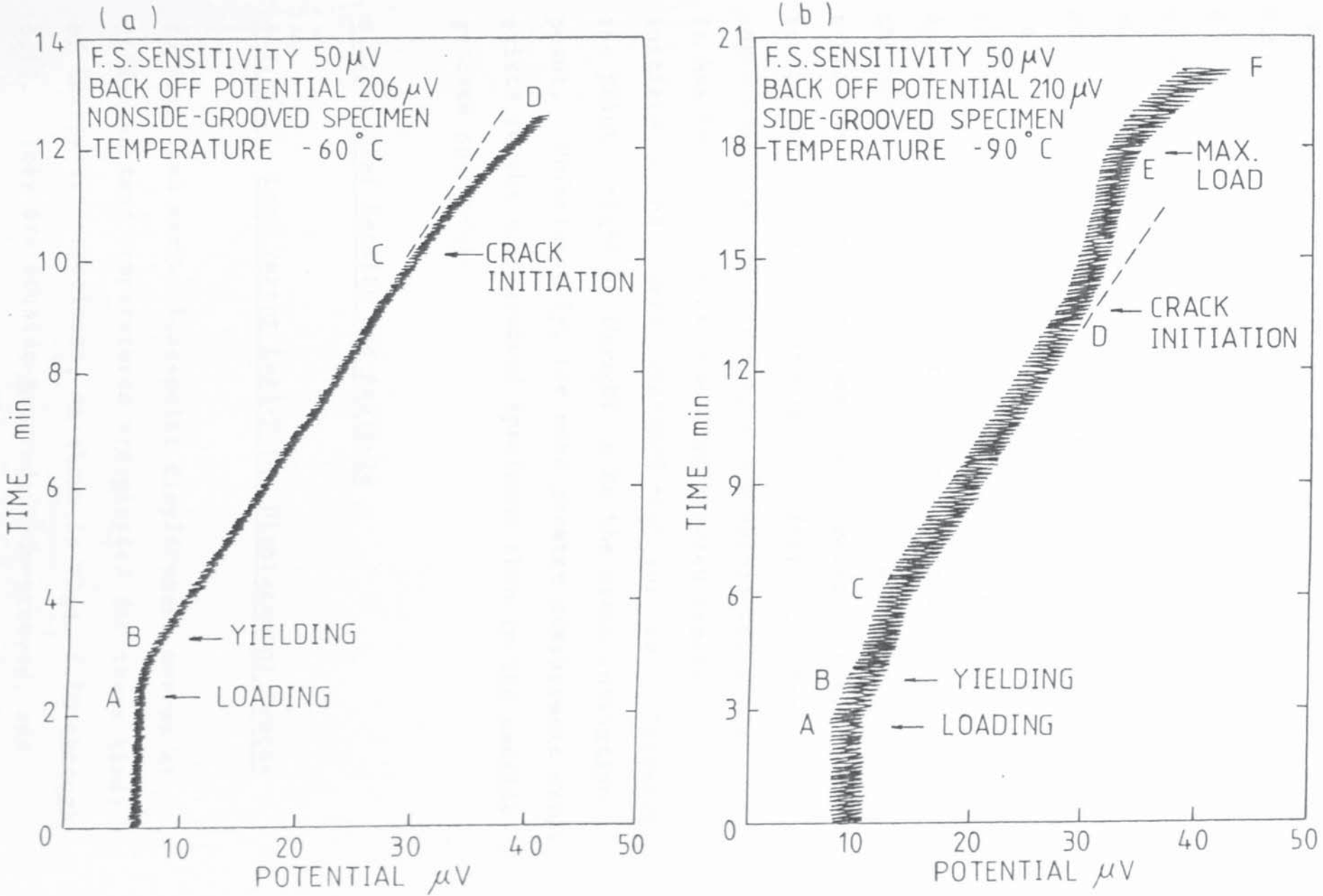

FIGURE 6.9 Typical electrical potential traces showing crack initiation

crack initiation in the side-grooved specimen. A typical electrical potential trace is shown in Fig. 6.9(b). During three-point bending test, the side-grooves on the compressed part of the specimen will close up gradually with loading. It may counteract the potential rise caused by the plastic deformation or crack growth ahead of the notch root. However, there is a relative linearity part (CD) in the recording trace. Thereafter, the potential changes at a decreasing rate until point E, which corresponds to the maximum load. About half of the total specimens tested were interrupted just beyond point D, where linear trace begins to incline. After unloading, the notch roots were observed by a 5 x magnifying glass. It has been found that some disconnected cracks initiate on the severe stretched root surface. Therefore, the point D might be thought to be the crack initiation point. Unfortunately, the more greater measurement error exists in the side-grooved specimens than in the nonside-grooved specimens.

6.2.2 Test Results and Analysis

6.2.2.1. Load versus Load-Point Displacement Traces

Typical load versus load-point displacement curves at different test temperatures are plotted for three kinds of Charpy-size specimens, as shown in Figs. 6.10 through 6.12. They are nonside-grooved, side-grooved, and

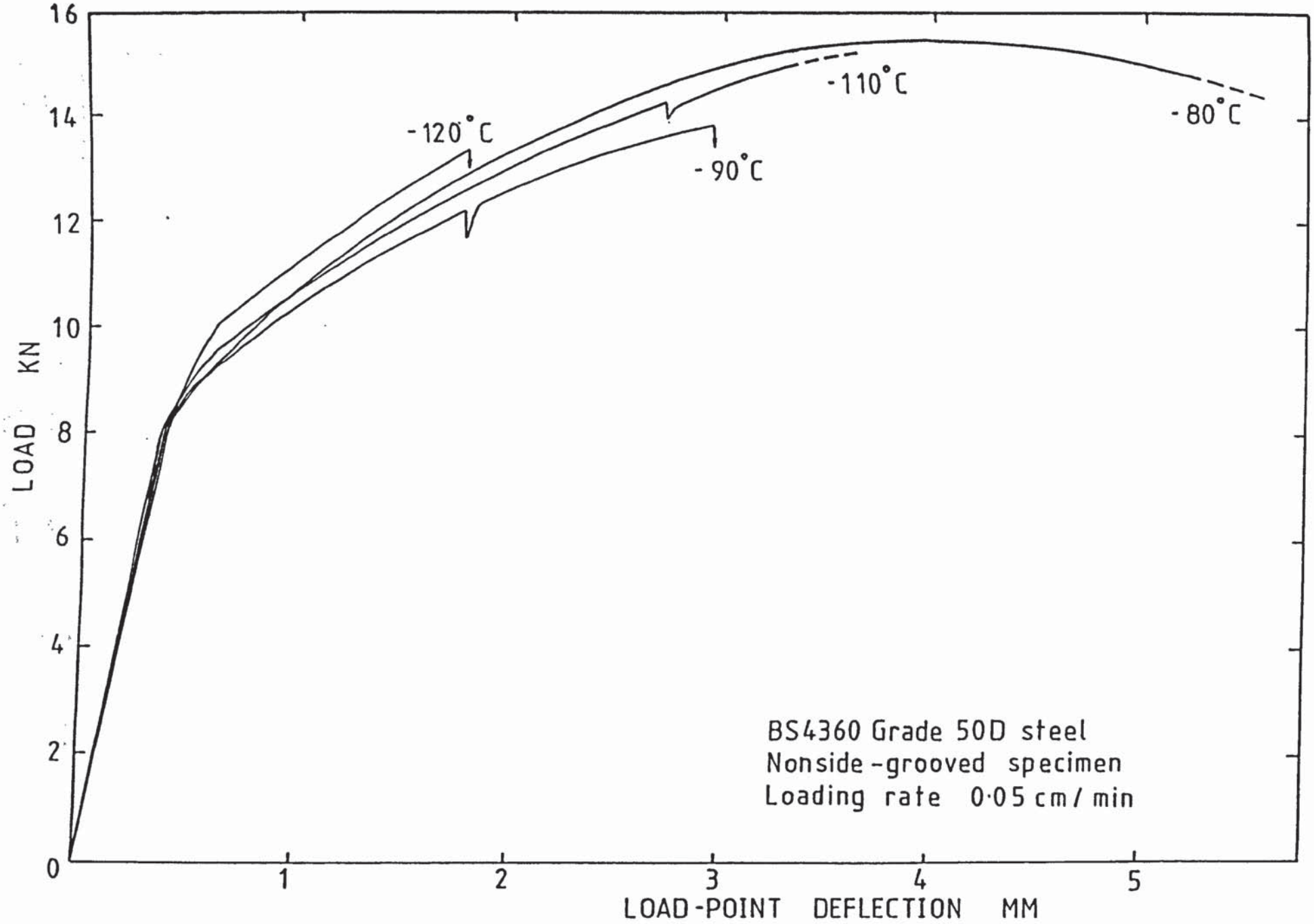

FIGURE 6.10 Load versus load-point displacement of nonside-grooved Charpy specimen

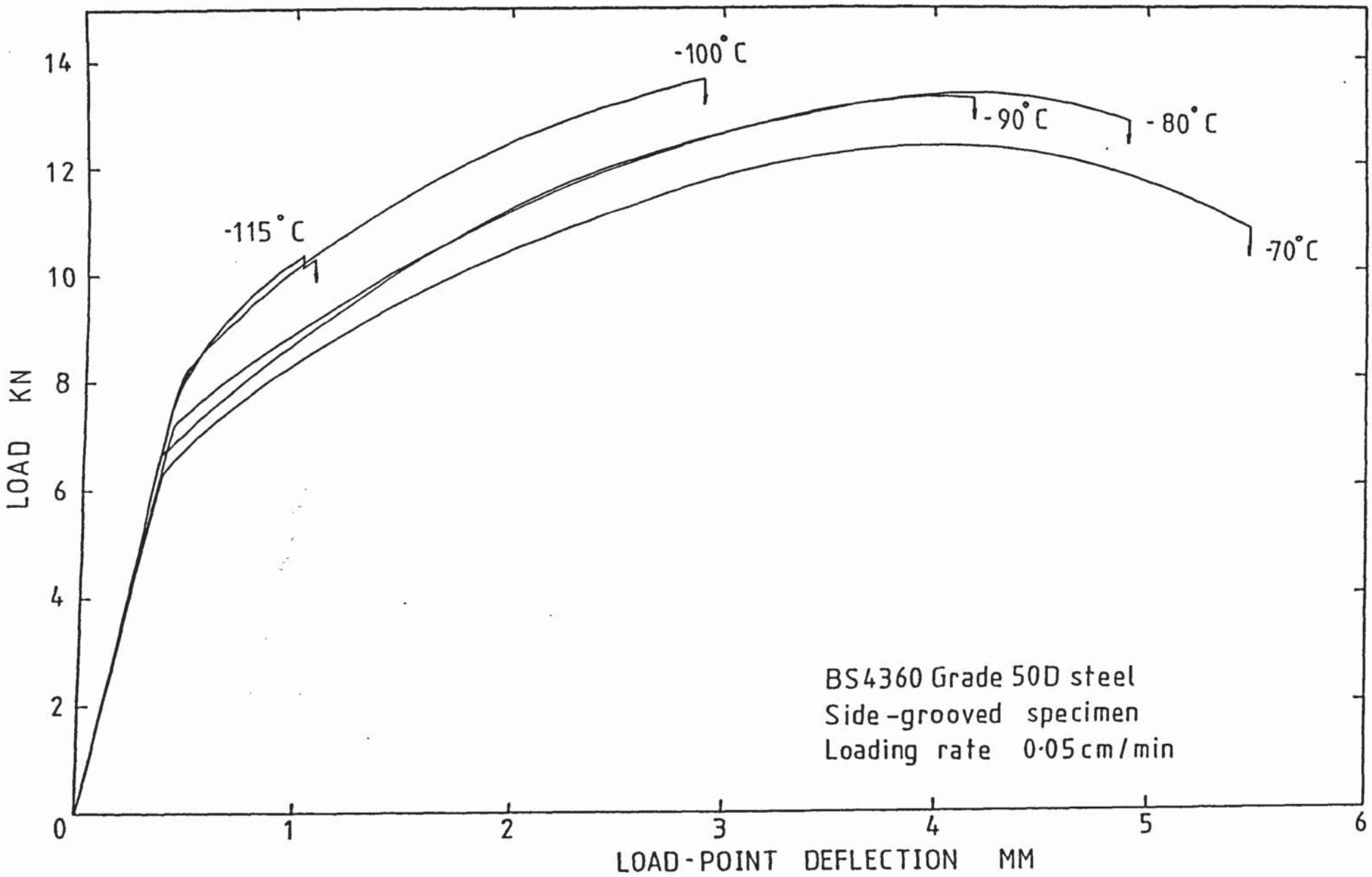

FIGURE 6.11 Load versus load-point displacement of side-grooved Charpy specimen

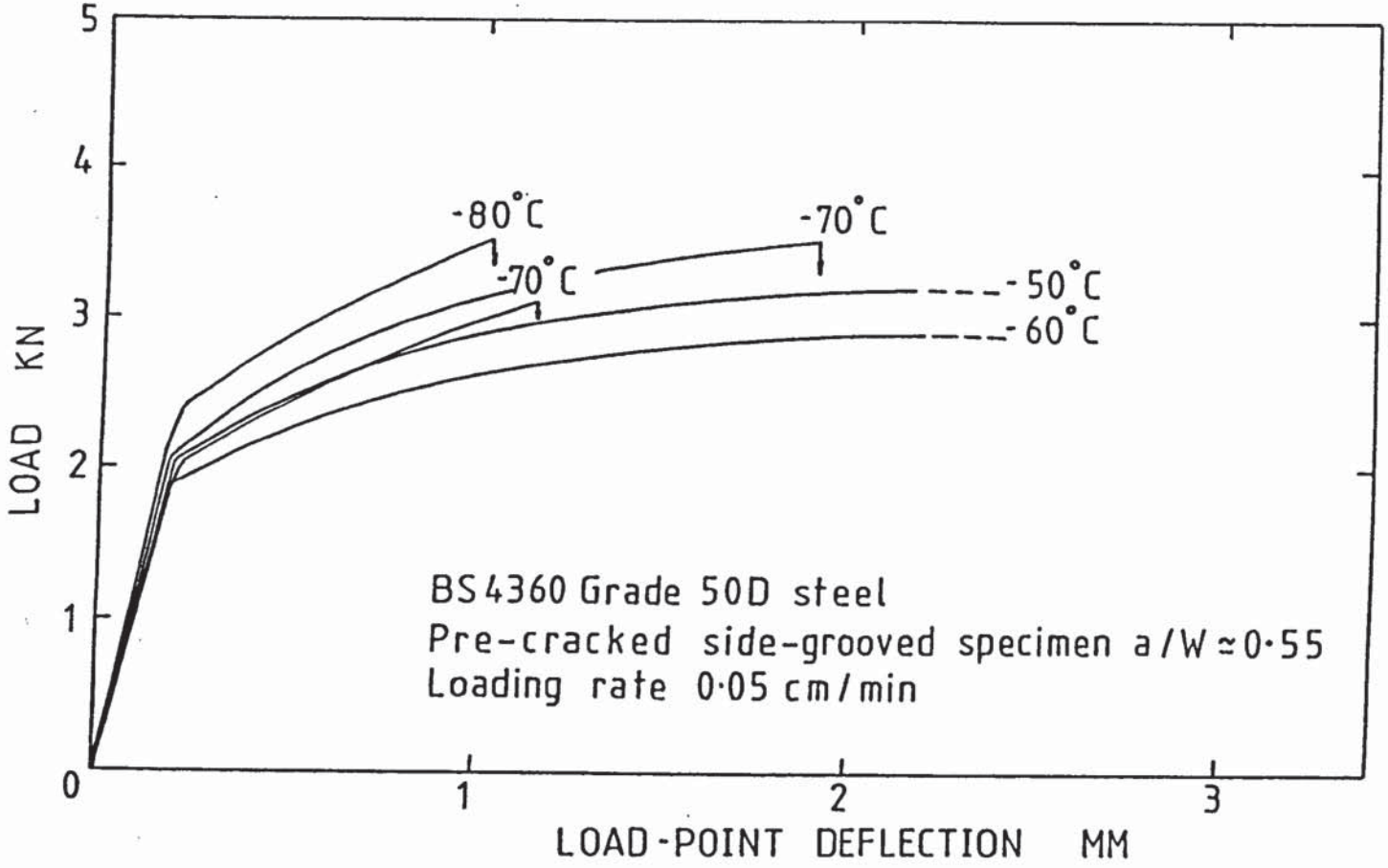

FIGURE 6.12 Load versus load-point displacement of pre-crackedside-grooved Charpy specimens

precracked side-grooved specimens.

After an initial linear region a deviation from linearity was observed. This non-linearity was caused by plastic deformation or stable crack extension. Dependent on temperature and specimen geometry, pop-in, complete fracture or continuous slow crack growth occurred. After reaching maximum load, the specimen fractured completely, or the crack arrested after some load drop, or slow crack continued extending to form a parabolic curve.

From the observation of the obtained traces, it was clear that the load versus load-point displacement traces of side-grooved specimens were below that of nonside-grooved specimens. Furthermore, the traces of precracked side-grooved specimens were much more below that of side-grooved specimens. It seems to exhibit the change of the load-bearing capacity due to different ligaments of specimens. There is the smallest ligament in pre-cracked specimen among the three kinds of Charpy-size specimens, thus it has the lowest load-bearing capacity.

For each kind of specimen, usually,the lower the test temperatures were, the higher the recording traces and deviation points from linearity were. The load corresponding to the deviation point is also named as general yielding load. In the condition of a constant

specimen geometry and loading arrangement, the general yielding load is only related to the yielding strength of the materials [92]. Because the yielding strength increases with decreasing test temperature, the change of the general yielding load with temperature leads to the change of the trace position.

Before reaching maximum load, the specimens may fracture completely or generate a rapid crack extension arrested after a large load drop. These fracture or part fracture might occur at the temperatures below -90°C for both nonside- and side-grooved specimens. All the side-grooved specimens, tested at the temperatures below -60°C, exhibited rapid crack extension with a sudden fracture after reaching maximum load, if the specimens preceded by stable crack extension did not fracture before reaching maximum load. This was because the crack front entered a more severe constraint region of the tapered side-grooves as the stable crack grows. It has demonstrated that an increase in the stress triaxiality local to the growing crack tip leads to a transition to cleavage fracture after some amount of ductile crack extension. If the test temperatures were above -60°C for side-grooved specimens or -80°C for nonside-grooved specimens, a large load-point deflection would be generated during the three-point bending tests. It was not found that the rapid crack extension occurred after reaching maximum load within maximum deflection of 5.5 mm allowanced by the loading fixture. Therefore, at the higher test temperature, it

is difficult for nonside- and side-grooved specimens to attain the stress triaxiality sufficient to cause the transition from a stable to a rapid crack growth.

Pop-in often occurred at the temperatures below -90°C for the standard CVN specimens, and -100°C for the side-grooved CVN specimens. Sometimes, several times of pop-in occurred in one stable crack extension process until reaching maximum load. Usually, pop-in in each time only causes a small load drop of about 400N, which is corresponding to be less than 4% of current load. It may be noted that for the short rod tests a Terra Tek Manual [95] stipulates that sudden crack advances which are accompanied by a load drop of less than 2% are not considered as crack jumps. However, similar stipulation has not been found in the CTOD testing standards. In the temperature range investigated, pop-in did not occur in pre-cracked side-grooved specimens.

At the test temperatures above -60°C, fracture or part fracture of the pre-cracked side-grooved specimens did not occur before reaching maximum load. It has been found that the initiation point of slow crack growth approaches maximum load or fracture instability. In this case the fibrous tear, initiated as a thumbnail crack in the region of maximum constraint at centre thickness, becomes less retarded by the plane stress side ligaments at the near lateral surfaces.

6.2.2.2 Ductile-Brittle Transitions

In order to evaluate the CTOD values on the load versus load-point displacement traces, it was decided to use the fitted equations (5.2), (5.3), and (5.12) of CTOD against the load-point deflection.

The question is as to whether these equations are still available at the low temperature. If it is assumed that the elastic modulus and Poisson's ratio of material do not change with temperature, thus the fitted equations can be used for all the test temperatures. There is evidence in Figs. 6.10 and 6.11 that the slopes of the linearity basically are constant at different test temperatures. The different slopes in Fig. 6.12 are due to different initial crack lengths.

Using those equations, four possible CTOD values on the load versus load-point displacement traces were obtained and given in Tables 6.3 through 6.5 for three kinds of specimens, separately. Additionally, the critical CTOD values are plotted as a function of temperature in Figs. 6.13 and 6.14. As would be expected, the general effects of temperature on critical CTOD values is similar to the effects of same conditions on CVN test results. That is, increasing the temperature increases critical CTOD values. For the pre-cracked side-grooved specimens, the tests have indicated very good repeatability at each test temperature. However, for the V-notch specimens

Table 6.3 : Slow-bend CTOD test results for nonside-grooved Charpy specimens

Specimen number	Test Temperature °C	CTOD, mm			
		δc	δi	δu	δm
B3	+17				1.068
B28	-12		0.522		
B47	-32		0.462		
B46	-56		0.512		
112	-60		0.597		0.793
109	-60		0.548		0.861
108	-70		0.497		0.698
110	-80		0.510		0.749
B50	-80		0.543		
105	-90	0.216			
B31	-91	0.126			
B35	-92	0.068			
B39	-110	0.389			
106	-110		0.450		
104	-120	0.121		0.746	
107	-120	0.219			

a. BS4360 Grade 50D normalized steel; plate number 2A52-1

b. δc, δi, δu, δm - as defined in BS5762:1979

c. δ values were determined by a photographic calibration technique

Table 6.4 : Slow-bend CTOD test results for side-grooved Charpy specimens

Specimen No.	Test Temperature °C	CTOD, mm			
		δc	δi	δu	δm
S2	+19				1.085
S1	+17				1.055
S32	-32		0.458		
S34	-64		0.528		
S26	-70		0.484		0.924
S20	-80		0.479		1.017
S14	-80		0.519		
S15	-80		0.447		0.928
S16	-90		0.553	0.928	
S21	-90		0.498		0.901
S23	-90		0.484	0.573	
S52	-90		0.447		0.700
S53	-90			0.611	
S35	-98		0.453		
S50	-100		0.492	0.506	
S54	-100	0.134			
S55	-100		0.450		0.882
S24	-113	0.258			
S12	-114		0.471		
S31	-114		0.428		
S10	-115	0.107			
S11	-124		0.466		0.863

a. BS4360 Grade 50D normalized steel; plate number 2A52-1,

b. δc, δi, δu, δm - as defined in BS5762:1979,

c. δ values were determined by a photographic calibration technique

Table 6.5 : Slow-bend CTOD test results for pre-cracked side-grooved Charpy specimens

Specimen number	Test Temperature ^{o}C	CTOD, mm			$\frac{a}{w}$
		δc	δi	δm	
S17	+14			0.468	0.546
S19	+12			0.424	0.587
S18	-50		0.434	0.434	0.587
S48	-50		0.451	0.451	0.531
S46	-60		0.439	0.439	0.531
S47	-70	0.407			0.542
S44	-70	0.227			0.528
S45	-80	0.198			0.518

a. BS4360 Grade 50D normalized steel; plate number 2A52-1

b. δc, δi, δu, δm - as defined in BS5762:1979

c. δ values were determined by a photographic calibration technique

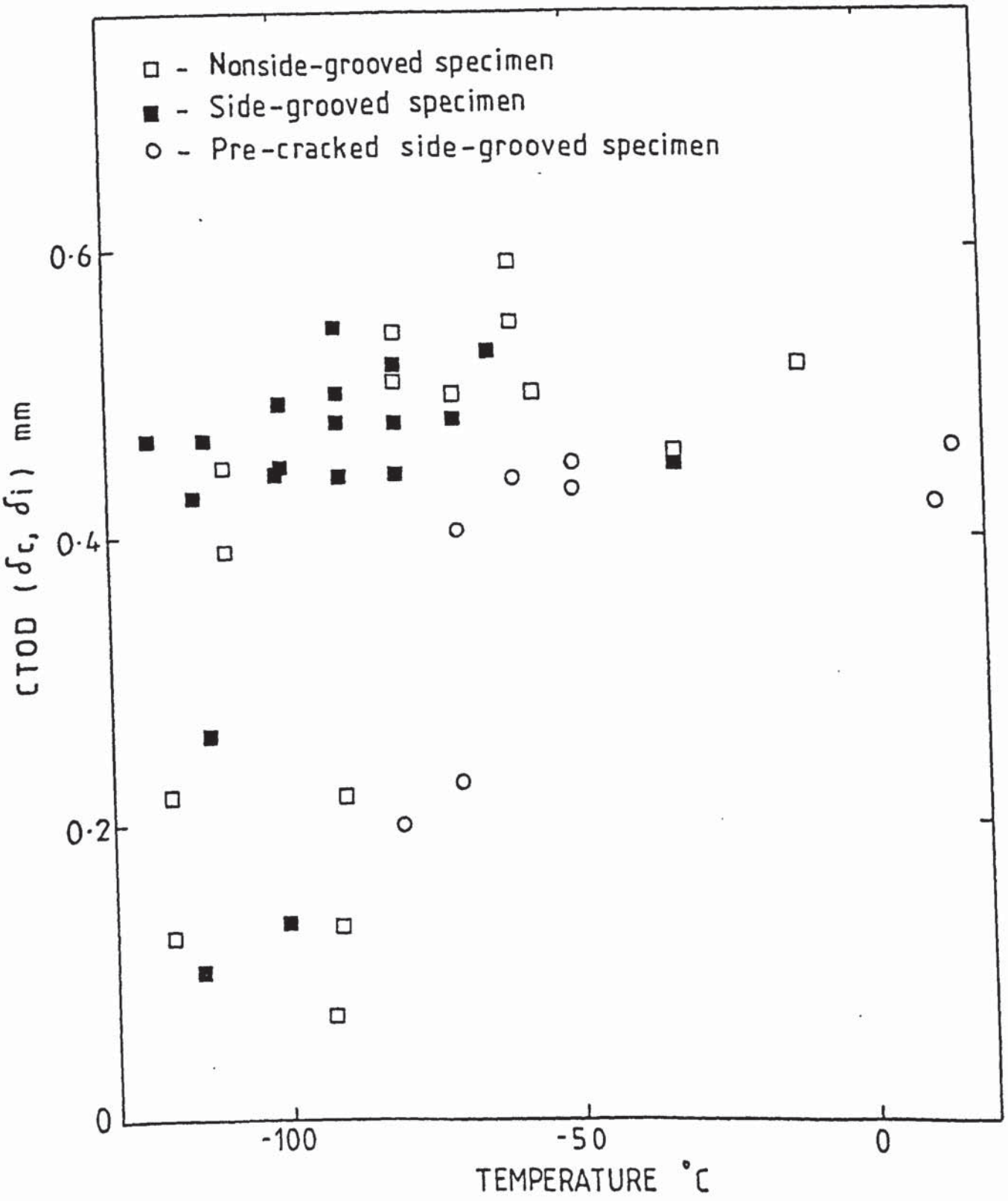

FIGURE 6.13 CTOD ($^{\delta}c$, $^{\delta}i$) ductile-brittle transitions for three kinds of Charpy-size specimens

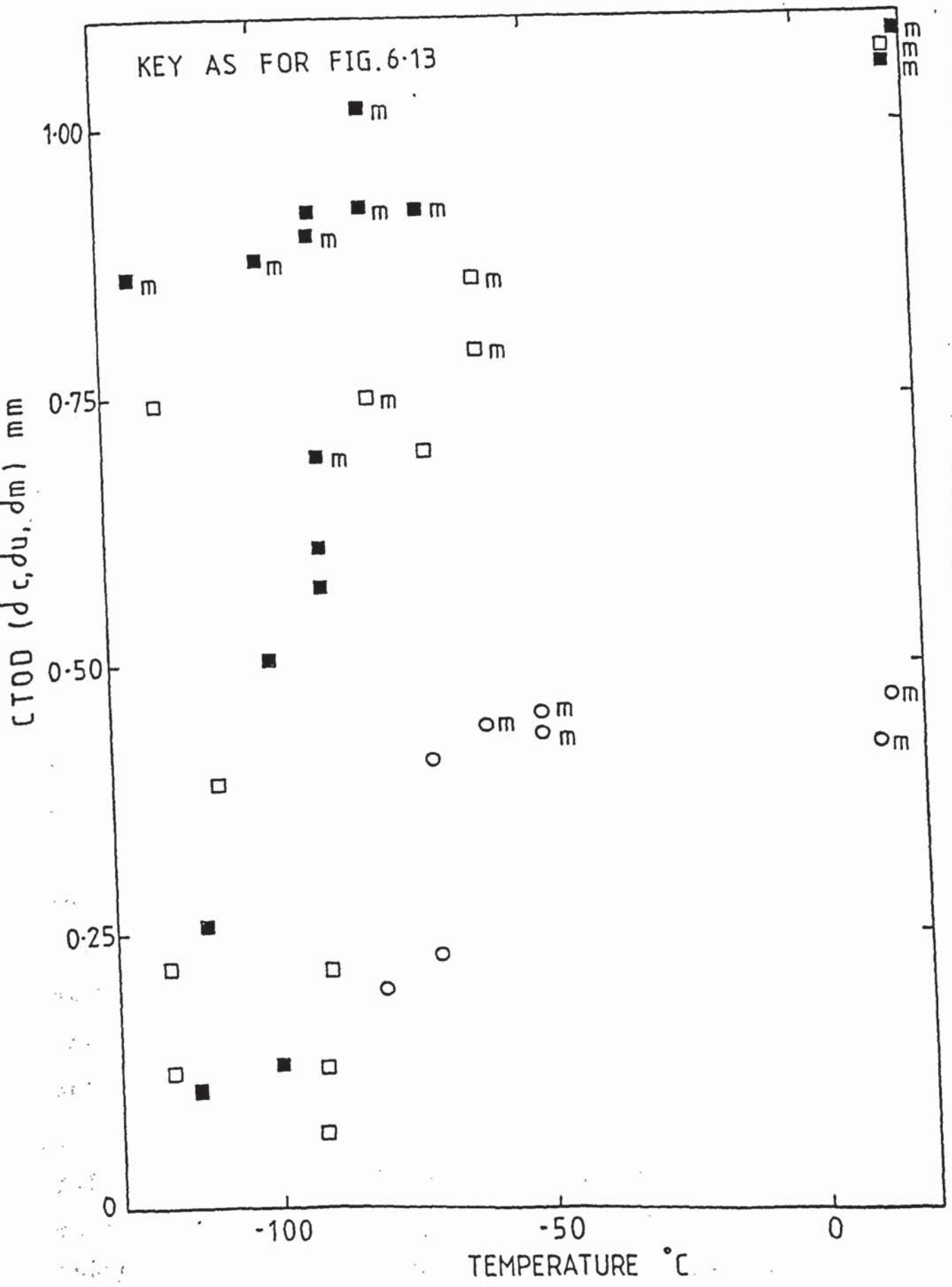

FIGURE 6.14 CTOD ($^{\delta}c, ^{\delta}u, ^{\delta}m$) ductile-brittle transitions for three kinds of Charpy-size specimens (Subscript m denotes $^{\delta}m$ value)

(nonside- or side-grooved) the test results in the transition region have shown a rather large scatter, specially if the δ_c and δ_i values are used to evaluate the toughness transition behaviour.

As shown in most of the literatures, usually the transition temperature increases, if the constraint in the test specimens is higher. According to the evaluation procedure, discussed in Section 5, the constraint factors ahead of the notch or crack tip are 0.95 for nonside-grooved specimen, 1.20 for side-grooved specimen, and 6.04 for pre-cracked side-grooved specimen at room temperature. It is clear in Fig. 6.13 that the transition temperature is higher in pre-cracked specimens than in two kinds of notched specimens. However, among the two kinds of notched specimens, the transition temperature seems to be less clear, even though the side-grooved CVN specimens show a rather high transition temperature during impact tests. Additionally, CTOD corresponding to the initiation of ductile tearing has been found to be relatively unaffected by the constraint of the specimens at the upper shelf temperature, except that there are a slightly lower δ_i values in pre-cracked side-grooved specimens.

A final point concerns the effect of specimen geometry on the values of maximum load CTOD measured on the upper shelf. Usually, a specimen with a small ligament tends to be smaller CTOD at collapse. For instance, the smallest CTOD at collapse occurred in pre-cracked side-

grooved specimens. In the case of the notched specimens, both nonside- and side-grooved specimens have the almost same δ_m at room temperature. However, in the transition region, there are higher δ_m values in side-grooved specimens. This can also be seen from the change of the load-point displacement corresponding to maximum load, when the specimens are tested in bending at different temperatures. As shown in Table 6.6, deflections corresponding to maximum load in the two kinds of notched specimens decrease with temperature. However, the deflection in nonside-grooved specimens decreases much rapidly than in side-grooved specimens. It is indicated that at low temperature the local strain becomes less important factor to control the failure process.

6.2.2.3 Metallographic Examination

Just after initiation of the fibrous tear, the specimen was unloaded and the notch root or pre-crack tip was examined by a magnifying glass, as shown in Plate 6.3. There were several crack initiation places along the notch root or crack tip in each specimen. These initiations basically were uniformly distributed in the thickness of the specimen, except the two ends of the notch root front. However, in pre-cracked side-grooved specimen, sometimes, the initiation occurred at the corners of the intersection of the pre-crack front and side-groove roots. The reason why the initiations could be directly observed by the magnifying glass on the notch root is the general

Table 6.6 : Deflections corresponding to maximum load versus test temperature

Test temperature ^{o}C		+19	+17	-60	-70	-80	-90	-100	-124
Load-point deflection, mm	Nonside-grooved specimen	-	4.92	4.21 4.40	3.92	4.08	-	-	-
	Side-grooved specimen	4.55	4.48	-	4.16	4.17, 4.39	3.53, 4.10	4.05	4.00

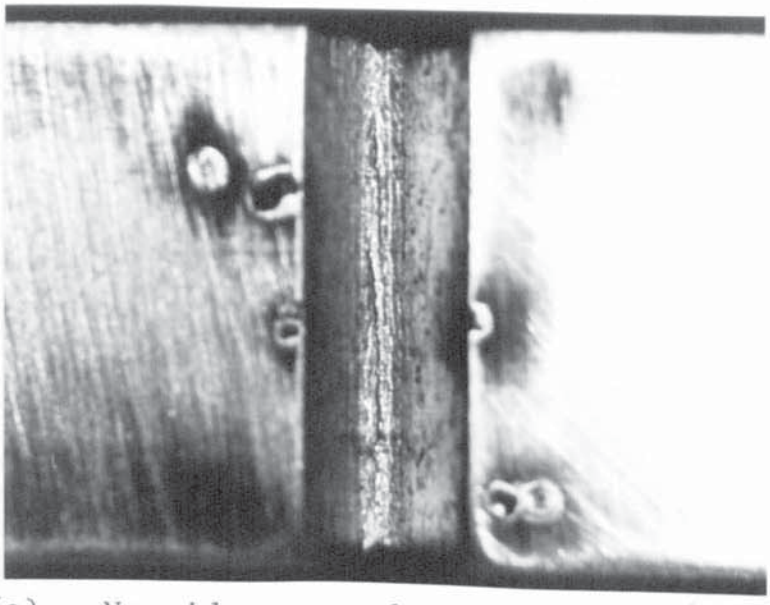

(a) : Nonside-grooved specimen, -80°C

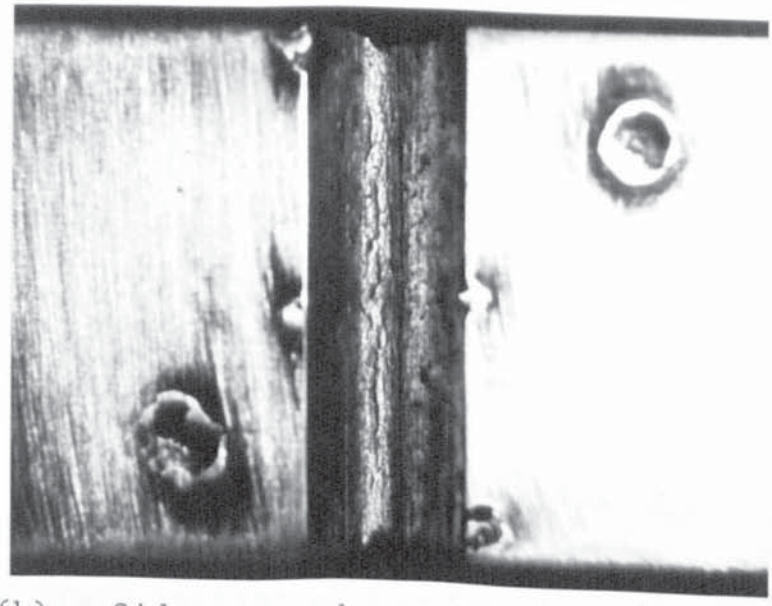

(b) : Side-grooved specimen, - 98°C

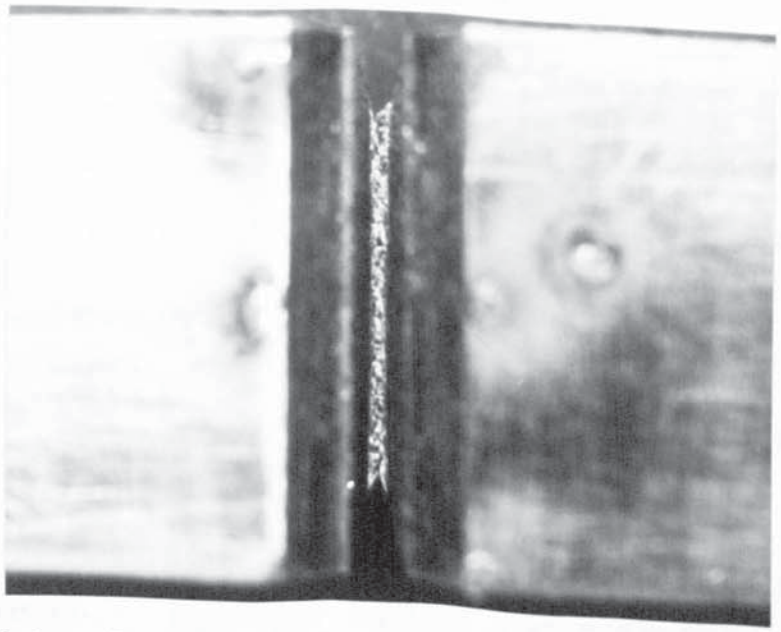

(c) : Pre-cracked side-grooved specimen, -50°C

Plate 6.3 : Tearing initiations observed on the blunted notch - or precrack tip (7x).

yielding of the specimens. In this case, the crack faces could not be completely closed after unloading.

The fracture appearance is mainly dependent on the test temperature in the Charpy-size specimens of mild steel. Additionally, the appearance is also related to the specimen geometry. The general characteristics of the fracture appearance in the transition temperature is shown in Plate 6.4. The failure process consists of the stretched zone, stable crack extension and unstable cleavage fracture. It has been found that some individual voids are distributed in the cleavage fracture region in the specimens with stable crack extension. This is due to yielding on the gross section of the specimens before the cleavage fracture. The stretched zone is caused by plastic shear deformation of the material in the plastic zone, and separated along 45^{o} to the crack-advancing direction. The shear deformation and subsequently tearing crack initiation may be also clearly seen in Plates 5.4 and 5.10 for photographic calibration in Section 5. In this case the stretch zone formed is very similar to the shear lips formed at the free side surfaces of the fractured specimen, and it is a part of new crack surfaces by ductile crack growth.

Plate 6.5 shows typical feature of the stretch zone in the notched and pre-cracked specimens. The stretch zone widths in these specimens were measured under scanning electron microscope. Measured values are listed in Table 6.7. The widths against the test temperature are

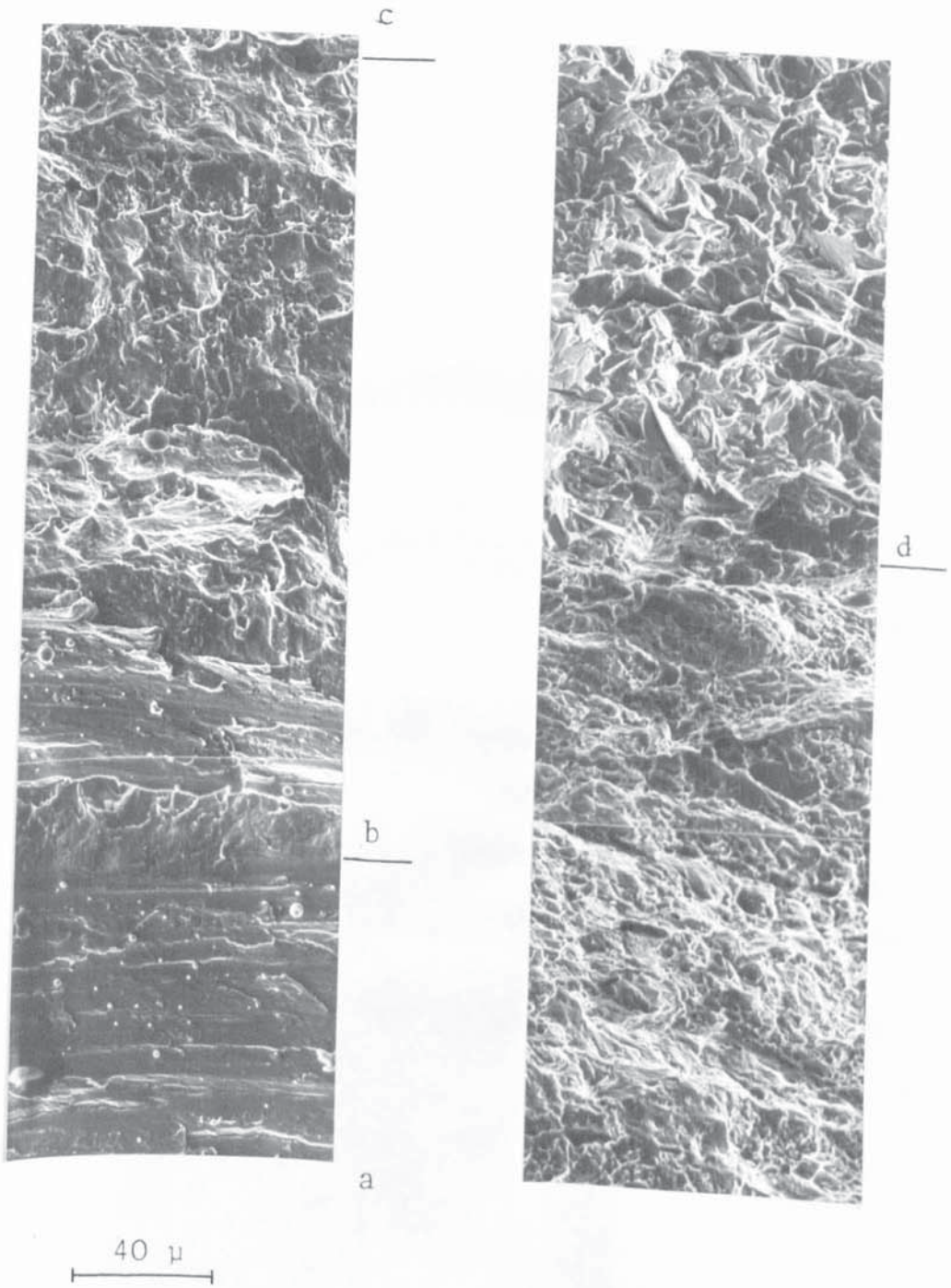

Plate 6.4 : Fracture surface of a standard CVN specimen, tested by slow bend at -90°C (a-notch surface; b-stretch zone; c-stable crack extension; d-unstable crack extension).

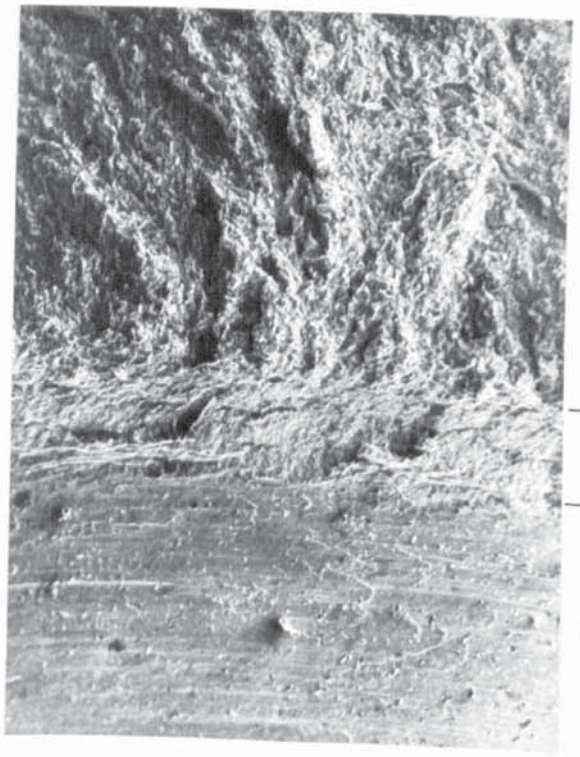

(a) : Side-grooved CVN specimen, -100°C

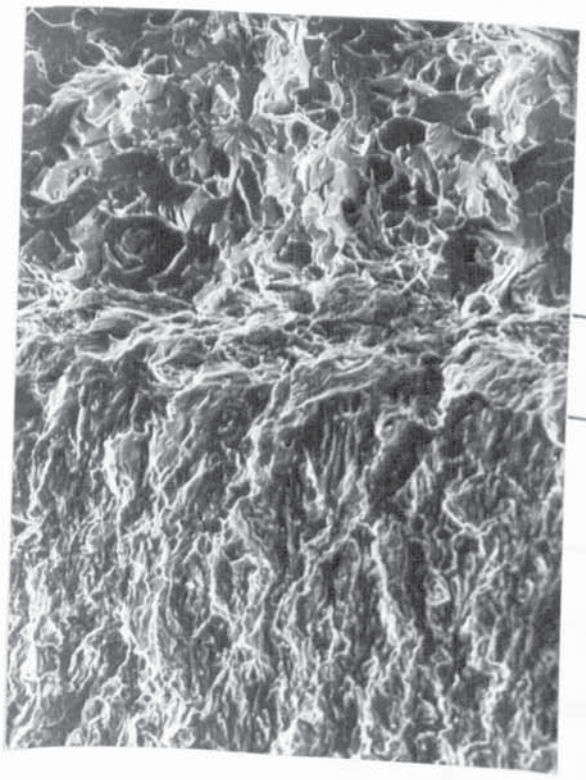

(b) : Pre-cracked side-grooved specimen, -80°C.

Plate 6.5 : Typical stretch zone under SEM.

Table 6.7 : Stretch zone widths measured for slow-bend Charpy-size specimens

Specimen number	Test Temperature °C	Stretch zone width, mm	Standard deviation, mm
NONSIDE-GROOVED SPECIMEN			
109	-60	0.473	0.063
110	-80	0.479	0.085
105	-90	0.219	0.079
104	-120	0.206	0.038
107	-120	0.162	0.054
SIDE-GROOVED SPECIMEN			
S26	-70	0.422	0.090
S15	-80	0.391	0.056
S23	-90	0.350	0.051
S50	-100	0.290	0.062
S24	-113	0.137	0.021
PRE-CRACKED SIDE-GROOVED SPECIMEN			
S48	-50	0.111	0.042
S47	-70	0.089	0.052
S45	-80	0.030	0.010

a. BS4360 Grade 50D normalized steel; plate number 2A52-1

b. Loading rate of slow bend = 0.05 cm/min

plotted for the three kinds of specimens in Fig.6.15. It has been found that the stretch zone widths are changed with temperature. Furthermore, the changing tendency is similar to the CTOD toughness transition behaviour of the specimens. That is, the stretch zone width of pre-cracked side-grooved specimens is much smaller than that of the two kinds of notched specimens. The variations of the stretch zone widths with temperatures are almost same for the two kinds of notched specimens.

Plate 6.6 shows the macroscopic fracture appearance for the side-grooved specimens. It is clear that in the corners of the intersection of the notch or pre-crack front and side-groove roots, the slow tearing crack extension is faster than that in the mid-thickness. This is because the side grooves increase the constraint in the side areas of the specimen. Furthermore, experiments indicate at upper shelf that for pre-cracked side-grooved Charpy specimen, stable crack extension except at the two corners is less than 0.2 mm, when maximum load is attained. At the crack tip, the total side-groove depths are 25% of the specimen thickness. Thus, this could lead to a rather small overestimates of CTOD, if the δ_m value is thought to be δ_i value.

6.2.2.4 J_C and K_{IJ} Values of Pre-cracked Side-grooved Specimen

In recent years increasing use has been made of the J-integral

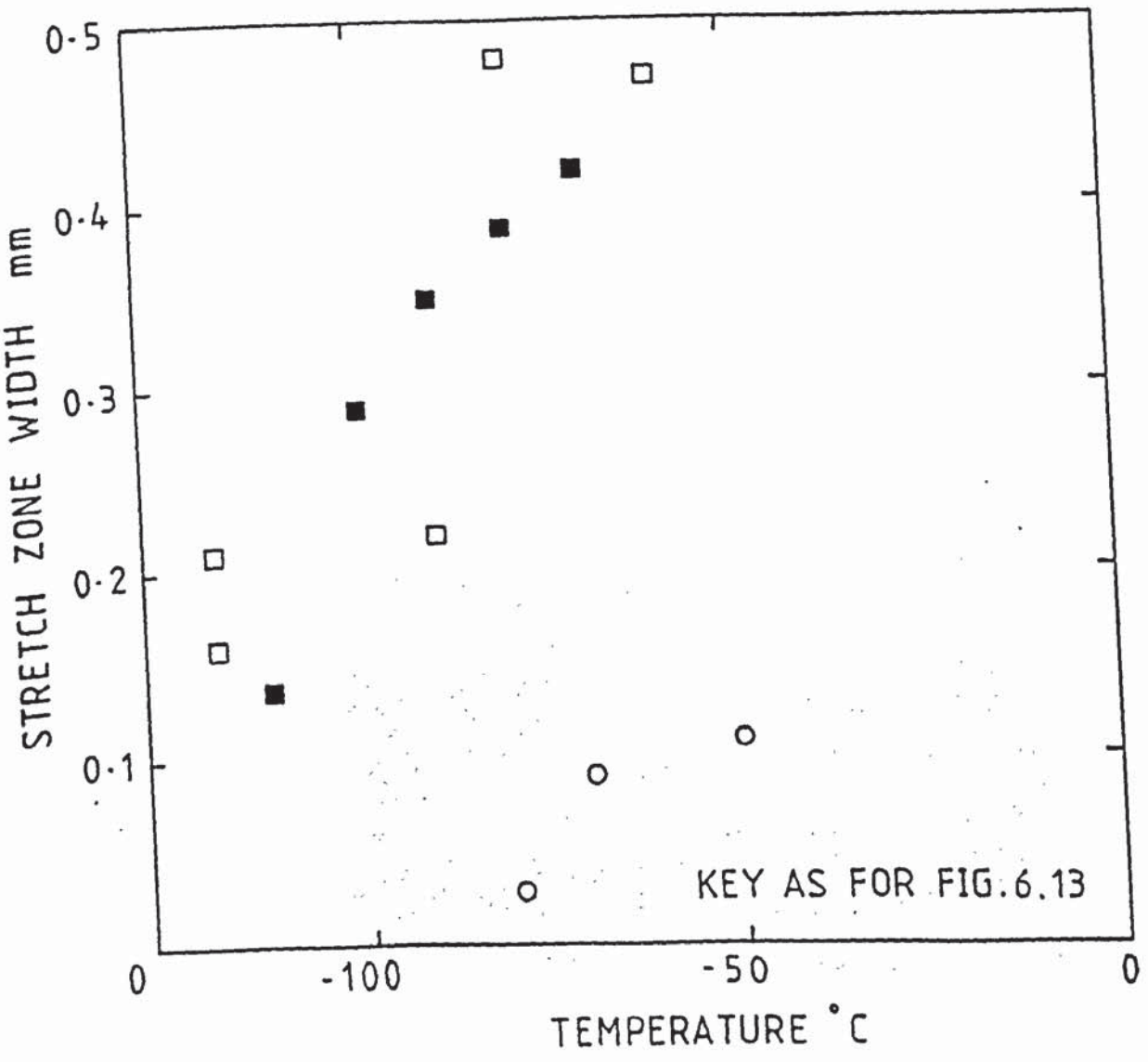

FIGURE 6.15 Stretch zone widths versus test temperature for three kinds of Charpy-size specimens

(a) : Side-grooved CVN specimen, -124^{o}C

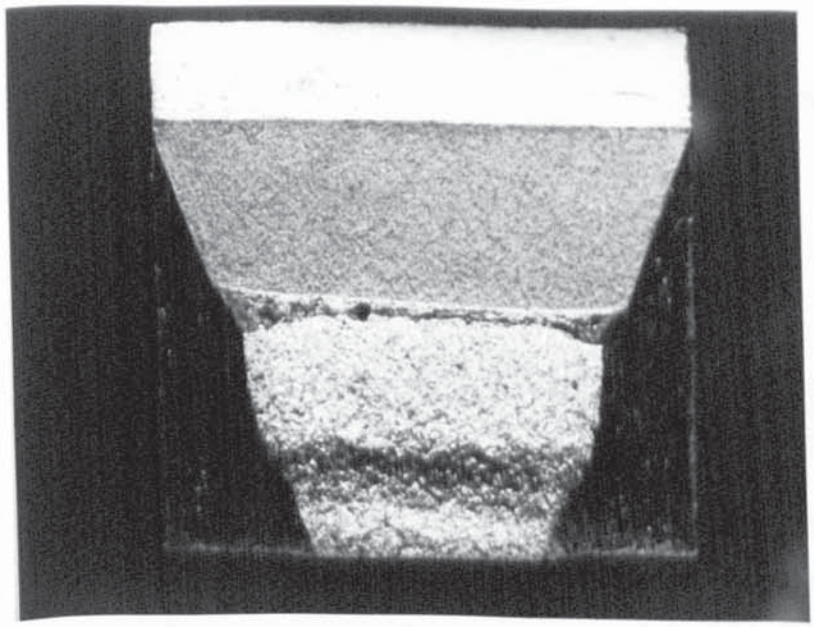

(b) : Pre-cracked side-grooved specimen, -50^{o}C

Plate 6.6 : Macroscopic appearance for the side-grooved specimens with stable crack extension (6.5x). The specimens were heat-tinted at 400^{o}C for 2 hr.

to characterise the fracture toughness of metals in the elastic-plastic regime. Much interest has been expressed regarding the prediction of K_{IC} from critical J-values which have been obtained from considerably smaller specimens than those required by the BS5447 and ASTM E399. This is because that J-integral is a method of characterizing the stress and strain field at crack tip by an integration path taken sufficiently far from the crack tip to be substituted for a path close to the crack tip region. Thus, even though considerable yielding occurs in the crack tip vicinity, if the region away from the crack tip can be analysed, behaviour of the crack tip region can be inferred. Thus this technique can be used to estimate the fracture behaviour of metals in elastic-plastic regime and is a means of directly extending fracture mechanics concepts from linear-elastic behaviour to elastic-plastic behaviour.

Usually for steels a sufficient degree of plane strain for a valid critical J values is ensured when the requirement of the Eq. (1.25) is met. Obviously for the pre-cracked Charpy-size specimens with $a/W = 0.5$, the valid size criterion is not attained. However, for the pre-cracked side-grooved specimens, the specimen is effectively thickened due to the influence of the side-grooves on the specimen constraint. In this case it is very difficult to calculate the specimen size condition using the Eq. (1.25). Based on the void growth studies discussed in Section 5, it seems that a fully plane

strain condition already forms in the pre-cracked side-grooved specimens.

The estimation of J_C values are based on the areas under single load versus displacement recordings which are directly related to the work done. The estimation procedures proposed by Rice et al were described in Section 1.3.4. Examination of the macroscopic appearance indicates that at the test temperature of $-50^{o}C$, a slow crack growth is less than 0.2 mm corresponding to 4% of the total crack length during attaining maximum load. Thus the critical J value may approximately be evaluated from the point of either the brittle initiation or maximum load. Table 6.8 shows the results of some calculating parameters and critical J-integral values for pre-cracked side-grooved specimens. In the table Beq is the equivalent thickness in the side-grooved ligament. A and A' are the total and specific areas or the work done measured from the load versus load-point displacement recordings. The remaining notations are the same as in Eqs. (1.26) to (1.28). Furthermore, the stress intensity fracture toughness K_{IJ} can be estimated from the relation, $K_{IJ} = (EJ_C/(1-\nu^2))^{\frac{1}{2}}$, where E is the elastic modulus and ν is Poisson's ratio. It is assumed that $\nu=0.5$ for the pre-cracked side-grooved specimens under the general yield condition. The estimated K_{IJ} values from J_C are also given in Table 6.8.

Table 6.8 : Jc and K_{IJ} values estimated for pre-cracked side-grooved specimens

Specimen No.	Test Temperature ^{o}C	A N-mm	Beq mm	W-a mm	I_4 mm^4	P N	δnon-crack mm	A' N-mm	Jc N/mm	K_{IJ} MPa$\sqrt{m}$
S13v	+12	5335.5	5.78	4.73	51.0	3157.5	0.401	633.1	344.0	307.4
S19v	+12	3556.1	5.53	4.11	32.0	2206.4	0.446	492.0	270.0	272.3
S18	-50	4075.3	5.53	4.13	32.5	2402.5	0.479	575.4	306.5	290.2
S48	-50	5582.2	5.76	4.69	49.5	3216.4	0.421	677.1	363.2	315.9
S46	-60	4445.3	5.76	4.69	49.5	2941.8	0.385	566.3	287.2	280.9
S47	-70	4791.8	5.72	4.58	45.8	3481.0	0.492	856.3	300.5	287.3
S44	-70	2736.0	5.77	4.72	50.6	3187.0	0.408	650.2	153.2	205.1
S45	-80	2696.4	5.81	4.82	54.2	3481.1	0.416	723.6	140.9	196.7

a. $A' = (P \cdot \delta_{non\text{-}crack})/2$;

b. $J_C = 2(A-A')/B(W-a)$;

c. $K_{IJ} = (EJc/(1-\nu^2))^{\frac{1}{2}}$; E=206000 MPa and ν=0.5.

6.3 Short Bar Testing

There is an increasing interest in the use of short rod and short bar specimen, because the short rod and short bar configuration potentially provides a simple and inexpensive method of determining the plane strain fracture toughness of materials. This is especially true for some brittle, non-metallic materials [51, 93]. Recently, the fracture toughness of some metallic materials such as high strength steel, aluminium alloy and titanium alloy have been evaluated by means of the elastic-plastic analysis procedure proposed by Barker [56]. The results are encouraging and have stimulated a number of laboratories to begin using short rod and short bar specimens to measure the fracture toughness of metallic materials.

However, for the structural steel such as BS4360 Grade 50 D of our interest, the elastic-plastic analysis cannot be used for determining its plane strain fracture toughness at room temperature, due to the plasticity which is too high. The main purpose of this work is to investigate the relation between the void growth and test temperature in short bar specimens. At the same time, the investigation also attempts to research on the possibility of determining the valid plane strain fracture toughness by short bar specimen at lower shelf temperatures.

6.3.1 Experimental Procedure

In the general view, the test specimen is shown in Plate 6.7. The short bar specimens were taken from a 50 mm - thick BS4360 Grade 50 D normalized steel plate. The specimens have L-T notch plane orientation which is the same as that for the Charpy-size bend bar specimens. The dimensions of the short bar specimen are given in Fig. 1.13, but the distance from the load line to the chevron tip, a_o, is 13.1 mm, and the slot angle, θ, is 55.0^o. The side-slots were cut by a spark machine. By measurements, the slot thickness is from 0.27 to 0.47 mm. The slot bottom is round with the radius of 0.21 mm. A typical slot bottom geometry is shown in Plate 6.8. The plane indicated is perpendicular to the slot bottom-line. According to Barker's paper [50], the plane strain constraint appears to be very good for this slot bottom geometry.

Fig. 6.16 shows the grip design. In order to have a good combination of the strength and toughness during the test at low temperature, the grips were made of the air hardening martensitic stainless steel. Before machinework, the steel was softened at 850^oC for 1 hr, then slow cool in furnace. After machinework the grips were heated at 980^oC in a vacuum heat treatment furnace for 0.5 hr and then continuously cooled to room temperature by blowing nitrogen. Finally, the grips were tempered at 315^oC for

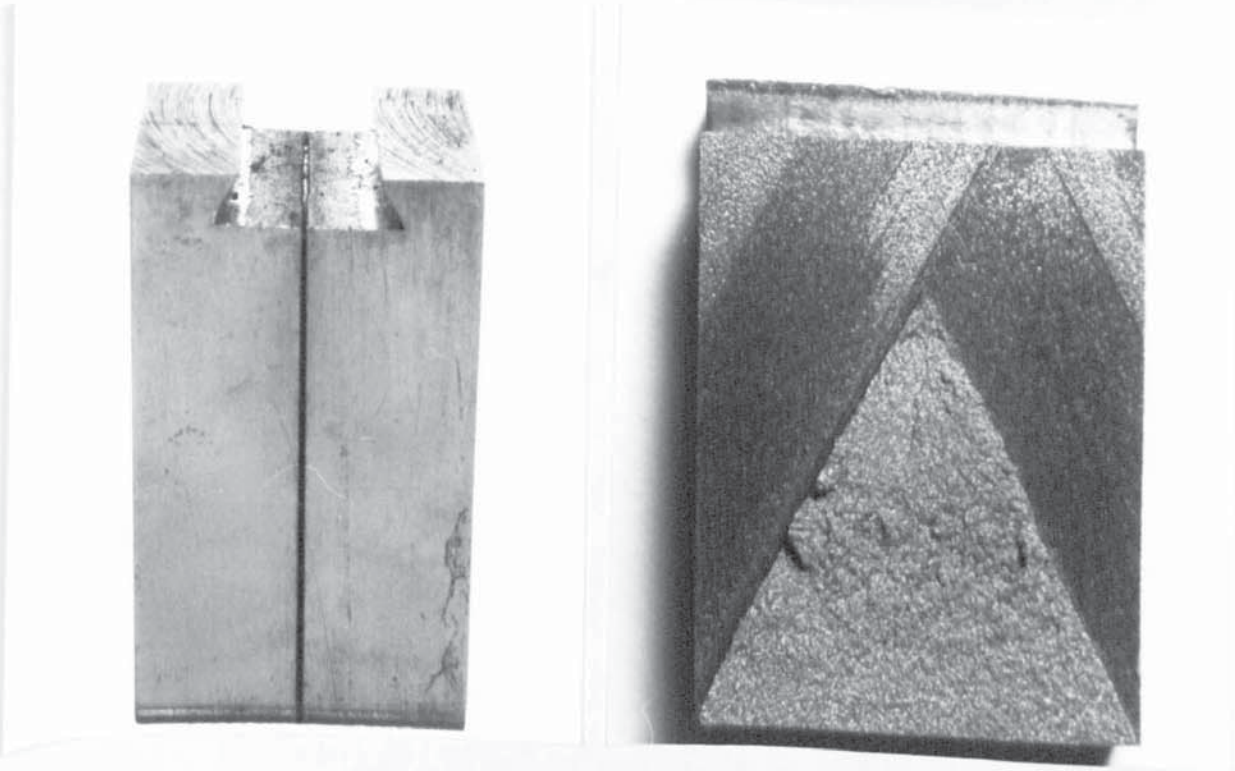

Plate 6.7 : General view of short bar specimen. The right is fracture appearance tested at -100°C.

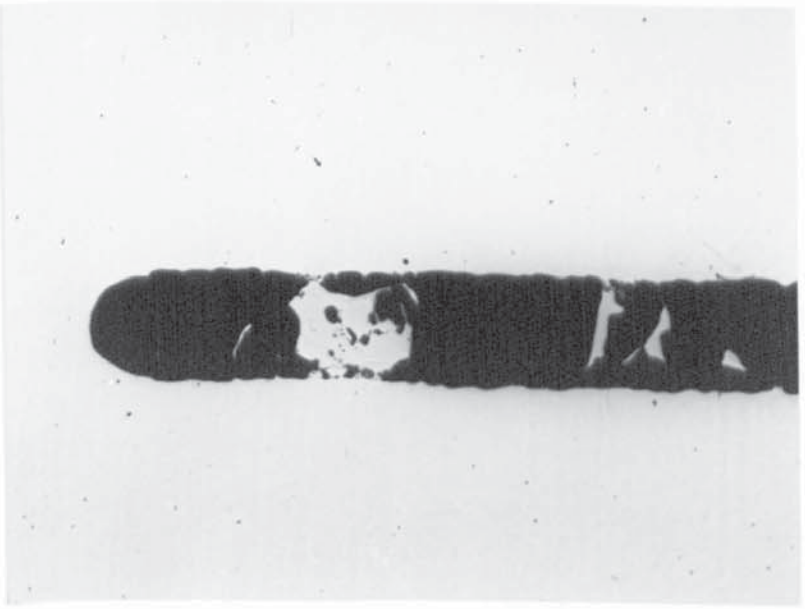

Plate 6.8 : Slot bottom geometry (30x).

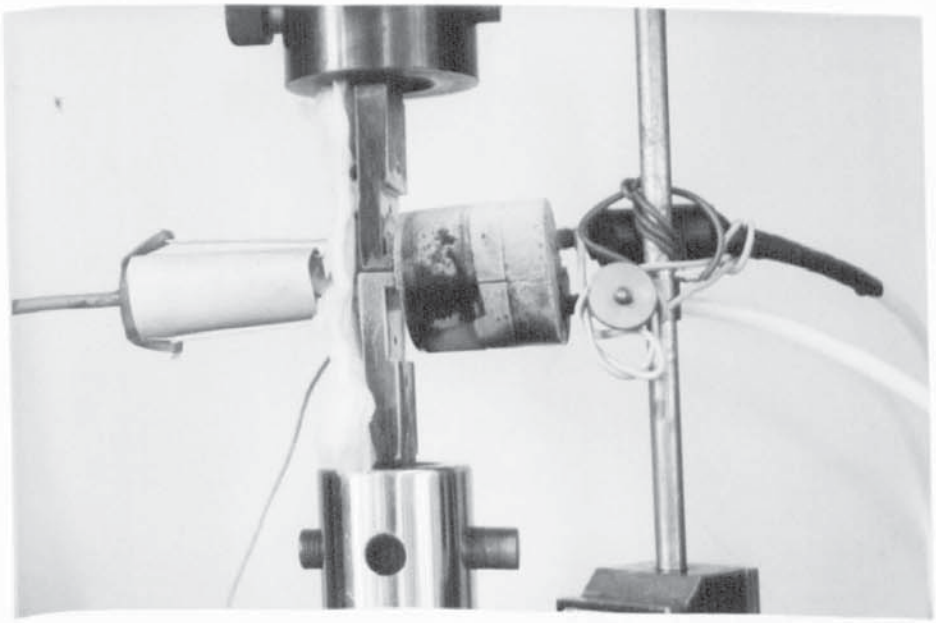

Plate 6.9 : Testing arrangement for short bar specimen.

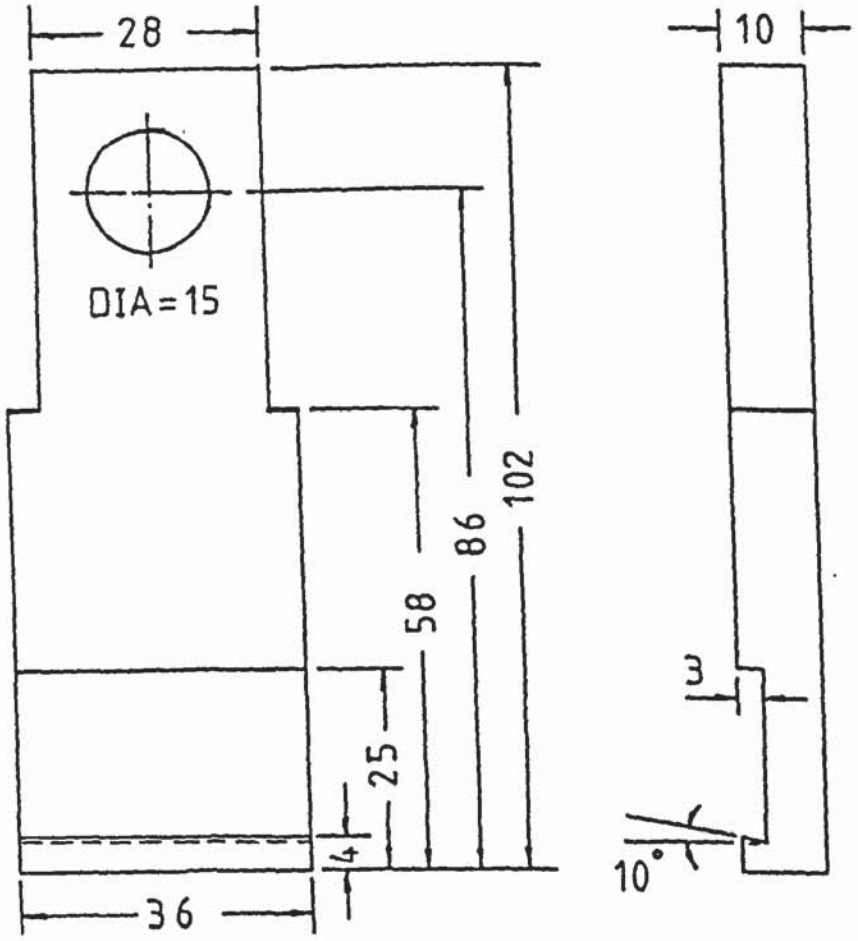

1. All the dimensios are in mm
2. Air hardening martensitic stainless steel

FIGURE 6.16 Grip design for the short bar test

0.5 hr to improve the toughness. Hardness survey was carried out with a 20 Kg load, HV 20 average/range = 447/(438-457).

The grips are attached to the arms of an Instron testing machine by the pin and clevis. During the tensile test, the grip lips are inserted into the grip slot in the specimen. In order to increase the bearing capacity of the grips, the grip lips were designed at an angle of 10° to the horizontal. A large radius of curvature at the bottom of the grip lips was helpful for improving the notch toughness during test at low temperature. Due to the grip slot of 30° in the specimen, the contact point between the grip lips and grip slot in the specimen is stable during loading process. However, the point contact would lead to excessive plastic deformation at the local region in the grip slot of the specimen. This is especially true for the ductile materials and which are tested at higher temperature. Furthermore, the local plastic deformation would cause a small variation in the load line position. Therefore, the grip slot of the specimen might be redesigned in the future.

The tensile test was conducted in the 5000 Kgf Instron testing machine with a loading rate of 0.05 cm/min. The full range of the load cell was chosen. The testing arrangement is shown in Plate 6.9. Most of the specimens were tested at the temperature of $-40^{\circ}C$, $-60^{\circ}C$, $-80^{\circ}C$, and $-100^{\circ}C$. A specially designed cooler by spraying

liquid nitrogen is shown in Fig. 6.7 (b). In order to maintain the specimen in a constant pre-set temperature, an automatic adjustment system is the same as that used in the three-point bending tests. For measuring the temperature, a copper-constantan thermo-couple of 0.2 mm diameter was spot-welded in the bottom of a small hole in the specimens. The hole of 1.5 mm diameter and 6 mm depth was located at about 5 mm away from the chevron tip to improve the accurancy and repeatability of the temperature measurement.

Short bar tests of ductile material involved the recording of the load applied to the specimen versus the opening displacement of the specimen mouth. The clip gauge for measuring the mouth opening was mounted on the back of the grips through the knife edges of screw-on type (see BS5762). Strain gauges and adhesive should be selected to suit testing temperature range. The types of the strain gauge and adhesive are FLA-10-11 (10 mm length and 120 ± 0.3 Ω resistance), and EA-2, respectively. Calibration of the gauge was made prior to the tests for each time. However, the calibration was carried out at an ambient temperature. Thus the opening displacement of the specimen mouth recorded at the test temperature might be smaller than the real displacement.

At the beginning of the cooling process, there is a rather larger fluctuation of the specimen temperature. A dynamic equilibrium condition could be attained in 15

minutes. The temperature deviation of the specimen was ± 1°C at the lowest testing temperature of -100°C. In this equilibrium condition, the specimen would begin to be loaded.

6.3.2 Test Results and Analysis

6.3.2.1 Tensile Behaviour of the Short Bar Specimen in the Transition Region

Short bar test records of load versus specimen mouth opening displacement can show very marked differences between tests, depending on the test temperature. Three basic behaviour types are indicated in Fig. 6.17 through 6.19. These recordings have very good repeatability at each test temperature.

During the tests at -40°C and -60°C, a deviation from linearity is observed after an initial linear loading. At the point of inflexion the crack initiates at the chevron tip of the ligament in the specimen. After that, the small increase in load is accompanied by a relatively large increase in the mouth opening of the specimen. A rather smooth recording with slowly increasing the load was obtained, as shown in Fig. 6.17, until the mouth opening displacement of near 6 mm, which is limiting work distance of the slip gauge. In the process of the slow mouth opening of the specimen, slow crack propagation is accompanied by the crack tip blunting and elastic-plastic bend deformation in each half beam of the short bar.

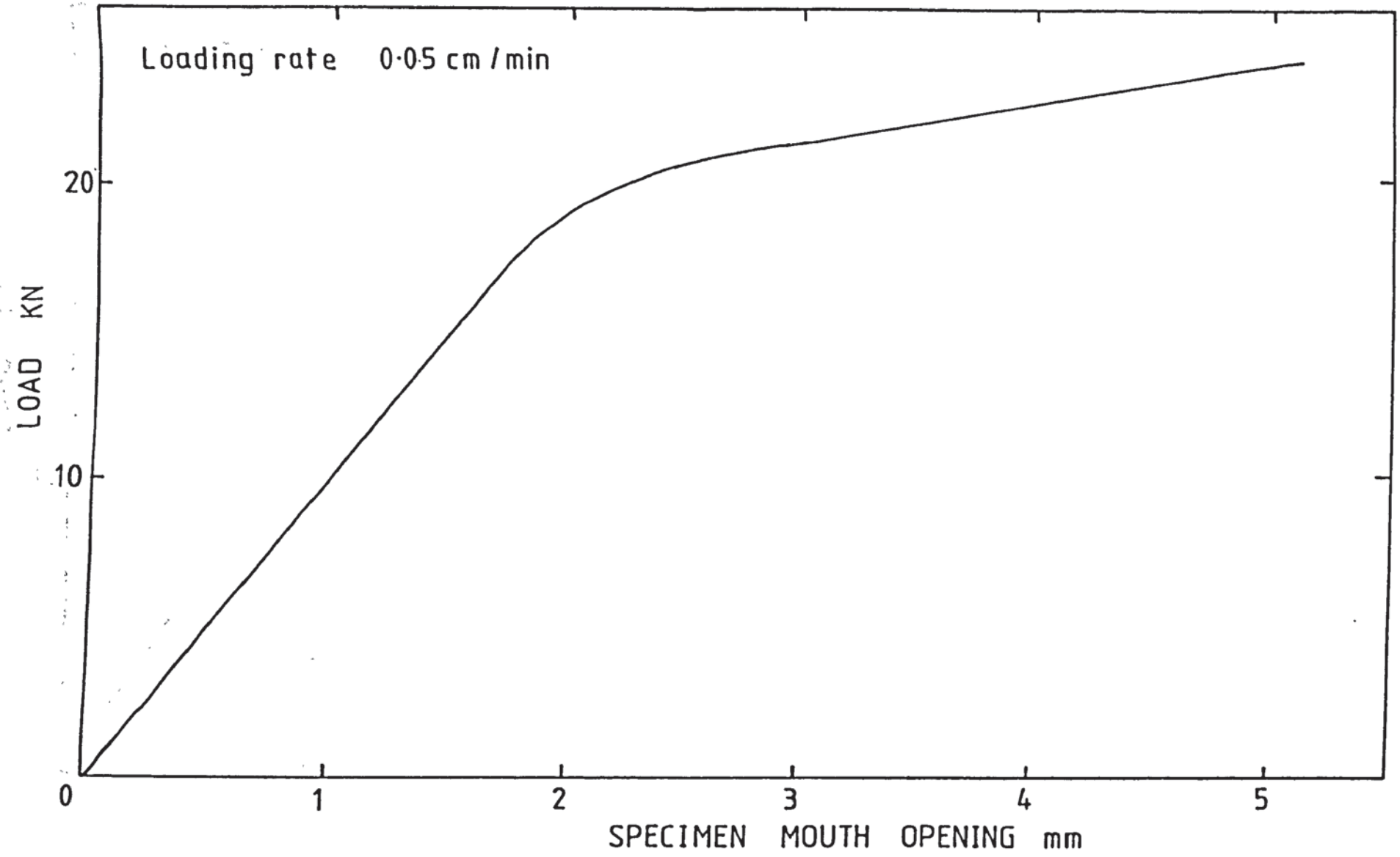

FIGURE 6.17 Typical record of load versus mouth opening, tested at -60°C

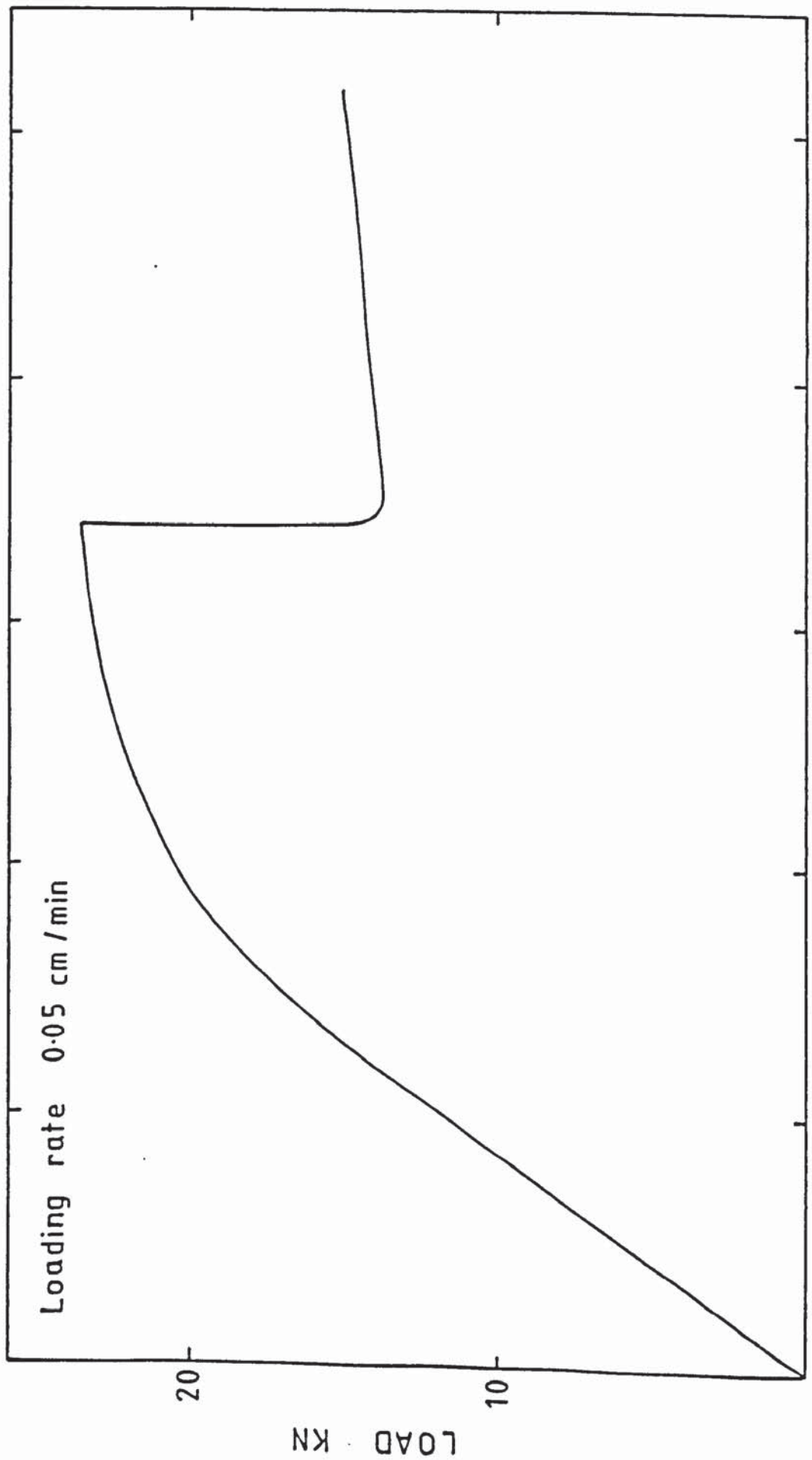

FIGURE 6.18 Typical record of load versus mouth opening, tested at -80°C

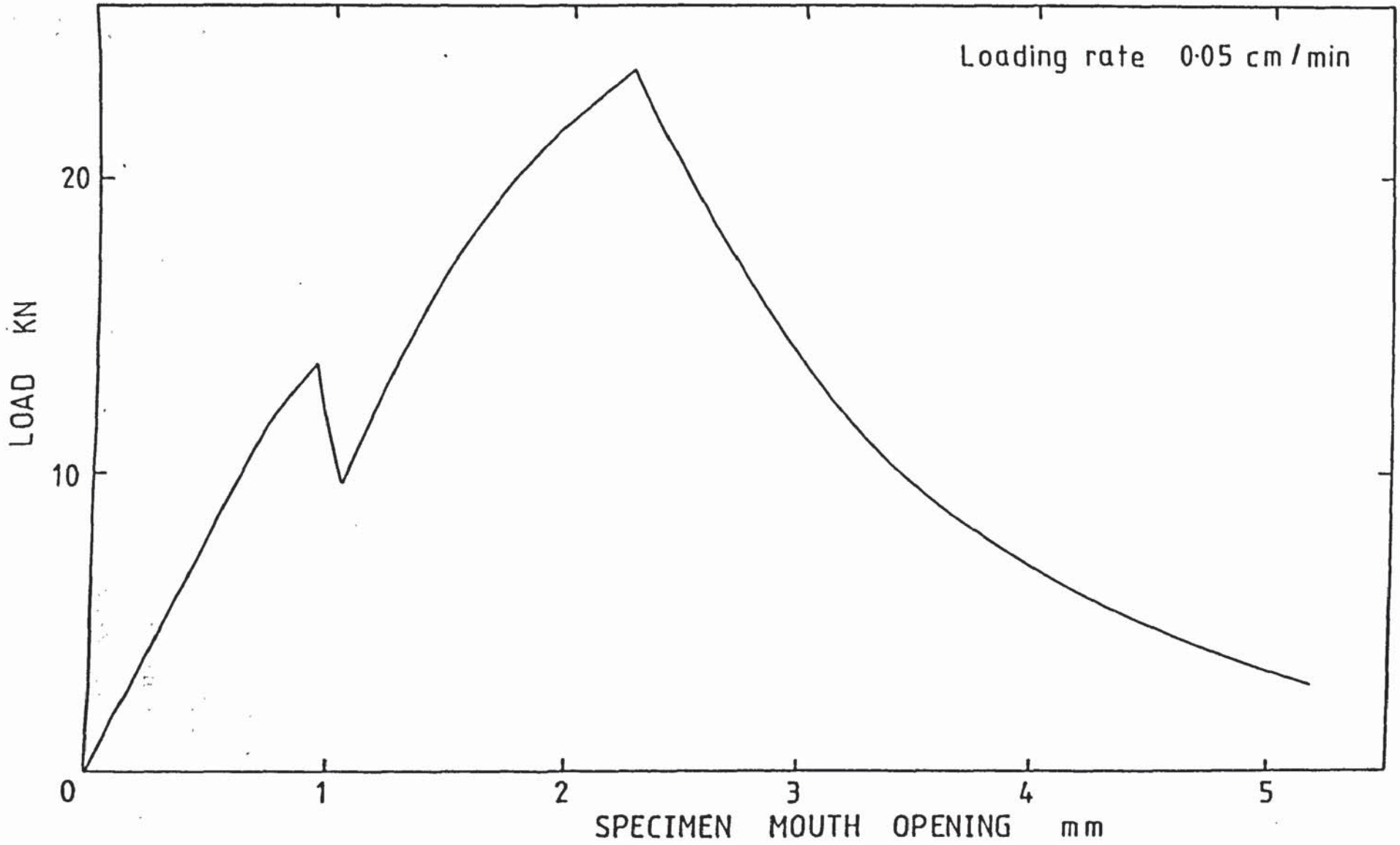

FIGURE 6.19 Typical record of load versus mouth opening, tested at -100°C.

Furthermore, the maximum load still can not be attained until the mouth opening displacement of near 6 mm. Plate 6.10 describes the shape and size of the plastic zone in the short bar specimen approximately. The material stretched within the plastic zone at the crack tip tends to prop the specimen mouth open such that a rather large residual opening of the specimen mouth forms after unloading. Because the maximum load cannot be obtained in the mouth opening range investigated and excessive plasticity forms in the specimen, the fracture toughness cannot be measured in the investigated test temperatures.

During the tests at -100°C, the crack suddenly jumps after nearly linear loading. The fast-moving crack may arrest at a lower load level after propagating a short distance, as shown in Fig. 6.19, or may completely fracture the specimen. The initial pop-in crack to catastrophically propagate through the entire specimen is caused by the insufficient stiffness of the testing machine including the grips [50]. However, as the rather large elastic-plastic deformation forms in the two beams of the short bar, the large elastic energy stored in the specimen may be thought to be another reason causing the pop-in crack to fracture the entire specimen. In the subsequent calculation the load corresponding to the crack jump is still used to determine the fracture toughness at low temperature.

During the tests at -80°C, the crack slowly propagates

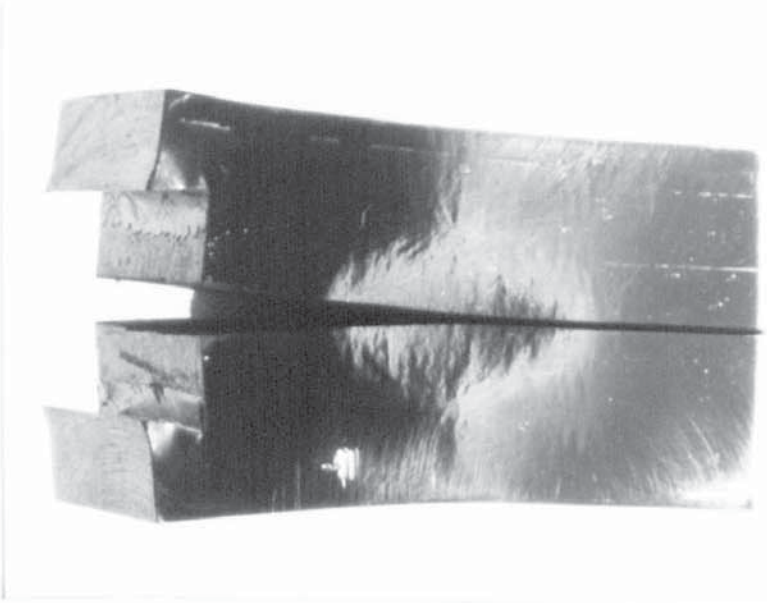

Plate 6.10 : Schematical plastic-zone observed on the side-surface of the short bar, tested at -60°C (2x).

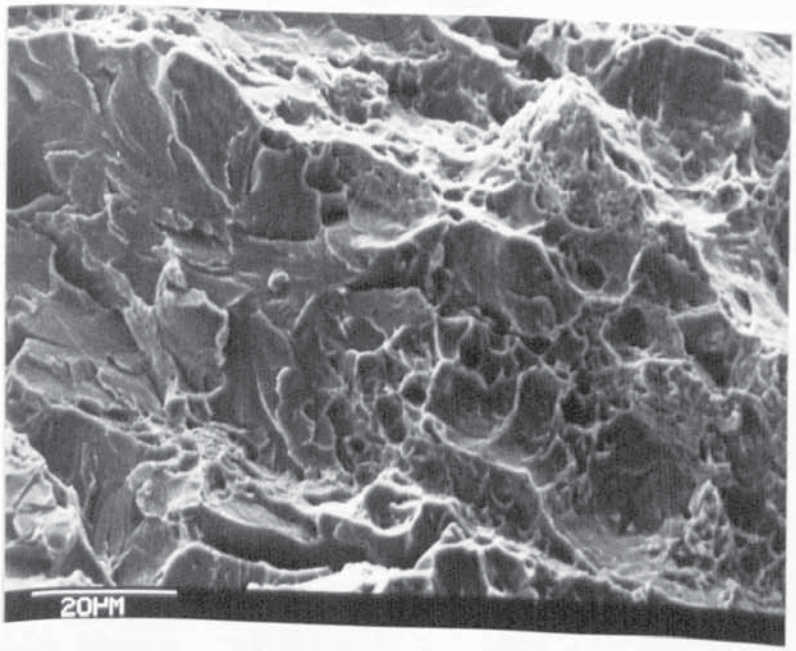

Plate 6.11 : Fracture mode transition at 2.5 mm ahead of the chevron tip, tested at -80°C.

by ductile mechanism after initial linear loading. Usually the crack will rapidly propagate after a slow crack growth for a short distance. This is because the changing shape and sharpness of the crack tip combine with other effects to increase the stress triaxiality local to the growing crack tip and lead to the transition from a ductile to a cleavage mode of cracking. The transition zone of the fracture mode in the fracture surface is shown in Plate 6.11. Fig. 6.18 shows a typical recording of the load versus mouth opening displacement. A sudden drop in the load occurs after a certain deviation from linearity. Usually the load drop might attain approximately half of the instantaneous loading. Then the load is linearly increased again, but the new loading slope is very low. For example, in the recording of the specimen No. 5, as shown in Fig. 6.18, the initial loading slope is 11.66 $^{KN}/mm$, but the loading slope after a crack jump become 0.83$^{KN}/mm$. It also reflects the increase of the specimen compliance as the crack suddenly propagates a rather long distance.

It should be pointed out that during the tests at -80^{o}C cracks always tunnel a curved way more into one side of the specimen than the other, instead of following the intended crack plane, as indicated in Fig. 6.20. In this case, the very thin slots cannot serve as crack guides except the initial crack growth within 2 to 3 mm

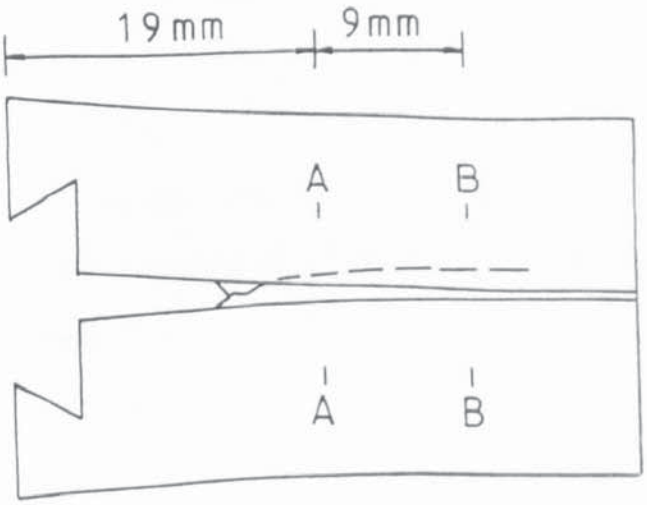

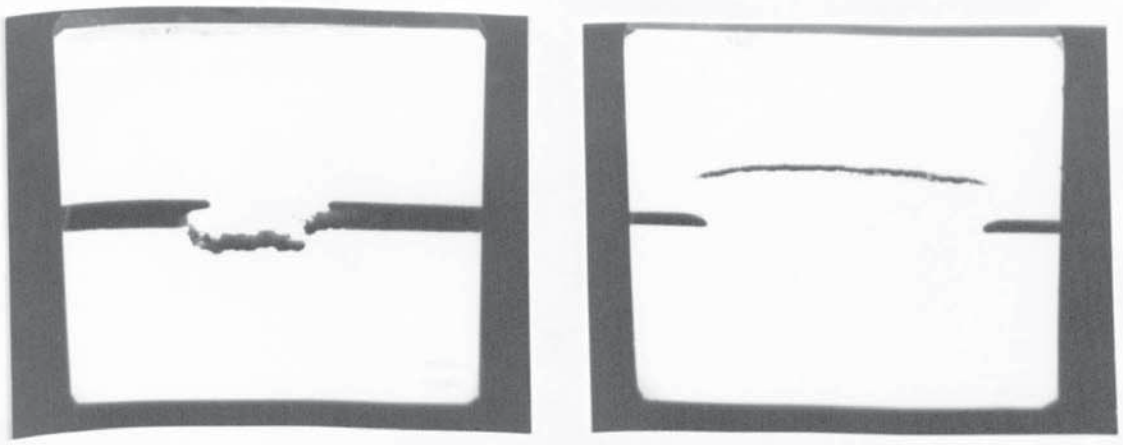

A — A

B — B

FIGURE 6.20 Crack tunnels a curved way more into one side of the specimen than the other (tested at -80°C)

ahead of the chevron tip. It has been thought that crack tunnels a curved way into one side of the specimen in which the material is substantially less tough, or poor centering of the chevron slot along the mid-plane of the specimen may aggravate the tendency to crack outside the intended plane [57]. Practically, the phenomenon of tunnel often occurs at the test temperature of -80°C. It may be expected that the plane strain constraint of the specimen geometry is insufficient in this experimental condition. If the tests are carried out at the temperature of -100°C, the crack is better guided in the intended plane.

Some specimens were broken along the one beam of the specimen during the tests at -80°C rarely at -100°C, as shown in Plate 6.12. It may be expected that its formation is similar to the phenomenon of tunnel. After the crack propagates for a short distance, the crack rapidly propagates much easier along the bended beam of the specimen than along the intended plane, due to bend stress in the beam. The metallographic examination has indicated that the fractography on the tunnel or the broken beam of the specimen from start to finish is cleavage fracture.

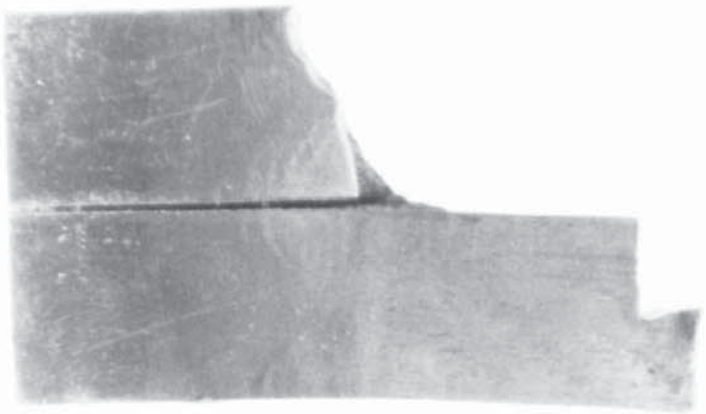

Plate 6.12 : Brittle fracture occurs along the half specimen, tested at -80°C (2.2x).

Plate 6.13 : Sample surface sectioned from a short bar specimen (20x).

6.3.2.2 Determination of K_{ICSB} at the Low Shelf Temperature

Short bar fracture toughness, K_{ICSB}, may be evaluated by the load correspondent to the crack jump point. In our experimental condition, usually there is only one jump in the recordings. If the number of crack jumps in a test is more than one, the average of a few values of K_{ICSB} calculated from a given test is used as the K_{ICSB} of the specimen. Although the ductile crack initially propagates for a short distance, the K_{ICSB} value is still calculated by the load at the jump point during the tests at the temperature of -80°C. The toughness value may tend towards conservative according to the LEFM analysis. However, this is much better information than simply a statement that the test result is invalid [94].

For each crack jump, the fracture toughness can be evaluated by Eq. (1.43). As the specimen geometry should be within the tolerances established for the calibrated configuration. Dimensions which are out-of-tolerance by up to three times the recommended tolerances can be accepted, provided the test result is multiplied by a configuration correction factor,

C_c. Thus the fracture toughness of the short bar specimen can be calculated by the following equation

$$K_{ICSB} = A\ C_c\ F/B^{3/2} \qquad \text{.....(6.1)}$$

where B is the nominal breadth of the short bar, F is the mouth opening load correspondent to the crack jump point, and A is a dimensionless function of the scaled crack length which has a value of 22.28 at $a_c/W = 0.512$ for the specimen configuration of this study [53].

Based on a Terra Tek's manual [95], the configuration correction factor, C_c, is equal to one, if the tolerances of the specimen dimension are in the following allowance range

Specimen breadth:

$$B \pm 0.004B_{nom}$$

Specimen length:

$$W \pm 0.010B_{nom}$$

Distance from specimen front end face to the chevron tip:

$$a_o \pm 0.005 B_{nom}$$

Chord angle of chevron slot:

$$\theta \pm 0.5^o$$

If the tolerances are up to three times the above allowance ranges, the C-factor can be evaluated by

$$C_c = C_B C_W C_a C_\theta \qquad \text{.....(6.2)}$$

where

$$C_B = 1 - \frac{5}{4}\Delta B / B_{nom}$$
$$C_W = 1 - \frac{1}{2}\Delta W / B_{nom}$$
$$C_a = 1 + \Delta a_o / B_{nom};$$
$$C_\theta = 1 - 0.01\Delta\theta$$

and,

$$\Delta a_o = a_o - (a_o)_{nom}$$
$$\Delta B = B - B_{nom}$$
$$\Delta W = W - W_{nom}$$
$$\Delta\theta = \theta - \theta_{nom}$$

In this study, the nominal values of a_o and θ are designed to be 13.10 mm and 55.0^o respectively.

The overall dimensions of the specimen were measured before testing. Values of a_o and θ were directly measured by a NIKON shadow graph projector with magnification of 10x on the slot plane of the half specimen fractured. The dimensions and calculated tolerance of the specimens, which were tested at -80^oC, and -100^oC, are listed in Table 6.9. According to Eq.(6.1), the fracture toughness of the short bar specimens can be calculated at -80^oC and -100^oC. The results are given in Table 6.10.

Table 6.9 : Measured dimensions and calculated tolerances of the short bar specimens

Specimen No	B	W	H	A_o	θ^o	Δ_c	C_B	C_W	C_a	C_θ	C_c
5	25.40	38.08	22.20			0.14	1.0	1.0			
6	25.40	38.14	22.20	13.44	54.75	0.18	1.0	1.0	1.013	1.003	1.016
7	25.40	38.20	22.20	13.25	55.30	0.00	1.0	1.0	1.006	0.997	1.003
9	25.40	38.08	22.20	12.94	54.03	0.22	1.0	1.0	0.994	1.010	1.004
11	25.30	38.14	22.20	12.20	54.72	0.21	1.0	1.0	0.965*	1.003	0.968
12	25.40	38.10	22.12	12.86	53.38	0.27	1.0	1.0	0.991	1.014	1.005
18	25.40	38.16	22.20	12.96	55.10	0.12	1.0	1.0	0.995	0.999	0.994

a. Notations are shown in Fig. 1.13 and Eq. (6.2),

b. Δ_c is the difference of distance from each side of the specimen to the chevron slot plane;

c. Dimensions for length are in millimetres;

d. Symbol * represents that the dimension is over the allowance range.

Table 6.10 : Measured fracture toughness, K_{ICSB}, from the short bar specimens

Specimen No.	Test Temperature ^{o}C	Load, F, KN	C_c	K_{ICSB}, $MPa\sqrt{m}$	Average K_{ICSB}, $MPa\sqrt{m}$	Comments
5	-80	23.63	-	130.0	130.0	Tunnelled
6	-80	23.98	1.016	134.1	134.1	Broken in one beam
7	-80	22.65	1.003	125.0	125.0	Tunnelled
9	-100	24.86	1.004	137.4	137.4	Broken in one beam
11	-100	24.34	0.968	129.7	129.7	Fracture along slot plane
12	-100	13.73 23.75	1.005	76.1 131.6	103.9	Fracture along slot plane
18	-100	23.14	0.994	126.5	126.5	Fracture along slot plane

a. BS4360 Grade 50D normalized steel;

b. Loading rate = 0.05 cm/min

c. For specimen No. 5, it is assumed that C_c=1.

6.3.2.3 Relative Void Volume Transition with Testing Temperature

In this investigation, we seek the relation between the relative void volume characterizing the ductile fracture process and testing temperature. For the short bar tests at the temperature of -40°C and -60°C, the ductile crack propagated very slowly with the mouth opening of the specimen. When maximum mouth opening of near 6 mm was attained, the specimen was unloaded. After that the specimen was sectioned at -196°C along the mid-breadth. The sample surface sectioned from the short bar specimen is shown in Plate 6.13. The relative void volume was measured by a statistic point counting technique. The measurement was directly conducted on the screen of scanning electron microscope. Regular square grid of 1cm and magnification of 1000x were chosen to count voids. The number of grid is 80. The range for measuring the relative void volume was chosen in 0.4 to 0.6 mm ahead of the growing crack tip. Typical fractography with voids in the observed region is shown in Plate 6.14. For the tests at the temperature of -80°C and -100°C, usually there is a certain extent of the ductile crack growth before the cleavage crack propagation. The extent of ductile crack growth is about 2 to 3 mm for the tests at -80°C and 30 to 500 μm for the tests at -100°C. In these cases, the relative void volume was directly measured on the fracture surface, as shown in Plate 6.15. The measurement was conducted in the range of 0.4 to 0.6 mm ahead of the ductile crack front. The results

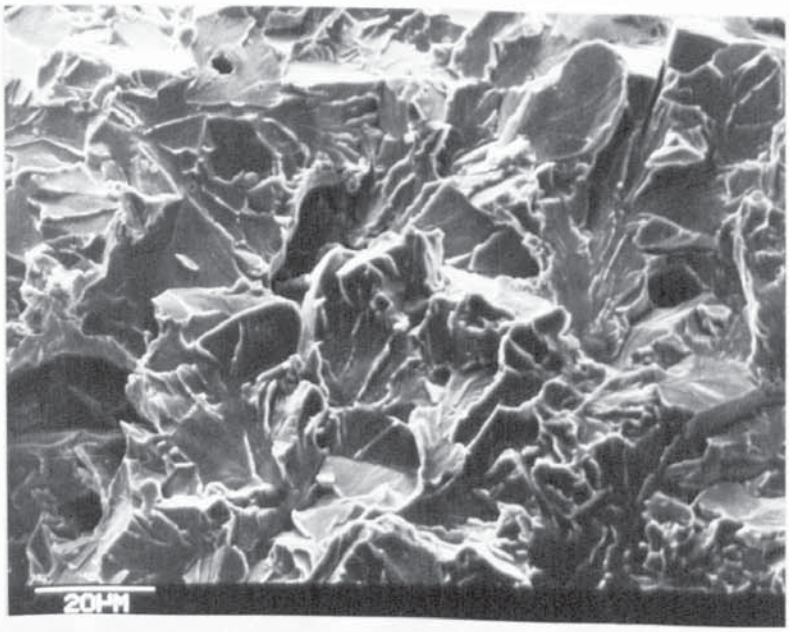

(a) : Observation is in 0.50 mm ahead of the growing crack tip.

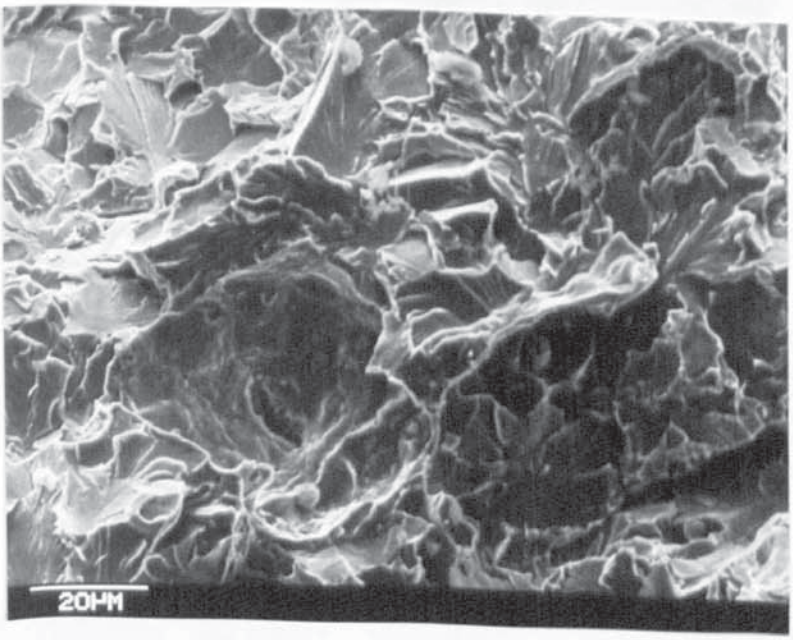

(b) : Observation is in 0.45 mm ahead of the growing crack tip.

Plate 6.14: Typical fractographys with voids in the observed region, tested at -60°C.

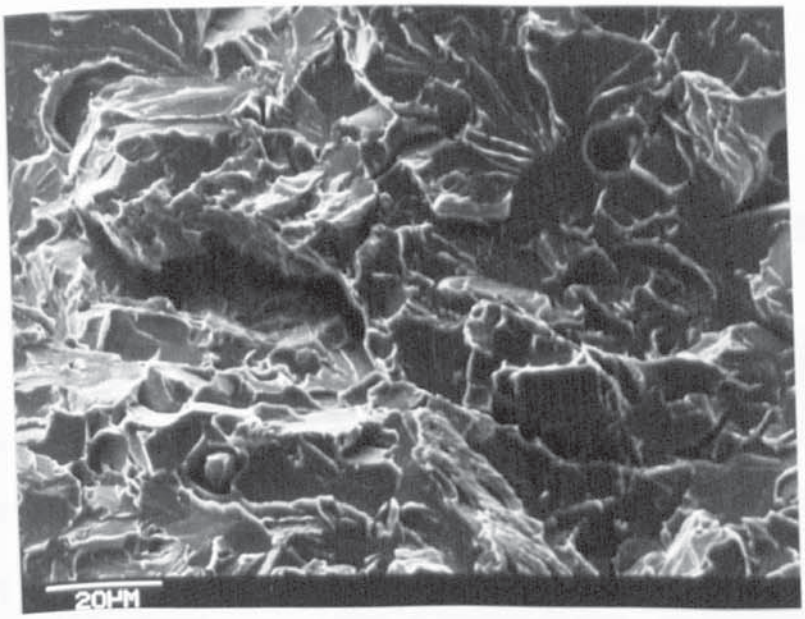

Plate 6.15 : Voids exhibited at 0.40 mm ahead of ductile crack front on cleavage fracture surface, tested at -80°C.

are given in Table 6.11 and Fig.6.21. It has been found that there is a temperature transition behaviour of the relative void volume measured ahead of the growing crack tip or ductile crack front.

The general effect of testing temperature on the relative void volume is similar to the effect of same condition on CVN test results. According to the micro-mode of fracture, the fracture process is controlled by the void growth at the upper shelf temperature. The measured results indicate that there is a critical void growth ahead of a growing crack tip in the upper shelf temperature. The average relative void volume of about 0.00641 is essentially independent of the testing temperature. At the low shelf temperature the fracture process is controlled by the cleavage cracking, although there is a small extent of ductile crack growth in the vicinity of the chevron tip. Some voids can still be measured in the specimens tested at the low shelf temperature. These voids might exist in the plastic zone ahead of the growing ductile crack tip before brittle cracking occurs.

Furthermore, the transition of the relative void volume ahead of the growing ductile crack tip or ductile crack front is similar to the transition of the fracture mode occurred in the CVN impact tests. If a 50% of the relative void volume ahead of the growing ductile crack tip measured in the upper shelf temperature is used to express the transition of the micromechanisms of fracture,

Table 6.11 : Measured relative void volumes with test temperature

Specimen No.	Test temperature ^{o}C	Relative void volume, Vv	Standard deviation, σ	Measured region
3	-40	0.00563	0.00802	0.4 to 0.6 mm ahead of the growing crack tip
8	-40	0.00700	0.00876	
4	-60	0.00563	0.00762	
15	-60	0.00738	0.00991	
1	-80	0.00150	0.00408	0.4 to 0.6 mm ahead of the ductile crack front on fracture surface
5	-80	0.00125	0.00377	
11	-100	0.00088	0.00320	
12	-100	0.00050	0.00276	

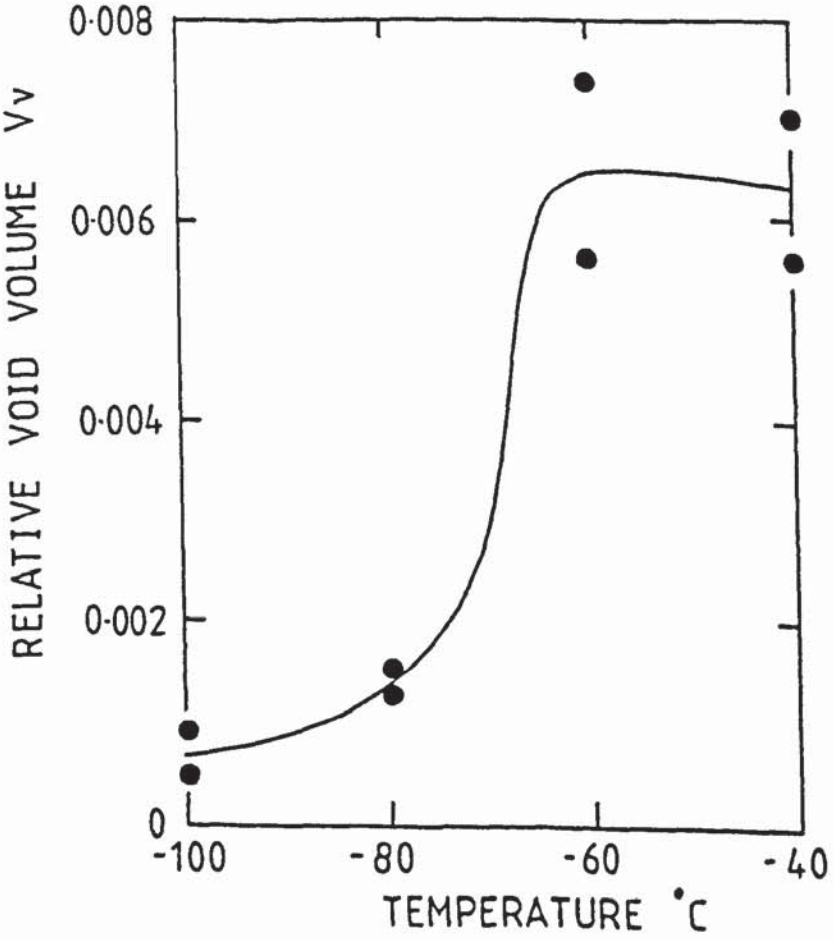

FIGURE 6.21 Relative void volumes at 0.4 to 0.6 mm ahead of the growing crack tip or ductile crack front as a function of test temperature

the transition temperature is about -70°C. This is approximately the same as the transition temperature determined by slow bend tests in the pre-cracked side-grooved CVN specimens.

Section 7

DISCUSSION

7.1 Void Nucleation and Its Growth

The theoretical analysis and experimental observation show that the ductile fracture of a structural steel is a progressive process with the void nucleation, growth and coalescence. The contribution of the deformation process in the development of voids has been well established. Many workers have proposed that the void nucleation takes place at a strain threshold. According to the experimental measurements on a series of the interrupted smooth tensile specimens, it is shown that voids nucleate at very low strain. The plastic shear strain at nucleation is 0.003 from the experimental observations, and 0.002 from the calculation which is based on the relation betwen the cumulative number of voids per unit area versus the plastic shear strain. The nucleation strain value is only a few times the yield strain. The relevant relative void volume at the nucleation strain is also rather small. It is 0.0018 from the calculation in Eq.(3.12).

It has been pointed that the critical strain to cause voids is inversely dependent upon the square-root of the particle radius, $\bar{\varepsilon}^{p}_{o} \propto r^{-\frac{1}{2}}$ (73). Voids only form from some larger inclusions at the critical nucleation strain. Plate 3.4 shows that voids occur from large inclusions at

the plastic shear strain of 0.003. This result is consistent with the idea that the energy of a surface increases as the particle curvature increases. Thus, some smaller particles might become the nuclei of voids with increasing the plastic shear strain.

The size of voids was measured from a series of the interrupted tensile specimens with incremental plastic shear strain. The diameter of voids was calculated from the area of voids which have approximately elliptical shape. The average diameter, d_{av}, of voids in each specimen was obtained from 15 voids, which were random selected on ten photomicrographs, as described in Section 3.4. The measured results are given in Table 7.1. The void distribution in the matrix can be described by the average intervoid spacing. The mean nearest-neighbour void spacing, λ, can be estimated by [98],

$$\lambda=\frac{1}{2}d_{av}\left(\sqrt{\frac{2\pi}{3V_v}}-\sqrt{\frac{8}{3}}\right) \qquad \ldots\ldots\ldots\ldots(7.1)$$

where Vv is the volume fraction of voids. Based on the previous measurements of the void growth, the relevant results about the average intervoid spacing in each specimen are obtained by using the above equation, and given in Table 7.1. Furthermore, the variation of the average void diameter and mean nearest-neighbour void spacing as a function of the plastic shear strain is shown in Fig. 7.1. It is found that the average void diameter slightly increases and the mean nearest-neighbour void

Table 7.1 : Average void diameter and mean nearest-neighbour void spacing measured from a series of the interrupted tensile specimens

Specimen No.	17T	16T	15T	14T	13T	12T	11T	10T	9T
$\bar{\varepsilon}^p$	0.011	0.018	0.029	0.034	0.043	0.057	0.067	0.078	0.093
Vv	0.00178	0.00171	0.00183	0.00187	0.00267	0.00190	0.00208	0.00201	0.00254
$d_{av.}$, μm	2.28	2.67	2.25	2.24	2.88	2.21	2.37	2.54	2.62
λ, μm	37.0	44.3	36.0	35.5	37.8	34.7	35.5	38.7	35.3

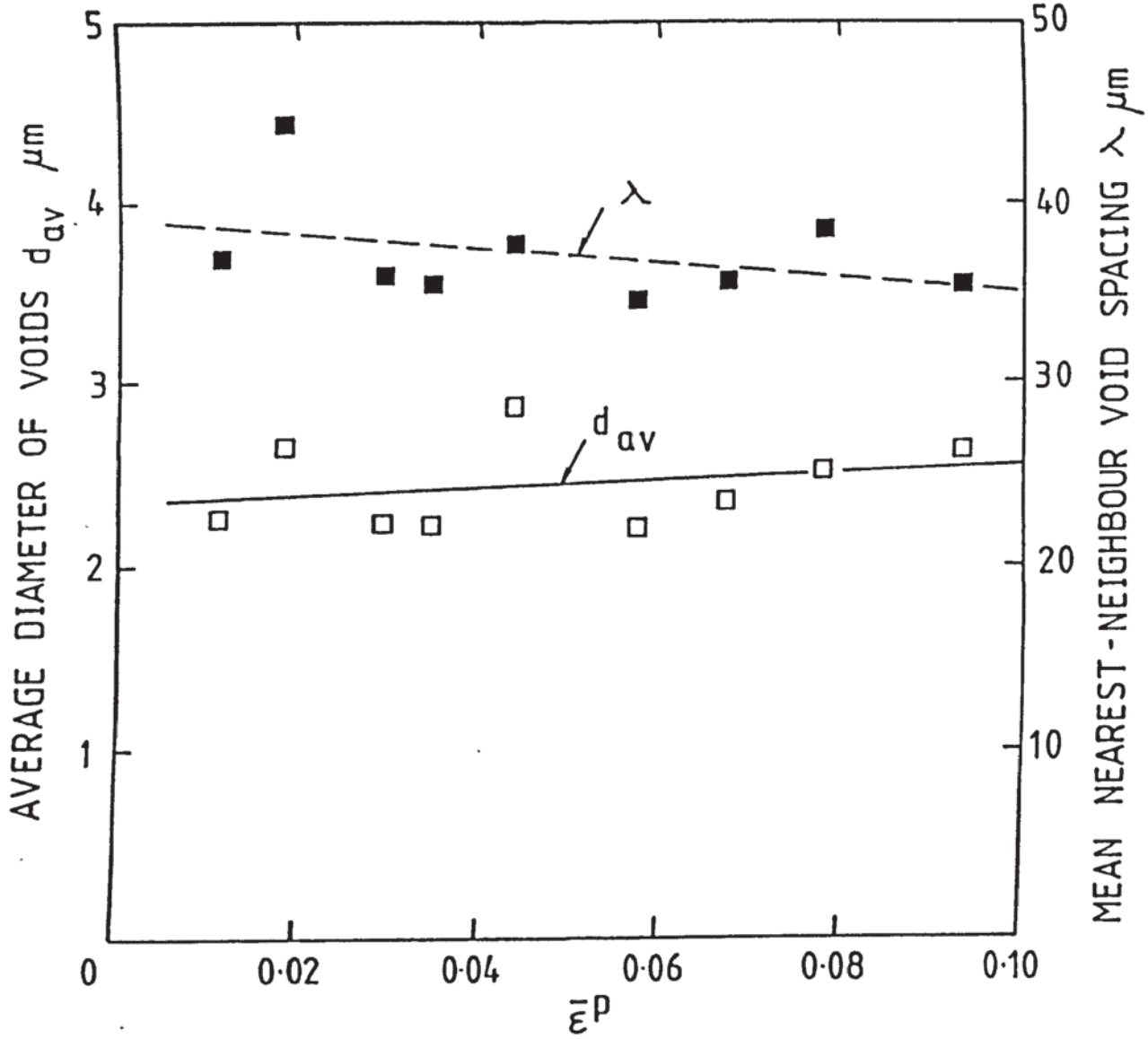

FIGURE 7.1 Variation of the average void diameter and mean nearest-neighbour void spacing as a function of the plastic shear-strain in uniaxial tension

spacing slightly decreases with increasing the plastic shear strain. That is, both the void nucleation rate and its growth rate are very slow with the plastic shear strain before the neck formation. It might be inferred that both further void nucleation and its growth contribute the increase in the relative void volume with increasing the plastic shear strain. The further void nucleation with the plastic strain may also be found in the measurements of the number of voids per unit area, as shown in Table 3.2.

Stress triaxiality enhances the void nucleation and its growth. It has been pointed that the hydrostatic stress causes the decrease of the nucleation strain [73]. The experimental observations indicate that under the condition of the higher stress triaxiality small-scale voids may occur besides the void growth. The average void diameter and intervoid spacing were also measured and calculated from random 15 voids in 0.4 to 0.6 mm ahead of the notch root in the Charpy-size bending specimens, as shown in Table 7.2. The specimens were tested in slow bend at room temperature. Compared with the smooth tensile tests, the average void diameter slightly increases and the average intervoid spacing slightly decreases. Additionally the side-groove constraint makes the average void diameter increasing slightly, and the average intervoid spacing decreasing slightly, compared with the standard Charpy specimens in the same location observed.

Table 7.2 : Average void diameter and mean nearest-neighbour void spacing, measured at 0.4 to 0.6 mm ahead of the notch root in Charpy-size specimens

Specimen type and No.		$\bar{\varepsilon}^p$	Vv	$\sigma_m/\bar{\sigma}$ (T_1=3.83)	dav. (μm)	λ (μm)
Standard Charpy	B1T	0.145	0.00313	1.01	3.1	37.4
	B2T	0.126	0.00275	0.89		40.0
Standard Charpy with side-grooves	S7T	0.215	0.00463	1.16	3.4	33.2
	S8T	0.190	0.00438	1.24		34.2

However, in the pre-cracked side-grooved specimens, the density and size of voids increase ahead of the precrack. Plate 5.14 shows the formation of the small-scale voids which are based on small-scale inclusions or iron carbide. Some voids large grow, even coalesce locally, as shown in Plate 5.15. Due to a larger difference in the size of voids, the average void diameter was not measured in the precracked specimen. Thus, it is clear from the above discussion that the hydrostatic stress can enhance the void nucleation and its growth. It should be noted from the experimental observations that the voids which develop from large inclusions may not always grow until they coalesce. At the same time, due to the local stress-strain concentration, the second generation small-scale voids already gradually nucleate and grow before the large voids coalesce.

It is well-known that inclusions play an important role in the ductile fracture processes. It is less clear whether the nucleation strain is sensitive to the volume fraction of the inclusions. Experimental observations show that for the test steel voids occur mainly at the inclusions of MnS, Al_2O_3 and CaO or their mixture. Occasionally, voids also occur at MnO, FeO, or the inclusion including cobalt. Basically voids form by the separation of the interface between the ferrite matrix and non-metallic inclusions. Plate 3.2 shows an intermediate stage of this separation. The voids tend to form over small regions of the particle surface, and spread gradually across the interface as the voids grow. Also

Plate 3.3 shows that a microcrack starts forming from the void.

7.2 Void Growth Coefficient

Current models of void kinetics [71] suggest that void growth, known to occur in ductile failure, depends on microstructure, plastic deformation, in particular on stress state, described by the ratio of mean stress to effective flow stress. On the basis of the experimental void growth law proposed by EPRI report [72], several methods were tried to determine the void growth coefficient, which is available for BS4360 Grade 50D steel. Additionally, this coefficient should reflect an influence of the plastic strain and stress triaxiality upon the practical void growth in a wide range of the constraint. Some aspects in regard to determining the void growth coefficient will be discussed as follows.

7.2.1 Conditions for Achieving the HRR Field in the Pre-cracked Side-Grooved Charpy-Size Bend Bar

In the Method III for determining the void growth coefficient, as mentioned previously, HRR field analysis were decided to use for estimating the stress triaxiality at some distance ahead of the crack tip in a pre-cracked side-grooved Charpy-size specimen.

Under large scale yielding condition, the dominance of the

HRR singularity appears to be quite dependent on the specimen types and work hardening exponent [41]. It has been pointed for a cracked bend bar that the stresses and strains in the specimen are in good agreement with the HRR fields over distance of $X\sigma_o/J<3$ for ligament down to $c\sigma_o/J=30$. The metallographic examination has been conducted at 0.5 mm ahead of the crack tip in the pre-cracked side-grooved specimen with $a/W= 0.5$. Is it true that the HRR field is still a good description of the stresses at this small distance in the specimen of our interest? Based on the relations of $\delta_t=d_n J/\sigma_o$ and $d_n\simeq 0.34$ for the $n=4.5$ [41], the characteristic length, J/σ_o, may be converted from the crack tip opening displacement, δ_t (note that here the δ_t value is obtained from the gauge length measurement at the blunted crack tip). Due to $\delta_t=0.40$mm at the tests of room temperature, thus, the $J/\sigma_o=1.18$mm. This result shows that x=3.5mm, corresponding to $x\sigma_o/J=3$, for ligament down to c=40mm, corresponding to $c\sigma_o/J=35$, for the pre-cracked side-grooved specimens, if we examine the metallography at 0.5mm ahead of the crack tip, this would correspond to $x\sigma_o/J=0.42$ and $c\sigma_o/J=4.2$. Thus, it is possible that the HRR field is still a good approximation to the stress singularity at this small distance ahead of the crack tip. It might be noted that the influence of the side-grooves upon thickening bend bar is ignored, when the stresses behaviour is evaluated by the work of Shih and German. Furthermore, the availability of the HRR field in the immediate vicinity of the crack tip is investigated by the void growth studies. The details

will be discussed in Section 7.4.

7.2.2 Comparison of the Void Growth Coefficients Determined by Several Methods

The void growth coefficient determined by Method I was based on a series of interrupted tensile specimens which were tested before neck formation. The relative void volume was measured in these specimens with different levels of plastic shear strains. In this case, the increase of the relative void volumes was very slow with increasing the plastic shear strain. At the same time, the standard deviations were much higher than the mean values in the statistical measurement of the relative void volume. Thus, the measurement error exerted a significant influence on the slope in the linear fit between ln $(^{Vv}/Vo)$ and $(\bar{\varepsilon}^p - \bar{\varepsilon}^p_o)$, subsequently on the void growth coefficient, T_1 (T_1 = slope of the linear fit/0.33).

As contrasted with the Method I, the void growth coefficient determined by Method II has a rather higher accuracy. A round tensile specimen was pulled to fracture. The relative void volume as large as possible might be obtained in the uniform deformation region of the specimen. The statistical measurement accuracy of the void growth also increases. In this case, the slope of the linear fit between ℓn $(^{Vv}/Vo)$ and $(\bar{\varepsilon}^p - \bar{\varepsilon}^p_o)$ basically depends on the two terminals. One is an original point in the co-ordinate, the other is a group of measured values, as shown in Fig. 4.5. It might be expected that

the linear fit slope established in this way is more rational. Both the round tensile tests and pre-cracked side-grooved bar tests were used in the Method III for determining the void growth coefficient. The void growth coefficient was obtained from the two groups of terminal values, which have very different stress triaxialities. It might be considered that the void growth coefficient determined by the Method III has much general significance in the wide range of the constraint. Thus, the void growth coefficient of 3.83 is selected to evaluate the stress triaxiality ahead of the notched or precracked bodies of our interest.

Fortunately, the void growth coefficient of 3.83 determined from BS4360 Grade 50 D steel in our research work is similar to the coefficient of 3.2 determined from A533B steel in EPRI report [72]. Only is our coefficient slightly higher than the EPRI's coefficient, as shown in Fig. 7.2. This may be related to the testing materials. The different materials have the different inclusion size distribution, which determines the relative void volume at nucleation. Furthermore, the void growth coefficients are determined from the different experimental procedures. In the EPRI report the coefficient was obtained experimentally from measurements on a series of notched and unnotched tensile specimens. The void growth was observed in the necking part of the specimens. A rather high threshold strain for nucleation was assumed. This strain was corresponding to the strain at the ultimate tensile strength of the material. At the

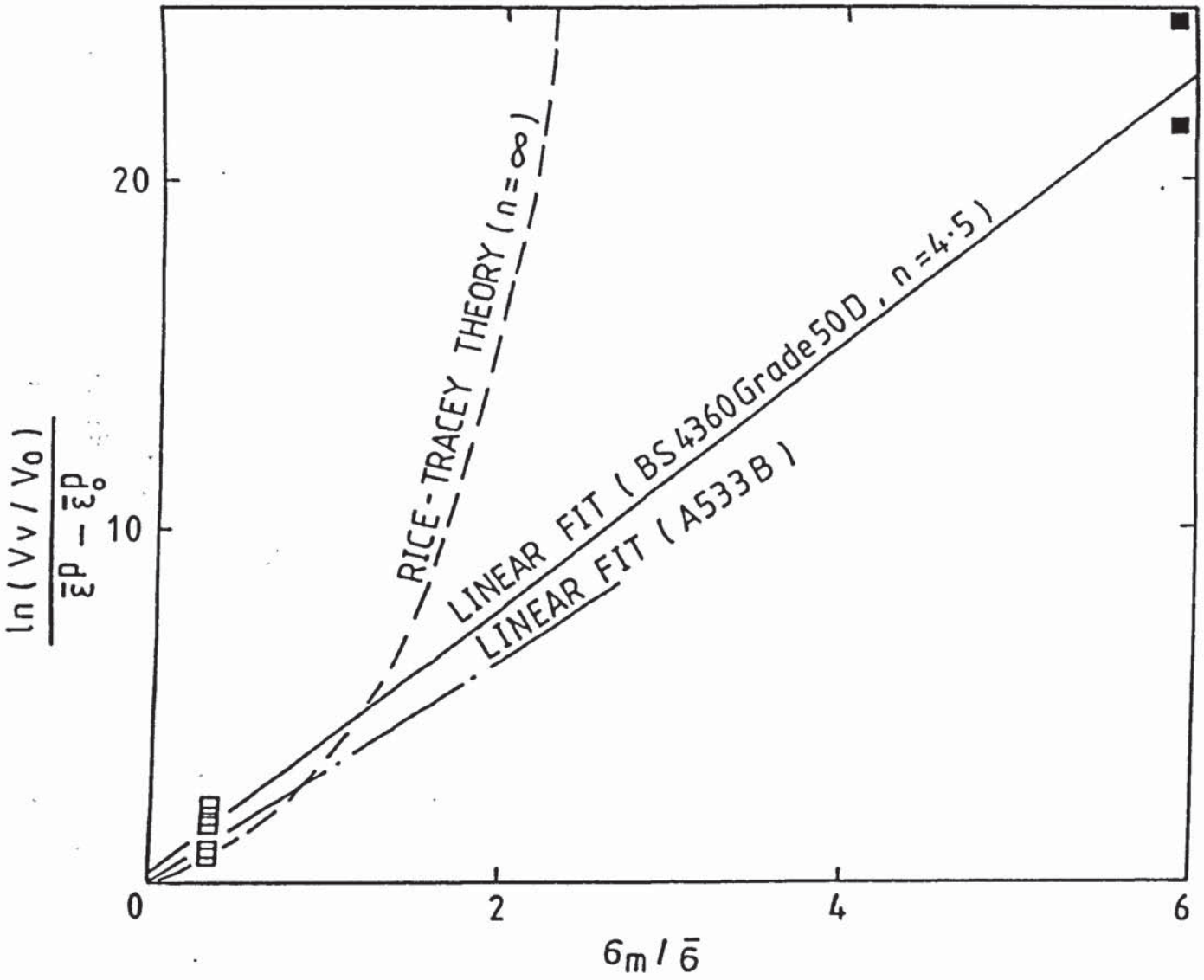

FIGURE 7.2 Void growth relations with plastic shear strain and stress triaxiality

same time, it was assumed that the nucleated voids occurred in a range of sizes corresponding to the range of inclusion sizes. Thus, the EPRI report took the specific volume of inclusion to be the initial relative void volume. However, in our experimental procedure, a rather low strain was determined to be the strain for nucleation in which only a partial inclusion cause void nucleation. Therefore it might be expected that the EPRI's assumption is still rational, as the strain for nucleation is largely overestimated. Although there are the above differences in testing procedure, the similar voids growth coefficient are obtained in the two pressure vessel materials.

7.3 Estimation of Stress Triaxiality Ahead of the Notch and Crack Tip

7.3.1 Constraint of the Charpy-Size Specimens

Using the experimental void growth law proposed by EPRI report[72], and the void growth coefficient determined by this experimental work, the level of the stress triaxiality ahead of the notch or crack tip in the Charpy-size specimens may be estimated. Additionally, it is possible to evaluate the effect of side-grooves on the constraint of Charpy-size specimens.

Estimating results have indicated that the average stress triaxiality ahead of the notch root, $\sigma_m/\bar{\sigma}$=0.95 and 1.20

for standard CVN and side-grooved CVN specimens, respectively; and the stress triaxiality ahead of the pre-cracked tip, $\sigma_m/\bar{\sigma}$=4.30 and 6.04 for nonside- and side-grooved specimens, respectively. These results combined with those estimated from the EPRI's coefficient are given in Table 7.3. It might be thought that the state of the plane strain has already been attained at the specific distance ahead of the notch root in the midthickness of the specimens. The through-thickness stress has been generated. The side-grooves raise the constraint ahead of the notch root. In the two kinds of pre-cracked specimens the constraint ahead of the crack tip is expected to approach to severe triaxial stress state. It is clear that the precrack is a very effective stress triaxiality raiser, compared with the influence of the side-grooves upon the triaxiality increase.

Usually, the influence of the side-grooves on the constraint may be explained as follows. For example, at the crack tip of the pre-cracked specimens, the side-grooves are 24% and 29% of gross thickness for specimen No. S13V and S19V, separately. Since the crack initiates in the centre of the specimen under plane strain condition the effect of side-grooves appears to be that of restricting or eliminating the plane stress 'side ligaments', i.e. the regions of through-thickness deformation [84]. In pre-cracked side-grooved specimens,

Table 7.3 : Stress triaxiality estimated at the distance of 0.5 mm ahead of the notch or crack tip in different CVN specimen geometries

Specimen type	Specimen No.	$\frac{\ell n(V_v/V_o)}{(\bar{\varepsilon}^p - \bar{\varepsilon}^p_o)}$	$\sigma_m/\bar{\sigma}$		
			Our linear fit (T_1=3.83)	EPRI linear fit (T_1=3.2)	Rice-Tracey theory (n=∞)
Standard Charpy	B1T	3.869	1.01	1.21	1.05
	B2T	3.418	0.89	1.07	0.97
Standard Charpy with side-grooves	S7T	4.436	1.16	1.39	1.13
	S8T	4.730	1.24	1.48	1.17
Pre-cracked Charpy	B19V	17.949	4.69	5.61	2.05
	B23V	14.929	3.90	4.67	1.93
Pre-cracked Charpy with side-grooves	S13V	24.682	6.44	7.71	2.21
	S19V	21.568	5.63	6.74	2.17
Smooth tensile bar ($\bar{\varepsilon}^p$=0.103)	-	1.55	0.41	0.48	0.55

severe constraint is imposed on the side ligaments producing a plane strain state. Thus the through-thickness stress is less likely to relax and the corresponding crack growth will initiate across the whole specimen thickness instead of merely at centre thickness. Typical photographs are shown in Plate 6.6.

It may be also clearly seen from the impact tests that the side-grooves raise the stress triaxiality of the notched specimen. At the test temperature of $0^{o}C$, the average lateral contraction at the notch root are 21.3% and 6.2% for standard CVN and side-grooved CVN specimens, separately. Furthermore, as discussed previously in Section 5.2.2. and 5.3.2, the influence of the different modified CVN specimen geometries upon the constraint may be inferred from four series of calibration photographs, as shown in Plates 5.4, 5.5, 5.10, and 5.11. If the white obscure regions corresponding to near maximum bending load were assumed to schematically indicate the plastic zone in lateral surfaces of the specimens, it is obvious that in the four series of photographs standard CVN specimen has the maximum dimension of the white obscure region. Side-grooves make the obscure region decreasing. No obscure region can be found on the lateral surfaces of the pre-cracked side-grooved specimen. That is, no severe plastic deformation which usually exists in the region of the near lateral surfaces occurs. At the same time, for the standard CVN and pre-cracked CVN specimens, the initial growth of the crack has an angle of about 45^{o}

with the loading direction. However, for side-grooved CVN and side-grooved pre-cracked CVN specimens, the crack growth are very well guided by the side-grooves constraint. Therefore, it is indicated that the stress triaxiality estimated by the void growth studies seems to be rational.

Based on these studies, it is concluded that the side-grooves raise the stress triaxiality ahead of the notch or crack tip. However, the precrack with a certain ratio of the crack length to specimen depth is much effective raiser of the stress triaxiality. If the stress state ahead of the crack tip and fracture mode in this small specimen is identical to that in large specimen or structure, the pre-cracked side-grooved Charpy-size specimen offers considerable promise in application of the inexpensive specimen to the elastic-plastic failure analysis.

7.3.2 Longitudinal Deformation Fields Ahead of the Notch or Crack Tip

In order to make a comparison of the constraints among the four kinds of the Charpy-size specimens, and investigate the influence of the side-grooves upon increasing the constraint of the specimens, it is also very helpful to observe the longitudinal deformation fields ahead of the notch or crack tip. In Section 5 the variation of the notch or crack opening displacement

field was calibrated with the load-point displacement in the Charpy-size specimen bend tests, as given in Tables 5.4, 5.5, 5.18 and 5.19. Using the interpolation, the notch or crack opening displacement and the longitudinal shear strain fields at the point of maximum load corresponding to the instability in bend specimens can be obtained. The interpolated values of the opening displacement (NOD or COD) and shear strain (γ) are given in Table 7.4 and Figs. 7.3 and 7.4 with the distance ahead of the notch or precrack tip.

It is clear from a comparison between the notched and pre-cracked specimens that the crack tip opening displacement during instability, δ_m, in the pre-cracked specimens is approximately half of the value in the notched specimens. This coincides with the explanation of that the COD at instability of ductile tearing is relatively dependent of the specimen dimension. The pre-cracked specimens with the small ligament lead to small δ_m values. It may be worth notice that the decrease in the specimen thickness, due to the side-grooves, does not cause the obvious change in δ_m values. This is specially true for the notched specimens. It may be seen from the pre-cracked specimens that the δ_m value in the nonside-grooved specimen is slightly larger than that in the side-grooved specimen. This may be related with the differences in the precrack length. $a/W = 0.525$ in the pre-cracked nonside-grooved specimen, No. B21V, while $a/W=0.546$ in the pre-cracked side-grooved specimen, No.S17V.

Table 7.4 : Longitudinal deformation fields ahead of the notch or crack tip for four Charpy-size specimens with different geometrical modification at maximum bending load.

Distance ahead of the notch root, mm		0.0	0.1	0.2	0.3	0.4	0.5	0.6	0.7	0.8	0.9	1.0	1.1	1.2	1.3	1.4	1.5
Specimen B3T	NOD,mm	1.08						0.33	0.29	0.27	0.23	0.19	0.15	0.12	0.10	0.09	0.08
	γ	0.431						0.176	0.156	0.147	0.130	0.107	0.089	0.071	0.059	0.053	0.046
Specimen S2T	NOD,mm	1.09	1.00	0.93	0.84	0.78	0.70	0.67	0.64	0.61	0.58	0.56	0.53				
	γ	0.429	0.404	0.381	0.356	0.340	0.317	0.305	0.296	0.287	0.278	0.269	0.257				

Distance ahead of the crack tip,mm		0.0	0.14	0.15	0.34	0.35	0.54	0.55
Specimen B21V	COD,mm	0.54		0.48		0.36		0.26
	γ	0.138		0.124		0.096		0.071
Specimen S17V	COD,mm	0.47	0.44		0.39		0.34	
	γ	0.122	0.115		0.103		0.091	

NOTE:

All the values are interpolated from Tables 5.4, 5.5, 5.18 and 5.19.

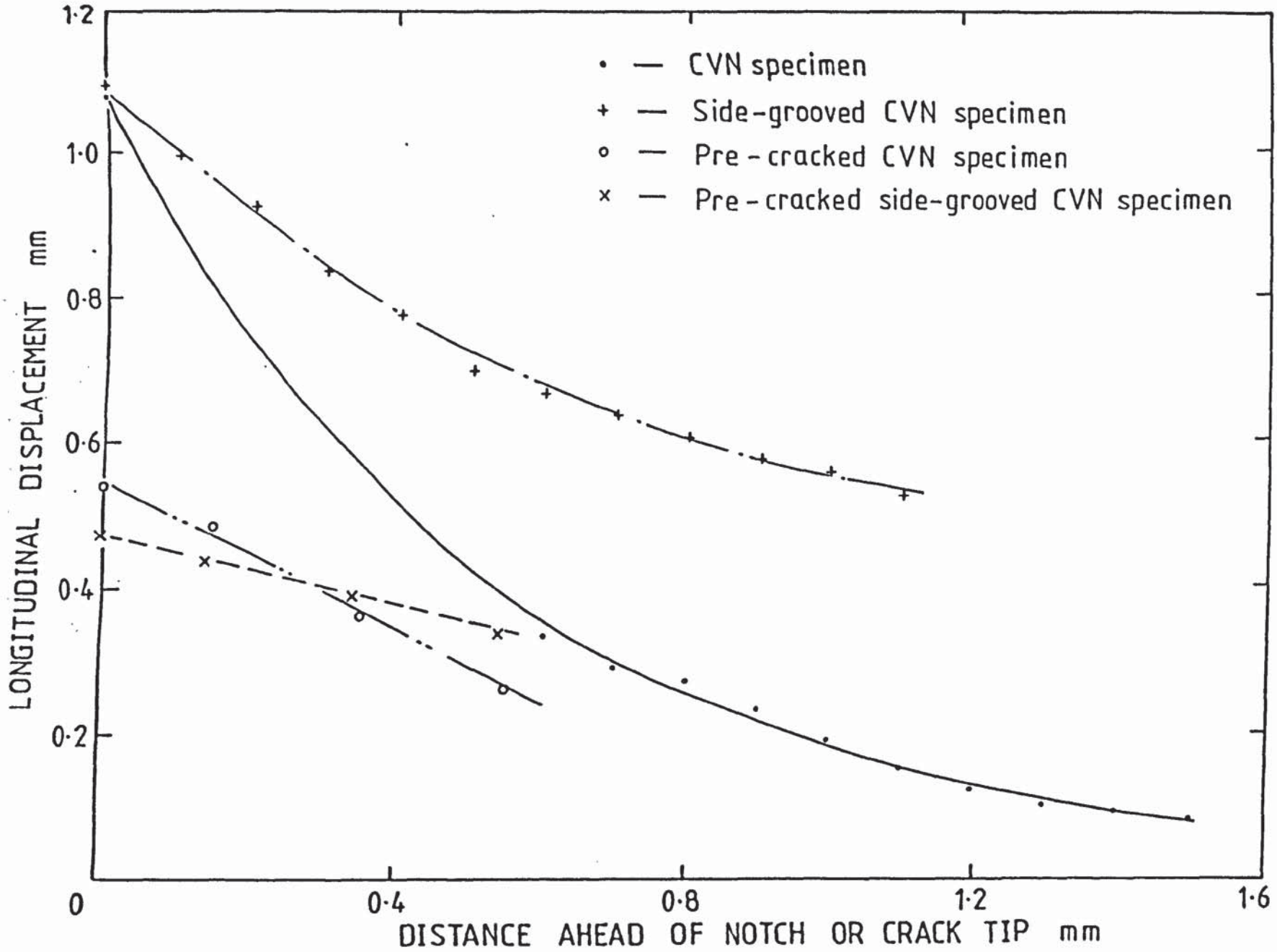

FIGURE 7.3 Longitudinal displacement fields at maximum bending load for four Charpy-size specimens with different geometrical modification, tested at room temperature.

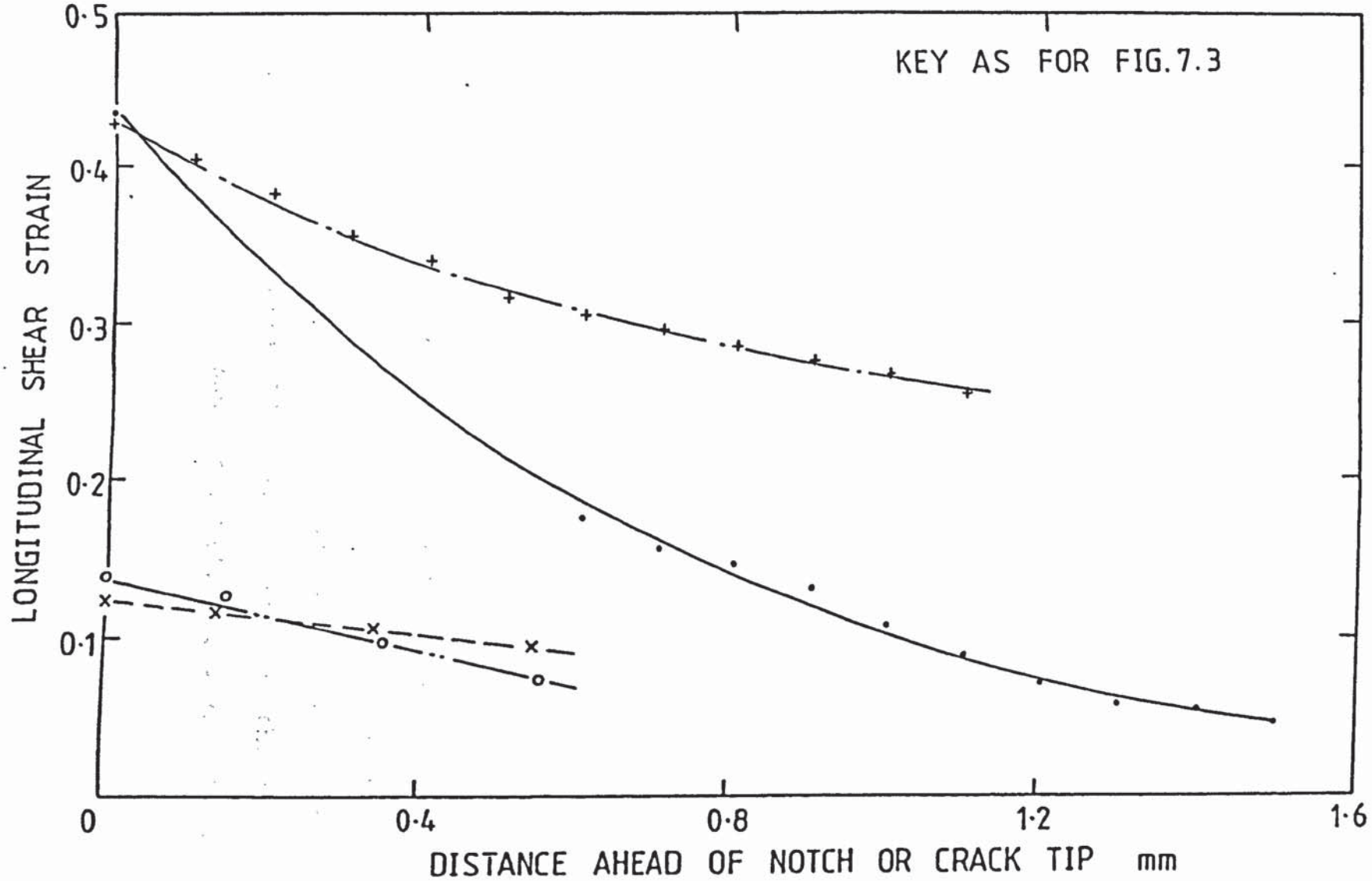

FIGURE 7.4 Longitudinal shear strain fields at the instantaneous maximum bending load for four Charpy-size specimens with different geometrical modification, tested at room temperature.

Side-grooves significantly change the characteristics of the longitudinal deformation fields ahead of the notch or crack tip. In the side-grooved specimens, generally, the notch or crack opening displacement and longitudinal shear strain fall much slowly with the distance ahead of the root or tip. This situation is similar to that which occurs in the round tension specimens with pre-machined circumferential notch in which the longitudinal strain distribution may be constant at the minimum cross-section when fully plastic condition is reached [69]. The rather weak singularity of the longitudinal strain ahead of the notch or crack tip is caused by the constraint of the three surface grooves. Thus, this strain distribution characteristics also reflects the increase in the constraint ahead of the notch or crack tip. The intense strain concentration ahead of the notch occurred in the standard CVN specimen is accompanied by the decrease in stress triaxiality produced by the large geometry change. Additionally, for the nonside-grooved specimens, the singularity of the longitudinal strain ahead of the notch tip is much weaker in the pre-cracked specimen than in the notched specimen. It is indicated that acuity of the notch has a significant influence upon the strain field, subsequently upon the constraint ahead of the notch tip.

7.3.3 Effect of the Strain Hardening Exponent on the Stress Triaxiality and Void Growth

In a perfectly plastic material for plane strain the stress triaxiality can be obtained from the Hencky equation of slip line field analysis. In the diamond ahead of the crack tip

$$\sigma_m/\bar{\sigma} = \frac{\pi+1}{\sqrt{3}} \qquad |\theta| < \pi/4 \qquad \text{.....(7.2)}$$

This slip-line field is only appropriate at distances from the crack tip which are large compared to the crack tip opening, that is, at a small geometry change case. The slip-line field can be regarded as the limiting case of a general power-hardening relation. From the HRR field analysis, the triaxiality ahead of the crack tip is a function of the strain hardening exponent, n, and the polar co-ordinate, θ

$$\sigma_m/\bar{\sigma} = f(n,\theta) \qquad \text{.....(7.3)}$$

Rice and Rosengren [40] have shown the very rapid rise of the ratio of the maximum normal stress to the equivalent stress along the summetry line ahead of the crack with strain hardening exponent, N, ($N=\frac{1}{n}$). The rapid rise over the value of $\sigma_{\theta\theta}/2\tau\big|_{\theta=0}=(1+\frac{\pi}{2})$ is anticipated from perfect plasticity. This value can be interpreted as follows. The two groupings $\sigma_m/\bar{\sigma}$ and $\sigma_{\theta\theta}/\bar{\sigma}$ are related in plane strain by

$$\frac{\sigma_m}{\bar{\sigma}} = \frac{\sigma_{\theta\theta}}{\bar{\sigma}} - \frac{1}{\sqrt{3}} \qquad \ldots\ldots\ldots\ldots (7.4)$$

For the von Mises yield criterion $\bar{\sigma} = \sqrt{3}\,\tau$. At $\theta=o$

$$\frac{\sigma_{\theta\theta}}{2\tau} = \frac{\sqrt{3}\sigma_{\theta\theta}}{2\bar{\sigma}} = 1 + \frac{\pi}{2}$$

Thus,

$$\frac{\sigma_m}{\bar{\sigma}} = \frac{2}{\sqrt{3}}\left(1+\frac{\pi}{2}\right) - \frac{1}{\sqrt{3}} = \frac{\pi+1}{\sqrt{3}}$$

This value is just equal to the slip-line field solution for perfect plasticity.

For the condition of n = 3 and 13, the θ-variations of the stresses at the tip of a tensile crack for plane strain was calculated numerically by Hutchinson [39]. Using the Eq. (4.14) and a simple linear interpolation, the stress triaxiality ahead of the crack with the hardening exponent, n, may be approximately estimated and shown in Table 7.5 and Fig. 7.5. A best fit relationship is given by

$$\frac{\sigma_m}{\bar{\sigma}} = 2.566 \exp\left(\frac{3.536}{n}\right) \qquad \theta = o \qquad \ldots\ldots\ldots (7.5)$$

It is found from the above equation that for the ideally plastic condition ($n=\infty$) $\sigma_m/\bar{\sigma}=2.57$.. This value is slightly higher than 2.39 expected. Thus the above equation leads to a reasonable approximation for describing the effect of the strain hardening exponent upon the stress triaxiality.

Table 7.5 : Estimated stress triaxiality ahead of a bending crack for plane strain with different n values, based on Ref. 39 and Eq. (4.14)

n	3	4	5	6	7	8	9	10	11	12	13
$\tilde{\sigma}_\theta$	1.93	(1.997)	(2.064)	(2.131)	(2.198)	(2.265)	(2.332)	(2.399)	(2.466)	(2.533)	2.60
$\tilde{\sigma}_r$	1.66	(1.669)	(1.678)	(1.687)	(1.696)	(1.705)	(1.714)	(1.723)	(1.732)	(1.741)	1.75
$\tilde{\sigma}_e$	0.24	(0.287)	(0.334)	(0.381)	(0.428)	(0.475)	(0.522)	(0.569)	(0.616)	(0.663)	0.71
$\sigma_m/\bar{\sigma}$	7.48	6.39	5.60	5.01	4.55	4.18	3.88	3.62	3.41	3.22	3.06

* The values in parentheses were calculated from interpolation.

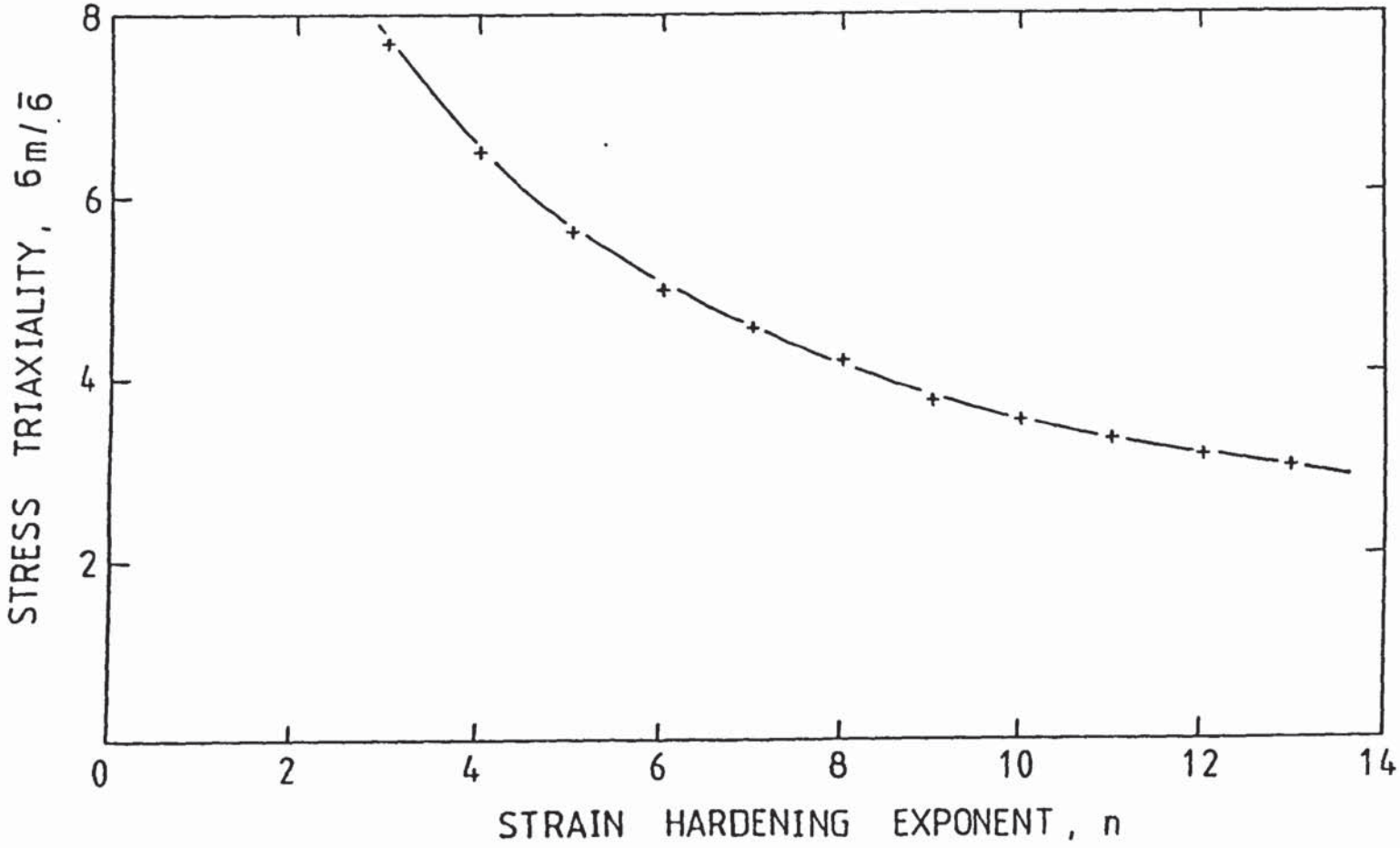

FIGURE 7.5 Influence of the work hardening exponent upon the stress triaxiality ahead of a tensile crack tip for plane strain.

However, due to n=4.5 for the testing material, the practical stress triaxiality ahead of the crack in plane strain condition will be larger than that based on the slip-line solution.

Strain hardening can increase stresses not only by increasing the yield stress with increasing strain but also by changing the stress state. Thus the mild steel having greater hardening behaviour may large develop local peak stresses and triaxiality ahead of a crack.

In this section the effect of the strain hardening exponent on the stress triaxiality in our interesting Charpy-size specimens may also be inferred by the void growth studies. Because the void growth coefficient of 3.83 was obtained from experimental investigation, the experimental void growth law, Eq.(4.1) must be representative of the practical relation between the void growth rate and triaxiality in our interesting mild steel with strain hardening. Additionally, Rice and Tracey [71] have proposed a theoretical law for the void growth relation in perfectly plastic material, as shown in Eq. (1.57). The void growth relations for perfectly plastic and practical materials are shown in Fig. 7.2.

Based on the measured relative void volumes and plastic shear strains, the stress triaxiality at 0.5mm ahead of the notch or crack tip in the Charpy-size specimens can be evaluated by the two void growth relations of n=4.5

and n=∞. The calculated results are given in Table 7.3. It is found for the notched specimens that the stress triaxiality estimated by the experimental void growth relation of n=4.5 is similar to that estimated by the void growth relation of n=∞. However, in the pre-cracked specimens there are important differences in the stress triaxiality, if the different void growth relations of n=4.5 and n=∞ are used to evaluate the triaxiality. The triaxiality estimated by the relation of n=∞ is lower than that by the experimental relation. Specially it is true for the pre-cracked side-grooved specimens with severe constraint. Therefore, for the small triaxiality, for example, generated in the notched specimens, it is a valid approximation that the stress triaxiality may be evaluated from the simple Rice-Tracey theoretical relation in a perfectly plastic material. However, for the large triaxiality, for example, generated in the pre-cracked specimens, it should be considered that the effect of the strain hardening exponent on the stress triaxiality and void growth rate.

As hardening can raise stresses, the presence of large tensile stresses ahead of the crack is obviously important for the ductile fracture processes involving the nucleation, growth and final coalescence of voids. McClintock [75] and Tracey[99] have studied the effect of the strain hardening on the rate of the void growth. From Tracey's consideration, the strain hardening no doubt reduces the void growth, but the increase in triaxiality with strain

hardening will increase the void growth., According to the investigation in this work, the net void growth is decelerated due to strain hardening for the values of the stress triaxiality, $\sigma_m/\bar{\sigma}$, of more than about one; but for the same hardening material, the void growth will increase due to the stress triaxiaility.

7.4 Availability of the HRR Field Analysis in the Vicinity of the Crack Tip by Void Growth Studies

Based on the previous discussion in Section 4, the stress triaxiality calculated from HRR analysis is only a function of the strain hardening exponent, n, and the polar co-ordinate, θ, $\sigma_m/\bar{\sigma} = f(n,\theta)$. Although the stress state is independent of the distance, r, it is expected that the HRR analysis is approximately valid at about 0.5mm ahead of the crack tip for the pre-cracked side-grooved bend specimens. The $\sigma_m/\bar{\sigma}$ value is 5.97. As the strain causes the crack tip to open and blunt and the crack tip moves forward by Poisson contraction along the crack plane producing the stretch zone, thus the state of the plane stress exists in this zone. Here we attempt to investigate the distribution of the relative void volume with the distance ahead of the crack tip. Subsequently, the stress state change may be evaluated in the immediate vicinity of the crack tip. Furthermore, it can be checked whether the stress triaxiality determined from HRR field analysis is available at 0.5 mm ahead of the crack tip, where the relative void volume has been measured.

The relative void volumes ahead of the blunting crack tip are measured with the distance over each 0.2 mm (along the crack plane) x 1.0 mm (perpendicular to the crack plane) in the pre-cracked side-grooved specimen No. S13V and S19V, as shown in Fig. 7.6. The point counting technique used is the same as mentioned previously. The measured relative void volumes are given in Table 7.6 and Fig. 7.7. The plastic shear strains ahead of the crack tip are obtained from the interpolating calculation, based on the gauge length change in the microhardness indentations listed in Table 5.25. The strain gradient ahead of blunting crack tip is also shown in Fig. 7.7. The distance ahead of blunting crack tip is normalized by crack tip opening displacement, δ_t. The measurement results show that there is a peak in the void growth rate at the distance of approximate 1.2 δ_t ahead of blunting crack tip. Apparently, the maximum in the void growth is related to the combination of decreasing strain and increasing stress triaxiality with the distance in the immediate vicinity of the crack tip.

The fracture process may be thought as follows. As the load applied to the specimen increases, the inclusions near the crack tip experience increasing strains. Manganese sulphide et al particles are bonded very poorly to the ferrite matrix and voids are formed at very low plastic shear strain. The void growth obtains maximum development at a specific distance ahead of the crack tip, due

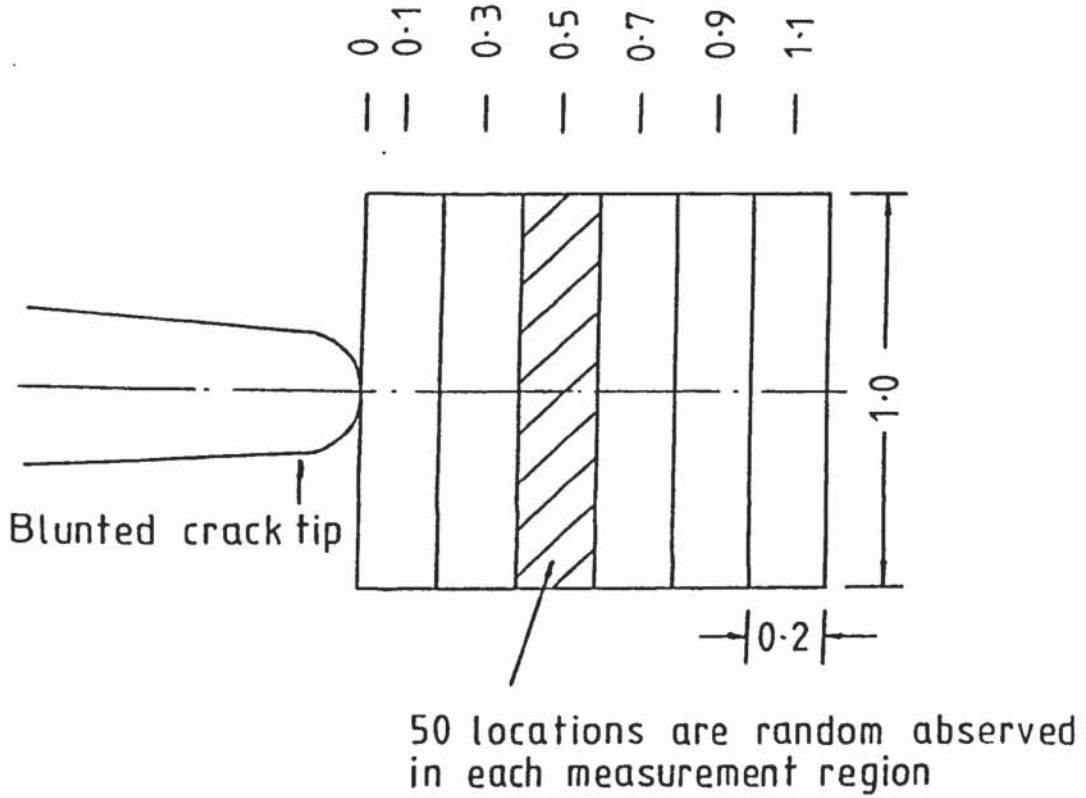

All the dimensions are in mm

FIGURE 7.6 Regions measuring the relative void volume ahead of the blunting crack tip

Table 7.6 : Void growth measured ahead of blunting crack tip in pre-cracked side-grooved specimens

Distance ahead of blunting crack tip, mm		0.1	0.3	0.5	0.7	0.9	1.1
Normalized distance ahead of blunting crack tip, x/δ_t	Specimen No.S13V (δ_t=0.39mm)	0.26	0.77	1.28	1.80	2.31	2.82
	Specimen No.S19V (δ_t=0.40mm)	0.25	0.75	1.25	1.75	2.25	2.75
$\bar{\varepsilon}^p$ interpolated from Table 5.25	Specimen No.S13V	0.093	0.081	0.072	0.060	0.047	
	Specimen No.S19V	0.095	0.086	0.076			
Measured V_v	Specimen No.S13V	0.00375	0.00975	0.01075	0.00600	0.00575	0.00425
	Specimen No.S19V	0.00450	0.00675	0.00800	0.00525	0.00550	0.00550
$\sigma_m/\bar{\sigma}$, calculated from our linear fit, T_1=3.83	Specimen No.S13V	2.11	5.58	6.67	5.42	6.74	
	Specimen No.S19V	2.57	4.11	5.26			

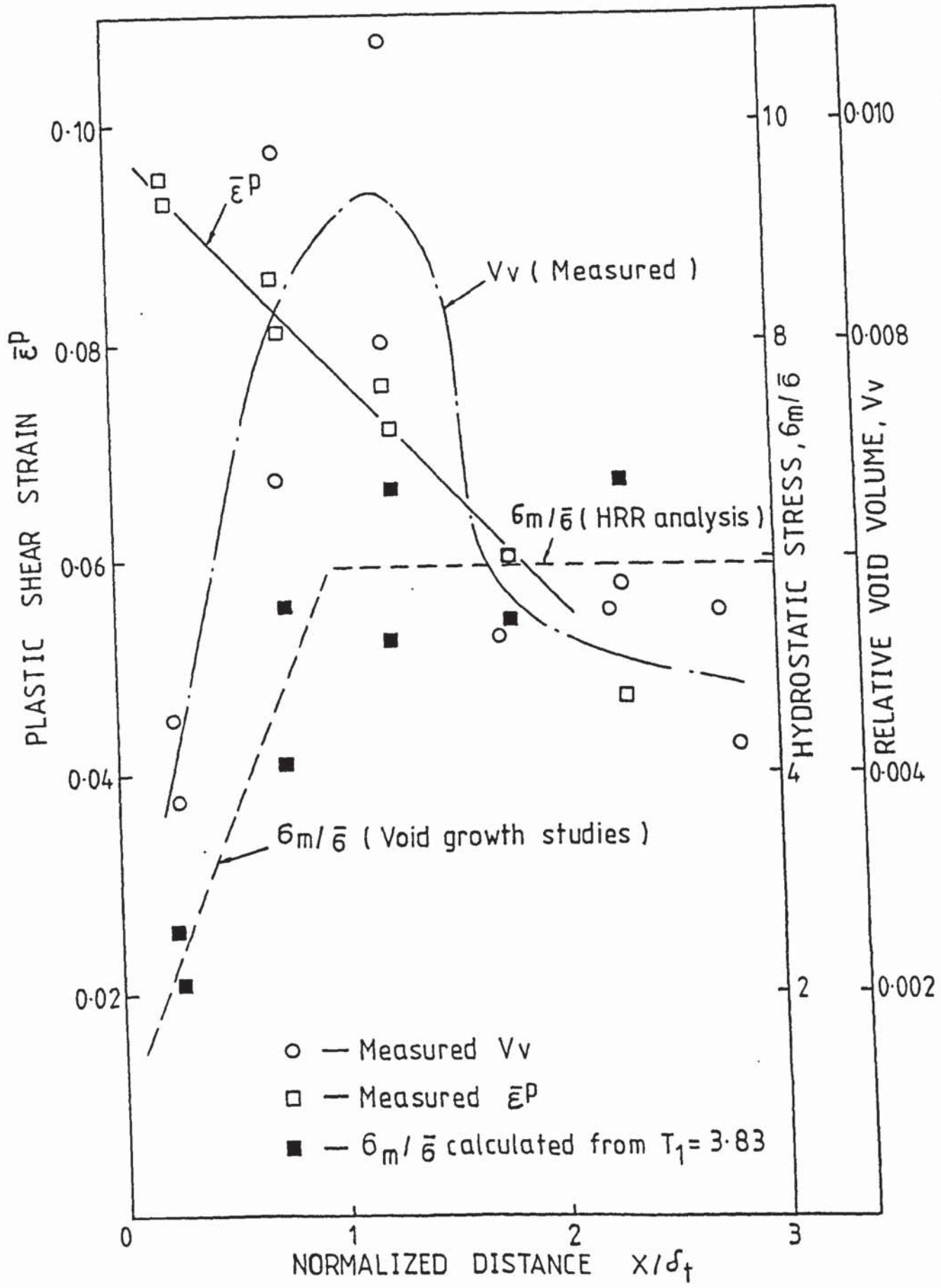

FIGURE 7.7 Stress triaxiality, plastic strain, and void growth distribution in front of the blunting crack tip at the crack initiation CTOD in pre-cracked side-grooved specimen, tested at 12°C

to the combined influence of the plastic strain and stress triaxiality. The initiation of macro-fracture may be considered as the point when the blunting crack tip first coalesces with the growing void nearest to the crack tip, as shown in Plate 7.1. This process of the linkage is similar to the process of void coalescence which takes place in the neck part during tensile specimen tests.

According to the void growth coefficient of 3.83, determined from the Method III, the variation of the stress triaxiality with distance ahead of the crack is estimated. The calculating results show that the stress triaxiality evaluated from HRR analysis is only appropriate at the distance beyond the $x/\delta_t > 1$ in our investigated range (x/δ_t=0.25 to 2.25). As the distance of interest approaches the crack tip ($x/\delta_t < 1$), the hydrostatic stress is linearly reduced. It is also indicated that the HRR field is a good description of the stresses at 0.5 mm ahead of the crack tip in the specimen of interest, where the void growth is measured and subsequently used to establish the void growth coefficient.

7.5 Critical Void Growth at Fracture Initiation in the Charpy-Size Specimen Bending Tests

In Section 5 the Charpy-size specimens used for estimating the stress triaxiality were loaded to initiate crack. If the void growth measured in the vicinity of 0.5 mm ahead

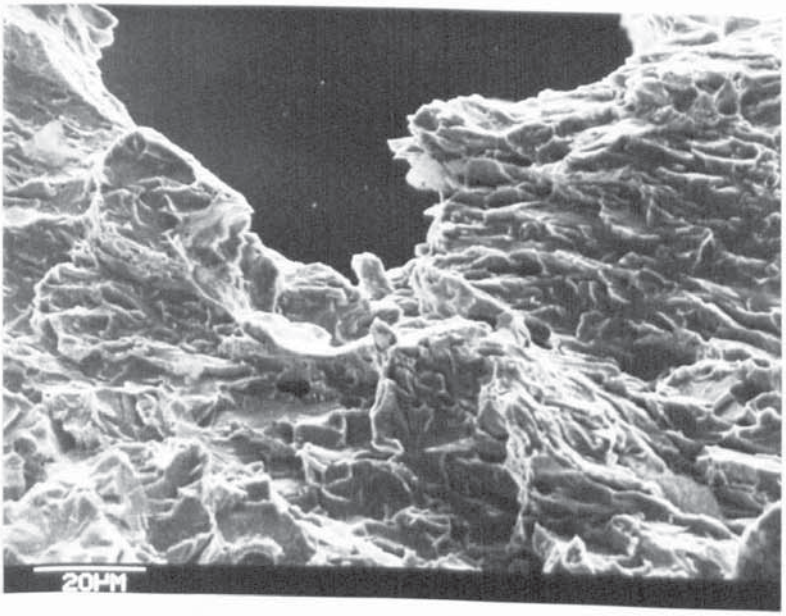

(a) Standard CVN specimen No. B2T

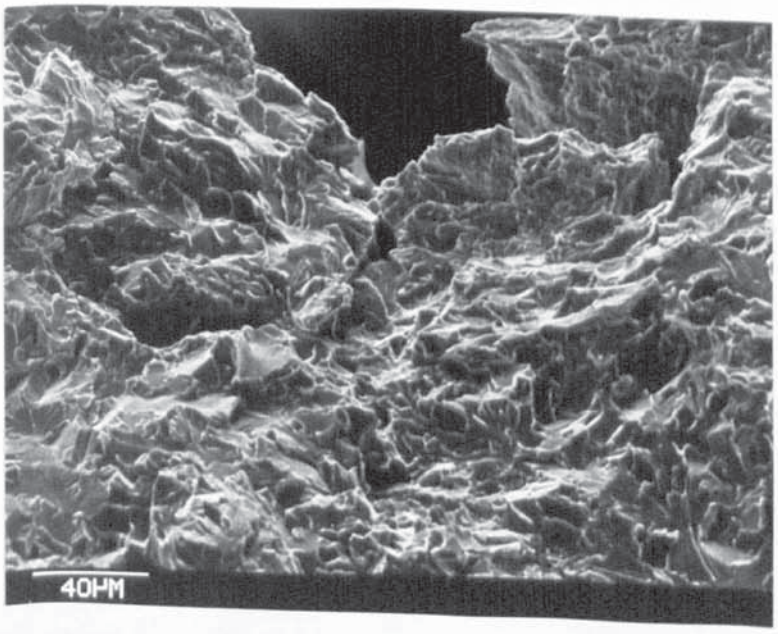

(b) Pre-cracked side-grooved specimen No. S13V

Plate 7.1 : Blunting notch tip and growing void nearest to the notch tip.

of the notch or crack tip can be thought to be the critical void growth at fracture, the critical relative void volume for the four kinds of the Charpy-size specimens are given in Tables 5.14 and 5.26. Additionally, the maximum value of the void growth may usually be obtained in the vicinity of that region, because the relative void volume distribution ahead of the notch or crack tip is not uniform with the distance. The critical void growth corresponding to initiate crack may also be indicated by

$$\frac{R_c}{R_o} = \left(\frac{(V_v)_c}{V_o} \right)^{\frac{1}{3}} \qquad \text{.....(7.6)}$$

where Ro and Vo are the initial radius and volume fraction of voids. Rc and (Vv)c are the critical radius and volume fracture of voids during fraction initiation. If it is assumed that the stress triaxiality estimated by the void growth studies is reasonable in principle, the critical void growth at fracture as a function of stress triaxiality is plotted in Fig. 7.8.

The results indicate that at fracture the values of Rc/Ro are very small. In fact the value of Rc also involves the contribution of the nucleation from small-scale inclusions at higher triaxiality. In the constraint range investigated, the maximum value of (Rc/Ro) is less than 1.8. It may be believed that the localized fracture on ligaments between the voids restricts their growth. As the variation of Rc/Ro as a function of $\sigma_m/\bar{\sigma}$ is rather small, the Rc/Ro is

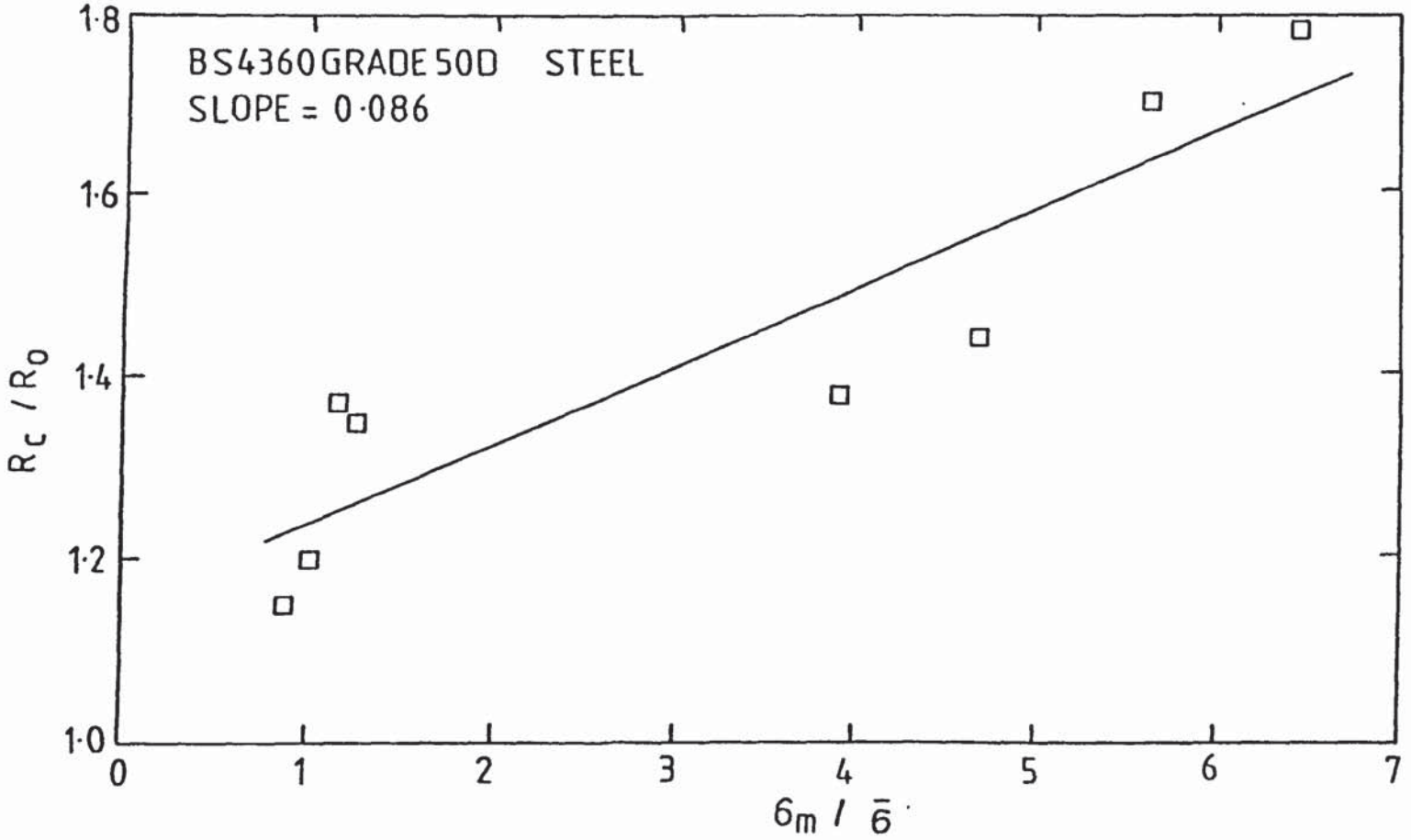

FIGURE 7.8 Critical void growth at fracture initiation as a function of stress triaxiality. Triaxiality derived from measured void volumes using $T_1 = 3.83$ in experimental void growth relation.

approximately assumed to reach a constant critical value for a given material loaded in a given direction [96], or the critical relative void volume at fracture is assumed to represent an average value of large experimental scatter [72]. Therefore, it can reasonably be assumed that there is a critical void growth of $(Vv)_c \simeq 0.01$ or $R_c \simeq 1.8Ro$ for the bodies containing the crack under the plane strain condition.

Based on the above assumption, the material failure is defined to begin when a critical void growth is attained. In this case, corresponded to the critical void growth, there must be a critical combination of the stress triaxiality and plastic shear strain at fracture. The critical combination will be in the form of the approximate hyperbola. On the left-hand side of the curve, a process of void growth is dominant; on the right-hand side of the curve, a process of void coalescence is dominant.

However, Fig.7.8 shows a tendency to slowly increase the Rc/Ro values with increasing the stress triaxiality. The slope of the critical void growth, Rc/Ro, to the stress triaxiality, $\sigma_m/\bar{\sigma}$, is about 0.09 in the constraint range investigated. This tendency has obviously been found during the statistical measurements of the relative void volume. For example, in the standard CVN specimens No. B1T or B2T with the lower triaxiality, the random point counting give rise to zero counted volume in 80% of the areas surveyed in the vicinity of 0.5 mm ahead of the notch root. In contrast only 40% of the similar areas

surveyed in the pre-cracked side-grooved specimens No. S13V or S19V give zero void volume counts. Thus it would appear that the void volume is greater for conditions at high triaxiality. Although it is difficult to accurately measure the critical relative void volume from the three-point bending tests, due to the non-uniform stress and strain field ahead of the notch or crack and considerably low density of the voids, the changing tendency is clear. Therefore it is felt that the relation between the critical void growth and the stress triaxiality should be concerned.

The results obtained by Lautridou and Pineau [96] are worth noting. In their work the maximum value of stress triaxiality obtained in the notched tensile specimens, calculated from the finite element method, is about 1.3. Additionally, it is scarcely considered that Rc/Ro reaches a constant critical value for testing steel A, C and D loaded in a given direction. Beremin [100] has also pointed out for those results that more surprising is the significant decrease in the critical growth rate when the stress triaxiality is increased. The reason for this behaviour are not yet clear, and it is felt that statistical considerations should have led to a reverse trend. It may be that there is an error in the analysis of data.

According to our experimental observation in higher constraint range, the reason for increasing the critical void growth with the stress triaxiality may be related to

the two aspects: First, the higher triaxiality combined with a certain plastic strain leads to large growth of voids. Plate 5.15 shows that large growth of voids occurs ahead of the crack tip in a pre-cracked side-grooved specimen. This plate reveals that about 15 voids have already coalesced locally. The local void coalesces are also found in Plate 5.15(b) for the same specimen. The large growth of voids can also be found in the short bar specimen tested at -60°C with higher constraint in general yielding condition, as shown in Plate 6.14. Second, some small-scale voids might easily be induced from the fine inclusions at higher constraint, as shown in Plate 5.14. In general these fine inclusions are not easy to debond from the matrix steel under low plastic strain or low stress triaxiality. Even the local higher stress concentration around a large void can also enhance the initiation and growth of smaller voids surrounding the large void, as shown in Plate 5.15.

It is well-known that at reaching the critical crack tip opening displacement, the formation of voids ahead of the crack tip and their growth are related to the metallurgical features of the steel, such as the size and spacing of the inclusions. During the initiation of the slow crack growth, the voids ahead of the crack tip only occur from a fraction of the inclusions. At the same time it is not possible for all the voids to grow large. The size and

amount of voids at fracture initiation, as described by the critical void growth, are dependent on the local stress-strain conditions, except the metallurgical features. Therefore, higher plastic strain associated with a certain stress triaxiality, as indicated by Ref.96, or higher triaxiality associated with a certain plastic strain, as investigated in this work, will lead to the more opportunity for the void nucleation and subsequent growth before the void coalescence. It is expected that the critical void growth should decrease, if the stress triaxiality further increases without a certain amount of the plastic strain to associate with the triaxiality. Therefore, when the critical void growth determined in the notched tensile specimens are used to calculate the fracture toughness in the bodies containing sharp crack, the critical void growth value may require to be somewhat modified. However, the critical void growth determined in the notched tensile specimens may be available for calculating the fracture toughness in the notch or blunted crack specimens with lower stress triaxiality.

7.6 Void Growth Rate Explanation of Fracture Initiation of the Bend Bars in the Transition Region

Table 7.7 summarizes the ductile-brittle transition temperatures determined by slow and impact bending tests. It can be seen for the notched specimens that the transition temperature determined by the impact tests is much

Table 7.7 : Ductile-brittle transition temperatures determined by slow and impact bending tests for the Charpy-size specimens

Specimen type	$\sigma_m/\bar{\sigma}$, estimated by void growth studies	Transition temperature, °C		Void growth rate, d(Vv)/d(COD) (from slow bend)
		Slow bend (from CTODi)	Impact bend (from 50% FATT)	
Standard Charpy specimen	0.95	-90*	-60	0.009
Side-grooved Charpy specimen	1.20	-100*	-23	0.014
Pre-cracked side-grooved Charpy specimen	6.04	-70	-	0.032

*This is the highest temperature at which crack initiates by cleavage

higher than that determined by the low bending tests. This reflects that the notch toughness of structural steel can decrease significantly with increasing loading rate. In the slow bend tests, the transition temperature for the pre-cracked specimens is higher than that for the notched specimens. In addition the transition temperature for the side-grooved CVN specimens is higher than that for the standard CVN specimens in the impact tests. However, it is very difficult for the notched specimens to correctly determine the transition temperature during slow bend tests, due to the large scatter in the critical CTOD value. It seems to be that the highest temperature, at which crack may initiate by cleavage, is slightly higher in the standard CVN specimens than in the side-grooved CVN specimens, as shown in Table 7.7.

Based on the current explanations for the ductile-brittle transition behaviour of the structural steel, the difference of the constraint and loading rate in these specimens can be used to explain the transition behaviour and their shift in the transition temperature, except that the transition temperature for the two kinds of the notched specimens in slow bending tests are less clear. The stress triaxiality estimated for these specimens are also listed in Table 7.7. It is clear that the higher the stress triaxiality of the specimens is, the higher the transition temperature is both in impact and in slow

bending tests, except the notched specimens in slow bending tests. The question is how the constraint influences the ductile fracture process, and subsequently the transition temperature. Thus this work attempts to describe this phenomenon by using the void growth studies.

In the transition temperature region, crack initiation usually starts by the ductile tearing. Then the crack propagates in a brittle manner after a certain of slow crack extension. It is well-known that the initiation of the ductile tearing, as the ductile fracture, is a progressive process with the void nucleation, growth, and coalescence. Due to a rather small plastic nucleation strain, this initiation processs of the ductile tearing is basically controlled by the void growth stage. If the void growth could be retarded, large increase in ductility could be achieved. Thus, we have investigated the relationship between the relative void volume and crack opening displacement for the different modified CVN specimens in the transition temperature.

To take the experimental work easy, the specimens were tested at the temperature below that crack probably initiated by cleavage. Before tests, microhardness indentations were made on the specimens as an original measurement gauge. Specimens were tested in three point bending until the initiation of ductile tearing, then unloaded. The loading parameter COD was measured at every location in front of the notch or crack tip, based

on the changes of the gauge lengths under the same microhardness tester and same magnification of 100x. The residual change of the gauge length was considered to be the plastic component of the COD value. Samples containing the notch or crack tip region were sectioned along the mid-thickness of the specimens in liquid nitrogen. The measurement manner of the relative void volume ahead of the notch or crack tip is the same with that as shown in Fig. 7.6.

The measurement results are given in Table 7.8. Assuming the relationship between the relative void volume, Vv, and crack opening displacement, COD, to be a linearity approximately, as shown in Fig. 7.9. The best fit equations are given as follows. For standard CVN specimen,

$$Vv = 0.00155 + 0.00893\ (COD),\ R = 0.96 \quad \ldots\ldots\ldots (7.7)$$

For side-grooved CVN specimen,

$$Vv = 0.00071 + 0.01429\ (COD),\ R = 0.85 \quad \ldots\ldots\ldots (7.8)$$

For pre-cracked side-grooved CVN specimen,

$$Vv = -0.00090 + 0.03233\ (COD),\ R = 0.99 \quad \ldots\ldots\ldots (7.9)$$

Here R is the correlation coefficient.

It is found from the slopes of the best-fit lines that the void growth rate, d(Vv)/d(COD), is much higher in pre-cracked specimens than in notched specimens. If the initial growth of a macrocrack can be assumed to be the occurrence of a constant critical micro-fracturing void

Table 7.8 : Variations of the relative void volume in front of the notch or crack tip as a function of crack opening displacement.

CODp, mm	Distance ahead of notch or crack tip,mm	Vv
NONSIDE-GROOVED CHARPY SPECIMEN, -80°C		
0.14	0.5	0.00275
0.09	0.7	0.00250
0.06	0.9	0.00200
0.05	1.1	0.00200
SIDE-GROOVED CHARPY SPECIMEN, -90°C		
0.20	0.5	0.00350
0.18	0.7	0.00350
0.17	0.9	0.00300
0.16	1.1	0.00300
PRE-CRACKED SIDE-GROOVED CHARPY SPECIMEN, -50°C		
0.27	0.5	0.00775
0.22	0.7	0.00650
0.19	0.9	0.00500
0.15	1.1	0.00400

a. Gauge length = 0.80 mm for notched specimens, 1.7 mm and 2.0 mm for pre-cracked specimen,

b. Loading rate = 0.05 cm/min

c. CODp means the plastic component of COD value.

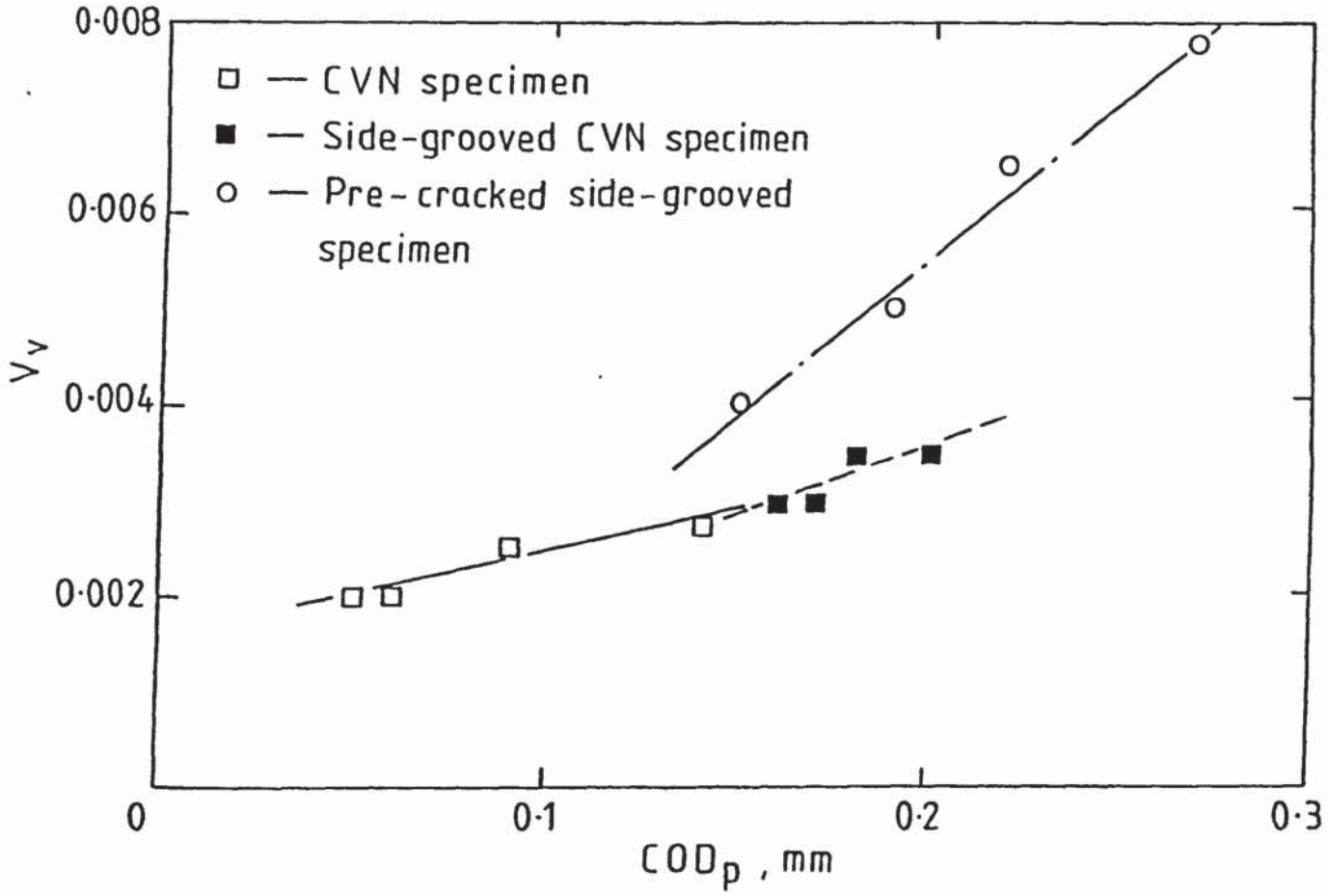

FIGURE 7.9 Measured variation of the void growth in front of the notch and crack as the function of crack opening displacement

volume in the region adjacent to the crack tip, the initial process of the ductile crack, or void growth will carry out much rapidly with increasing the COD value in the pre-cracked specimens than in the notched specimens. In the pre-cracked specimen, the critical void growth required for fracture initiation might be attained at a smaller COD value. Thus, the high void growth rate results in the low toughness or high transition temperature. However, the high void growth rate was caused by the high stress triaxiality ahead of the notch or crack tip. It might be expected that the effect of the specimen constraint on the ductile-brittle transition behaviour can be investigated by the void growth rate studies.

According to the experimental results of impact tests, side-grooved CVN specimens has a higher transition temperature, compared with standard CVN specimen. It is related with the higher constraint of the side-grooved specimen. This analysis is also proved by the above void growth rate studies. That is, side-grooves increase the void growth rate against the COD value. This phenomenon in fact is consistent with that discussed in Fig.7.2. Unfortunately, the slow bend tests for the CVN and side-grooved CVN specimens do not give out the obvious transition temperature, due to large scatter in the critical COD value. The highest temperature at which crack probably initiates by cleavage seems to be higher in the

CVN specimens than in the side-grooved CVN specimens. This may be related to the occurrence of the pop-in during the tests at lower temperature.

According to BS4362, the CTOD corresponding to pop-in is considered to be a critical CTOD at cleavage initiation. Practically, after small pop-in, a specimen is immediately unloaded, heat-tinted, and broken at -196°C, the brittle crack area cannot be found on the fracture surface by the naked eye and SEM, although the small pop-in often causes the load drop of about 4% of the current load, as discussed in Section 6.2.2.1. However, some delamination-like tearing was found, as shown in Plate 7.2. These delaminations were sited right below the notch of the specimen and linked with the notch during ductile crack initiation. The occurrence of the delaminations during bend tests changed the local constraint condition and thereby affected the load versus load-point displacement record. The delamination in rolling steel is a possible reason for the pop-in occurrence. Similar phenomena were also found by the Welding Institute [101]. Thus this kind of pop-in probably has a considerable contingency.

7.7 Variations of Stress Triaxiality Estimated in Front of the Notch Root and Crack Tip at Transition Temperature

It is of considerable interest to investigate the stress and strain distribution in front of the notch or crack tip.

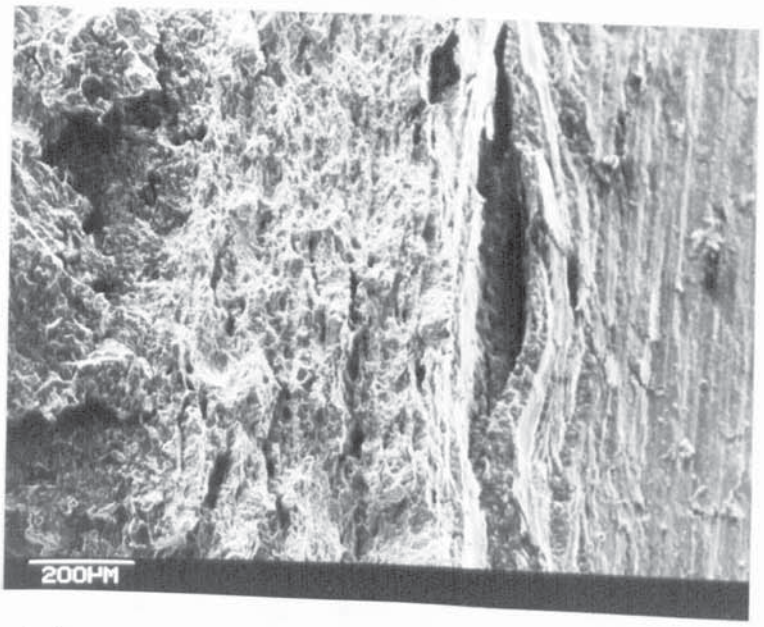

(a)

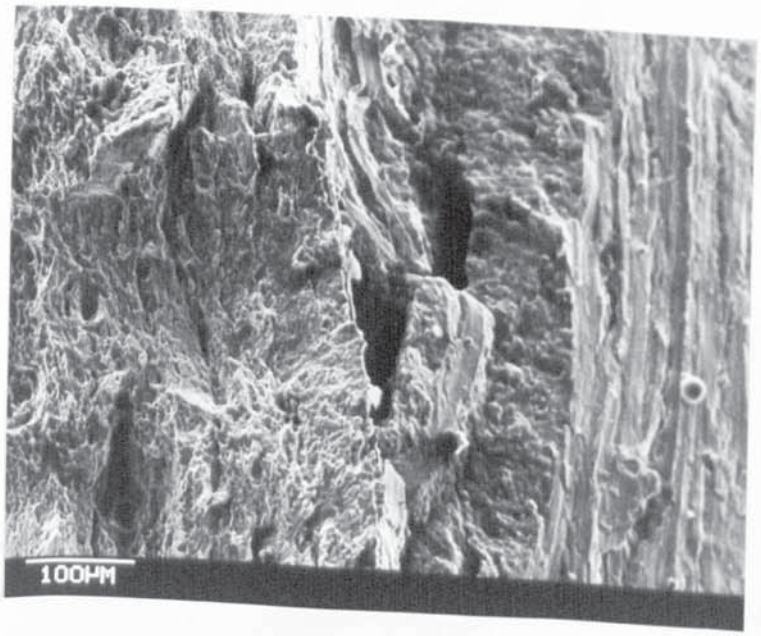

(b)

Plate 7.2 : Some delaminations were linked with the notch during ductile crack initiation (nonside-grooved specimen No. 104, tested at -120°C).

At the upper shelf temperature the different near-tip stress states in different specimen geometries could presumably affect the micrstructural mechanisms of ductile cracking, notably void growth and coalescence. At the lower shelf temperature, generally, a critical tensile stress is considered as fracture criterion.

Substantial work has been made in recent years in analysing the stress and deformation fields near crack tip in elastic-plastic materials. The conventional small geometry change solution is based on the slip-line field analysis [102]. Slip-line field theory predicts the stress distribution in front of notch root assuming plane strain condition, a non-hardening material inside the plastic zone. Slip-lines are lines of maximum shear stress which spread in the form of logarithmic spirals in front of the notch. The stress triaxiality at a distance x ahead of the root of the notch along the axis of symmetry is given by the equation [102]

$$\frac{\sigma_m}{\bar{\sigma}} = \frac{1}{\sqrt{3}}\left(1+2\ell n\left(1+\frac{x}{r}\right)\right) \qquad \ldots\ldots\ldots\ldots (7.10)$$

where r is the radius of the notch root and the von Mises yield criterion is adopted. Similarly, for a circularly blunting crack tip, the appropriate slip-line field can be obtained from the Hencky equation as

$$\frac{\sigma_m}{\bar{\sigma}} = \frac{1}{\sqrt{3}}\left(1+2\ell n\left(1+\frac{2x}{\delta_t}\right)\right) \qquad \ldots\ldots\ldots\ldots (7.11)$$

where $x/\delta_t \leq 1.96$, and in fact it is assumed that the blunting crack tip opening displacement, δ_t, is equal to 2 r.

As mentioned previously, the stress triaxiality given by the HRR field analysis is that $\sigma_m/\bar{\sigma} = f(n,\theta)$. The slip-line field can be regarded as the limiting case of the power hardening solution with the substitution $n = \infty$, identifying σ_o with $\bar{\sigma}$ [103]. Although the stress state is independent of the distance, there is a strain singularity which causes the crack tip to open and blunt. Rice and Johnson [104] have given a small scale contained yielding solution for a crack tip in plane strain. The solution takes account of blunting of the crack tip. It is shown that the stress distribution σ_{yy}/σ_o, due to large tip geometry changes, is dependent on initial yield strain, σ_o/E, and hardening exponent, n. At the same time, it is concluded that with consideration of actual geometry changes at the crack tip, the maximum stress achievable over a specific size scale in the material is limited, contrary to the HRR singularity solution. Although it is approximate, it seems likely to contain the essential features or crack tip stress and strain fields. At the present work, the stress triaxiality distribution at the general yielding condition is attempted to evaluate by the experimental void growth studies. Subsequently the evaluated results are compared with the results based on the Rice-Tracey's theory for the non-hardening material, and the slip-line field results.

Standard CVN specimen and pre-cracked side-grooved Charpy-size specimen were examined to make a comparison in their features of the stress distribution. Three-point bending tests were conducted at -80°C for the standard CVN specimen and at -50°C for the pre-cracked side-grooved specimen. The testing temperatures were slightly higher than the highest temperature at which the crack probably initiated by cleavage. The specimens were loaded just for the crack initiation, which was monitored by the potential technique. The plastic shear strains in front of the notch or crack tip are measured from the gauge length change of the microhardness indentation. The relative void volume distribution is measured by the point counting technique with the distance, as shown in Fig. 7.6. Table 7.9 gives the distribution values in front of the notch or crack tip of the plastic shear strain, void growth, and stress triaxiality calculated from the three methods. These results also are shown in Figs. 7.10 and 7.11.

For the two different Charpy-size specimens, the longitudinal plastic shear strain distributions on the symmetrical plane ahead of the notch or crack are rather different. The maximum value of the plastic strain near the notch root is two times as large as that near the crack tip. Additionally, the singularity of the plastic strain is much stronger in the standard CVN specimen than in the pre-cracked side-grooved specimen. Based on the measurement results of the relative void volume, there is

Table 7.9 : Variation of stress triaxiality ahead of the notch or crack tip in Charpy-size specimens.

Distance ahead of notch or crack tip, X, mm	$-p/\varepsilon$	Vv	$\sigma_m/\bar{\sigma}$			x/r or x/δ_t
			Linear law, T_1=3.83	Rice-Tracey theory, n=∞	Slip-line theory, n=∞	
STANDARD CHARPY SPECIMEN - 80°C						
0.1	0.194	0.00250	0.45	0.60	0.70	0.11
0.3	0.131	0.00250	0.67	0.81	0.91	0.33
0.5	0.081	0.00275	1.40	1.25	1.08	0.55
0.7	0.053	0.00250	1.68	1.37	1.24	0.77
0.9	0.036	0.00200	0.81	0.92	1.37	0.99
1.1	0.030	0.00200	0.98	1.03	1.49	1.21
PRE-CRACKED SIDE-GROOVED CHARPY SPECIMEN -50°C						
0.1	0.091	0.00420	2.49	1.63	1.09	0.28
0.3	0.084	0.00825	4.85	2.07	1.71	0.83
0.5	0.073	0.00775	5.37	2.13	2.11	1.39
0.7	0.061	0.00650	5.68	2.17	2.41	1.94
0.9	0.045	0.00500	6.20	2.23	-	2.50
1.1	0.036	0.00400	6.13	2.23	-	3.06

*Root radius of the deformed notch, r, of 0.91 mm was measured by microscope with the magnification of 50x; The δ_t of 0.36mm was measured from the change of the gauge length corresponding to the blunting crack tip.

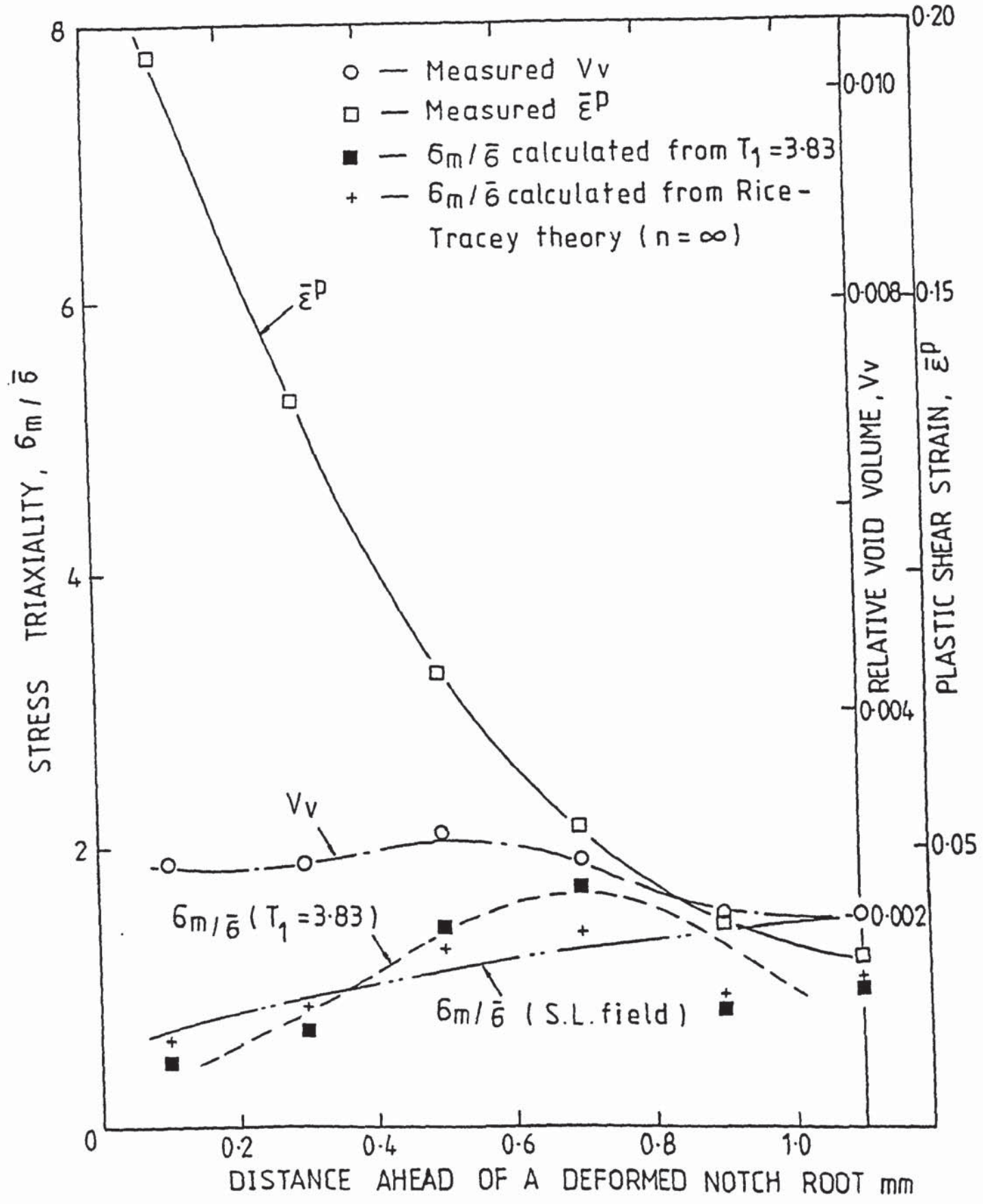

FIGURE 7.10 Stress triaxiality, plastic strain, and void growth distribution in front of the notch root at the crack initiation CTOD in standard Charpy specimen tested at -80°C

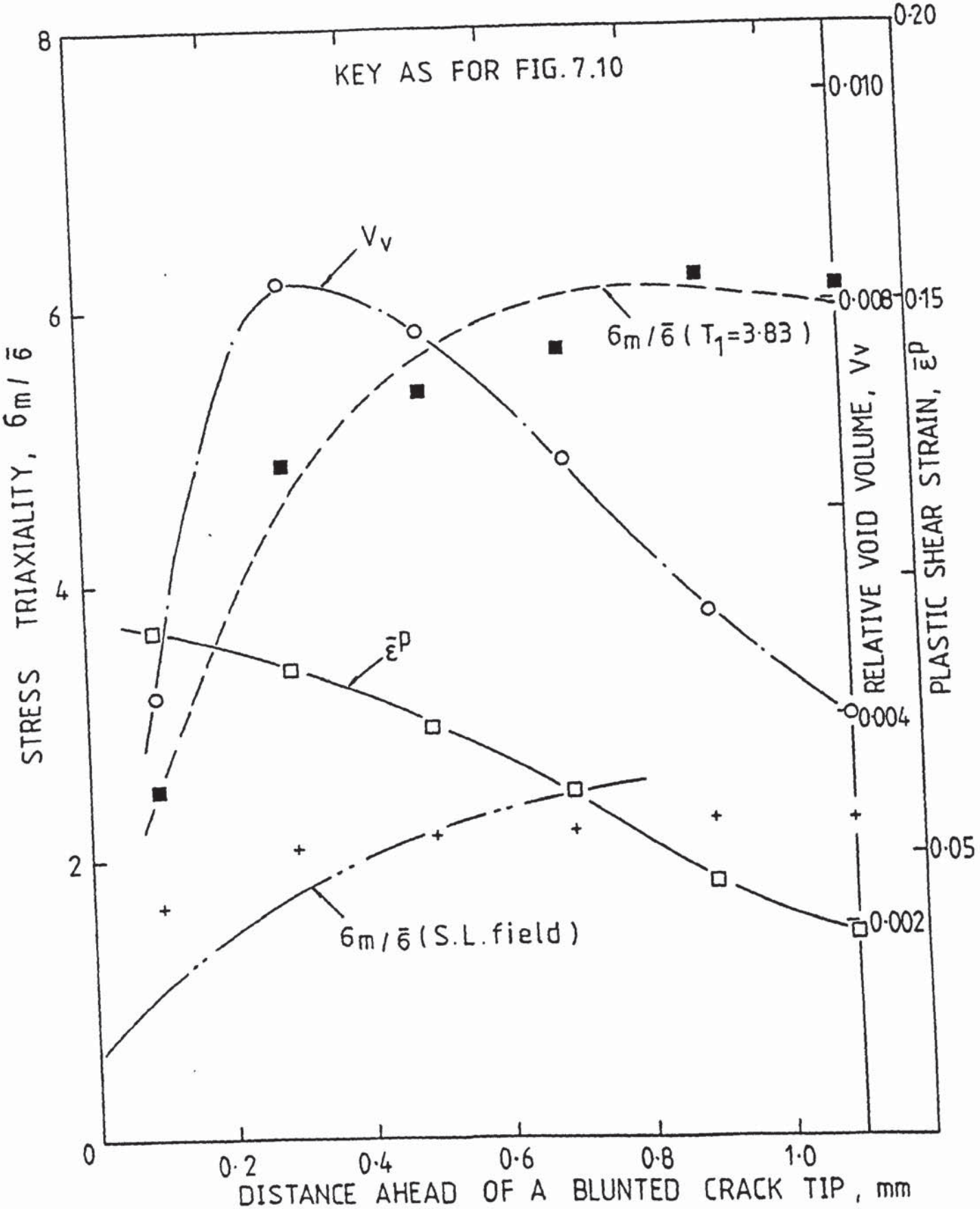

FIGURE 7.11 Stress triaxiality, plastic strain, and void growth distribution in front of the blunting crack tip at the crack initiation CTOD in precracked side-grooved specimen, tested at -50°C.

a maximum in the void growth at some distance ahead of the notch or crack tip. This maximum is specially clear for the pre-cracked side-grooved specimen. The peak of the void growth is much higher in the pre-cracked side-grooved specimen than in the standard CVN specimen. According to the experimental observation including other specimens tested at room temperature and loaded slightly beyond the crack initiation, in general, the position producing the peak value is more slightly approximate to the tip in the pre-cracked side-grooved specimen than in the standard CVN specimen. The former is about 0.3 to 0.5 mm ahead of the crack tip, and the latter is about 0.4 to 0.6 mm ahead of the notch root.

The stress triaxiality distribution are estimated by the experimental void growth relation ($n = 4.5$), and the theoretical Rice-Tracey relation ($n = \infty$). The results have indicated that in a very short distance ahead of the notch or crack tip, the stress triaxiality decreases with the distance near to the notch or crack tip. It is specially clear for the pre-cracked side-grooved specimen. As discussed previously, in the pre-cracked side-grooved specimen, the stress triaxiality calculated from the HRR field analysis will large deviate from that evaluated from the void growth studies, when the interesting distance is less than about 0.4 mm ahead of the crack tip.

Furthermore, for the pre-cracked side-grooved specimen, the stress triaxiality evaluated ahead of the crack is

much higher by the experimental void growth relation ($n = 4.5$) than by the Rice-Tracey's relation ($n = \infty$). These results show an influence of the hardening material upon the stress triaxiality. As discussed in Section 7.3.3, under higher stress triaxiality condition strain hardening decreases the void growth coefficient, and increases the stress triaxiality. It is also worth noting that the variation of the stress triaxiality estimated by the Rice-Tracey's relation ($n = \infty$), is quite similar to that calculated by the slip-line field solution, Eq. (7.11).

For the standard CVN specimen, the variations of the stress triaxiality evaluated ahead of the notch root by the experimental void growth relation, Rice-Tracey's relation and slip-line field solution, Eq. (7.10) are quite similar to each other, as shown in Fig. 7.10. These results indicate that under the lower stress triaxiality condition, there is no important influence of the strain hardening upon the void growth coefficient, subsequently upon the stress triaxiality. It is felt that in the general yielding condition the variation of the stress triaxiality in the vicinity of the notch root may be approximately described by the slip-line solution.

Therefore, the above discussion has proposed an approximate method for estimating the stress triaxiality variation ahead of the notch or crack tip under the general

yielding condition, based on the plastic shear strain field and void growth investigation, although there is a certain deviation in the measurements of the void growth.

7.8 Influence of Side-Grooves on the Energy Absorbed in Charpy V-Notch Impact Tests

The energy absorption values in the CVN impact tests consist of the initiation and propagation energies, and do not differentiate between them. For the side-grooved CVN specimen the practical cross-section area is only 70% of that of the standard CVN specimen. In order to compare the testing results of different specimens, the energy absorbed, E, is taken into account the difference of remaining specimen ligament area, A, The energy absorbed per unit area, E/A, of different specimens is calculated from the results given in Tables 6.1 and 6.2. Fig 7.12 shows a comparison of the CVN and side-grooved CVN impact energy absorption as a function of testing temperature from -100°C to + 100°C.

Based on the examination of the fracture appearance in Section 6.1, fully plastic temperature, T_{FP}, and fracture appearance transition temperature of 50% shear area, T_{50-50}, are obviously shifted to the higher temperature by the side-groove constraint in the CVN specimens. At the same time, it is found that the scatter of the experimental results in the transition region decreases

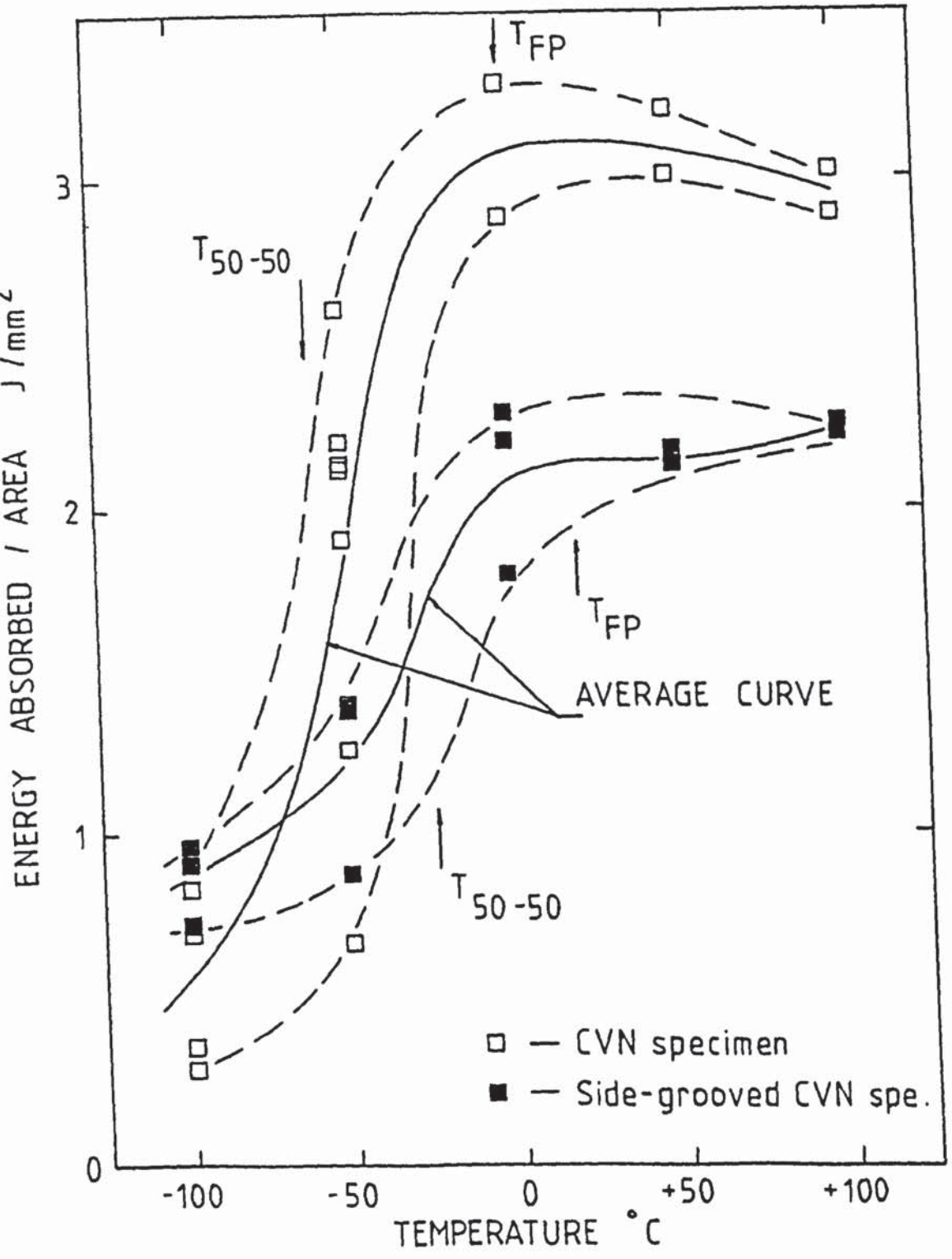

FIGURE 7.12 Comparison of the energy absorbed per unit area in the CVN and side-grooved CVN specimens.

for the side-grooved CVN specimens. For the standard CVN specimens, the maximum scatter of about 1.45 $^{J}/mm^{2}$ occurs at -60°C corresponding to T_{50-50}. For the side-grooved CVN specimens, the maximum scatter of about 0.85 $^{J}/mm^{2}$ occurs at -23°C corresponding to T_{50-50}. The smaller scatter occurred in the transition temperature region for the side-grooved CVN specimens is not related with the sampling location of the specimen, may associate with the higher constraint. Similar results have also been obtained by other research workers [105].

Based on the observation of the fracture appearance for all the specimens tested in the transition temperature range, the fracture initiated by ductile cracking. After a certain amount of ductile crack growth, crack propagated by cleavage in the centre of the specimen thickness. Near the lateral surfaces of the specimens, the material failed by ductile tearing. As usual, the material presents a mixed mode of the fracture. For the side-grooved CVN specimens the initial ductile crack growth and ductile tearing on the lateral surface regions are significantly decrease. The typical photographs are shown in Plate 7.3 (a).

Although the difference of remaining specimen ligament area is taken into account, the average energy level on the upper shelf temperature is about 3.04 $^{J}/mm^{2}$ for standard CVN specimens, whereas that is about 2.18 $^{J}/mm^{2}$ for the side-grooved CVN specimens. Plate 7.3 (b) shows the

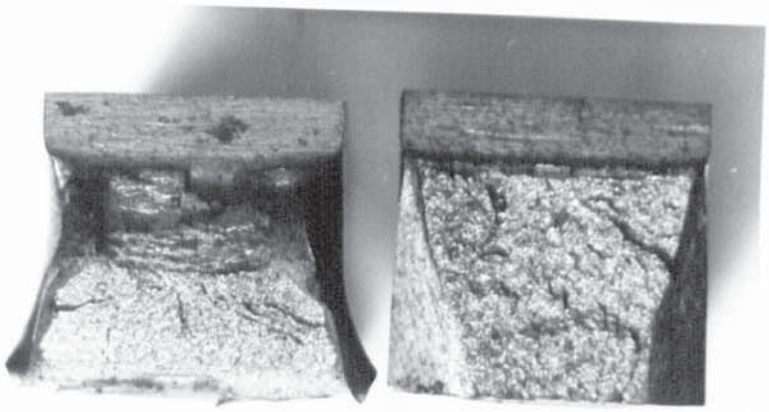

(a) At -50°C

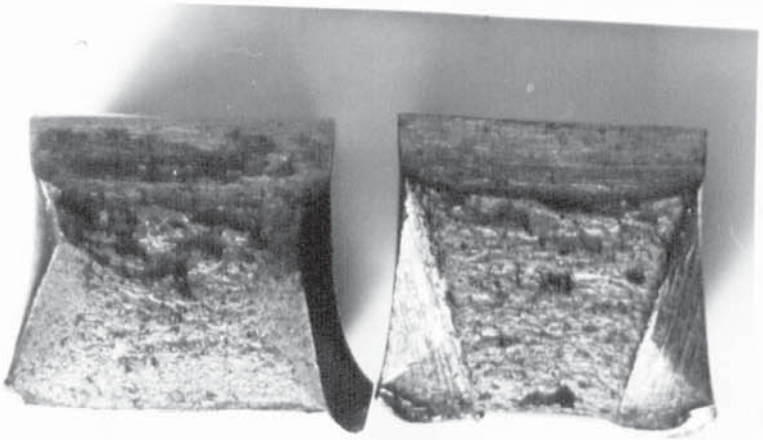

(b) At +50°C

Plate 7.3 : Effect of side-grooves on the fracture appearance in impact tests.

fracture appearance for the different specimens tested at +50°C. For the standard CVN specimens tested at the upper shelf temperature, severe plastic deformation and shear tearing occur in the near lateral surfaces of the specimens except a small plane strain zone observed at the centre of the specimens. The energy absorbed by the plane stress zone in the near lateral surfaces (or shear lips) is larger than the energy absorbed by the plane strain zone in the centre of the specimens. Due to the side-grooves, the shear lips eliminate significantly, and the proportion of the plane strain deformation in the total fracture surface increases. Therefore, the energy absorption per unit area on the upper shelf is lower for the side-grooved CVN specimens than for the standard CVN specimens.

Similar results can also be found from the measurements about the lateral contraction at the notch root and the lateral expansion on the back of the specimen. According to the results at the upper shelf given in Tables 6.1 and 6.2, the average lateral contraction of about 23% and the average lateral expansion of about 92 mils for the standard CVN specimens decrease respectively to about 8% and 52 mils for the side-grooved CVN specimens. Therefore the influence of the side-grooves on the energy absorption is mainly realized by eliminating the shear lips and increasing the proportion of the plane strain deformation in the fracture at upper shelf temperature.

7.9 Evaluation of Elastic-Plastic Fracture Toughness Based on Small Specimens

Many experimental works confirm that good estimation of K_{IC} may be obtained from the specimens which are smaller than required for valid K_{IC} measurement. It is obvious that predictions of K_{IC} from small specimens are attractive. This is specially true for the low strength steels. For example it is assumed that valid K_{IC} value can be obtained from a 100 mm thick three-point bend specimen at -100°C. If the K_{IC} value can be predicted from the specimens such as Charpy-size bend specimens or short bar tensile specimens, the specimen volumes will be down to 3346 or 860 times smaller than that necessary for the direct determination of K_{IC}. This will lead to relatively low specimen and test cost. Furthermore in some cases such as in reactor surveillance programmes, the specimen size is limited. Nevertheless, there is increasing evidence which indicates that in certain situations reliable K_{IC} predictions cannot be obtained and K_{IC} may be overestimated from small specimens.

If the results of the short bar specimens broken in one beam are excluded from consideration, the average values of K_{ICSB} are 127.5 MPa $\sqrt{m}$ and 120.0 MPa$\sqrt{m}$ at -80°C and -100°C, respectively. Pisarski [106] has investigated the valid K_{IC} values of BS4360 Grade 50D steel at low temperature. The chemical compositions of the steel

including sulphur content are quite similar to our experimental steel. The plane strain values of K_{IC} were measured in the 100 mm thick three-point bend tests. Two data of the valid K_{IC} at -100°C are 71 and 50 MPa$\sqrt{m}$. Average value of the valid K_{IC} at -100°C is about 61 MPa$\sqrt{m}$. It is obvious that the values of K_{ICSB} from small short bar tests may give large overestimation of valid K_{IC} values in this steel. However, if the initial jumping load in specimen No.12 is used to calculate K_{ICSB}, the K_{ICSB} will be 76.1 MPa$\sqrt{m}$ which appears to agree fairly well with the Pisarski's results.

Use is made of the correlation, Eq. (1.34), established by Sailors-Corten, the value of K_{IC} may be predicted from the average energy absorption in standard CVN impact tests at -100°C.

$$K_{IC} = 14.62(43)^{\frac{1}{2}} = 95.9 \ (MPa\sqrt{m})$$

This prediction value is also lower than that measured by the short bar tests at the same temperature.

Barker (57) has considered that in principle, a value of K_{ICSB} can be calculated for each crack jump load. In practice only that crack jump which initiates in the vicinity of the critical crack length, a_c, is used. This ideal situation with several crack jumps cannot be obtained under the condition of this testing material and

specimen size. Usually the sole crack jump occurs in the vicinity of the chevron tip. The compliance and stress intensity coefficient of the specimen are different from the calibration case. Therefore, the above calculation procedure may not be available in the tests of displaying only one or two crack jump behaviour.

Based on the Barker's suggestion[94], the toughness values are independent of the specimen size within experimental scatter, whenever the specimen breadth exceeds $1.25\ (K_{ICSB}/\sigma_{ys})^2$. Pisarski [106] has also investigated the influence of temperature on the tensile properties of the Grade 50 D steel. The average yield strength at -100°C is about 408 MPa. Therefore, the minimum short bar breadth, B, at -100°C should satisfy

$$B \geq 1.25\ (K_{IC}/\sigma_{ys})^2$$

$$= 1.25\ (61/408)^2 = 28\ (mm)$$

here it is assumed that both the valid K_{IC} and K_{ICSB} are interchangeable in the above expression. It is clear that the size condition for obtaining the valid plane strain fracture toughness is nearly realized. Furthermore, the measurements of the residual bend of the specimen beam indicate that the maximum deflection amount is less than 0.040 mm over the span of specimen length excluding the grip slot part in the specimen tested at -100°C. The

measurement of deflection was conducted in the shadow graph projector with magnification of 10x. Thus the plasticity of the specimen tested at -100°C is rather small. If the expression should use the measured K_{ICSB} value, and not K_{IC} [107],

$$B > 1.25 \, (K_{ICSB}/\sigma_{ys})^2$$

$$= 1.25 \, (120/408)^2 = 108 \text{ (mm)}$$

Therefore, it is indicated that the size validity requirement would have to be increased for the crack jump type material.

However, it is assumed that the stress intensity coefficient, A, at the vicinity of the chevron tip is selected to calculate the values of K_{ICSB}. For example, $a/W=0.357$ corresponding to the stable crack growth of 0.5 mm ahead of the chevron tip, the value of A is 27.42, based on an analytical function of the stress intensity coefficients with a/W for this short bar geometry [53]. Using the Eq. (6.1), the calculated values of K_{ICSB} will be further larger than the values based on A=22.28 and $a_c/W = 0.512$. Additionally, it is assumed that a 5% secant offset in the load-displacement curve is chosen to measure K_{IC} at which the crack propagates 2% greater than that at the beginning of the test. Although the estimation procedure similar to measuring K_{IC} in the LEFM approach is rather approxi-

mate, the calculated results of K_{IQSB}, as shown in Table 7.10, are quite similar to those based on A=27.42, and $^{a}/W = 0.357$.

Observing the fracture processes of the short bar specimens tested at -80°C and -100°C, it is found that the side-slot blunting occurs in the chevron tip vicinity with loading. The deformed chevron tip region tested at -100°C is shown in Plate 7.4. Then the slow crack growth occurs and final failure mode is rapid cleavage crack growth. The extent of the ductile crack growth, where it preceded cleavage decreases with decreasing the test temperature. For example, the extent of the slow crack growth is about 30 to 500μm in the specimens tested at -100°C, but is about 2 to 3 mm in the specimens tested at -80°C. As discussed previously, during the tests at -60°C and above, slow crack growth is accompanied by the severe blunting of the crack tip and plastic deformation in the specimen beam. The transition from the ductile to cleavage mode of cracking cannot occur, while the ductile crack is growing.

Is there a slow elastic crack growth during the tests at -100°C? A short bar specimen is loaded at -100°C. After a certain extent of the slow crack growth, the specimen is unloaded at the same temperature. Then the specimen is reloaded at the room temperature. The two cycles of the loading-unloading are shown in Fig. 7.13. The different limit loads indicate the influence of temperature on the yield strength of the steel.

Table 7.10 : Fracture toughness in short bar tensile tests estimated from different procedure (tested at -100°C)

Specimen No.	9	11	12	18
C_c	1.004	0.968	1.005	0.994
F_{max} (N)	24858	24343	23751	23142
F_5 (N)	21573	21965	13336	20200
$K_{ICSB}=AC_cF_{max}B^{-3/2}$ (MPa$\sqrt{m}$) ($A=27.42$, $a/w=0.357$)	169.1	144.0	93.5	155.9
$K_{IQSB}=AC_cF_5B^{-3/2}$ (MPa$\sqrt{m}$) ($A=31.04$ $a_o/_w=0.344$)	166.1	163.0	102.8	154.0
$K_{ICSB}=AC_cF\ B^{-3/2}$ (MPa$\sqrt{m}$) ($A=22.28$, $a_c/_w=0.512$	137.4	129.7	103.9	126.5

a. Specimen No. 9 was broken in one beam
b. W=38.1 mm; a_o= 13.1 mm; and $\theta=55^o$

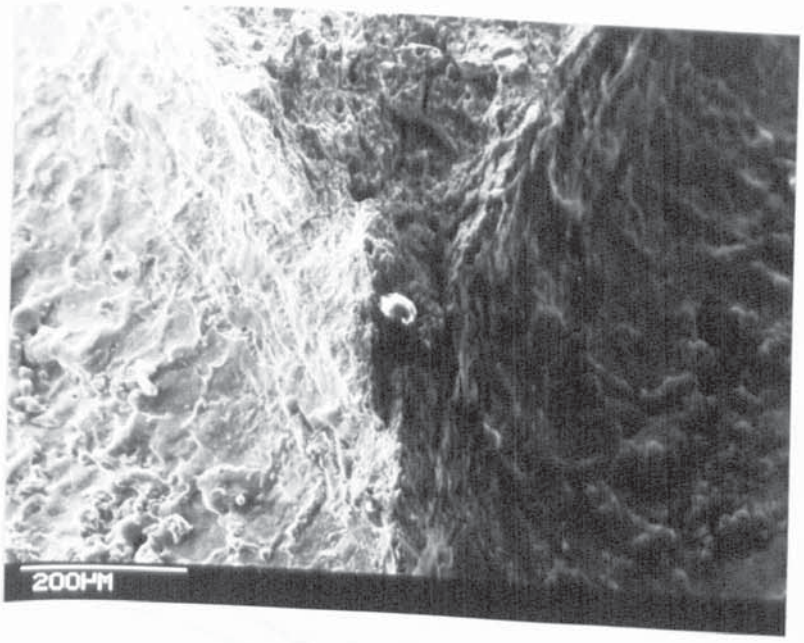

Plate 7.4 : Deformed chevron tip region, in specimen No. 12, tested at -100°C

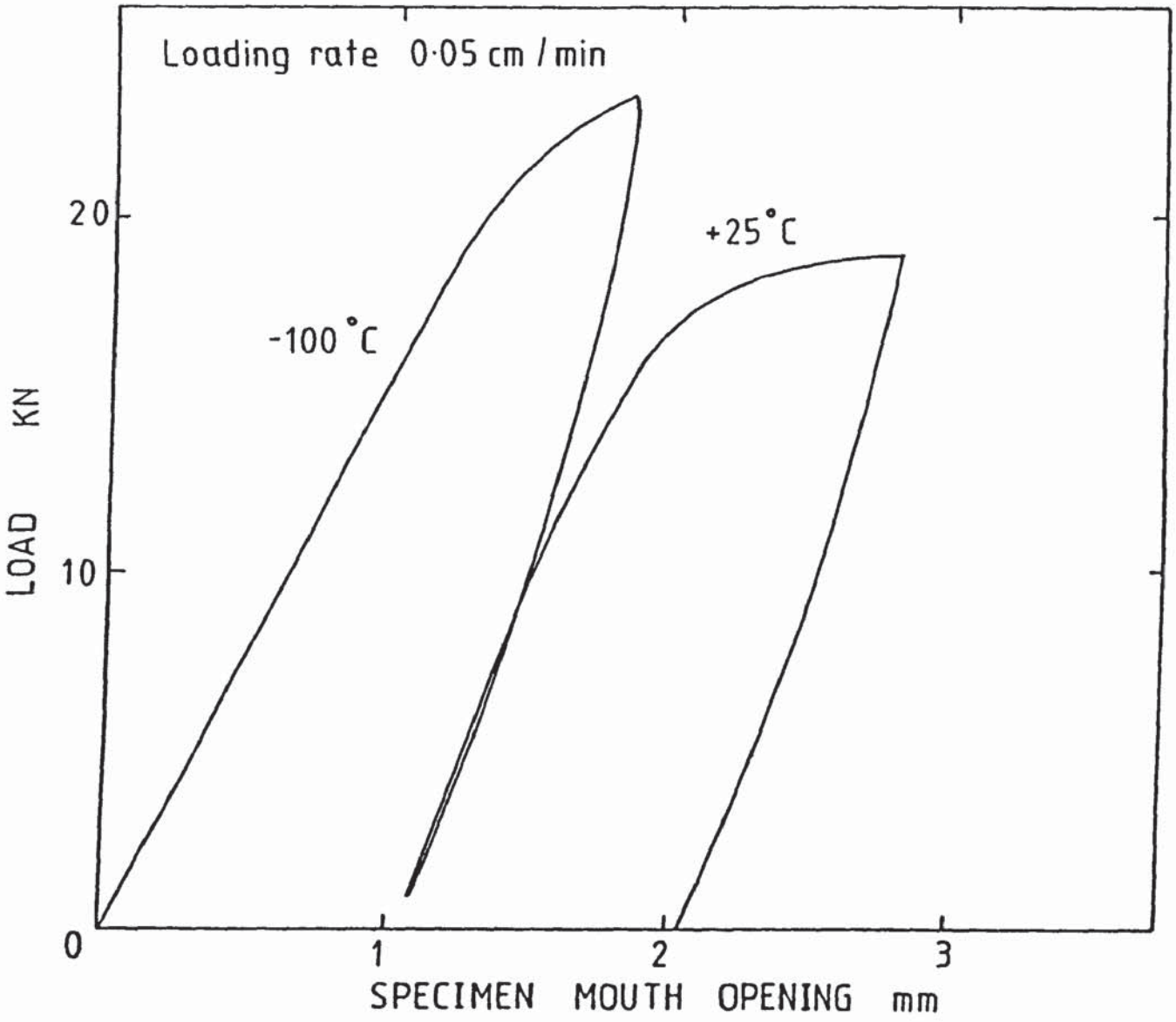

FIGURE 7.13 Two cycles of the loading-unloading conducted at $-100^{o}C$ and $+25^{o}C$

Observation of the fracture surface shows that there is no evidence of slow crack growth by brittle cleavage.

Therefore, when the short bar specimens are tested at -80°C and -100°C, the macroscopically fracture processes consist of three stages of the side-slot root blunting in the vicinity of the chevron tip, slow ductile crack growth and finally rapid cleavage cracking. As the slow crack grows, notch tip sharpening increase. Subsequently, the stress triaxiality ahead of the growing crack tip increases. The transition of the fracture mode may be regarded to be due to the increase in stress triaxiality ahead of the growing crack tip or the increase in the ductile-brittle transition temperature. The rapid cleavage cracking may arrest at about half of the current load for the tests at -80°C, or may completely pass through the whole specimen for the tests at -100°C. This may be influenced by the stored elastic energy within the loading system. The high load and insufficient stiffness leads to more elastic energy stored in the cross-head and grips. Furthermore, brittle crack arrest becomes more difficult during the tests at -100°C, as soon as the rapid cracking initiates.

The blunting of the growing crack tip reduces the stress triaxiality. There must be a large amount of plastic strain resulting from loss of stress triaxiality. During the tests at -60°C, the longitudinal plastic shear strain,

$\bar{\varepsilon}^p$, at a growing crack tip, which is in 1.9 mm ahead of the chevron tip, is 0.304. The measurement was conducted by the method described in Section 5. The variation of the longitudinal displacement in the vicinity of the chevron tip is shown in Fig. 7.14. This plastic shear strain value of 0.304 is less than the plastic shear strain at the notch root of the standard CVN and side-grooved CVN specimens, but larger than the plastic shear strain at crack tip of the pre-cracked CVN specimens during slow bend instability at room temperature.

The slow crack growth by microvoid coalescence needs a large amount of plastic deformation. Although the extent of ductile crack growth during the tests at $-100^{o}C$ is very small, such as 30 to 500 μm, the F values for calculating the fracture toughness in short bar specimens probably just associate with the ductile fracture mode. Thus the K_{ICSB} values may be expected to be higher than those measured in large specimens, where initiation is by cleavage. Therefore it may be thought that the ductile crack initiation has large influence on the plane strain fracture toughness over-estimation of the small short bar specimens, tested at $-80^{o}C$ and $-100^{o}C$.

Fortunately, the short bar experiments indicate a very good reproducibility for different test temperatures. The degree of scatter of the testing results is very

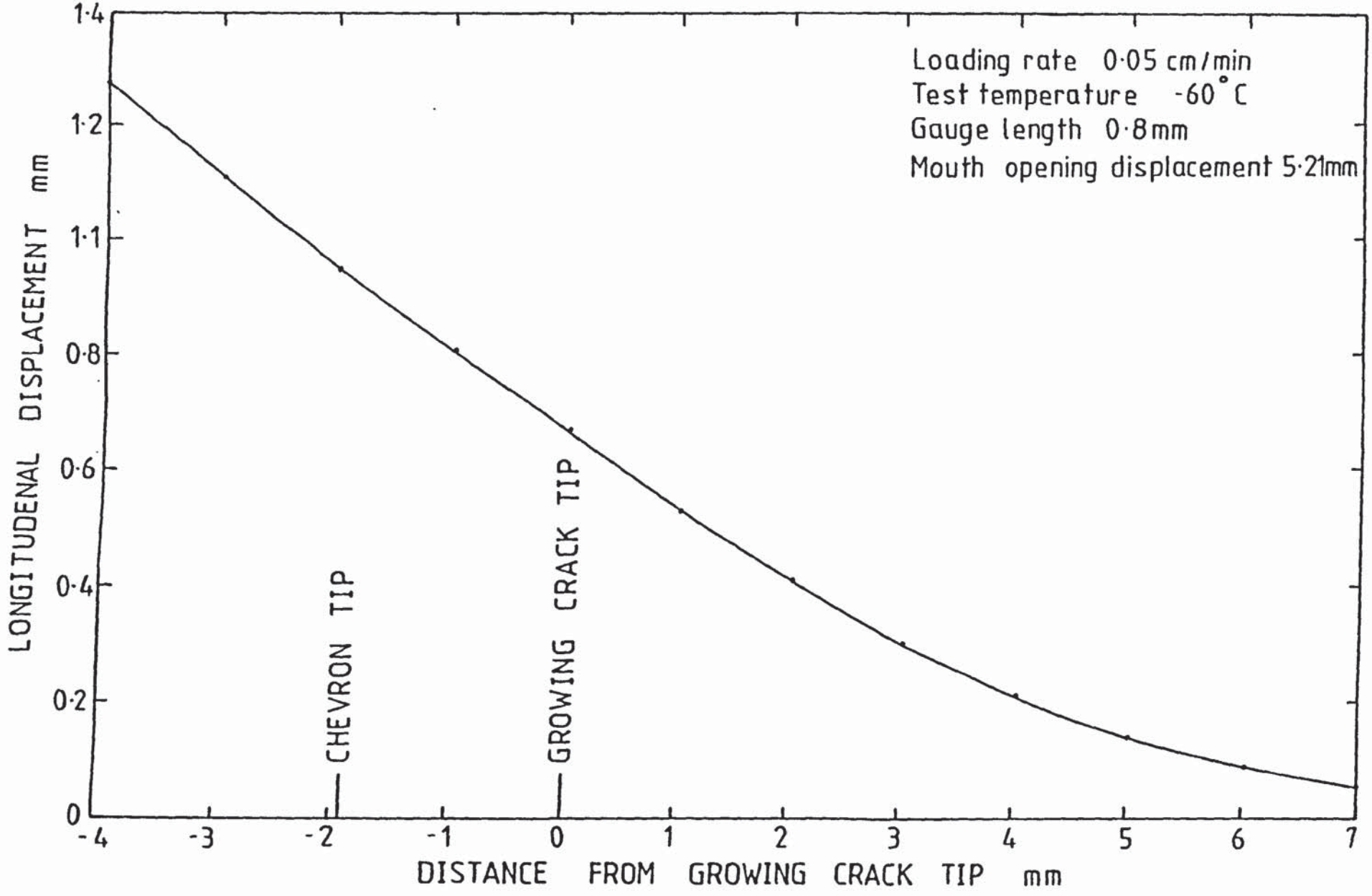

FIGURE 7.14 Longitudinal displacement field for short bar specimen

small,even though the small specimens may be sampled from the different region exhibited different local toughness. It may be expected that the overestimation of the plane strain fracture toughness in the short bar specimens is not related with the sampling location, which leads to a Weibull type phenomenon [14], but related with the fracture mode at crack initiation. Compared with the Pisarski's results of valid K_{IC} tests, the plane strain fracture toughness is overestimated from short bar tests by a factor of 2. The values of the K_{IC} and K_{ICSB} are shown in Fig. 7.15.

The elastic-plastic fracture toughness, K_{IJ}, measured from the pre-cracked side-grooved specimens is also shown in Fig. 7.15. Although the stress triaxiality is rather high in the pre-cracked side-grooved specimens, the K_{IJ} values are still larger than the values measured in the 100 mm thick specimens. For a specimen tested at -80°C, SEM examinations indicate the presence of microvoid coalescence ahead of the stretch zone. The average extent of the slow crack growth along the crack front is about 27 μm, as shown in Plate 7.5 (a); but Plate 7.5 (b) also shows that there is very little slow crack growth region following the stretch zone in the central region, but considerable slow crack growth near the side faces. Such that the maximum extent of slow crack growth may rise to about 100 μm. It may be thought that the rather large K_{IJ} values arise because of the slow crack growth near the side faces. A similar feature arises in the short bar tests where again the crack front has the "wrong" curvature.

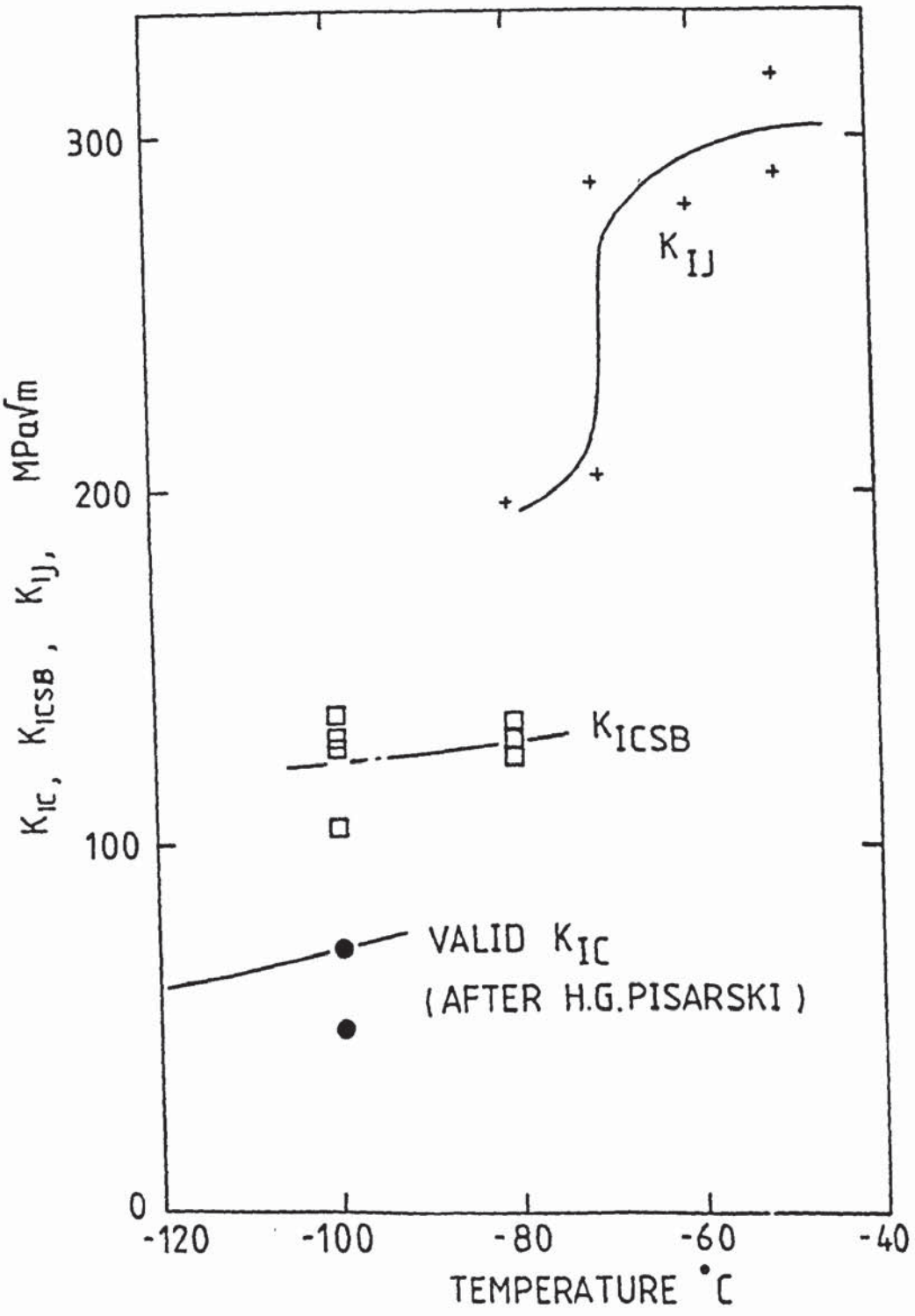

FIGURE 7.15 Overestimation of plane strain fracture toughness, based on small specimen tests.

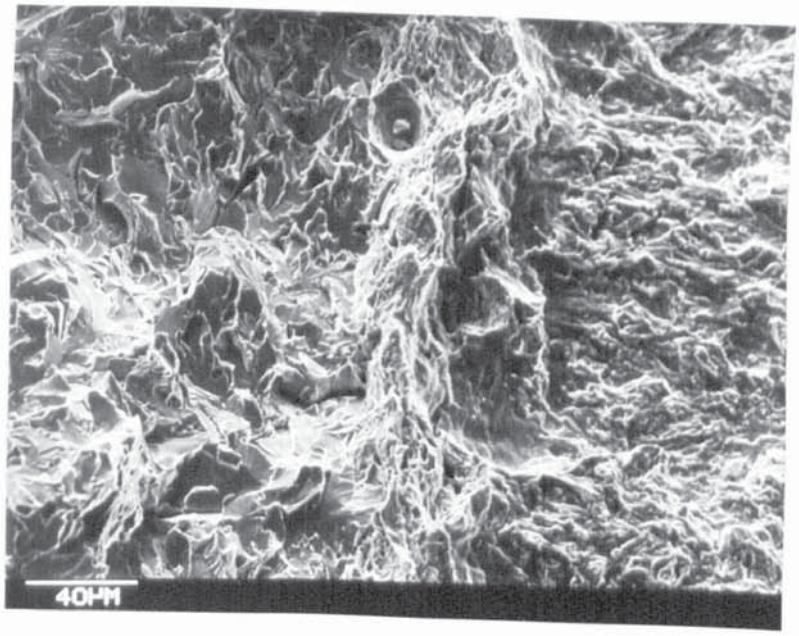

(a) A small ductile crack extension after stretch zone

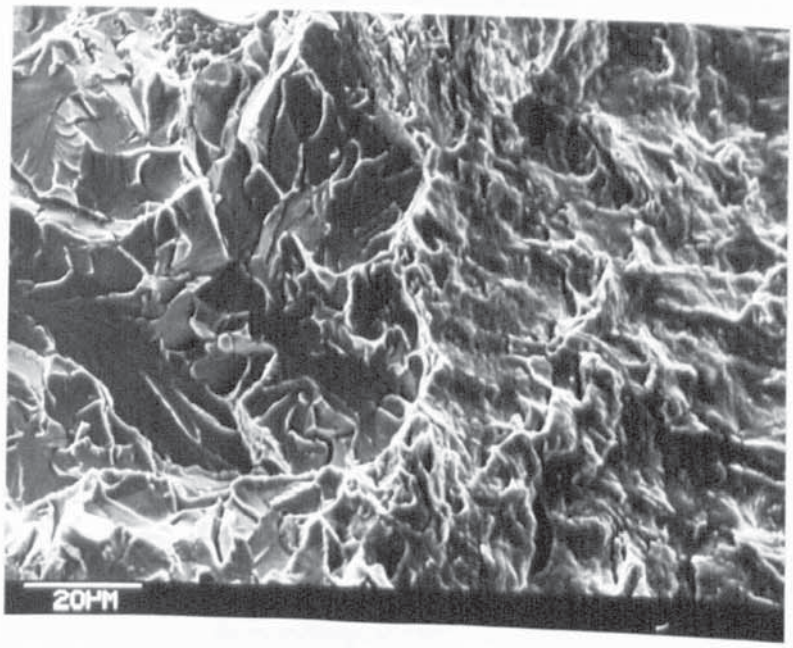

(b) A region where crack extension is cleavage after stretch zone

Plate 7.5 : Fracture appearance of a pre-cracked side-grooved specimen tested at -80°C (δ_c= 0.198 mm, K_{IJ}=207.6 MPa$\sqrt{m}$).

The larger J_c values for calculating the K_{IJ} values are not a valid J_{IC} values.

Therefore, it is felt that the micromode of fracture initiation has a significant influence on fracture toughness. Although the small specimens may have a sufficient constraint, and very small extent of the ductile crack growth, the overestimation of the plane strain fracture toughness may still occur because of slow crack growth near the side surfaces which becomes a significant proportion of the crack front length.

Section 8

CONCLUSIONS

1. Experimental investigations of a BS4360 Grade 50 D steel with low sulphur content show that voids occur mainly at inclusions of MnS, Al_2O_3 and CaO or their mixtures. Occasionally, voids also occur at MnO, FeO or the inclusion containing cobalt. Voids mainly form by the separation of the interface between the ferrite matrix and non-metallic inclusions. Some smaller voids associated with submicrometer Fe_3C particles can be found in the matrix at local higher constraint.

2. In tensile tests where specimens were stopped and sectioned at various strains, void nucleation has directly observed at a plastic shear strain of 0.003. Void counting versus strain experiments were used to extrapolate back to zero void numbers and thus gave a nucleation strain of 0.002. The void nucleation strain is only a few times the yield strain. Additionally, the relative void volume at the nucleation strain is estimated to be 0.0018.

3. Based on the smooth tensile specimen tests, the average void diameter slowly increases and the mean nearest-neighbour void spacing slowly decreases with increasing the plastic shear strain.

4. The void growth coefficient of 3.83, determined by the smooth tensile specimen and pre-cracked side-grooved bend specimen tests, may be applicable over a wide range of constraints.

5. The stress triaxiality ahead of the notch or crack tip may be evaluated by the void growth studies given the calibration curve for the material. The investigated results from the different modified CVN specimen geometries tested by slow bend at room temperature indicate that the state of the plane strain has already been attained ahead of the notch in the mid-thickness of the standard CVN specimens at and just after crack initiation. Severe stress triaxiality is generated ahead of precrack tip in the pre-cracked side-grooved specimens. Both side-grooves and precrack with a certain $^{a}/_{W}$ ratio are the effective stress triaxiality raisers.

6. Side-grooving and precracking significantly changes the characteristics of the longitudinal deformation fields ahead of the notch tip in the Charpy-size bend specimens. The singularity of the longitudinal strain field ahead of the notch tip is much weaker in the pre-cracked or side-grooved specimens than in the notched or nonside-grooved specimens.

7. For the low triaxiality, exhibited in the notched specimens, it is a valid approximation that the stress triaxiality may be evaluated from the Rice-Tracey theoretical relation in a perfectly plastic material. However, for the high triaxiality, exhibited in the pre-cracked specimens, it is necessary to consider the effect of strain hardening on the stress triaxiality.

8. According to the investigation of the void growth coefficient, the void growth increases with the stress triaxiality, and decreases with strain hardening. The net void growth arising from these two factors is decelerated in the hardening material for the values of the stress triaxiality, $\sigma_m/\bar{\sigma}$, more than about one.

9. There is a peak in the void growth rate at the distance of about $1.2\delta_t$ ahead of the blunting crack tip in the pre-cracked side-grooved CVN specimens at room temperature. The maximum in the void growth is related to the combination of decreasing strain and increasing stress triaxiality with the distance in the immediate vicinity of the crack tip. There is no obvious peak in the void growth rate ahead of the notch root during crack initiation in the standard CVN specimens.

10. For the pre-cracked side-grooved specimens, the stress triaxiality evaluated from HRR field analysis is only appropriate at the distance beyond the $^{x}/\delta_{t}>1$ in our investigated range ($^{x}/\delta_{t}$= 0.25 to 2.25). As the crack tip is approached ($^{x}/\delta_{t}<1$), the hydrostatic stress rapidly reduces.

11. The critical void volume at fracture initiation increases with the stress triaxiality in the investigated triaxiality range. Higher triaxiality associated with a certain plastic strain will lead to the more opportunity for the void nucleation and growth. Maximum value of the critical void volume of $(Vv)_{c}\simeq 0.01$ is found in the pre-cracked side-grooved specimens, and $(Vv)_{c}\simeq 0.003$ is found in the standard CVN specimens.

12. The effect of the specimen constraint on the ductile-brittle transition behaviour may be explained by the void growth rate studies. The higher the void volume growth against the COD value is, the higher the ductile-brittle transition temperature is. Thus the pre-cracked side-grooved specimen has the highest transition temperature in the different modified CVN specimens.

13. Variations of the stress triaxiality in front of the notch or crack tip under general yielding condition may be estimated by the plastic strain field and void growth investigations. Usually the peak position of the void growth is nearer notch tip in the pre-cracked side-grooved specimen than in the standard CVN specimen. For the standard CVN specimen, the variation of the stress triaxiality in the vicinity of the notch root may be approximately described by the slip-line field solution. However, for the pre-cracked side-grooved specimen, the variation of the triaxiality may be described by the experimental void growth relation which is strongly affected by the strain hardening.

14. In the CVN impact tests, side-grooves lead to increasing the transition temperature and decreasing the scatter of the energy absorption in the transition region. The smaller scatter occurred in the transition temperature region for the side-grooved CVN specimens is not related with the sampling location, but is more likely to be a consequence of the higher constraint. The energy absorption per unit fracture area and lateral deformation at upper shelf temperature

are smaller for the side-grooved CVN specimens than for the standard CVN specimens. The influence of side-grooves on the energy absorption and lateral deformation of the CVN specimens at upper shelf are mainly controlled by the elimination of the shear lips and increasing the proportion of the plane strain zone in the fracture surface.

15. The elastic-plastic fracture toughness values from small laboratory tests, such as short bar tensile specimen and pre-cracked side-grooved bending specimen, may give large overestimates of valid K_{IC} values in the testing material. It is felt that the micromode of fracture initiation can have a significant influence on fracture toughness. Small pre-cracked side-grooved bend specimens may have a sufficient constraint and very small extent of the ductile crack growth in the centre but extensive slow crack growth may occur near the side surfaces and this will tend to increase the fracture toughness value.

Section 9

REFERENCES

1. J. T. Barnby, The need for fracture control, Fracture Mechanics, Series 6, Non-destructive Testing. August 1972, pp.229-234.

2. S. T. Rolfe and J. M. Barsom, Fracture and fatigue control in structures. Applications of fracture mechanics, Prentice-Hall, Inc., Englewood Cliffs, New Jersey 1977.

3. The <<Alexander L. Kielland>>accident, Norwegian Public Reports, NOU 1981:11 March 1981, Norway.

4. M. G. Dawes, Introduction, Developments in Fracture Mechanics - 1, Edited by G. G. Chell, Applied Science Publishers Ltd, London 1979.

5. A. A. Griffith , The phenomena of rupture and flow in solids, Philosophical Transactions, Royal Society of London, Series A, Vol. 221, March 1920, pp. 163-198.

6. G. Irwin, Fracture dynamics, Fracturing of Metals, Published by the American Society for Metals, Cleveland, Ohio, 1948, pp.147-166.

7. G. R. Irwin and J. A. Kies, Fracturing and fracture dynamics, Welding Journal, AWS. Vol.31, 1952, pp. 95s-100s.

8. G. R. Irwin and J. A. Kies, Critical energy rate analysis of fracture strength, Welding Journal, AWS. Vol. 33, 1954, pp. 193s-198s.

9. G. R. Irwin, Analysis of stresses and strains near the end of a crack transversing a plate, Journal of Applied Mechanics, Vol. 24, 1957, pp. 361-364.

10. J. T. Barnby, An introduction to fracture mechanics, Fracture mechanics, Series 2, Non-destructive Testing, Dec. 1971, pp.385-390.

11. G. Green and J. F. Knott, Effects of side grooves on initiation and propagation of ductile fracture, Metals Technology, Sept. 1975, pp. 422-427.

12. R. O. Ritchie, W. L. Server and R. A. Wullaert, A single test method for measuring 'valid' J_{IC} fracture toughness in Charpy-size surveillance specimens of nuclear pressure vessel steel, International Journal of Fracture, Vol. 14, 1978, R329-R334.

13. W. R. Andrews and C. F. Shih, Thickness and side-groove effects on J- and δ-resistance curves for A533B steel at 93°C, Elastic-Plastic Fracture, ASTM STP668, American Society for Testing and Materials, Philadelphia, 1979, pp. 426-450.

14. J. D. Landes and D. H. Shaffer, Statistical characterization of fracture in the transition region. Fracture Mechanics: Twelfth Conference, ASTM STP700, American Society for Testing and Materials, 1980, pp.368-382.

15. Methods of test for plane strain fracture toughness (K_{IC}) of metallic materials, BS.5447:1977.

16. Standard test method for plane strain fracture toughness of metallic materials, ANSI/ASTM E399-78a, Part 10, ASTM Annual Standards.

17. A. A. Wells, Application of fracture mechanics at and beyond general yielding, British Welding Journal, Vol. 10, Nov. 1963.

18. A. A. Wells, Notched bar tests, fracture mechanics and the brittle strengths of welded structures, British Welding Journal, Vol. 12, Jan. 1965.

19. D. S. Dugdale, Yielding of steel sheets containing slits, Journal of the Mechanics and Physics of Solids, Vol. 8, 1960, pp.100-104.

20. Methods for Crack Opening Displacement (COD) testing BS.5762:1979, British Standard Institution.

21. T. C. Harrison and G. D. Fearnehough, The influence of specimen dimensions on measurements of the ductile crack opening displacement, International Journal of Fracture Mechanics, Vol. 5, 1969, pp. 348-349.

22. J. M. Lowes and G. D. Fearnehough, The detection of slow crack growth in crack opening displacement specimens using an electrical potential method, Engineering Fracture Mechanics, Vol. 3, 1971, pp. 103-108.

23. J. T. Barnby and I. S. Al-Daimalani, Assessment of the fracture toughness of cast steels, Part I, low alloy steels, Journal of Materials Science, Vol. 11, Nov. 1976, pp. 1979-1988.

24. G. D. Fearnehough and B. Watkins, Application of the crack opening displacement approach to the prediction of pressurised tube failure, The International Journal of Fracture Mechanics, Vol. 4, No. 3, Sept. 1968, pp. 233-243.

25. P. Terry, the fracture toughness of low alloy steel, Ph. D, Thesis, the University of Aston in Birmingham, March 1972.

26. J. N. Robinson and A. S. Tetelman, Measurement of K_{IC} on small specimens using critical crack tip opening displacement, Fracture Toughness and Slow-stable Cracking, ASTM STP 559, American Society for Testing and Materials, 1974, pp.139.

27. C. G. Chipperfield, J. F. Knott, and R. F. Smith, Critical crack opening displacement in low strength steels, 3rd International Conference on Fracture, Munich 1973.

28. C. E. Turner, Methods of post-yield fracture safety assessment, Post-Yield Fracture Mechanics, Edited by D. G. H. Latzko, Applied Science Publishers, London, 1979, pp. 23-210.

29. J. R. Rice, A path independent integral and the approximate analysis of strain concentration by notches and cracks, Journal of Applied Mechanics Transactions ASME, Vol. 35 June 1968, pp. 379-386.

30. P. C. Paris, Fracture mechanics in the elastic-plastic regime, Flaw Growth and Fracture, ASTM STP 631, American Society for Testing and Materials, 1977, pp. 3-27.

31. G. A. Clarke, W. R. Andrews, J. A. Begley, J. K. Donald, G. T. Embley, J. D. Landes, D. E. McCabe and J. H. Underwood. A procedure for the determination of ductile fracture toughness values using J-integral techniques, Journal of Testing and Evaluation, JTEVA, Vol. 7, No. 1, Jan. 1979, pp. 49-56.

32. J. D. Landes and J. A. Begley, Test results from J integral studies: an attempt to establish a J_{IC} testing procedure, Fracture Analysis, ASTM STP 560, American Society for Testing and Materials, 1974, pp. 170-186.

33. J. R. Rice, P. C. Paris and J. G. Merkle, in progress in flaw growth and fracture toughness testing, ASTM, STP536,American Society for Testing and Materials Philadelphis, 1973, pp. 231-245.

34. G. A. Clarke, W. R. Andrews, P. C. Paris and D. W. Schmidt, Single specimen tests for J_{IC} determination, Mechanics of Crack Growth, ASTM, STP590, 1976, pp. 27-42.

35. J. D. Landes and J. A. Begley, Experimental methods for elastic-plastic and post-yield fracture toughness measurements, Post-Yield Fracture Mechanics, Edited by D. G. H. Latzko. Applied Science Publishers, London 1979, pp. 211-253.

36. J. N. Robinson, An experimental investigation of the effect of specimen type on the crack tip opening displacement and J-integral fracture criteria, International Journal of Fracture, Vol. 12, 1976, pp. 723-739.

37. P.M.S.T. De Castro, J. Spurrier and P. Hancock, Comparison of J testing techniques and correlation J-COD using structural steel specimens, International Journal of Fracture, Vol. 17, No. 1, Feb. 1981.

38. J. W. Hutchinson, Singular behaviour at the end of a tensile crack in a hardening material, Journal of the Mechanics and Physics of Solids, Vol. 16, 1968, pp. 13-31.

39. J. W. Hutchinson, Plastic stress and strain fields at a crack tip, Journal of the Mechanics and Physics of Solids, Vol. 16, 1968, pp.337-347.

40. J. R. Rice and G. F. Rosengren, Plane strain deformation near a crack tip in a power-law hardening material, Journal of the Mechanics and Physics of Solids, Vol. 16, 1968, pp.1-12.

41. C. F. Shih and M. D. German, Requirements for a one parameter characterization of crack tip fields by the HRR singularity, International Journal of Fracture, Vol. 17, No. 1 Feb. 1981, pp. 27-43.

42. BS.131: Part 2: 1972, Methods for notched bar tests, Part 2, The Charpy V-notch impact test on metals,British Standards Institution.

43. R. O. Ritchie, W. L. Server and R. A. Wullaert, Discussion of 'A simple test method for measuring 'valid' J_{IC} fracture toughness in Charpy-size surveillance specimens of nuclear pressure vessel steel', International Journal of Fracture, Vol. 15, 1979, R139-141.

44. R. H. Sailors and H. T. Corten, Relationship between material fracture toughness using fracture mechanics and transition temperature tests, Stress Analysis and Growth of Cracks, ASTM STP 514, American Society for Testing and Materials, 1972, pp.164-191.

45. G. M. Orner and C. E. Hartbower, Sheet fracture toughness evaluated by Charpy impact and slow bend, Welding Journal, Vol. 30, No. 9, 1961, pp. 405S-416S.

46. T. J. Koppenaal, Dynamic fracture toughness measurements of high strength steels using Precracked Charpy Specimens in Instrumental Impact Testing, ASTM, STP563, American Society for Testing and Materials, 1974, pp. 92-117.

47. J. M. Barsom, Development of the AASHTO fracture-toughness requirements for bridge steels, Engineering Fracture Mechanics, Vol. 7, No. 3, 1975, pp. 605-618.

48. A. A. Willoughby, Discussion : 'A simple test method for measuring 'valid' J_{IC} fracture toughness in Charpy-size surveillance specimens of nuclear pressure vessel steel', International Journal of Fracture, Vol. 15, 1979, R125-R126.

49. L. M.Barker, A simplified method for measuring plane strain fracture toughness, Engineering Fracture Mechanics, Vol. 9, 1977, pp. 361-369.

50. L. M.Barker, Short rod and short bar fracture toughness specimen geometries and test methods for metallic materials, Terra Tek Report, TR80-11, March 1980.

51. L. M. Barker and R. V. Guest, Compliance calibration of the short rod fracture toughness specimen, Terra Tek Report, TR78-20, April 1978.

52. R. T. Bubsey, D. Munz, W. S. Pierce, and J. L. Shannon, Compliance calibration of the short rod chevron-notch specimen for fracture toughness testing of brittle materials, International Journal of Fracture, Vol. 18, No. 2, 1982, pp. 125-133.

53. J. T. Barnby and S. B. Biner, Experimental and analytical determination of stress intensity coefficients and compliance functions of non-standard short-bar fracture toughness test specimens, to be published, 1982.

54. J. F. Beech and A. R. Ingraffea, Three-dimensional finite element calibration of the short-rod specimen, International Journal of Fracture, Vol. 18, No. 3, 1982, pp. 217-229.

55. L. M. Barker and F. I. Baratta, Comparisons of fracture toughness measurements by the short rod and ASTM standard method of test for plane strain fracture toughness of metallic materials (E399-78), Journal of Testing and Evaluation, JTEVA, Vol. 8, No. 3, May 1980, pp. 97-102.

56. L. M. Barker, Theory for determining K_{IC} from small, non-LEFM specimens, supported by experiments on aluminium, Internaiton Journal of Fracture, Vol. 15, No. 6, Dec. 1979, pp.515-536.

57. L. M. Barker, Data analysis methods for short rod and short bar fracture toughness tests of metallic materials, Terra. Tek Report, TR80-12, March 1980.

58. Failure Analysis and Prevention, Metals Handbook, Vol. 10, 8th edition, American Society for Metals 1975, p. 61.

59. E. Smith, Cleavage fracture in mild steel, International Journal of Fracture Mechanics, Vol. 4, Nr. 2, June 1968, pp. 131-145.

60. Jun Kameda and C. J. McMahon, Solute segregation and brittle fracture in an alloy steel, Metallurgical Transactions A, Vol. 11A, Jan.1980, pp. 99-101.

61. J. T. Barnby, The initiation of ductile failure by fractured carbides in an austenitic stainless steel, ACTA Metallurgica, Vol. 15, May 1967, pp. 903-909.

62. D. A. Curry and P. L. Pratt, The role of second phase particles in the ductile fracture of higher carbon steels, Metal Science Engineering Vol. 37, 1979, p.223.

63. J. T. Barnby and M. R. Johnson, Fracture in pearlitic steels, Metal Science Journal, Vol. 3, 1969, pp. 155-159.

64. D. A. Curry and J. F. Knott, Current aspects of crack growth under monotomic loading.

65. G. T. Hahn, R. G. Hoagland, and A. R. Rosenfield, The variation of K_{IC} with temperature and loading rate, Metallurgical Transactions, Vol. 2, Feb. 1971, pp. 537-541.

66. J. Malkin and A. S. Tetelman, Relation between K_{IC} and microscopic strength for low alloy steels, Engineering Fracture Mechanics, Vol. 3, 1971, pp. 151-167.

67. R. O. Ritchie, J. F. Knott and J. R. Rice, On the relationship between critical tensile stress and fracture toughness in mild steel, Journal of the Mechanics and Physics of Solids, Vol. 21, 1973, pp. 395-410.

68. R. O. Ritchie, W. L. Server, and R. A. Wullaert, Critical fracture stress and fracture strain models for the prediction of lower and upper shelf toughness in nuclear pressure vessel steels, Metallurgical Transactions A, Vol.10A, Oct. 1979, pp. 1557-1570.

69. A. C. Mackenzie, J. W. Hancock and D. K. Brown, On the influence of state of stress on ductile failure initiation in high strength steels, Engineering Fracture Mechanics, Vol. 9, 1977, pp. 167-188.

70. R. K. Pandey and S.Banerjee, Strain induced fracture in low strength steels, Engineering Fracture Mechanics Vol. 10, 1978, pp. 817-829.

71. J. R. Rice and D. M. Tracey, On the Ductile enlargement of voids in triaxial stress fields, Journal of the Mechanics and Physics of Solids Vol. 17, 1969, pp. 201-217.

72. D. A. Shockey, K. C. Dao, L. Seaman, R. Burback and D. R. Curran, Computational modelling of microstructural fracture processes in A533B pressure vessel steel, NP-1398. Final Report, Electric Power Research Institute, May 1980.

73. S. H. Good and L. M. Brown, The Nucleation of cavities by plastic deformation, Overview No. 1, Acta Metallurgica, Vol. 27, 1979, pp. 1-15.

74. J. W. Hancock and A. C. Mackenzie, On the mechanisms of ductile failure in high-strength steels subjected to multi-axial stress-states, Journal of the Mechanics and Physics of Solids, Vol. 24, 1976, pp. 147-169.

75. F. A. McClintock, a criterion for ductile fracture by the growth of holes, Transactions ASME, Series E, Journal of Applied Mechanics, Vol. 35, 1968, pp. 363-371.

76. BS.4360_1979, Specifications for weldable structural steels, British Standards Institution.

77. F. B. Pickering, The basis of quantitative metallography, Metals and Metallurgy Trust for the Institute of Metallurgical Technicians.

78. Standard method for estimating the average grain size of metals, ASTM. E112-80, Annual Book of ASTM Standards, Part II.

79. J. R. Fisher and J. Gurland, Void nucleation in spheroidized carbon steels, Part 1 : Experimental, Metal Science, May 1981, pp.185-192.

80. N. L. Coldman and J. W. Hutchinson, Fully plastic crack problems : the centre-cracked strip under plane strain, International Journal of Solids and Structures, Vol. 11, 1975, pp.575-591.

81. V. Kumar, M. D. German and C. F. Shih, An Engineering Approach for Elastic-Plastic Fracture Analysis, NP-1931, Research Project 1237-1, Topical Report, Electric Power Research Institute, July 1981.

82. J. T. Barnby, Notes on Yielding Fracture Mechanics, April 1982.

83. Rapid inexpensive tests for determining fracture toughness, National Materials Advisory Board, National Academy of Sciences, Washington, D.C., 1976.

84. W. L. Serven, R. A. Wullaert, and R. O. Ritchie, On the use of side-grooves in estimating J_{IC} fracture toughness with Charpy-size specimens, Transactions of the ASME, Journal of Engineering Materials and Technology, Vol. 102, April 1980, pp. 192-199.

85. M. G. Dawes, Elastic-plastic fracture toughness based on the COD and J-contour integral concepts, Elastic-Plastic Fracture, ASTM STP 668, American Society for Testing and Materials, 1979, pp.307-333.

86. George Succop, R. T. Bubsey, M. H. Jones and W. F. Brown, Investigation of some problems in developing standards for pre-cracked Charpy slow bend tests, Developments in Fracture Mechanics Test Methods Standardisation, ASTM STP632, American Society for Testing and Materials, Philadelphia, 1977, pp. 153-178.

87. Standard methods and definitions for mechanical testing of steel products, ASTM A370-77, Annual Book of ASTM Standards, 1980.

88. I. Milne and D. A. Curry, The effect of triaxiality on ductile-cleavage transitions in a pressure vessel steel, 1980.

89. D. Munz and H. P. Keller, Effect of specimen size on fracture toughness in the ductile brittle transition region of steel, 1981.

90. I. Milne and G. G. Chell, Effect of size on the J fracture criterion, Elastic-Plastic Fracture, ASTM STP668, American Society for Testing and Materials, 1979, pp. 358-377.

91. J. D. Harrison, The 'state-of-the-art' in crack tip opening displacement (CTOD) testing and analysis, Metal Construction, Sept. and Oct.1980.

92. W. L. Server, General yielding of Charpy V-notch and precracked Charpy specimens, Transactions of the ASME, Journal of Engineering Materials and Technology, Vol. 100, April 1978, pp. 183-188.

93. D. Munz, R. T. Bubsey, and J. L. Shannon, Performance of chevron-notch short bar specimen in determining fracture toughness of silicon nitride and aluminium oxide, Journal of Testing and Evaluation, JTEVA, Vol. 8, No. 3, 1980, pp. 103-107.

94. L. M. Barker, Specimen size effects in short rod fracture toughness measurements, Sandia National Laboratories, Albuquerque, New Mexico 87185.

95. The fractometer II systems 4210 and 4211 owner's manual. Terra Tek, 1980.

96. J.C.Lautridou and A. Pineau, Crack initiation and stable crack growth resistance in A508 steels in relation to inclusion distribution, Engineering Fracture Mechanics Vol. 15, No. 1-2, 1981, pp. 55-71.

97. D. M. Norris, Jr. Computer simulation of the Charpy V-notch toughness test, Engineering Fracture Mechanics, Vol. 11, 1979, pp.261-274.

98. G. LeRey, J. D. Embury, G. Edward and M. F. Ashby, A model of ductile fracture based on the nucleation and growth of voids, Acta Metallurgica, Vol. 29, No. 8, 1981, pp. 1509-1522.

99. D. M. Tracey, Strain-hardening and interaction effects on the growth of voids in ductile fracture, Engineering Fracture Mechanics, Vol. 3, 1971, pp. 301-315.

100. F. M. Beremin, Study of fracture criteria for ductile rupture of A508 steel, Advances in Fracture Research, Ed. D. Francois, 1981, pp. 809-816.

101. P. Farsetti and P. Bufalini, Measurement of COD values at crack initiation in steels exhibiting delamination, Metal Construction, Vol.13, No.8, 1981, pp. 464-465.

102. R. Hill, The Mathematical Theory of Plasticity, Clarendon Press, Oxford, 1950, p. 248.

103. J. W. Hancock and M. J. Cowling, Role of state of stress in crack-tip failure processes, Metal Science, Vol. 14, 1980, pp. 293-304.

104. J. R. Rice and M. A. Johnson, The role of large crack tip geometry changes in plane strain fracture, Inelastic Behaviour of Solids, Ed. by M. F. Kanninen, et al, McGraw-Hill Book Company, 1970, pp. 641-672.

105. Phuc Nguyen - Duy and Serge Bayard, Brittle-ductile transition curve determined by Charpy impact testing on CVN, precracked CVN and side-grooved precracked CVN specimens, International Journal of Fracture, Vol. 18, No. 2, 1982, R23-29.

106. H. G. Pisarski, Influence of thickness on critical crack opening displacement (COD) and J values, International Journal of Fracture, Vol. 17, No. 4, 1981, pp. 427-440.

107. L. M. Barker, A letter to Dr. Kevin Selby, Nov. 17, 1980, Terra Tek.